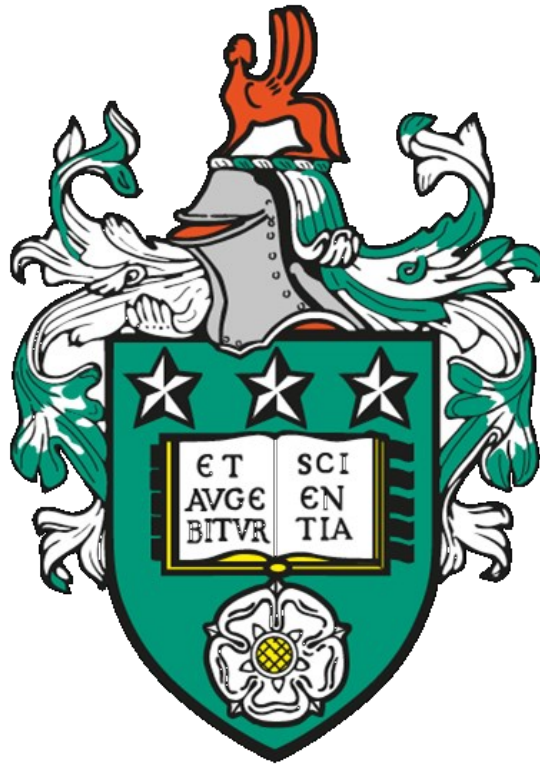


# Experimental Validation of Pulsed Sieve-Plate Extraction Column Models



Alexander Scott Fells

The University of Leeds

School of Chemical and Process Engineering

March 2023

Submitted in accordance with the requirements for the degree of

Doctor of Philosophy

The candidate confirms that the work submitted is their own, except where work which has formed part of jointly authored publications has been included. The contribution of the candidate and the other authors to this work has been explicitly indicated below. The candidate confirms that appropriate credit has been given within the thesis where reference has been made to the work of others.

The work in chapter 6 of the thesis has appeared in publication as follows:

Predicting Mass Transfer in Liquid–Liquid Extraction Columns, 2022, Fells, A., De Santis, A., Colombo, M., Theobald, D.W., Fairweather, M., Muller, F. and Hanson, B.

The author was responsible for sections 1, 2, 3.2 and 4 and Andrea De Santis was responsible for sections 1, 2 and 3.1.

All other authors contributed towards the review and editing of the manuscript.

This copy has been supplied on the understanding that it is copyright material and that no quotation from the thesis may be published without proper acknowledgement.

The right of Alexander Scott Fells to be identified as Author of this work has been asserted by Alexander Scott Fells in accordance with the Copyright, Designs and Patents Act 1988.

## ACKNOWLEDGEMENTS

My sincerest thanks go to my supervisors, Professor Bruce Hanson and Professor Frans Muller, for their guidance and support throughout this project. Without their insight and encouragement, I wouldn't have been able to develop as an independent researcher. I'm immensely grateful for the assistance they've provided.

I'm also thankful to all those who have contributed to the successful completion of my thesis. In particular, I want to express my deepest appreciation to Dr Daniel Theobald for the invaluable advice, guidance and friendship he has provided. Dr Alastair Baker, Dr Andrea De Santis, Dr Kieran Jervis, and Maram Al-Sayaghi have also given me invaluable guidance and fruitful discussions. I'm also grateful to Chris Bulman and Alex Holdsworth for their technical assistance, advice, and guidance. Finally, I thank the University of Leeds Nuclear Engineering group for their support and encouragement.

I want to express my sincerest gratitude to my wife Ellie and my family, who have been an unwavering source of support and encouragement throughout my PhD journey.

## ABSTRACT

Pulsed Sieve-plate Extraction Columns (PSECs) are a counter-current solvent extraction unit operation used in a variety of industries. They are notoriously hard to design due to their complex hydrodynamics and traditionally this has necessitated pilot plant study or the use of empirical correlations which result in expensive oversized columns. This thesis presents the development and validation of a modelling and simulation framework for PSECs using a combination of Computational Fluid Dynamics (CFD) and Compartment Modelling.

A PSEC pilot plant was used to generate experimental data to validate CFD-predicted droplet size distribution, mean values and rise velocities with good agreement between the two. The model was further developed to predict mass transfer and accurately model the axial solute concentrations in both phases.

Due to the large amount of time required to perform the simulation, an alternative Compartment Modelling approach was developed using the results of a CFD-predicted residence time distribution study and the resulting model accurately predicted mass transfer performance over a range of operating conditions. The model was further developed to predict the hydrometallurgical PUREX (Plutonium, Uranium, Reduction, Extraction) process using tributyl phosphate, uranium and nitric acid and was experimentally validated over a range of operating conditions, successfully predicting the transient evolution of solute concentrations at the column outlets.

The resulting modelling and simulation framework provides an accurate predictive tool for predicting PSEC performance and provides a foundation for further exploration of the hydrodynamics and mass transfer performance of PSECs.

## CONTENTS

|   |    |
|---|----|
| 1. Introduction.....  | 1  |
| 1.1. Project Motivation.....  | 1  |
| 1.2. Aim and objectives.....  | 3  |
| 1.3. Novelty of research.....   | 4  |
| 1.4. Thesis structure .....   | 4  |
| 2. Literature Review.....   | 7  |
| 2.1. Liquid-liquid extraction .....   | 7  |
| 2.2. Operational envelope .....   | 17 |
| 2.3. Droplet diameter .....   | 22 |
| 2.4. Dispersed phase holdup.....  | 28 |
| 2.5. Mass transfer.....   | 31 |
| 2.6. Modelling and simulation.....  | 35 |
| 3. The design and commissioning of a Pulsed Sieve-plate Extraction Column .....     | 44 |
| 3.1. Introduction.....  | 44 |
| 3.2. Design.....  | 44 |
| 3.3. Commissioning.....   | 52 |
| 4. The dispersed phase hydrodynamics of a Pulsed Sieve-plate Extraction Column..... | 53 |
| 4.1. Introduction.....  | 53 |
| 4.2. Methodology.....   | 54 |
| 4.3. Results and discussion.....  | 57 |
| 4.4. Summary .....  | 72 |

|  |     |
|--|-----|
| 5. Computational Fluid Dynamics simulation of Pulsed Sieve-plate Extraction Columns .... | 74  |
| 5.1. Introduction .....  | 74  |
| 5.2. Methodology.....  | 76  |
| 5.3. Results and discussion.....   | 92  |
| 5.4. Summary .....   | 103 |
| 6. Compartment modelling of Pulsed Sieve-plate Extraction Columns.....                   | 105 |
| 6.1. Introduction .....  | 105 |
| 6.2. Methodology.....  | 106 |
| 6.3. Results and discussion.....   | 110 |
| 6.4. Summary .....   | 127 |
| 7. Uranium extraction in a Pulsed Sieve-plate Extraction Column .....                    | 128 |
| 7.1. Introduction .....  | 128 |
| 7.2. Methodology.....  | 129 |
| 7.3. Results and discussion.....   | 134 |
| 7.4. Summary .....   | 141 |
| 8. Conclusions and Future work .....   | 143 |
| 8.1. Conclusions.....  | 143 |
| 8.2. Future work .....   | 146 |
| Bibilography .....   | 149 |
| Appendix 1 – P&ID equipment list.....  | 160 |
| Appendix 2 – P&ID Instrument list .....  | 161 |
| Appendix 3 – P&ID Valve list .....   | 162 |
| Appendix 4 – Axial solute concentrations .....   | 163 |
| Appendix 5 – Transient outlet compositions.....  | 173 |

## LIST OF TABLES

|  |     |
|--|-----|
| Table 1: Details of column geometry and operating parameters (Yadav and Patwardhan, 2008).....   | 16  |
| Table 2: Details of physical properties in experimental studies reviewed by Yadav and Patwardhan (2008).....   | 17  |
| Table 3: Correlations used to evaluate the phase-specific mass transfer coefficients for the absorption of acetone from water with fluid properties presented in Table 11, $d_{3,2} = 3.0$ mm, $U_s = 100$ mm.s <sup>-1</sup> , $\alpha = 10\%$ . (Attarakih et al., 2012). .... | 34  |
| Table 4: Summary of column geometry and operating parameters .....   | 49  |
| Table 5: Physical properties of water and Exxsol D80 at 20 °C (Zeppieri et al., 2001; Caudwell et al., 2004; Bajoria et al., 2013). ....   | 57  |
| Table 6: Investigated experimental conditions.....   | 57  |
| Table 7: Summary of column geometry and operating parameters (Garthe, 2006).....   | 85  |
| Table 8: Reported mesh quality using checkMesh utility. ....   | 86  |
| Table 9: Boundary conditions used for 3D LES case .....  | 87  |
| Table 10: Boundary conditions used for 2D URANS case .....   | 89  |
| Table 11: Fluid properties for mass transfer investigation (Garthe, 2006).....   | 90  |
| Table 12: Boundary conditions used for mass transfer case .....  | 91  |
| Table 13: $d_{3,2}$ and standard deviation, enclosed in brackets, for experimental, LES and URANS.....   | 94  |
| Table 14: Droplet rise velocity for experimental, LES and URANS.....   | 99  |
| Table 15: Overview of operational and performance parameters (Garthe, 2006) .....  | 106 |
| Table 16: Simulated experimental conditions and aqueous, solvent and total errors. ....  | 126 |
| Table 17: Calculated NTU and HTU.....  | 126 |
| Table 18: Physical properties of 3 mol.L <sup>-1</sup> nitric acid and 30 v% TBP in dodecane at 20 °C in the absence of uranium (Tian and Liu, 2007; Bajoria et al., 2013).....  | 130 |

|   |     |
|---|-----|
| Table 19: Physical properties of 0.001 mol.L <sup>-1</sup> nitric acid and 30 v% TBP in dodecane at 20 °C in the absence of uranium (Tian and Liu, 2007; Bajoria et al., 2013). ..... | 130 |
| Table 20: Experimental conditions and steady-state results. ....  | 135 |
| Table 21: Calculated RMSE from modelled experiments. ....   | 141 |
| Table 22: PSEC pilot plant equipment list. ....   | 160 |
| Table 23: PSEC pilot plant instrument list .....  | 161 |
| Table 24: PSEC pilot plant valve list .....   | 162 |
| Table 25: Operating parameters and results associated with Figure 77. ....  | 163 |
| Table 26: Operating parameters and results associated with Figure 78. ....  | 164 |
| Table 27: Operating parameters and results associated with Figure 79. ....  | 165 |
| Table 28: Operating parameters and results associated with Figure 80. ....  | 166 |
| Table 29: Operating parameters and results associated with Figure 81. ....  | 167 |
| Table 30: Operating parameters and results associated with Figure 82. ....  | 168 |
| Table 31: Operating parameters and results associated with Figure 83. ....  | 169 |
| Table 32: Operating parameters and results associated with Figure 84. ....  | 170 |
| Table 33: Operating parameters and results associated with Figure 85. ....  | 171 |
| Table 34: Operating parameters and results associated with Figure 86. ....  | 172 |

## LIST OF FIGURES

|   |    |
|---|----|
| Figure 1: Graphical representation of thesis structure showing links between chapters. .... | 6  |
| Figure 2: An example of multistage crosscurrent extraction. ....                            | 8  |
| Figure 3: An example of multistage counter current extraction. ....                         | 9  |
| Figure 4: PUREX flow sheet (Herbst et al., 2011). ....                                      | 12 |
| Figure 5: An example of a counter-current mixer settler cascades (Treybal, 1980). ....      | 13 |
| Figure 6: Schematic representation of a Pulsed Sieve-plate Extraction. ....                 | 15 |

|   |    |
|---|----|
| Figure 7: Flow regimes in a PSEC (Yadav and Patwardhan, 2008).....  | 18 |
| Figure 8: Mixer-settler operation (Yadav and Patwardhan, 2008).....   | 19 |
| Figure 9: Dispersed, emulsion and unstable operation (Yadav and Patwardhan, 2008). .....  | 20 |
| Figure 10: (A) Spherical, (B) ellipsoidal and (C) spherical capped droplets (Clift et al., 2005)23  |    |
| Figure 11: Shapes for droplets in unhindered gravitational flow-through liquid (Clift et al., 2005). Calculated for $\Delta\rho = 0-400 \text{ kg.m}^{-3}$ , $d = 0 \text{ to } 10 \text{ mm}$ , $\sigma = 1.75-46 \text{ N.m}^{-1}$ , $\mu = 0.486-4.88 \text{ N.s.m}^{-2}$ , $U = 0-1 \text{ m.s}^{-1}$ and $\rho d = 660-1590 \text{ kg.m}^{-3}$ (Yadav and Patwardhan, 2008). ..... | 25 |
| Figure 12: Comparison of measures of central tendency for different mean diameters calculated from a simulated droplet size distribution consisting of 20000 droplets with a mean diameter of 5 mm and a standard deviation of 1 mm. ....   | 26 |
| Figure 13: Force balance on a droplet in a swarm (Wang et al., 2022).....   | 28 |
| Figure 14: Schematic representation of two-film theory. ....  | 33 |
| Figure 15: Pulsed Sieve-plate Extraction Column pilot plant.....  | 45 |
| Figure 16: 3 mm thick Sieve-plates with a constant fractional free area of 0.23 and hole diameters of 1, 2 and 4 mm.....  | 46 |
| Figure 17: Dimensions of “PSEC configuration A” . ....  | 47 |
| Figure 18: Dimensions of “PSEC configuration B” . ....  | 48 |
| Figure 19: Pneumatic pulsation via the pulse leg. ....  | 49 |
| Figure 20: Pulsation control and instrumentation cabinet.....   | 50 |
| Figure 21: Process and Instrumentation Diagram (P&ID) of the Pulsed Sieve-plate Extraction Colum Pilot Plant.....   | 51 |
| Figure 22: Segmentation workflow using Ilastik with labelled data (left) and segmented image (right). Droplets are blue, edges are red and background is yellow. ....   | 55 |
| Figure 23: Droplet measurement workflow using OpenCV with: (a) the original image; (b) the masked image; (c) the down selected drops; and (d) the distance transform. ....  | 56 |
| Figure 24: PSEC operational envelope for: (a) $dp = 1 \text{ mm}$ ; (b) $dp = 2 \text{ mm}$ ; (c) $dp = 4 \text{ mm}$ .....   | 58 |

|   |    |
|---|----|
| Figure 25: Linear regression and experimental data showing maximum column throughput as a function of pulse amplitude and plate hole diameter.....  | 59 |
| Figure 26: Comparing the recirculation and accumulation of droplets in a PSEC that is: (a) flooding ( $dp = 2$ mm, $Q_{tot} = 60$ L.hr <sup>-1</sup> , $A = 2.96$ mm) and; (b) operating ( $dp = 2$ mm, $Q_{tot} = 60$ L.hr <sup>-1</sup> , $A = 3.70$ mm)..... | 60 |
| Figure 27: Sauter mean diameter as a function of total throughput ( $Q_{tot}$ ), grouped by hole diameter. ....   | 62 |
| Figure 28: Sauter mean droplet diameter for a total throughput ( $Q_{tot}$ ) of 30 L.hr <sup>-1</sup> for pulse amplitudes ( $A$ ) of 2.96 mm and 3.70 mm. ....   | 62 |
| Figure 29: Parity plot showing the relationship between $d_{3,0}$ and $d_{3,2}$ .....   | 63 |
| Figure 30: Droplet size distribution as a function of total throughput ( $Q_{tot}$ ) and pulse amplitude ( $A$ ) for a hole diameter ( $dp$ ) of 1 mm. $d_{3,2}$ values are denoted in red.....   | 64 |
| Figure 31: Droplet size distribution as a function of total throughput ( $Q_{tot}$ ) and pulse amplitude ( $A$ ) for a hole diameter ( $dp$ ) of 2 mm. $d_{3,2}$ values are denoted in red.....   | 65 |
| Figure 32: Droplet size distribution as a function of total throughput ( $Q_{tot}$ ) and pulse amplitude ( $A$ ) for a hole diameter ( $dp$ ) of 4 mm. $d_{3,2}$ values are denoted in red.....   | 66 |
| Figure 33: Standard deviation of the droplet size distribution grouped by hole diameter vs total throughput.....  | 67 |
| Figure 34: Standard deviation of the droplet size distribution grouped by hole diameter vs pulse amplitude. ....  | 67 |
| Figure 35: Standard deviation of the droplet size distribution grouped by hole diameter vs mean droplet size.....   | 68 |
| Figure 36: Droplet swarm rise velocity grouped by hole diameter vs total throughput. ....   | 69 |
| Figure 37: Droplet swarm rise velocity grouped by hole diameter vs pulse amplitude. ....  | 70 |
| Figure 38: Droplet swarm rise velocity grouped by hole diameter vs pulse amplitude. ....  | 70 |
| Figure 39: Calculated and measured droplet swarm rise velocities grouped by hole diameter vs pulse amplitude.....   | 71 |

|  |     |
|--|-----|
| Figure 40: Droplet swarm averaged rise velocities for a total throughput ( $Q_{tot}$ ) of 30 L.hr <sup>-1</sup> for pulse amplitudes ( $A$ ) of 2.96 mm and 3.70 mm. ....  | 72  |
| Figure 41: Flow chart showing logic for the switching of the large interface identifier $Ca$ . ...   | 77  |
| Figure 42: Geometry and mesh used in 3D CFD simulations. Boundary patches are highlighted in red. ....   | 84  |
| Figure 43: Geometry and mesh used in 2D CFD simulations. Boundary patches are highlighted in red. ....   | 85  |
| Figure 44: Instantaneous and mean velocity magnitude plots for the 2D and 3D cases. ....   | 93  |
| Figure 45: Time-averaged DSD for experimental (left), LES (middle) and URANS (right). Mean values are denoted in red. ....   | 95  |
| Figure 46: $d_{3,2}$ plotted for stage number with error bars corresponding to the standard deviation. ....  | 96  |
| Figure 47: LES (left), URANS (middle) and averaged values (right) for turbulent kinetic energy dissipation rate. ....  | 97  |
| Figure 48: Stage and time-averaged droplet rise velocity. ....   | 100 |
| Figure 49: Axial dispersed phase holdup. ....  | 101 |
| Figure 50: Axial Sauter mean droplet diameter. ....  | 102 |
| Figure 51: Axial solute concentration. ....  | 102 |
| Figure 52: Counter-current extraction model block flow diagram. ....   | 107 |
| Figure 53: Compartmentalisation strategy for a PSEC. Yellow boxes represent the aqueous phase, blue boxes represent solvent phase. Red arrows represent fluid transport and green arrows represent mass transfer. .... | 109 |
| Figure 54: Experimental and modelled axial dispersed phase holdup. ....  | 111 |
| Figure 55: Experimental and modelled Sauter mean droplet diameter. ....  | 111 |
| Figure 56: Experimental and modelled profiles of PSEC solute concentration in the organic and aqueous phase. ....  | 112 |

|  |     |
|--|-----|
| Figure 57: CFD predicted aqueous phase RTD curve for lower separator, lower inlet, all stages grouped, upper inlet and upper separator. ....   | 113 |
| Figure 58: CFD predicted aqueous phase RTD curve for column stages. ....   | 114 |
| Figure 59: CFD predicted dispersed phase RTD curve for lower separator, lower inlet, all stages, upper inlet and upper separator. ....   | 115 |
| Figure 60: CM predicted aqueous phase RTD curve for lower separator, lower inlet, all stages grouped, upper inlet and upper separator. ....  | 116 |
| Figure 61: CM predicted aqueous phase RTD curve for column stages. ....  | 117 |
| Figure 62: Box and whisker plots showing the aqueous phase RTD curves for CFD in blue and the CM in red. ....  | 118 |
| Figure 63: CM predicted dispersed phase RTD curve for lower separator, lower inlet, all stages, upper inlet and upper separator. ....  | 119 |
| Figure 64: Box and whisker plots showing the solvent phase RTD curves for CFD in blue and the CM in red. ....  | 120 |
| Figure 65: Compartment diagram showing implementation of batch mass transfer using two compartments. ....  | 121 |
| Figure 66: Isotherm showing equilibrium concentrations for acetone between the aqueous and solvent phases with distribution ratio given by the gradient. ....  | 122 |
| Figure 67: Axial solute concentration for $Q_{tot} = 88 \text{ L.hr}^{-1}$ , $Af = 1 \text{ cm.s}^{-1}$ . ....   | 123 |
| Figure 68: Transient solute concentration for aqueous (left) and organic (right) phase for lower outlet, stage 5, stage 15, stage 22 and upper outlet. Y axis denotes solute concentration ( $\text{mol.L}^{-1}$ ) and X axis denotes time (s). .... | 124 |
| Figure 69: Distribution ratio of nitric acid between aqueous and solvent phases as a function of aqueous phase acid concentration (Davis Jr, 1962). ....   | 130 |
| Figure 70: Distribution ratio of uranium between aqueous and solvent phases as a function of aqueous phase acid concentration (Apelblat and Faraggi, 1966). ....   | 131 |

|  |     |
|--|-----|
| Figure 71: Compartment model structure for PSEC. Yellow boxes represent the aqueous phase, blue boxes represent solvent phase. Red arrows represent fluid transport and green arrows represent mass transfer. .... | 133 |
| Figure 72: Experiment 3 results and modelled solute concentrations for: (A) aqueous outlet nitric acid; (B) solvent outlet nitric acid; (C) aqueous outlet uranium; and (D) solvent outlet uranium.....            | 137 |
| Figure 73: Model predicted axial nitric acid concentration. ....   | 138 |
| Figure 74: Modelled nitric acid operating and equilibrium lines.....   | 139 |
| Figure 75: Model predicted axial uranium concentration.....  | 140 |
| Figure 76: Modelled uranium operating and equilibrium lines.....   | 140 |
| Figure 77: Axial solute concentrations for $Q_{tot} = 88 \text{ L.hr}^{-1}$ , $Af = 1 \text{ cm.s}^{-1}$ .....   | 163 |
| Figure 78: Axial solute concentrations for $Q_{tot} = 88 \text{ L.hr}^{-1}$ , $Af = 2 \text{ cm.s}^{-1}$ .....   | 164 |
| Figure 79: Axial solute concentrations for $Q_{tot} = 135 \text{ L.hr}^{-1}$ , $Af = 1 \text{ cm.s}^{-1}$ .....  | 165 |
| Figure 80: Axial solute concentrations for $Q_{tot} = 135 \text{ L.hr}^{-1}$ , $Af = 2 \text{ cm.s}^{-1}$ .....  | 166 |
| Figure 81: Axial solute concentrations for $Q_{tot} = 159 \text{ L.hr}^{-1}$ , $Af = 1 \text{ cm.s}^{-1}$ .....  | 167 |
| Figure 82: Axial solute concentrations for $Q_{tot} = 159 \text{ L.hr}^{-1}$ , $Af = 2 \text{ cm.s}^{-1}$ .....  | 168 |
| Figure 83: Axial solute concentrations for $Q_{tot} = 182 \text{ L.hr}^{-1}$ , $Af = 1 \text{ cm.s}^{-1}$ .....  | 169 |
| Figure 84: Axial solute concentrations for $Q_{tot} = 182 \text{ L.hr}^{-1}$ , $Af = 2 \text{ cm.s}^{-1}$ .....  | 170 |
| Figure 85: Axial solute concentrations for $Q_{tot} = 205 \text{ L.hr}^{-1}$ , $Af = 1 \text{ cm.s}^{-1}$ .....  | 171 |
| Figure 86: Axial solute concentrations for $Q_{tot} = 205 \text{ L.hr}^{-1}$ , $Af = 2 \text{ cm.s}^{-1}$ .....  | 172 |
| Figure 87: Experiment 1 results and modelled solute concentrations for: (A) aqueous outlet nitric acid; and (B) solvent outlet nitric acid.....  | 173 |
| Figure 88: Experiment 2 results and modelled solute concentrations for: (A) aqueous outlet nitric acid; and (B) solvent outlet nitric acid.....  | 174 |

|   |     |
|---|-----|
| Figure 89: Experiment 3 results and modelled solute concentrations for: (A) aqueous outlet nitric acid; (B) solvent outlet nitric acid; (C) aqueous outlet uranium; and (D) solvent outlet uranium..... | 175 |
| Figure 90: Experiment 4 results and modelled solute concentrations for: (A) aqueous outlet nitric acid; (B) solvent outlet nitric acid; (C) aqueous outlet uranium; and (D) solvent outlet uranium..... | 176 |
| Figure 91: Experiment 5 results and modelled solute concentrations for: (A) aqueous outlet nitric acid; (B) solvent outlet nitric acid; (C) aqueous outlet uranium; and (D) solvent outlet uranium..... | 177 |
| Figure 92: Experiment 6 results and modelled solute concentrations for: (A) aqueous outlet nitric acid; (B) solvent outlet nitric acid; (C) aqueous outlet uranium; and (D) solvent outlet uranium..... | 178 |
| Figure 93: Experiment 7 results and modelled solute concentrations for: (A) aqueous outlet nitric acid; (B) solvent outlet nitric acid; (C) aqueous outlet uranium; and (D) solvent outlet uranium..... | 179 |
| Figure 94: Experiment 8 results and modelled solute concentrations for: (A) aqueous outlet nitric acid; (B) solvent outlet nitric acid; (C) aqueous outlet uranium; and (D) solvent outlet uranium..... | 180 |

## ABBREVIATIONS

|       |  |
|-------|--|
| ACC   | Annular Centrifugal Contactor                                  |
| AMUSE | Argonne Model for Universal Solvent Extraction                 |
| ANL   | Argonne National Lab   |
| ATR   | Agitated Tube Reactor  |
| CEA   | Commissariat à l'énergie atomique et aux énergies alternatives |
| CFD   | Computational Fluid Dynamics                                   |
| CM    | Compartment Model  |
| CNN   | Convolutional Neural Networks                                  |
| CSTR  | Continuously Stirred Tank Reactor                              |
| DIH   | Digital In-line Holography                                     |
| DNS   | Direct Numerical Simulation                                    |
| DSD   | Droplet Size Distribution                                      |
| FEP   | Fluorinated Ethylene Propylene                                 |
| GDF   | Geological Disposal Facility                                   |

|        |   |
|--------|---|
| GEMMA  | Generalised Multifluid Modelling Approach   |
| HAR    | High Active Raffinate   |
| HLW    | High-Level Waste  |
| HPC    | High-Performance Computer   |
| HTU    | Height of a Transfer Unit   |
| ID     | Internal Diameter   |
| IRQ    | Interface Resolution Quality  |
| LES    | Large Eddy Simulation   |
| LLE    | Liquid-liquid Extraction  |
| LLEC   | Liquid-liquid Extraction Column   |
| MB     | Mass Balance  |
| MIBK   | Methyl isobutyl ketone  |
| MOX    | Mixed Oxide Fuel  |
| MULES  | Multidimensional Universal Limiter for Explicit Solution  |
| NS     | Navier-Stokes   |
| NTU    | Number of Transfer Units  |
| OPOSPM | One Primary One Secondary Particle Method   |
| ORNL   | Oak Ridge National Laboratory   |
| PBM    | Population Balance Model  |
| PDDC   | Pulsed Donut-disk Columns   |
| PIMPLE | Pressure Implicit with Splitting of Operators, Semi-Implicit Method for Pressure Linked Equations |
| PISO   | Pressure Implicit with Splitting of Operators   |
| PIV    | Particle Image Velocimetry  |
| PPE    | Personal Protective Equipment   |
| PSEC   | Pulsed Sieve-plate Extraction Column  |
| PTFE   | Polytetrafluoroethylene   |
| PTV    | Particle Tracking Velocimetry   |
| PUREX  | Plutonium, Uranium, Reduction, Extraction   |
| P&ID   | Process and Instrumentation Diagram   |
| RDC    | Rotating Disc Column  |
| RMSE   | Root-mean Squared Error   |
| RTD    | Residence Time Distribution   |
| SASPE  | Spreadsheet Algorithm for Speciation and Partitioning Equilibria                                  |
| SASSE  | Spreadsheet Algorithm for Stagewise Solvent Extraction  |
| SE     | Stage Efficiency  |
| SEPHIS | Solvent Extraction Process Having Interaction Solvents  |
| SGS    | Sub-Grid Scale  |
| SIMPLE | Semi-Implicit Method for Pressure Linked Equations  |
| SMD    | Sauter Mean Diameter  |
| SNF    | Spent Nuclear Fuel  |
| SOLVEX | Solvent Extraction  |
| SQMOM  | Section Quadrature Method of Moments  |
| SX     | Solvent Extraction  |
| S:A    | Solvent Aqueous ratio   |
| TBP    | Tributyl phosphate  |
| THORP  | Thermal Oxide Reprocessing Facility   |

|       |  |
|-------|--|
| TRUEX | Trans Uranium Extraction                 |
| URANS | Unsteady Reynolds-Averaged Navier Stokes |
| VOF   | Volume of Fluid                          |
| 2D    | 2 dimensional                            |
| 3D    | 3 dimensional                            |

## NOMENCLATURE

|                |  |
|----------------|--|
| $a$            | Interfacial area per unit volume, $\text{m}^2.\text{m}^{-3}$                         |
| $A$            | Pulse amplitude, m   |
| $A_p$          | Plate free area, dim   |
| $Bo$           | Bond number, dim   |
| $c_k$          | Smagorinsky constant, 0.094, dim   |
| $C$            | Concentration, $\text{mol}.\text{m}^{-3}$  |
| $C_d$          | Drag coefficient, dim  |
| $C_d^*$        | Dispersed phase concentration driving force, $C_d^* = K_{eq}C_C$                     |
| $C_\alpha$     | Large interface identifier, dim  |
| $d$            | Droplet diameter, m  |
| $d_p$          | Plate hole diameter, m   |
| $d_{3,0}$      | Volume weighted droplet diameter, m  |
| $d_{3,2}$      | Sauter mean droplet diameter, m  |
| $D$            | Diffusion coefficient, $\text{m}^2.\text{s}^{-1}$                                    |
| $D_{col}$      | Column diameter, m   |
| $f$            | Pulse frequency, $\text{s}^{-1}$   |
| $F$            | Force, $\text{kg}.\text{m}.\text{s}^{-2}$  |
| $g$            | Acceleration due to gravity, $\text{m}.\text{s}^{-2}$                                |
| $h$            | Plate spacing, m   |
| $h_f$          | Final film thickness, assumed to be $1 \times 10^{-8}$ m (Prince and Blanch, 1990)   |
| $h_0$          | Initial film thickness, assumed to be $1 \times 10^{-4}$ m (Prince and Blanch, 1990) |
| $H$            | Column height, m   |
| $HTU$          | Height of a transfer unit, m   |
| $i$            | Mass attenuation coefficient, $\text{m}^2.\text{kg}^{-1}$                            |
| $k$            | Turbulent kinetic energy, $\text{m}^2.\text{s}^{-2}$                                 |
| $k_c$          | Continuous phase mass transfer coefficient, $\text{m}.\text{s}^{-1}$                 |
| $k_d$          | Dispersed phase mass transfer coefficient, $\text{m}.\text{s}^{-1}$                  |
| $K_{eq}$       | Equilibrium distribution of solute, dim  |
| $m$            | Mass, kg   |
| $M$            | Mass concentration, $\text{kg}.\text{m}^{-3}$  |
| $Mo$           | Morton number, dim   |
| $MTR$          | Mass transfer rate on molar basis, $\text{mol}.\text{m}^{-3}.\text{s}^{-1}$          |
| $n$            | Number, dim  |
| $n_{daughter}$ | Mean number of daughter drops, dim   |
| $NTU$          | Number of transfer units, dim  |
| $N_d$          | Droplet number density, $\text{m}^{-3}$  |
| $P$            | Pressure, $\text{N}.\text{m}^{-2}$   |

|                   |  |
|-------------------|--|
| $Q$               | Volumetric flow rate, $\text{m}^3.\text{s}^{-1}$                               |
| $r_{breakage}$    | Droplet break-up rate  |
| $r_{coalescence}$ | Droplet coalescence rate   |
| $Re$              | Reynolds number for multi-particle system, $Re = d_{3,2}U_s\rho_x/\mu_x$ , dim |
| $Re_{drop}$       | Reynolds number for single droplet system, $Re = dU_s\rho_x/\mu_x$ , dim       |
| $S$               | Source term, dim   |
| $S_{mass}$        | Mass transfer rate source term, $\text{kg}.\text{m}^{-3}.\text{s}^{-1}$ .      |
| $S_{ij}$          | Resolved rate-of-strain tensor   |
| $S_x$             | Dimensionless scalar of phase x, dim   |
| $Sc$              | Schmidt number, $Sc = \mu/\rho D$  |
| $SE$              | Stage Efficiency   |
| $t$               | Time, s  |
| $U$               | Velocity, $\text{m}.\text{s}^{-1}$   |
| $U_c$             | Compressive velocity, $\text{m}.\text{s}^{-1}$                                 |
| $U_s$             | Slip velocity, $\text{m}.\text{s}^{-1}$  |
| $v$               | Superficial velocity, $\text{m}.\text{s}^{-1}$                                 |
| $v_{slip}$        | Slip velocity, $\text{m}.\text{s}^{-1}$  |
| $V$               | Volume, $\text{m}^3$   |
| $V_c$             | Cell volume, $\text{m}^3$  |

### Greek symbols

|            |  |
|------------|--|
| $\alpha$   | Dispersed phase holdup, dim                            |
| $\beta$    | Ratio of backflow to new forward flow, dim             |
| $\Gamma$   | User-defined value, dim                                |
| $\epsilon$ | Turbulent dissipation rate, $\text{m}^2.\text{s}^{-3}$ |
| $\kappa$   | Local interface curvature, dim                         |
| $\mu$      | Dynamic viscosity, $\text{N}.\text{s}.\text{m}^{-2}$   |
| $\nu$      | Kinematic viscosity, $\text{m}^2.\text{s}^{-1}$        |
| $\pi$      | 3.1416, dim  |
| $\rho$     | Density, $\text{kg}.\text{m}^3$                        |
| $\sigma$   | Interfacial tension, $\text{N}.\text{m}^{-1}$          |
| $\tau$     | Sub-grid scale stress tensor                           |

### Subscript

|         |                   |
|---------|-------------------|
| $aq$    | Aqueous phase     |
| $c$     | Continuous phase  |
| $d$     | Dispersed phase   |
| $eq$    | Equilibrium value |
| $heavy$ | Heavy phase       |
| $i$     | Interface         |
| $in$    | Inlet             |
| $light$ | Light phase       |
| $LI$    | Large interface   |
| $m$     | Maximum value     |
| $out$   | Outlet            |
| $sol$   | Solvent phase     |

|            |                 |
|------------|-----------------|
| <i>st</i>  | Surface tension |
| <i>t</i>   | Transition      |
| <i>tot</i> | Total           |
| <i>x</i>   | Generic phase   |

## 1. INTRODUCTION

Pulsed sieve-plate extraction columns (PSECs) are a counter-current solvent extraction unit operation used in various industries, most notably in the nuclear industry for separating uranium and plutonium from spent nuclear fuel. This is achieved using the PUREX (Plutonium, Uranium, Reduction, Extraction) process which uses the organic solvent tributyl phosphate (TBP) to selectively extract and partition uranium and plutonium from spent nuclear fuel dissolved in nitric acid (Bertelsen et al., 2022).

PSECs have several advantages over alternative unit operations such as the mixer-settler or the centrifugal contactor, notably their reliability and low maintenance requirement due to having no moving mechanical parts. This is particularly relevant for nuclear reprocessing applications, where equipment is contained within radiological shielding and access for maintenance is difficult or impossible. Additionally, PSECs can operate with particulate-laden streams due to the system being sufficiently agitated, including insoluble particulates generated during fuel dissolution or in situ generated precipitates and interfacial crud.

### 1.1. Project Motivation

Despite their numerous advantages and widespread industrial usage, PSECs are notoriously hard to design due to their complex hydrodynamics and the “practical applications are advanced far ahead of sound design data” (Treybal, 1980). Traditionally, the design of PSECs has required pilot plant study to acquire the necessary data for scaling up the process. This includes the operation of a pilot scale PSEC and the quantification of the maximum throughput and mass transfer, following which the column diameter is adjusted to the desired throughput and column height to achieve the desired separation. However, there is evidence that these parameters are not always scalable, necessitating oversized columns. Furthermore, pilot plant scale-up is often expensive and impractical, especially in nuclear applications where facilities that can operate in active environments are rare.

Much effort has been expended in pursuing empirical correlations to predict column performance for dispersed phase holdup, Sauter mean droplet diameter and mass transfer coefficients. However, a review of several prominent correlations against a sizeable experimental dataset concluded that these often perform poorly, and many of these equations

are not fit for purpose (Yadav and Patwardhan, 2008). This is because correlations are usually developed with a small number of chemical systems, limited sets of column geometries or operational parameters, which limits their application. Recent studies have investigated the potential of data-driven models to accurately predict flooding curves, which indicate the maximum operational throughput before bulk entrainment of a phase in the other phases outlet. However, these black box approaches rely on the availability of large, consistent data sets, which are not easily accessible and therefore remain an area of active research (Brockkötter et al., 2020).

In recent years, there has been a surge of interest in applying higher-order computational techniques, such as CFD, to model the performance of PSECs. There are several factors that can be attributed towards this, including a lowering of the barrier to entry due to the emergence of user-friendly CFD modelling software like ANSYS Fluent, STAR-CCM+, and OpenFOAM and an increased prevalence of High-Performance Computing (HPC) which has enabled large scale industrially relevant simulations. Numerous investigations have been carried out to assess the appropriate representation of the computational domain (Sen et al., 2015; Tu et al., 2021), the suitability of different multifluid formulations (Khatir et al., 2016; Khatir et al., 2017; Theobald, 2020; Theobald et al., 2020), the identification of appropriate turbulence models (Khatir et al., 2016; Khatir et al., 2017; Theobald, 2020; Theobald et al., 2020), calculation of Droplet Size Distribution (DSD) (Yadav and Patwardhan, 2009; Sen et al., 2016; Alzyod et al., 2017; Alzyod et al., 2018; Sen et al., 2018; Sen et al., 2019; Theobald, 2020; Yi et al., 2020; Theobald et al., 2020; Tu et al., 2021; Sen et al., 2021), interphase momentum transfer (Sen et al., 2016; Sen et al., 2018) and the prediction of mass transfer (Alzyod et al., 2018). However, due to the complexity and interdependence of the modelled phenomena, there is still a significant gap in validation.

Despite its benefits, CFD requires significant time for the simulation to run. Due to the transient behaviour of column operation, small time steps, typically 1000s per second of simulated time, are required to ensure a stable simulation, however, due to the large column volumes, this can result in several hours of simulated time being needed to achieve pseudo steady state for mass transfer. The computational domain requires many cells due to the large size of columns and the small size of plate holes, requiring a high grid resolution for stability, which increases the time needed for each time step. As a result, a full-fidelity simulation of an

industrial-scale PSEC that accounts for all relevant phenomena, including mass transfer, is at the limits of what is currently computationally feasible.

Despite being limited by the computational time required for a CFD simulation, a validated CFD model can still provide a powerful predictive tool which can be used to inform the development of reduced-order models. Representing the computational domain in 2D can reduce the time required by several orders of magnitude, enabling the interrogation of the column's hydrodynamics and mass transfer performance. Through this information, a Compartment Model (CM) can be developed where phenomenologically similar regions are grouped, which are networked using intercompartment flows and relevant phenomena such as mass transfer implemented. Providing the number of compartments is kept low, this process is significantly quicker than CFD and can perform simulations at a rate comparable to or faster than real-world operations. This has several benefits as it enables the rapid prototyping of different designs, sensitivity analysis to variations in column operating parameters and design optimisation.

## **1.2. Aim and objectives**

This project aims to develop a modelling and simulation framework for the design of PSECs to reduce the inherent uncertainty associated with their empirical or pilot plant design. This will be done by performing experimental validation of high fidelity and reduced order CFD simulations, which will be used to develop a Compartment Model for the prediction of mass transfer using the PUREX process. The project objectives are:

1. Summarise the relevant theory of PSEC operation and review applicable modelling and simulation tools.
2. Design and commission a PSEC to characterise dispersed phase hydrodynamics and mass transfer.
3. Characterise the PSEC operational envelope, droplet size distribution, mean diameters, and rise velocities.
4. Validate high fidelity and reduced order CFD simulations of PSEC hydrodynamics and validate CFD predicted mass transfer in a reduced order CFD model.
5. Use CFD to inform the development of a Compartment Modelling framework and validate mass transfer performance over various operating conditions.

6. Extract uranium and nitric acid using the PUREX process in a PSEC, implement the chemistry within the Compartment Modelling framework and evaluate the model's predictive capability.

### **1.3. Novelty of research**

This thesis will present a novel modelling and simulation framework for the design of PSECs that reduces the inherent uncertainty associated with their empirical or pilot plant design. The novelty of the work lies in the generation of an experimental dataset of droplet size distribution, mean values and rise velocities as a function of column operating conditions and plate designs. This will be used to validate the Generalised Multifluid Modelling Approach (GEMMA), which is a novel hybrid methodology which can dynamically switch between interface averaging and interface tracking methodologies, for both high fidelity and reduced order CFD simulations of PSEC operation. Additionally, this thesis will present the implementation and experimental validation of mass transfer within the GEMMA methodology to model PSEC performance, the use of CFD to inform the development of a novel PSEC Compartment Model for the prediction of mass transfer in PSECs, and the implementation of the PUREX solvent extraction process within a Compartment Modelling framework and experimental validation of the transient performance within a PSEC.

### **1.4. Thesis structure**

The thesis structure is presented below, with a graphical representation shown in Figure 1.

Chapter 2 will address objective 1 by providing an overview of the relevant theory for PSEC operation, informing the design of an experimental apparatus in chapter 3, and reviewing modelling and simulation tools for validation in chapters 5 and 6.

Chapter 3 will address objective 2 and present the design and commissioning of a PSEC suitable for characterising dispersed phase hydrodynamics in chapter 4, validating CFD models in chapter 5 and validating uranium extraction in chapter 7.

Chapter 4 will cover the characterisation of the PSEC operational envelope to identify suitable operating conditions for mass transfer experiments in chapter 7 and the characterisation of the droplet size distribution, mean values and rise velocities for validation of CFD models in chapter 5, thereby achieving objective 3.

To address objective 4, chapter 5 will validate high fidelity 3D Large Eddy Simulation (LES) and reduced order 2D Unsteady Reynolds-Averaged Navier Stokes (URANS) CFD simulations against the experimentally measured hydrodynamic data from chapter 4. It will also implement the local calculation of mass transfer in the reduced order 2D URANS CFD model and validate the mass transfer performance against data from the literature.

Objective 5 will be addressed in chapter 6, using the reduced order 2D URANS CFD model developed in chapter 4 to predict droplet diameters and dispersed phase holdup with a simplified steady-state model to predict axial solute concentrations. The CFD model will also be used to conduct a residence time distribution study and use the results to develop a Compartment Model of a PSEC. Mass transfer will be implemented within the Compartment Modelling framework and validated for various operating conditions using data from the literature.

Chapter 7 will use the operational envelope characterised in chapter 4 to identify a range of experiments to generate mass transfer data for the PUREX process. It will implement the PUREX process chemistry within the Compartment Modelling framework and validate the mass transfer performance against experimental data, thereby addressing objective 6.

Chapter 8 will conclude the results of this study and provide an overview for future work.

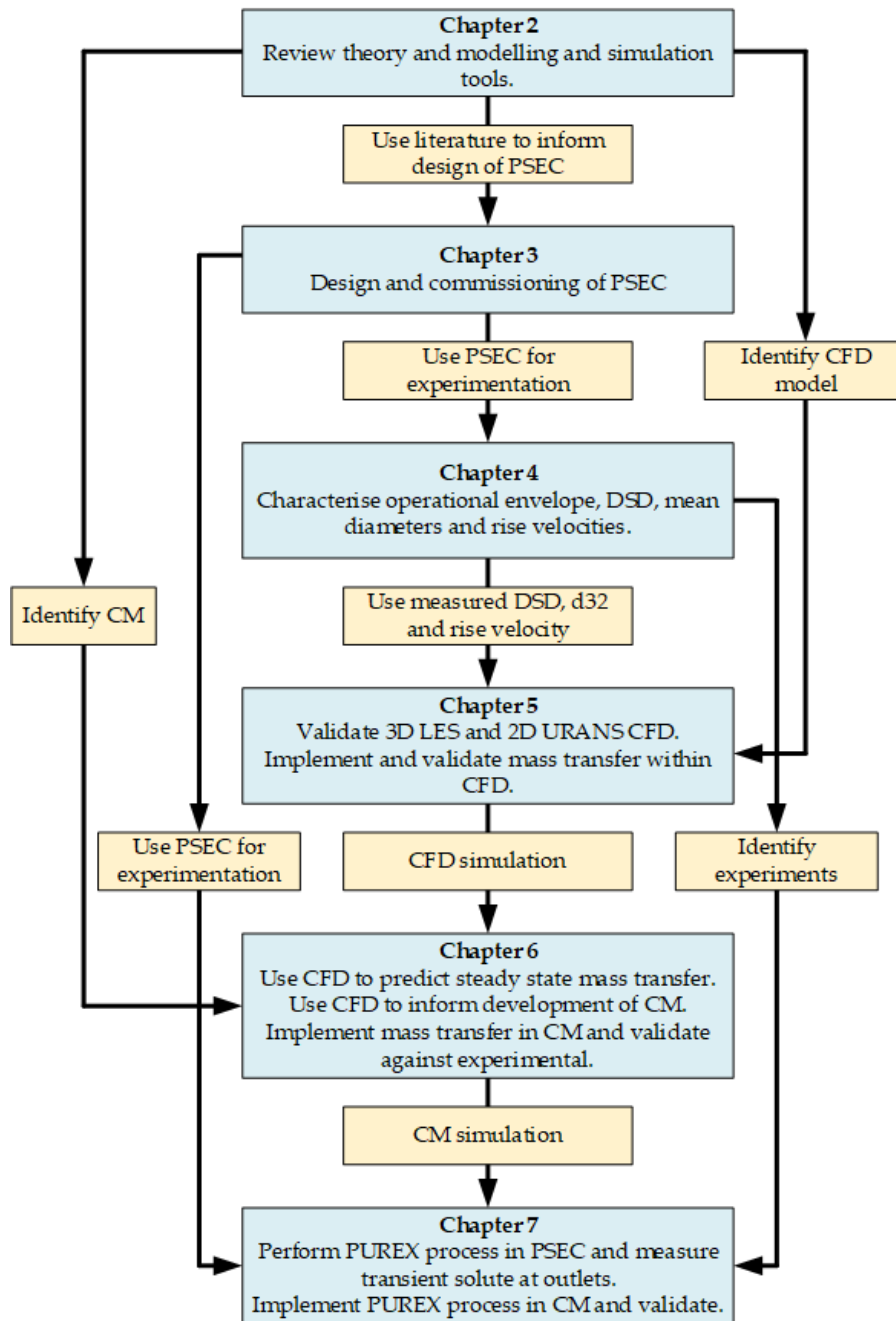


Figure 1: Graphical representation of thesis structure showing links between chapters.

## 2. LITERATURE REVIEW

### 2.1. Liquid-liquid extraction

Solvent extraction (SX) or liquid-liquid extraction (LLE) is the process by which components of a liquid are separated by contacting with another liquid (Treybal, 1980). When the components of the initial solution distribute themselves between the two, a certain level of separation can be achieved. The transfer can be driven by relative solubility or chemical extraction.

Generally, LLE is often used as a preparatory step before product purification using other techniques to achieve the desired purity level. It is often used when other processes such as evaporation or distillation are impractical. For example, removing contaminants from wastewater would require a significant amount of energy (Rodríguez-Llorente et al., 2020). Alternatively, some processes, such as the separation of long-chain fatty acids from vegetable oils, are sensitive to temperature resulting in the thermal decomposition of the products. For some processes such as separating aromatic and paraffinic hydrocarbons using evaporation or distillation may not be possible due to their similar vapour pressures.

For example, acetone can be separated from water by contacting it with toluene as it is soluble in both liquids, while water and toluene are generally immiscible. First, the two solutions are placed in a container, with the less dense toluene sitting above the more dense acetone-water mixture, separated by an interface. Next, the fluids are mixed, allowing the acetone to redistribute between the two phases. After the mixture is agitated for a sufficient time, the acetone will reach equilibrium and its concentration in the two phases will no longer change with time. Finally, the two liquids are allowed to separate and are decanted into separate containers.

When describing LLE processes it is common for the different liquids to be referred to as either the aqueous and organic, the continuous and dispersed or the light and heavy phases. This nomenclature is used interchangeably depending on the context. In the example, the initial solution of water and acetone is referred to as the feed material and the initial toluene is referred to as the solvent. After contacting and separating, the solute-depleted water is referred to as the raffinate and the solute-enriched toluene is referred to as the extract.

The ratio of the concentrations of the solute at equilibrium,  $C_x$ , is referred to as the distribution ratio,  $K_{eq}$  and is expressed as:

$$K_{eq} = \frac{C_{sol}}{C_{aq}} \quad (2.1)$$

In this example, the solute distribution has achieved equilibrium and is said to have undergone one separation stage in the context of LLE. A measure of the degree to which separation has been reached is referred to as stage efficiency (SE).

$$SE = \frac{C_{in} - C_{out}}{C_{in} - C_{eq}} \times 100\% \quad (2.2)$$

The above is an example of a batch or a single-stage extraction. If a greater separation of the solute from the raffinate is required, this can be improved by performing multi-stage extraction.

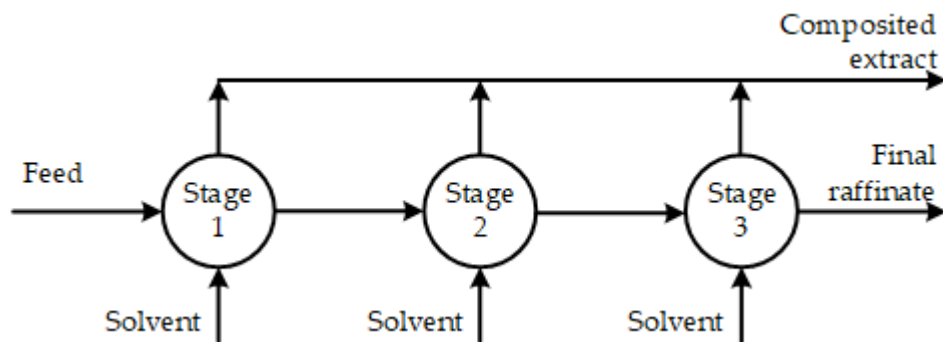


**Figure 2:** An example of multistage crosscurrent extraction.

In the case of batch multi-stage extraction, fresh toluene can be contacted with the aqueous solution, further extracting acetone before decanting off. This process can be repeated until the desired separation is achieved and the extracts combined to provide a single composite solution. The process can also be performed continuously where the raffinate is successively contacted with fresh solvent. A flowsheet showing a three-stage extraction is shown in Figure 2.

An extraction process can also be performed using counter-current multistage extraction where the extract and raffinate streams flow from stage to stage in opposite directions across a flowsheet. Calculating the number of stages, also known as the Number of Transfer Units (NTU), for a given extraction is performed similarly to calculating the stage efficiency.

$$NTU = \frac{C_{in} - C_{out}}{C_{in} - C_{eq}} \quad (2.3)$$

An example flowsheet is presented in Figure 3. This type of extraction is more efficient than cross-current extraction as it requires less solvent for a given separation or fewer stages for a given amount of solvent.

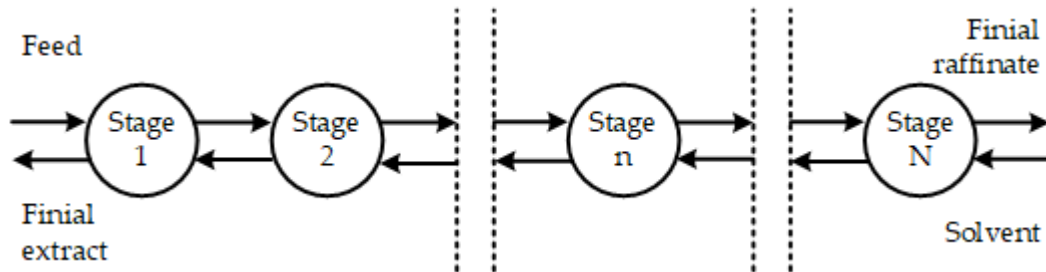


**Figure 3:** An example of multistage counter current extraction.

### 2.1.1. Nuclear reprocessing

Solvent extraction is notably used for the reprocessing of Spent Nuclear Fuel (SNF) where uranium and plutonium are partitioned for storage or reuse, while the resulting High-Level Waste (HLW) is vitrified for geological storage (Taylor et al., 2022).

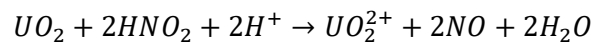
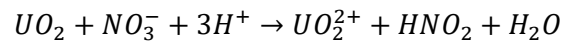
Before irradiation in a nuclear reactor, nuclear fuel is usually composed of uranium dioxide enriched with uranium-235. When a critical mass of the fuel is exposed to a controlled criticality, it produces heat, which is then used to generate electricity by creating steam and powering turbines. Post-irradiation, it consists of 94.3% uranium, 1.17% plutonium, and 4.55% fission products and minor actinides (Poinssot et al., 2015). Fission products, which can remain radioactive for thousands of years, are usually considered waste, but the fuel also contains a lot of energetically valuable material in the form of enriched uranium and minor actinides. Through complex chemical processes, it is possible to extract the fissile and fertile material and use them to create new fuel.

Initially developed in 1949 as a method for separating plutonium for nuclear weapons, PUREX involves the use of TBP in an organic diluent to extract uranium and plutonium from spent nuclear fuel dissolved in nitric acid. This produces relatively pure streams of plutonium and uranium nitrate solutions with minimal losses to the waste streams (Lanham and Runion, 1949). In France, Russia and the UK, PUREX is used to reprocess an annual capacity of

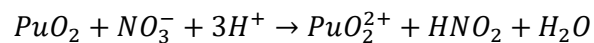
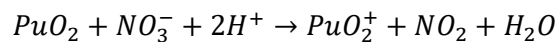
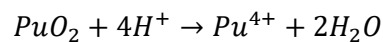
5500 tonnes of heavy metal per year (Herbst et al., 2011). By employing PUREX as part of a twice-through nuclear fuel cycle, with plutonium utilised in a Mixed Oxide Fuel (MOX), several benefits can be achieved, such as the extraction of an additional 25% more energy from the original uranium, a reduction in the overall volume of HLW, and the conversion of waste into a form suitable for long-term storage, such as vitrified borosilicate glass. Moreover, further development of the PUREX process to include additional processing steps to separate minor actinides and fission products can result in a 5-fold reduction of HLW and reduce the waste lifetime to around 300 years (Poinssot et al., 2016).

The PUREX process has a straightforward chemistry, which depends on the solvent TBP's high selectivity for actinides in the +4 and +6 oxidation states, the stability of U(VI), and the reduction of Pu(IV) to Pu(III) (Herbst et al., 2011).

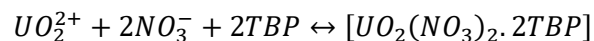
Prior to chemical separation, spent nuclear fuel is dissolved in nitric acid to produce a liquor containing approximately 3 mol.L<sup>-1</sup> nitric acid and 1.0-1.3 mol.L<sup>-1</sup> uranium and plutonium (Carrott et al., 2012). In the process, uranium reacts to form U(VI) in accordance with the following equations, depending on the nitric acid concentration.



Plutonium is converted into Pu(IV), Pu(V) or Pu(VI). To ensure the majority of plutonium is in the +4 oxidation state, which is suitable for extraction using TBP, the nitric acid concentration is kept in the 2-4 mol.L<sup>-1</sup> range (Nash and Nilsson, 2015).

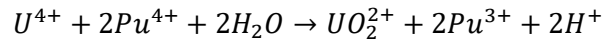


U(VI) and Pu(IV) are extracted from an aqueous phase containing 2-4 mol.L<sup>-1</sup> nitric acid into an organic phase containing TBP, forming neutral nitrate-TBP complexes (Herbst et al., 2011).

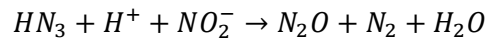
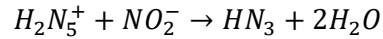


The reduction of Pu(IV) to Pu(III) is used to separate plutonium from uranium. Since TBP cannot form complexes with Pu(III), this causes the plutonium to be back-extracted from the

organic phase into the aqueous. The addition of U(IV) to reduce Pu(IV) is a relatively recent development in the PUREX process and is advantageous because U(IV) is oxidised to create U(VI), which is already present in the process (Paviet-Hartmann et al., 2013).

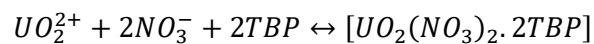


The addition of hydrazine is required in order to stabilize Pu(III) in the system, as nitric acid has oxidizing properties that form nitrous oxide.



Historically, ferrous sulfamate has been used to reduce Pu(IV) to Pu(III) as the sulfamate ion stabilizes Pu(III). However, this method has several disadvantages, such as increased waste volume, accelerated corrosion of stainless steel and incompatibility with glass-based waste forms.

U(IV) is stripped from the organic phase by adding dilute nitric acid. The decrease in nitric acid concentration causes the chemical equilibrium to shift to the left, resulting in U(VI) being transferred to the aqueous phase.



Following chemical separation, almost all uranium and plutonium is recovered, with the majority of fission products remaining in the High Active Raffinate (HAR). Uranyl nitrate is recovered from aqueous nitric acid by the addition of ammonium salts and is reduced to form  $U_3O_8$ , also known as yellow cake. Plutonium nitrate is recovered by oxalate precipitation and calcination to form  $PuO_2$  (Nash and Nilsson, 2015). Due to TBP's solubility in nitric acid, it is necessary to back-extract TBP from the HAR to the organic phase. Finally, HAR is concentrated by evaporation prior to vitrification in borosilicate glass and long-term storage.

A typical PUREX flowsheet utilising pulsed columns and based on La Hague and Rokkasho-mura reprocessing plants is described in Figure 4.

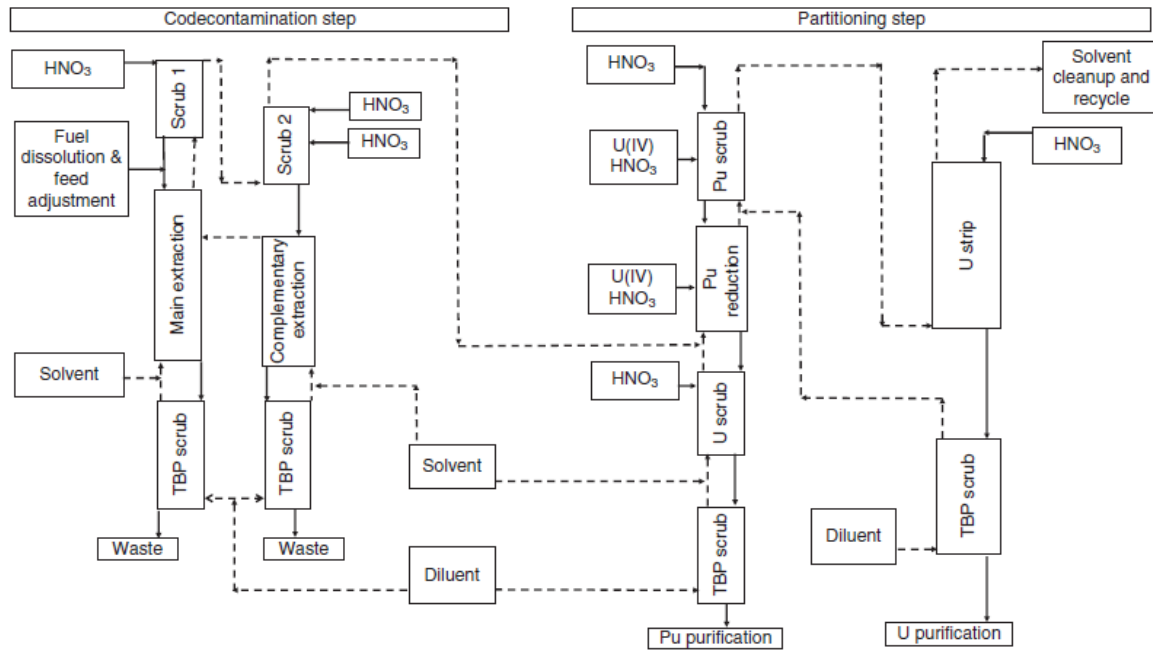


**Figure 4:** PUREX flow sheet (Herbst et al., 2011).

### 2.1.2. Unit operations

LLE operations can be performed with a range of different equipment including plate-type separators (Parrington, 2018), Agitated Tube Reactors (ATRs) (Miller et al., 2019) and Annual Centrifugal Contactors (ACCs) (Baker et al., 2022), however the most common is using a cascade of mixer-settlers. This is a single-stage device composed of a mixer where the two liquids are contacted and mass transfer occurs connected to a settler where the two phases are separated. This equipment is used in many industrial applications and provides a simple and cost-effective way to carry out LLE operations.

In the mixer section of the device, liquids enter the vessel and are agitated using an impellor. This agitation produces a dispersion which is fed to the settler section. The resulting mixture of liquids consists of droplets of one liquid dispersed in the others with droplet diameters typically ranging from 0.1 to 1 mm. If droplets are too small it may be difficult to separate them later, so it is important to control the droplet size. Stable emulsions, consisting of small droplets of one liquid dispersed throughout the continuous phase, must be avoided since separating the phases in each extraction stage is necessary. The rate of sedimentation of an emulsion is more rapid if the size of droplets and density difference are large and the viscosity of the continuous phase is small. Coalescence of settled droplets is more rapid for high

interfacial tensions, low viscosity in the continuous phase and particles at the interface can also hinder coalescence. Generally after entering the settler, the mixture will rapidly settle and coalesce into two phases with the appearance of a sharply defined interface between the phases, known as the primary break. Often, one of the two phases may remain clouded by a fine dispersion of the other and will eventually settle and leave the phase clear, known as the secondary break.

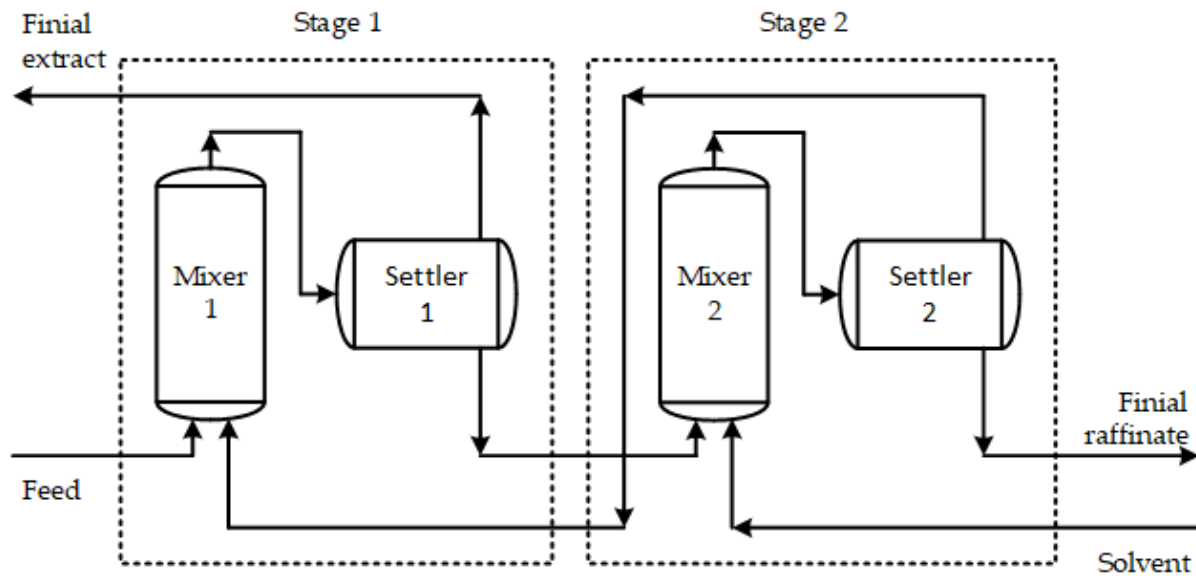


**Figure 5:** An example of a counter-current mixer settler cascad(Treybal, 1980).

Mixer-settlers are an effective, low-cost, and reliable method of separation, however they require large volumes to achieve the necessary residence times to achieve fluid separation. This makes them impractical in cases where there is limited available space or when it is desirable to minimise liquid volumes. In the context of nuclear reprocessing, large volumes of fluid should be avoided due to the radiolytic degradation of the solvent and the risk of criticality associated with the accumulation of fissile material. To address these issues, extraction can also be performed using a Liquid-Liquid Extraction Column (LLEC).

LLECs typically consist of a large column where the heavy phase enters the top before flowing down and exiting via the base. The less-dense phase of the two enters the column at the bottom, where it travels upwards before leaving at the top. A large surface-area-to-volume ratio between the two phases is desirable to ensure a high mass transfer rate, necessitating a small dispersed phase diameter; however, droplets must be sufficiently large to prevent

entrainment. The performance of a LLEC is often described by calculating the Height of a Transfer Unit (HTU) using the following equation.

$$HTU = \frac{H}{NTU} \quad (2.4)$$

Where  $H$  is the column height in m.

LLECs come in many different designs, and these can generally be categorized as either static or agitated. Static LLECs are columns such as packed or tray columns, and they are typically used in systems where the interfacial tension is low and agitation is not necessary to create a good dispersion. For systems with high interfacial tension, mechanical agitation facilitates drop breakage improving mass transfer rates.

There are many different designs of mechanically agitated LLECs, broadly categorised as rotating, reciprocating and pulsed. Examples of rotating columns include the Rotating Disk Contactor (RDC) which uses impellers to disperse and mix the liquids, and the Scheibel Column which also includes doughnut-type baffles to reduce axial mixing. The Karr reciprocating column uses plates attached to a central shaft which is moved vertically up and down over a short distance. Pulsed columns have no moving parts and rely on the contents of the column being hydraulically pulsed up and down. The degree to which a column is agitated is characterised by the pulse amplitude, representing the vertical displacement of the fluid, and pulse frequency, representing the number of pulses per second. These are commonly multiplied to give the pulse velocity. Various column internals can be used including sieve-plates, doughnut-disks or structured or unstructured packing. They are used extensively in reprocessing radioactive solutions as they require relatively little maintenance.

The pulsed column was initially patented in 1935, however there was relatively little interest until an investigation at the Hanford Chemical Research and Development Sections considered the adaptability of PSECs to nuclear reprocessing and concluded that PSECs offered a very favourable advantage over packed columns with the HTU being lower for an equivalent throughput (Dijck, 1935; Cooper and Groot, 1950). Further investigations at Hanford confirmed this to be the case, with the height of a transfer unit being one-third of that of a packed column (Sege and Woodfield, 1954). Going forwards, PSECs were utilised in

several nuclear facilities in the UK, including at Windscale (Davey, 1958) and Dounreay (Thompson et al., 2002).

Following the decision to build the Thermal Oxide Reprocessing Plant (THORP) in the 1970s, it was necessary to find an alternative to mixer-settlers, which had been successfully operated in the MAGNOX reprocessing plant since the 1960s (Lo et al., 1983). Due to the increased fuel enrichment and burn-up, it was no longer possible to control the risk of criticality using concentration, and it would be necessary to use PSECs which have a narrow column diameter making it possible to control for criticality by geometry (Phillips, 1992). The reduced solvent residence times were also beneficial as it reduced radiological solvent degradation via the radioactive decay of fission products. Finally, using pulsed columns eliminated the requirement for moving parts within the biological containment.

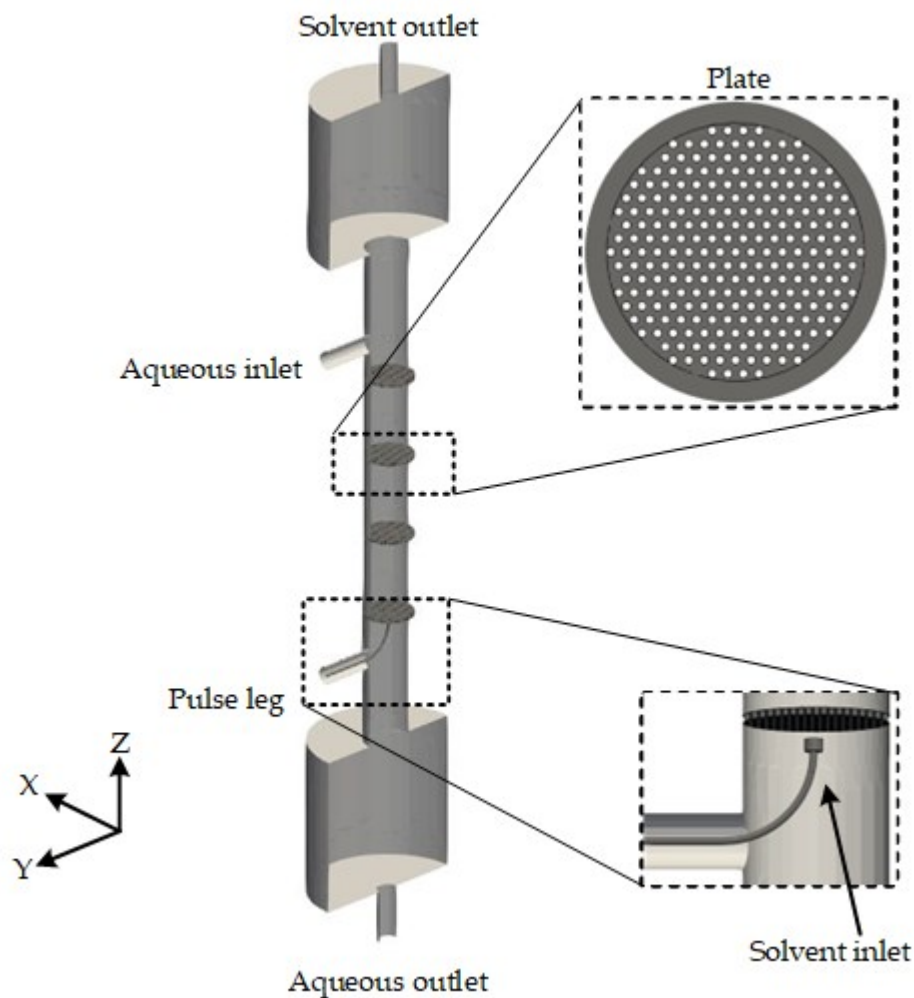


**Figure 6:** Schematic representation of a Pulsed Sieve-plate Extraction.

Pulsed sieve-plate extraction columns have been the subject of decades of research and development, identifying several "rules of thumb" that are often considered during the design process (Glatz and Cross, 2022). When designing a column, the choice of dispersed phase should be based on the desired outcome. For maximum efficiency, the least viscous phase should be selected as it will allow for greater diffusion of the solute in droplets. If greater capacity is required, the more viscous phase should be chosen as it will reduce the drag and increase the maximum throughput before flooding. For optimal mass transfer, it is best to ensure that the column internals are wetted by the continuous phase. This reduces coalescence, leading to increased interfacial area and mass transfer. If the continuous phase is aqueous, use metal internals; if it is organic, use plastic internals. Generally, PSEC performance is optimized when the direction of mass transfer is from the continuous phase to the dispersed phase, due to the Marangoni effect, where local variations in solute concentration at the droplet interface induces convection and promotes mass transfer. This repulsion reduces coalescence and the energy required to achieve a specific droplet diameter. A summary of typical PSEC geometry and operating parameters presented in the literature is shown in Table 1

**Table 1:** Details of column geometry and operating parameters (Yadav and Patwardhan, 2008).

| Parameter  | Value             |
|--|-------------------|
| Column diameter (mm)                             | 25.4-600          |
| Column height (m)                                | 0.37-5.40         |
| Plate hole diameter (mm)                         | 1-8               |
| Plate spacing (mm)                               | 12.5-200          |
| Plate free area (%)                              | 0.067-60          |
| Material of construction                         | SS, PTFE, others. |
| Heavy phase flow rate (L.hr <sup>-1</sup> )      | 0-2232            |
| Light volumetric flow rate (L.hr <sup>-1</sup> ) | 0-2862            |
| Pulse frequency (s <sup>-1</sup> )               | 0.17-7.00         |
| Pulse amplitude (mm)                             | 1.5-51.6          |

The design of column internals has been the subject of much research, particularly at Hanford in the 1950s. Early investigations developed a standard plate geometry consisting of 3.175 mm holes positioned in a triangular pitch with a fractional free area of 23%, resulting in a balance of high throughput and extraction efficiency (Sege and Woodfield, 1954). Additionally, the impact of manufacturing on column performance has been considered. When manufacturing

plates by punching holes out of a sheet of steel, a small burr is left protruding, acting as a nozzle. Investigations at Hanford concluded that if the length of this nozzle is less than 1 mm, it is possible to increase column throughput without reducing mass transfer efficiency.

A cartridge is an assembly of plates, the simplest of which have plates placed at equal distances in a column. There are more intricate designs, such as the graded cartridge, which has varying plate spacing throughout the column. This can produce a uniform dispersion along the length of the column (Lo et al., 1983). Redistributor plates are used to lower scale-up effects (Sege and Woodfield, 1954).

Table 2 summarises the typical fluid properties of the chemical systems used in PSEC investigations. Water is the most utilised continuous phase due to its ready availability and as it is the only fluidic system recommended in the EFEC Standard Test System (Misek, 1985). Nitric acid is also often studied as it is the continuous phase utilised in the PUREX process (Lanham and Runion, 1949). A much wider range of dispersed phase fluids is investigated in the literature, including commonly used industrial solvents such as toluene, kerosene, methyl isobutyl ketone (MIBK), various acetates, and carbon tetrachloride. TBP in various diluents is also widely used due to its use in the PUREX process. The solutes investigated are varied and include the EFCE-recommended acetone, uranyl nitrate for the PUREX process, and various other chemicals. Table 2 contains an overview of the physical properties of typical fluids from previous investigations.

**Table 2:** Details of physical properties in experimental studies reviewed by Yadav and Patwardhan (2008)

| Parameter  | Value      |
|--|------------|
| Continuous phase density ( $\text{kg.m}^{-3}$ )            | 996-1060   |
| Dispersed phase density ( $\text{kg.m}^{-3}$ )             | 660-1590   |
| Continuous phase dynamic viscosity ( $\text{N.s.m}^{-2}$ ) | 0.842-1.70 |
| Dispersed phase dynamic viscosity ( $\text{N.s.m}^{-2}$ )  | 0.486-4.88 |
| Interfacial tension ( $\text{N.m}^{-1}$ )                  | 1.75-46.0  |

## 2.2. Operational envelope

During column operation, two immiscible fluids of different densities flow counter-currently with the heavy phase fed through the top, flowing downwards before exiting through a lower vessel, while the light phase enters at the base and travels upwards before leaving via the

upper separator (Lo et al., 1983). When the light phase is dispersed, droplets travel upwards and accumulate beneath sieve-plates where they are held by the downcoming liquid. Mechanical energy is applied to the system by pulsing the column contents, forming droplets which travel upwards and are arrested by the next plate. Over repeated pulsations, the dispersed phase travels through the column and separates from the continuous phase, exiting the column. In this example, we assume the heavy phase is continuous and the light phase is dispersed. However, the discussion is still valid for a dispersed heavy phase.

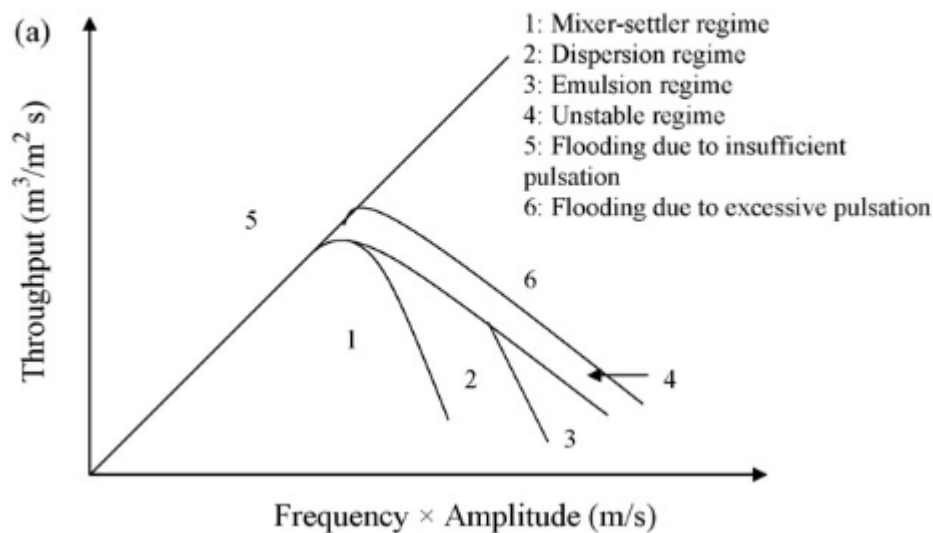


**Figure 7:** Flow regimes in a PSEC (Yadav and Patwardhan, 2008).

The pulse frequency and amplitude dictate the amount of energy put into the system, the multiple of which is referred to as the pulse velocity. Depending on the degree of pulsation, PSECs can operate in one of three stable operating regimes: mixer-settler, dispersion, and emulsion. Additionally, there are two flooding regimes: upper-limit flooding and lower-limit flooding. Figure 7 shows a graphical representation of the column's operating envelope.

During lower-limit flooding, insufficient pulsation results in the accumulation of the light phase beneath the plate. This is caused by insufficient energy to force the light phase through the plate holes, accumulating beneath the plate over time. As the thickness of the light phase increases, it eventually exits via the lower column outlet. This mode of operation is also known as flooding due to insufficient pulsation.

Increasing column pulsation until enough energy is generated to force the light phase through the plate holes causes the transition from lower-limit flooding to the mixer-settler regime. This mode of operation is characterised by the accumulation of the light phase beneath the plate before it is pulsed and jetted through the holes. Pulsation causes the formation of droplets, which travel upwards and accumulate beneath the next plate which repeats over many pulses, and the dispersed phase travels through the length of the column before accumulating in the upper separator and exiting the column. This is illustrated in Figure 8. This mode of operation is characterised by low throughput and high hold-up due to the layer of dispersed phase beneath the plates (Yadav and Patwardhan, 2008). A layer of light phase below the plate is not productive to mass transfer performance as this reduces the surface area available for mass transfer. Increasing pulse velocity reduces this layer, reducing the hold-up and improving mass transfer performance.

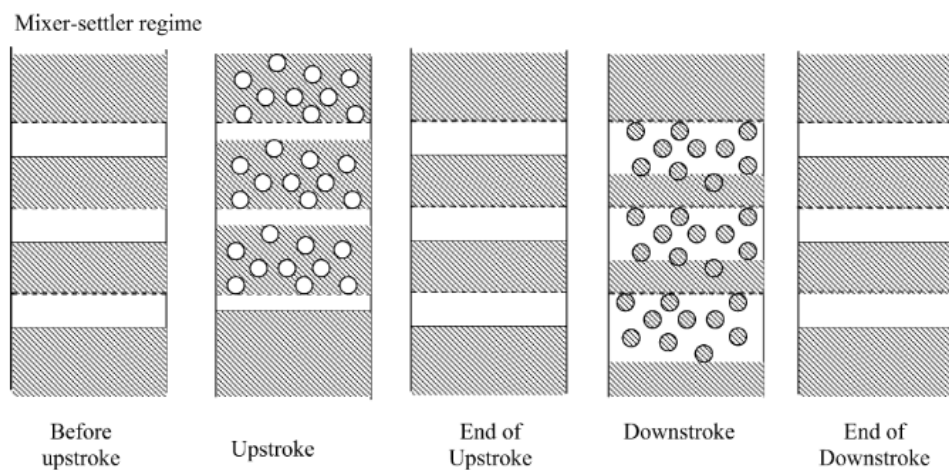


**Figure 8:** Mixer-settler operation (Yadav and Patwardhan, 2008).

Further increasing the pulse velocity causes hold-up to reach a minimum, with no accumulated light phase below the plate. This mode of operation is known as the dispersion regime. Increasing pulse velocity causes a reduction in droplet diameter, droplets to rise more slowly and the dispersed phase hold-up to increase. This results in a significant increase in the surface area available for mass transfer, which is why it is considered the most efficient mode of operation (Sege and Woodfield, 1954).

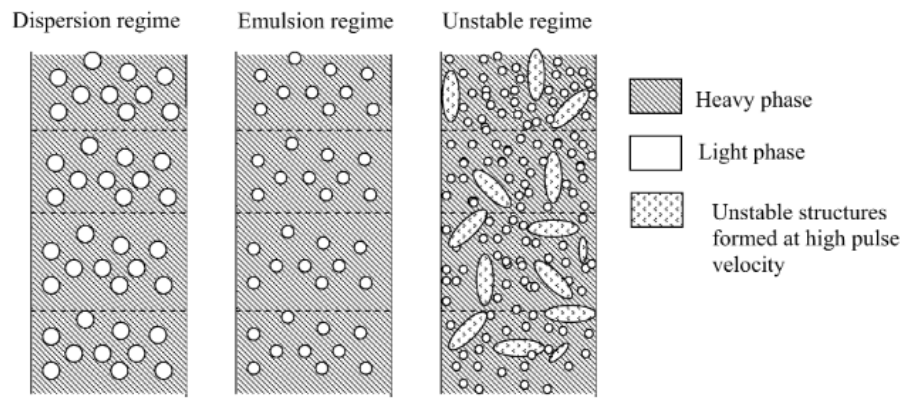


**Figure 9:** Dispersed, emulsion and unstable operation (Yadav and Patwardhan, 2008).

Increasing pulsation results in increased shear acting on droplets causing further breakage and the formation of an emulsion, the entrainment of fine droplets with the continuous phase in the regions of plates and a rapid increase in column hold-up (Yadav and Patwardhan, 2008). This mode of operation is referred to as the emulsion regime. If the pulse amplitude is further increased, it leads to a transition into the unstable regime, with local phase inversion in the column, large column hold up and inefficient mass transfer (Sege and Woodfield, 1954).

During upper-limit flooding, also known as flooding due to excessive pulsation, small drops are produced with a terminal settling velocity less than the continuous phase's superficial velocity. These droplets become entrained in the downcoming fluid and exit via the lower separating vessel.

### 2.2.1. Predicting regime transition

The ability to accurately predict regime transition is important, as it significantly impacts the column's performance and operability. Over the years, many correlations have been developed to predict the point of regime transition. These correlations have been discussed in detail in previous literature (Kumar et al., 1988; Yadav and Patwardhan, 2008), however, many of them have been developed for a single PSEC geometry and their applicability to other column geometries is limited and should be taken into account.

An investigation that examined published data from 15 studies for 23 liquid-liquid systems, comprising a total of 1574 data points, identified a correlation that can determine the pulse velocity,  $(Af)_t$ , that signals the transition from the mixer-settler regime to the dispersion regime to an accuracy within 17% (Kumar et al., 1988).

$$(Af)_t = 9.69 \times 10^{-3} \left( \frac{\sigma \Delta \rho^{\frac{1}{4}} A_p}{\mu_d^{\frac{3}{4}}} \right)^{\frac{1}{3}} \quad (2.5)$$

Where  $\sigma$  is the interfacial tension in  $\text{N.m}^{-1}$ ,  $\Delta\rho$  is the density difference in  $\text{kg.m}^{-3}$ ,  $A_p$  is the plate fractional free area and  $\mu_d$  is the dispersed phase dynamic viscosity in  $\text{N.s.m}^{-2}$ .

A correlation has been developed to predict the transition from the dispersion regime to the emulsion regime based on the maximum kinetic energy dissipated into the dispersed phase (Boyadzhiev and Spassov, 1982). The correlation was developed using experimental data from 12 previous investigations, with a range of fluid properties including continuous phase densities from 805 to 1000  $\text{kg.m}^{-3}$ , dispersed phase densities from 816 to 1595  $\text{kg.m}^{-3}$  and interfacial tensions from 8 to 51.5  $\text{mN.m}^{-1}$ . Column geometries studied include plate hole diameters from 2 to 12.7 mm and plate free areas between 5.2 to 55%. The correlation achieved an error of 20%.

$$(Af)_t = 0.5 \left( \frac{0.96 A_p^2}{\rho_c} \right)^{\frac{1}{3}} \quad (2.6)$$

Where  $\rho_c$  is the continuous phase density in  $\text{kg.m}^{-3}$ .

### 2.2.2. Predicting flooding

The prediction of upper and lower-limit flooding in a PSEC has been the subject of numerous correlations. Most of these correlations have been developed for specific column geometries and chemical systems, while some are more general. Previous investigations that considered a number of correlations tested against an experimental dataset consisting of 400 data points found no correlation general enough to predict the entire flooding curve (Yadav and Patwardhan, 2008). However, when tested against an experimental dataset consisting of 64 data points, the correlation of Tribess and Brunello (1998) was found to be effective for predicting the maximum column throughput. This equation is based on an existing correlation that formulates a column's maximum throughput as a function of the interfacial tension, plate fractional free area and column throughput expressed in  $\text{m}^3.\text{m}^{-2}.\text{h}^{-1}$ , however the influence of viscosity, density difference and pulsation are not included (Berger and Walter, 1985). Additional experiments investigated the effect of plate spacing and initial acetone mass fraction, and the correlation was further modified. Notably, the original correlation by Berger,

used as the basis for the new equation, is copied across incorrectly. Berger's actual correlation is presented below, with modifications by Tribess and Brunello incorporated, however, it is not advised to use the equation without first assessing which form of the equation was used to generate the data in the revised paper.

$$(Q_c + Q_d)_m = (24.528 + 2.537\sigma - 0.0548\sigma^2)(1 - 1.455.A_p + 3.247A_p^2) \left(1 + 0.1778 \ln\left(\frac{Q_c}{Q_d}\right) + 0.0437 \left(\ln\left(\frac{Q_c}{Q_d}\right)\right)^2\right) (0.2115D^{0.20}h^{0.18}) \left(1 + \left(\frac{Q_c}{Q_d} \frac{h}{d_p} C_{sol.in}\right)\right)^{0.09} \quad (2.7)$$

Where  $Q_c$  is the continuous phase volumetric throughput in  $m^3.s^{-1}$ ,  $Q_d$  is the dispersed phase volumetric throughput in  $m^3.s^{-1}$ ,  $D$  is the diffusion coefficient in  $m^2.s^{-1}$ ,  $h$  is the plate spacing in m and  $d_p$  is the plate hole diameter in m.

Recently, efforts pertaining towards the development of data-driven approaches to the identification of flooding have been developed. This includes both black-box and physics-informed grey-box approaches developed using a dataset consisting of 3048 data points which cover a set of geometric, performance and chemical properties which can be considered representative of operations carried out in small and medium-scale pulsed columns (Brockkötter et al., 2020).

### 2.3. Droplet diameter

Droplets, which are small volumes of liquid separated from a surrounding fluid, be it liquid or a gas (Clift et al., 2005), are held together by intermolecular forces that attract the molecules in the middle of the droplet in all directions. This causes molecules at the surface to be drawn towards the middle and along the surface, creating the phenomenon known as interfacial tension, where, droplets attempt to reduce their surface area-to-volume ratio and form a sphere.

When two droplets collide, the interfacial tension causes them to merge into a single droplet with a smaller surface area to volume ratio. This process, referred to as coalescence, occurs in several steps. Initially, the droplets collide, followed by the draining of liquid between them, forming a "neck" or "bridge" before fully coalescing. The coalescence rate is governed by the viscous, inertial and surface forces, and larger droplets take longer to coalesce as more fluid needs to drain out.

In cases where the fluid is incompressible, the shape of a droplet can be described using the Bond, Morton and Reynolds dimensionless numbers. A droplet can be either spherical, ellipsoidal or spherical capped.

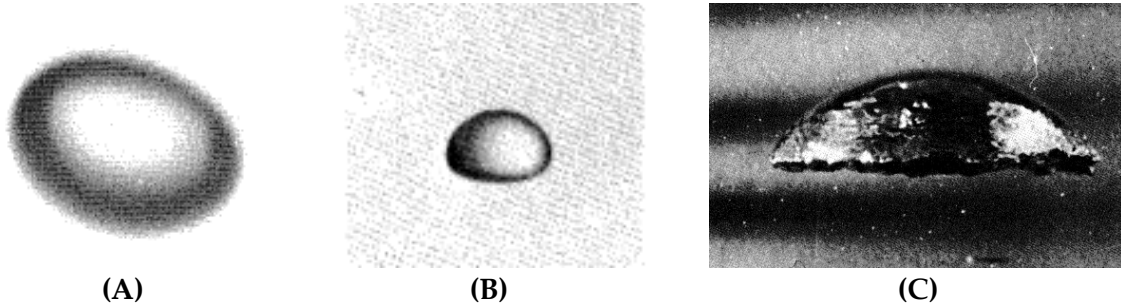


**Figure 10:** (A) Spherical, (B) ellipsoidal and (C) spherical capped droplets (Clift et al., 2005)

The Bond ( $Bo$ ) or Eotvos number is a dimensionless number which describes the relationship between gravitational forces that act on a droplet and its interfacial tension. Interfacial tension acts to form droplets into spheres while gravity pulls them downwards into a spherical capped shape. Droplets of greater diameter will have more mass, so they are more affected by gravity than interfacial tension and will have a larger Bond number. On the other hand, interfacial tension is dominant for small droplets with lower mass, so they will tend to form spheres and have a small Bond number.

$$Bo = \frac{g\Delta\rho d^2}{\sigma} \quad (2.8)$$

Where  $g$  is the acceleration due to gravity in  $\text{m}\cdot\text{s}^{-2}$  and  $d$  is the droplet diameter in m.

The Morton number ( $Mo$ ) is a dimensionless number used in combination with the Bond number to determine the shape of droplets. It is important to highlight that the number is independent of the droplet's geometry and only depends on the properties of the two fluids.

$$Mo = \frac{g\mu^4\Delta\rho}{\rho^2\sigma^3} \quad (2.9)$$

The Reynolds number ( $Re$ ) is a measure of the ratio of inertial forces to viscous forces. When the Reynolds number is low, inertial forces dominate, and droplets become more spherical. At larger droplet diameters, the Reynolds number increases and the droplet becomes more disturbed by turbulent forces, making its shape distorted.

$$Re = \frac{\rho dU}{\mu} \quad (2.10)$$

By combining the Bond, Morton, and Reynolds numbers, Figure 11 can be used to determine the shape of a droplet in unhindered gravitational flow based on the fluid's densities, viscosities, interfacial tensions, and the size, speed, and drag coefficient of the droplet. Using experimental conditions identified in Table 1 and Table 2, the maximum Reynolds number and Bond/Eotvos number are calculated to be approximately 1000 and 0.2 respectively, indicating that droplets will tend to be spherical. However, while the continuous phase superficial velocity in a PSEC tends to be relatively low, the fluid is not static and therefore, it cannot be assumed that all droplets in PSECs are spherical.

Droplet size is an important factor in the performance of a PSEC, as it affects droplet rise velocity and mass transfer rate. It is important to note that droplets in a PSEC are not of a single diameter but exist in a distribution around a mean value (Rhodes, 2008). To make this information easier to work with, reducing it to a single number is often useful. However, this is not always straightforward, as the droplet size distribution of a population of droplets can vary dramatically depending on its geometry and the number, surface area and volume distributions can also vary drastically. The best way to determine the correct distribution is to measure the droplet size directly and converting between distributions should be avoided as it introduces errors.

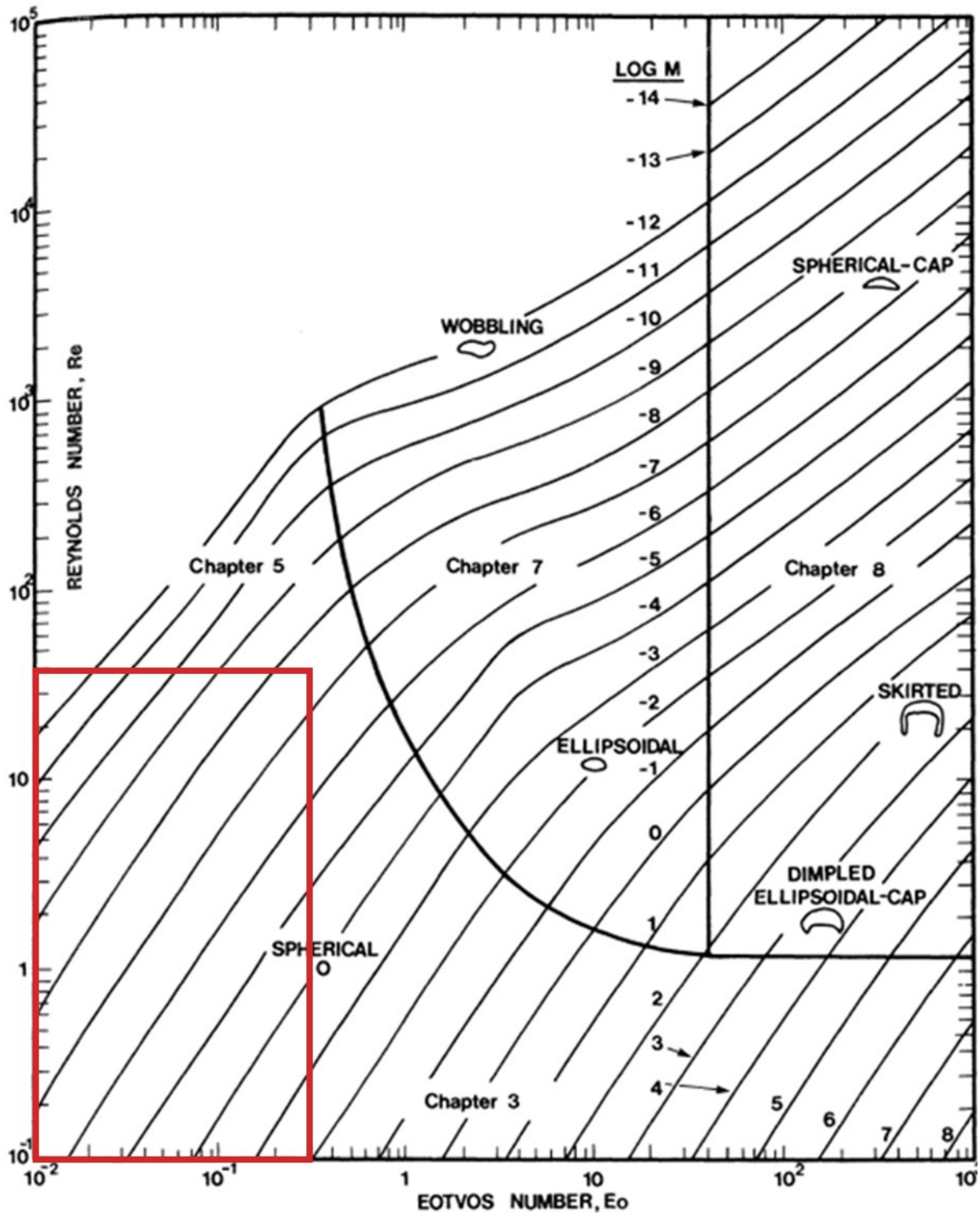


**Figure 11:** Shapes for droplets in un hindered gravitational flow-through liquid (Clift et al., 2005). Calculated for  $\Delta\rho = 0\text{-}400 \text{ kg}\cdot\text{m}^{-3}$ ,  $d = 0 \text{ to } 10 \text{ mm}$ ,  $\sigma = 1.75\text{-}46 \text{ N}\cdot\text{m}^{-1}$ ,  $\mu = 0.486\text{-}4.88 \text{ N}\cdot\text{s}\cdot\text{m}^{-2}$ ,  $U = 0\text{-}1 \text{ m}\cdot\text{s}^{-1}$  and  $\rho_d = 660\text{-}1590 \text{ kg}\cdot\text{m}^{-3}$  (Yadav and Patwardhan, 2008).

When describing the droplet size of a population using a single number, many options are available depending on the phenomena that are conserved. One of the most frequently used means is the Sauter Mean Diameter (SMD),  $d_{3,2}$ . This is an arithmetic mean of a surface distribution with the same surface area to volume ratio of the distribution. Figure 12 presents the calculated number weighted,  $d_{1,0}$ , volume weighted,  $d_{3,0}$ , and SMD,  $d_{3,2}$  means for a simulated, normal, droplet size distribution consisting of 20000 droplets with a mean diameter of 5 mm and a standard deviation of 1 mm.

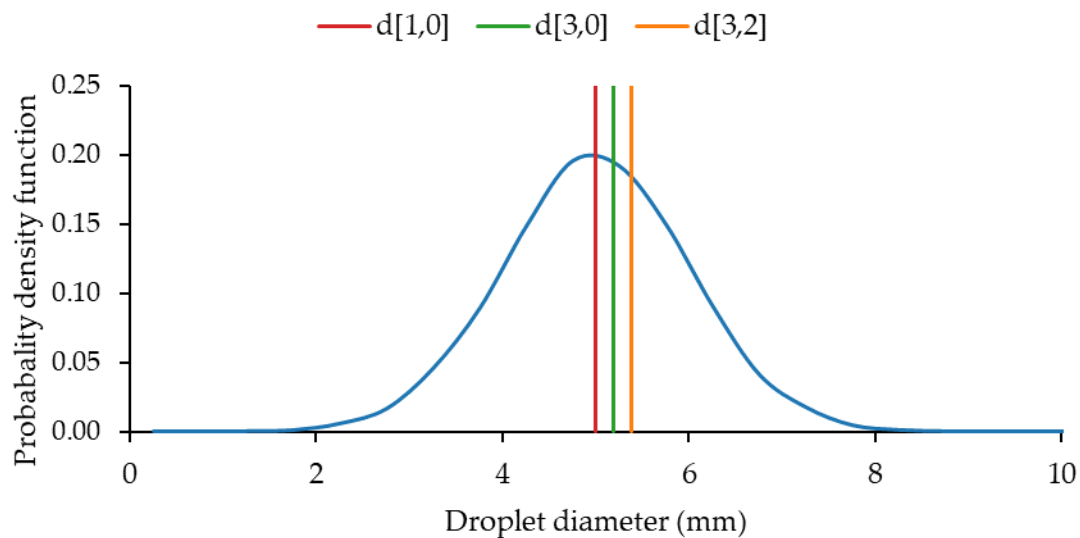


**Figure 12:** Comparison of measures of central tendency for different mean diameters calculated from a simulated droplet size distribution consisting of 20000 droplets with a mean diameter of 5 mm and a standard deviation of 1 mm.

Much research has been undertaken to understand the influence of column geometry and operation on the size of droplets produced in PSECs, the results of which are summarised by Yadav (2008).

Regarding the geometry of the column, the key parameters affecting droplet size is the plate design, specifically plate hole diameter and free area, as smaller holes produce smaller droplets than large holes, increasing the shear forces acting on the droplets. This is most important when the column operates in the mixer-settler regime where droplets are larger than the plate hole diameter, however, this effect is less pronounced when operating in the dispersion regime where droplets are smaller than the plate hole diameter. The impact of plate

spacing should also be considered, as increasing this results in larger droplets due to the opportunity for droplet coalescence between pulses. On the other hand, column diameter does not significantly affect droplet size, as the energy input is evenly distributed over the column's cross-sectional area. Regarding column height, several investigators have identified that most droplet breakage occurs over the first two or three plates, after which the droplet diameter is consistent over the column height.

In terms of column operation, pulse amplitude and frequency are the most important parameters when it comes to determining droplet size. When increased, the average droplet diameter decreases due to the increased shear forces acting on the droplets. At low levels of pulsation, a range of droplet diameters are produced, whereas higher levels of pulsation produces more homogenous droplets. Furthermore, the effects of the continuous and dispersed phase flowrates on droplet diameter are negligible.

### **2.3.1. Predicting mean droplet size**

Predicting mean droplet diameter is important due to its impact on both column hydrodynamics and mass transfer performance. Numerous correlations are available in the published literature, however, these are typically derived using limited column geometries, operating conditions or fluidic systems and have a limited range of validity. A review by Yadav (2008) discussed many of these correlations and assessed their performance against published experimental data.

The correlation of Sreenivasulu (1997) was developed using experimental data from 11 different investigations, including columns with plate hole diameters of 2 to 8 mm, plate free areas of 8 to 46 %, plate spacings of 30 to 100 mm, continuous and dispersed phase velocities of 3.15 to 7.20 mm.s<sup>-1</sup> and 0.68 to 7.50 mm.s<sup>-1</sup> and pulse velocities of 4 to 78 mm.s<sup>-1</sup>. A variety of representative fluidic systems were studied with and without mass transfer. The density and viscosity of the continuous phases were 992 to 1000 kg.m<sup>-3</sup> and 0.84 to 1.0 mN.s.m<sup>-2</sup> respectively. The density and viscosity of the dispersed phases were 796 to 1000 kg.m<sup>-3</sup> and 0.55 to 1.75 mN.s.m<sup>-2</sup>, while interfacial tensions studied ranged from 10.2 to 45 mN.m<sup>-1</sup>. The correlation performs relatively well when compared against experimental data, with a Root-Mean Squared Error (RMSE) of 0.162 mm.

The correlation is presented below where  $C = 0.08$  in the absence of mass transfer and  $C = 0.1$  when mass transfer is from the dispersed phase to the continuous phase (Sreenivasulu et al., 1997). As no value for  $C$  is given when mass transfer is from the continuous phase to the dispersed, this value is assumed to be 0.1.

$$d_{3,2} = C \left( \frac{\sigma}{\rho_c} \right)^{0.4} (Af)^{-0.8} A_p^{0.48} d_p^{0.26} h^{0.34} \quad (2.11)$$

Where  $d_{3,2}$  is the Sauter Mean Droplet diameter in m,  $A$  is the pulse amplitude in m and  $f$  is the pulse frequency in  $s^{-1}$ .

## 2.4. Dispersed phase holdup

The rate at which droplets rise through the column directly affects the dispersed phase holdup, which has implications for the column's hydrodynamics and mass transfer performance. Upon formation, several forces will act upon a droplet, including gravity, buoyancy, drag, lift, virtual mass, and turbulent dispersion (Wang et al., 2022). Figure 13 demonstrates a force balance on a single droplet within a swarm, illustrating how these forces interact.

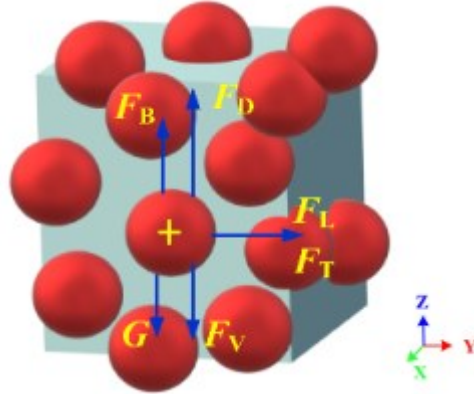


**Figure 13:** Force balance on a droplet in a swarm (Wang et al., 2022).

Using Newton's second law of motion, the force balance acting on a droplet travelling upwards can be represented as:

$$\rho_{drop} V_{drop} a_a = F_g + F_b + F_d + F_l + F_v + F_t \quad (2.12)$$

Where  $V_{drop}$  is the droplet volume in  $m^3$  and  $a$  is the interfacial area per unit volume in  $m^2.m^{-3}$ .

However, due to the complex interrelation of the drag force ( $F_d$ ), lift ( $F_l$ ), virtual mass ( $F_v$ ) and turbulent dissipation ( $F_t$ ), it is useful to combine these within the total drag force,  $F_D$  (Wang et al., 2022).

$$\rho_{drop}V_{drop}a_a = F_g + F_b + F_D \quad (2.13)$$

The gravitational force acting on a spherical droplet is calculated using the following equation:

$$F_g = -mg = -V_{drop}\rho_{drop}g = -\frac{\pi d^3}{6}\rho_{drop}g \quad (2.14)$$

Where  $m$  is mass in kg.

The buoyancy force acting on a droplet is calculated using Archimedes principle, which states that the upward buoyant force acting on an object equals the weight of the displaced fluid. Assuming spherical droplets gives the following equation:

$$F_b = V_{drop}\rho_c g = \frac{\pi d^3}{6}\rho_c g \quad (2.15)$$

The total drag force acting on a spherical droplet is calculated as a function of the droplet geometry, fluid properties and the drag coefficient ( $C_d$ ) which is a dimensionless number used to quantify the drag.

$$F_D = -\frac{C_d\pi\rho_c d^2 v_{slip}^2}{8} \quad (2.16)$$

Assuming a droplet is travelling at its terminal velocity and is in equilibrium, substitution and rearrangement of equations 2.13 to 2.16 gives an equation for the terminal slip velocity ( $v_{slip}$ ) of a droplet as a function of its diameter, fluid densities, acceleration due to gravity and the droplets drag coefficient.

$$v_{slip} = \sqrt{\frac{4d\Delta\rho g}{3C_d\rho_c}} \quad (2.17)$$

From the above equation, it is evident that the droplet's slip velocity and the corresponding dispersed phase holdup is dependent on the droplets diameter, the density of the two fluids, the gravitational constant and the drag coefficient. There are many empirical correlations which have been developed for predicting the drag coefficient, however these are typically only valid for dilute dispersions.

Many investigations have examined the dispersed phase holdup as a function of column design and operation. The most important parameter is droplet size, as larger droplets have a greater rise velocity, corresponding to a lower holdup (Yadav and Patwardhan, 2008).

Regarding geometric considerations, increasing plate hole size and fractional free area reduces shear, producing larger droplets and decreasing holdup. This is most noticeable when the column is operating in the mixer-settler regime with droplets larger than the plate holes, however once droplets become smaller than the plate holes this no longer has a significant effect. Plate spacing is also significant, as it provides more opportunities for droplet coalescence and therefore larger droplets. Interestingly, holdup is generally independent of column diameter which can be attributed to the even distribution of energy across the columns cross-sectional area.

From an operational perspective, the amount of energy inputted into the system via pulse amplitude and frequency significantly affects dispersed phase holdup. Usually, holdup is high in the mixer-settler regime due to the layer of coalesced dispersed phase beneath the plate. This layer has a low surface area to volume ratio, so it does not contribute significantly to mass transfer performance in the column. Increasing pulse frequency or amplitude leads to a decrease in the thickness of this layer, resulting in a reduction of holdup. The minimum dispersed phase holdup is reached at the transition from mixer-settler to the dispersion regime. If pulse amplitude or frequency are further increased, it produces smaller droplets and the dispersed phase holdup increases until the column floods. Previously, it was discussed that droplet diameter is not significantly affected by the continuous and dispersed phase flow rates. Therefore, increasing the dispersed phase flow rate leads to more droplets and a greater dispersed phase holdup. In contrast, dispersed phase holdup is largely unaffected by the continuous phase flow rate.

#### **2.4.1. Predicting dispersed phase holdup**

Much effort has been invested into finding empirical correlations to predict dispersed phase holdup, due to its importance in calculating the surface area available for mass transfer. Unfortunately, many of these correlations are limited in their usefulness because they are developed using limited datasets that do not include representative column geometries, operating parameters, or fluidic systems. Yadav (2008) provides an in-depth discussion of

these correlations, and when compared to published experimental data, identified the correlation of Venkatanarasaiah and Varma (1998) as the most representative.

The correlation was developed using experimental data from 17 different investigations, including columns with plate hole diameters of 2 to 8 mm, plate free areas of 23 to 46 %, plate spacings of 50 to 200 mm, continuous and dispersed phase velocities of 1.74 to 7.50 mm.s<sup>-1</sup> and 0.14 to 7.50 mm.s<sup>-1</sup> and pulse velocities of 7 to 89 mm.s<sup>-1</sup>. A variety of representative fluidic systems were studied with and without mass transfer. The density and viscosity of the continuous phases were 996 to 1102 kg.m<sup>-3</sup> and 0.842 to 1.11 mN.s.m<sup>-2</sup> respectively, and the density and viscosity of the dispersed phase were 652 to 1590 kg.m<sup>-3</sup> and 0.287 to 1.89 mN.s.m<sup>-2</sup>, while interfacial tensions studied ranged from 9.02 to 46.6 mN.m<sup>-1</sup>. The correlation performs relatively well when compared with experimental data, with a RMSE of 18.9 %.

The correlation is presented below, where  $K$  is 116.5 in the absence of mass transfer, 84.6 when mass transfer is from the continuous phase to the dispersed and 92 from the dispersed to the continuous phase (Venkatanarasaiah and Varma, 1998).

$$\alpha = Ke^{42.56|Af-(Af)_m|} v_d^{1.02} v_c^{0.02} \Delta\rho^{-0.23} \mu_d^{0.52} d_p^{-0.3} A_p^{-0.4} h^{-0.4} \quad (2.18)$$

## 2.5. Mass transfer

Many studies have been conducted to understand how PSECs' design and operation affect their mass transfer performance, however, the complex relationship between hydrodynamics and mass transfer makes it more difficult to quantify this than for droplet size and dispersed phase holdup (Yadav and Patwardhan, 2008).

Traditionally, the design of a PSEC for a given separation was achieved by first calculating the NTU required and then using pilot plant study to determine the HTU which was scaled accordingly (Naylor and Larkin, 1971). However, this process is complicated due to the differences in HTU caused by changes in column geometry, operational parameters, and fluidic systems used. Despite attempts to parameterise HTU using pilot scale facilities operating at the same Solvent-Aqueous (S:A) flow ratio, residence time, and extraction performance, these methods are inaccurate due to the incorrect assumption that column residence time is unaffected by the effect of scale-up.

Several investigations have looked at the impact of column design on mass transfer performance (Yadav and Patwardhan, 2008). The effect of changing column diameter is highly nonlinear. Previous investigations showed that increases in diameter for small columns has a minimal impact on mass transfer while larger columns experienced a significant reduction in performance. This is mainly due to an increase in axial dispersion along the length of the column with increasing column diameter, which reduces the mass transfer driving force. In addition, plate design has a significant influence on mass transfer. Generally, mass transfer decreases with increasing plate hole diameter, fractional free area and plate spacing. This is because the droplet diameter increases, decreasing the surface area to volume ratio within the column. Furthermore, plate wettability can have a significant impact on mass transfer. If the dispersed phase wets the plate, it promotes coalescences, further reducing the surface area to volume ratio.

Mass transfer performance in the mixer-settler regime can be improved by increasing the pulse amplitude or frequency. This reduces the layer of coalesced droplets beneath the plate, which have a low surface area to volume ratio and do not contribute significantly to mass transfer. Further increasing pulsation will cause the dispersed phase holdup to increase, however, this results in an increase in axial dispersion within the column, reducing mass transfer performance. Mass transfer performance is positively correlated with increasing dispersed phase throughput and negatively correlated with increasing continuous phase throughput. To maximise mass transfer performance for a given column design, finding the optimal balance between pulsation and throughput is important.

### **2.5.1. Predicting mass transfer**

During PSEC operations, the dispersed phase droplets are in contact with the continuous phase. When performing mass transfer operations, both phases will contain a certain concentration of solute, and if these are not at their equilibrium concentrations, the system will attempt to reach equilibrium by the transfer of solute between the two phases.

This can be described using the two-film theory (Levenspiel, 1999), shown in Figure 14, to evaluate the molar transfer rate,  $MTR$ , which is based on the total fluid volume, inclusive of dispersed and continuous phases. The  $MTR$  of a solute from the bulk aqueous to the interface and from the interface to the bulk organic is given by:

$$MTR = k_c a (C_c - C_{c,i}) = k_d a (C_{d,i} - C_d) \quad (2.19)$$

where  $k_c$  and  $k_d$  are the mass transfer coefficients expressed in  $\text{m.s}^{-1}$  of the continuous and dispersed phases,  $a$  is the interfacial area per unit volume of reactor in  $\text{m}^2.\text{m}^{-3}$  and  $C$  is the solute concentration in  $\text{mol.m}^{-3}$ , with the subscripts  $c$  and  $d$  denoting if the concentration refers to the continuous or dispersed phase and the subscript  $i$  indicating if the concentration refers to the interface.

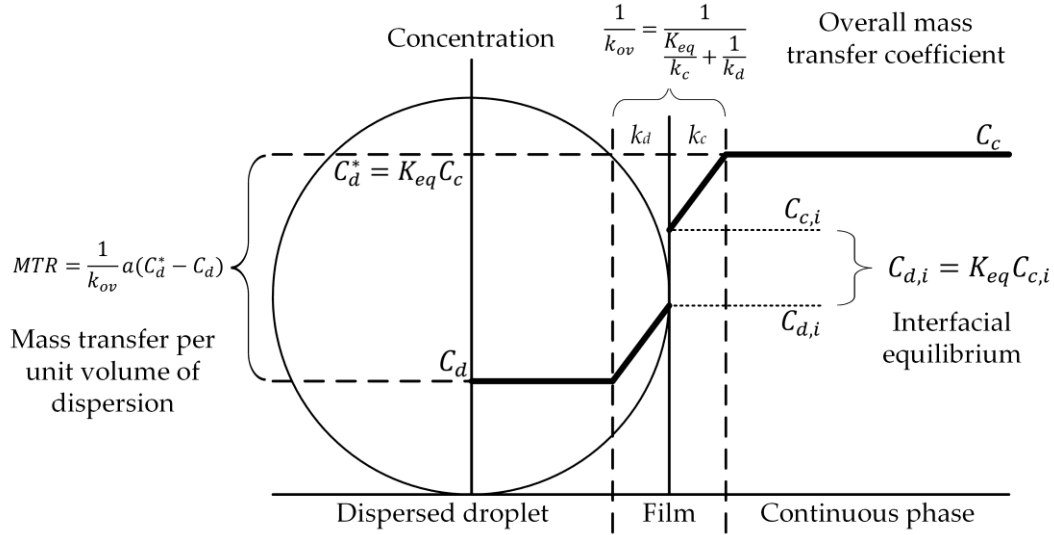


**Figure 14:** Schematic representation of two-film theory.

Assuming there is negligible resistance to mass transfer at the interface, the equilibrium distribution  $K_{eq}$  can be calculated using:

$$K_{eq} = \frac{C_{d,i}}{C_{c,i}} \quad (2.20)$$

Rearrangement and substitution gives the equation for the rate of interphase mass transfer:

$$MTR = \left( \frac{1}{\frac{K_{eq}}{k_c} + \frac{1}{k_d}} \right) a (K_{eq} C_c - C_d) \quad (2.21)$$

The phase-specific mass transfer coefficients are expressed as a function of the physical properties of the fluids (e.g., density, viscosity, diffusion coefficient) as well as a function of the hydrodynamic conditions within the system (e.g., droplet Reynolds number, the diameter of the dispersed phase and the relative velocity between the two phases). A review of correlations used for the prediction of multiphase mass transfer coefficients was published by Attarakih (2012) and is summarised in Table 3.

As shown in Table 3, for a droplet with a  $d_{3,2}$  of 3 mm, a rise velocity of 100 mm.s<sup>-1</sup> and a dispersed phase holdup of 10 %, the correlations give comparable predictions for both phases; the only exception is the Handlos and Baron (1957) correlation, which overestimates  $k_d$  markedly with respect to the other correlations. For the continuous phase mass transfer coefficient, the correlation of Treybal (1980) is recommended as it was developed to be used in swarms of droplets rather than single droplets. For the dispersed phase mass transfer coefficient, the correlation of Laddha and Degaleesan (1978) is recommended since this was derived from penetration theory, as opposed to the empirical nature of the Pilhofer and Mewes (1979) correlation.

**Table 3:** Correlations used to evaluate the phase-specific mass transfer coefficients for the absorption of acetone from water with fluid properties presented in Table 11,  $d_{3,2}= 3.0$  mm,  $U_s = 100$  mm.s<sup>-1</sup>,  $\alpha = 10\%$ . (Attarakih et al., 2012).

| Phase      | Reference                    | Correlation  | Value (m.s <sup>-1</sup> ) | Equation number |
|------------|------------------------------|--|----------------------------|-----------------|
| Continuous | Ranz and Marshall (1952)     | $k_c = \frac{D_c}{d_{32}} \left( 2 + 0.6 Re_{drop}^{\frac{1}{2}} Sc_c^{\frac{1}{3}} \right)$ | $1.23 \times 10^{-5}$      | (2.22)          |
|            | Treybal (1980)               | $k_c = \frac{D_c}{d_{32}} \left( 0.725 Re_{drop}^{0.57} Sc_c^{0.42} (1 - \alpha_d) \right)$  | $3.04 \times 10^{-5}$      | (2.23)          |
|            | Heertjes et al. (1954)       | $k_c = 0.83 \sqrt{\frac{D_c U_r}{d_{32}}}$   | $5.01 \times 10^{-5}$      | (2.24)          |
|            | Kronig and Brink (1951)      | $k_c = \frac{D_c}{d_{32}} \left( 0.6 \sqrt{Re_{drop} Sc_c} \right)$                          | $3.62 \times 10^{-5}$      | (2.25)          |
| Dispersed  | Handlos and Baron (1957)     | $k_d = 0.00375 \frac{U_d}{1 + \frac{\mu_d}{\mu_c}}$  | $1.38 \times 10^{-4}$      | (2.26)          |
|            | Laddha and Degaleesan (1978) | $k_d = 0.023 \frac{U_r}{Sc_d^{0.5}}$   | $1.30 \times 10^{-5}$      | (2.27)          |
|            | Pilhofer and Mewes (1979)    | $k_d = 0.002 \frac{U_r}{1 + \frac{\mu_d}{\mu_c}}$  | $1.27 \times 10^{-5}$      | (2.28)          |

## 2.6. Modelling and simulation

Modelling and simulation are useful tools for understanding and optimising complex processes. By formulating a mathematical description of a system, it allows for a deeper understanding and further investigations. The development of dynamic models is especially important for predicting the transient behaviour of unit operations. They can enhance flowsheet development and reduce the need for experimental and piloting work. Due to the widespread use of solvent extraction in nuclear reprocessing, many models have been developed for different flowsheets. Unfortunately, these models are generally not made public due to commercial confidentiality.

The Solvent Extraction Process Having Interaction Solvents (SEPHIS) model was developed at Oak Ridge National Laboratory (ORNL) in 1975 and was originally used for modelling the PUREX solvent extraction process (Tranter and Haefner, 2008). This model has now been extended to account for a wider range of flowsheets by modelling distribution ratios which are empirically fitted to experimental data (Law et al., 2011). The model can calculate the transient and steady-state evolution of solute concentrations using mixer-settlers, which are assumed to have a stage efficiency of 100%. A similar model, SOLVEX, was developed at Savannah River Laboratory in 1975 and can model both transient and steady-state behaviour (Tranter and Haefner, 2008).

The Argonne Model for Universal Solvent Extraction (AMUSE) was developed by Argonne National Lab (ANL) in 1997 to model the TRUEX (Trans Uranium Extraction) process and has since been expanded to model other processes (Law et al., 2011). AMUSE builds on the Spreadsheet Algorithm for Stagewise Solvent Extraction (SASSE) and the Spreadsheet Algorithm for Speciation and Partitioning Equilibria (SASPE), which perform mass balance (MB) for each cascade of extraction contactors and calculate distribution ratios on either a thermodynamic or empirical basis (Tranter and Haefner, 2008).

The PAREX code was developed by CEA (Commissariat à l'énergie atomique et aux énergies alternatives) in the 90s to simulate the PUREX process (Sorel et al., 2011). It has since been further developed to model more advanced reprocessing flowsheets for actinide partitioning and is used extensively for flowsheet optimisation, troubleshooting, safety analysis and operator training at the La Hague nuclear-reprocessing facility (Bisson et al., 2016). The model

can simulate the steady state and transient hydrodynamics and mass transfer performance of a range of industrial equipment, such as MS and ACC, which are approximated as Continuously Stirred Tank Reactors (CSTRs) and pulsed columns which are modelled using an axial dispersion model.

Various tools are available where it is possible to build a process flowsheet from a library of prebuilt unit operations, such as the commercially available HYSYS and CHEMCAD and the open-source DWSIM, which are all well developed and used extensively within the chemical processing industries. Generally, these tools are used to perform steady-state simulations, however, dynamic simulation is also possible (Tranter and Haefner, 2008). Typically, these models are not able to comprehensively model LLE operations out of the box, however there exists the ability to implement custom models within the code. An additional notable software is gPROMS (General Process Modelling System), which solves user-defined equations numerically, and due to its flexibility as a modelling tool, it has been used to model a variety of PUREX type flowsheets (Tranter and Haefner, 2008; Chen et al., 2016).

A variety of different approaches for the modelling PSECs within a flowsheet are available, including axial dispersion models, droplet Population Balances Models (PBM), Compartment Modelling and CFD.

An axial dispersion model assumes plug flow with deviations for idealised hydrodynamic behaviour quantified via the axial dispersion coefficient. Although this does not accurately reflect the actual hydrodynamic behaviour of the column, it can still be used to achieve representative mass transfer results, however this requires the measurement or estimation of the axial mixing coefficient. Significant uncertainty is associated with this due to pulsation of the column contents, which is attributed to the non-ideal behaviour of the continuous phase and the differences in droplet rise velocity caused by droplet size distribution in the dispersed phase.

The droplet PBM approach considers the dispersed phase as discontinuous and accounts for complex dispersed phase interactions such as coalescence, breakage, rise and back mixing (Bart et al., 2020). These models are advantageous as they can predict the droplet size distribution, dispersed phase holdup and concentrations. However, they are complicated in

terms of their mathematical formulation and currently, there are no known analytical solutions for the solute concentration and droplet diameters (Bart et al., 2020).

Compartment Modelling is a method for modelling complex chemical engineering systems, formulated by dividing the system into different zones known as compartments (Jourdan et al., 2019). It is a highly flexible technique, allowing different models of phenomena to be incorporated into separate compartments, whilst still providing resolution of local phenomena within the system. Traditionally, CMs were formulated empirically based on experimental observations, however, with the increased prevalence of computing power, they are often formulated using CFD-predicted hydrodynamics. CMs are advantageous, as they require significantly less simulation time when compared to other spatially resolved techniques such as CFD. They typically employ bespoke formulations using various programming languages, though more generalised tools are also available. CompArt is a recently developed tool which provides a generic language to input compartments and phenomena, generating the appropriate mathematical formulation of the system and then numerically solving it (Jervis, 2022).

CFD is a branch of fluid mechanics that uses numerical methods to solve the Navier-Stokes (NS) equations and to predict the flow characteristics of the fluid, such as pressure and velocity, an overview of which is given in chapter 5. It is a powerful tool used to simulate the behaviour of various chemical engineering systems due to its ability to provide insight into various physical processes such as turbulence, heat transfer, and chemical reactions. Generally, CFD simulations are prepared using a computational mesh which is a set of points that physically represents the geometry and the specification of appropriate boundary conditions, which are solved and subsequently analysed. A significant disadvantage of CFD is that a large amount of computation is required due to the complexity of the equations used to simulate fluid flow and the large mesh sizes needed to accurately resolve the flow fields. This results in large amounts of time required to solve industrially relevant systems. Despite this, CFD is a valuable predictive tool that provides information that cannot be easily measured experimentally, and as a result, a considerable number of investigations have looked at the application of CFD to the simulation of PSECs.

### 2.6.1. Computational Fluid Dynamics simulation of PSECs

Since 2009, there have been 17 notable investigations into the simulation of PSECs using CFD in the literature. These studies have mainly been concerned with verifying and validating various modelling methods, such as the representation of the geometry and mesh, multiphase formulations, turbulence modelling, interphase momentum transfer, calculation of droplet size, axial dispersion and mass transfer.

#### 2.6.1.1. Geometry and meshing

The geometry of a PSEC can be represented in 3D, capturing the entire column cross-section or as an axisymmetric wedge, or in 2D as a slice across the column section or as an axisymmetric slice across the column. Simplification of the column is desirable as it can result in a significant reduction in the time taken for a simulation. Sen (2015) looked at different approaches for representing a PSEC in 2D by comparing the results of CFD-predicted Residence Time Distribution (RTD) studies. In their investigation, they compared the effect of plate hole diameter and pitch and concluded that maintaining plate hole diameter is necessary when preparing a 2D CFD simulation. Tu (2021) compared full 3D, axisymmetric 3D as a 60° wedge, a 2D slice and an axisymmetric 2D slice and identified differences in the predicted dispersed phase holdup. In their work, they conclude that a 3D axisymmetric wedge is the most appropriate, however, Theobald (2020) identified that intercompartment flows typically recirculate, and this approximation would not be able to capture these effects due to the symmetrical boundary conditions. Unfortunately, there have been no experimental investigations into the experimental characterisation of flow fields within PSEC geometries, however due to the known presence of large recirculating regions it is recommended that geometry be either represented as the full 3D cross section, or a 2D slice across the entire column.

When performing a CFD simulation, the geometry is represented as a computational mesh that must be sufficiently resolved to not affect the solution. This can be determined by performing a mesh independence test, where the mesh is refined until phenomena no longer change with increasing mesh resolution. Sen (Sen et al., 2015) calculated a typical cell edge length of 1 mm for pressure drop and residence time distribution in a 2D slice, while Tu (2021) determined a typical cell edge length of 1.5 mm for full 3D and axisymmetric 3D, and 1.0 mm

for 2D and axisymmetric 2D cases using the continuous phase axial velocity and turbulence kinetic energy.

### 2.6.1.2. Multifluid formulation

Many investigations have been conducted to determine an appropriate multifluid model for practical applications. These include single-phase models, interface averaging, interface-resolving and hybrid methods which dynamically switch between interface-averaging and interface-resolving.

Single-phase models, where the effect of the dispersed phase are ignored, have been used to predict axial dispersion (Kolhe et al., 2011; Sen et al., 2015) and compare turbulence models (Khatir et al., 2016). These models provide valuable data to assess underpinning phenomena, however, these models are limited in their real-world application.

Interface-averaging, a Euler-Euler framework where the two fluids are treated as interpenetrating continua and coupled via interphase momentum transfer, is the most well-validated approach, with studies into turbulence (Theobald, 2020; Theobald et al., 2020) dispersed phase holdup and interfacial momentum transfer (Yadav and Patwardhan, 2009; Sen et al., 2016; Sen et al., 2018), droplet population balance models (Alzyod et al., 2017; Alzyod et al., 2018; Sen et al., 2019), axial dispersion (Din et al., 2010; Yi et al., 2020; Sen et al., 2021) and mass transfer (Alzyod et al., 2018). This approach is well validated but depends on accurate modelling of various sub-phenomena, which tend to be fitted empirically, furthermore, the formulation is not necessarily suitable for describing the large interface and jetting phenomena in the near-plate region.

Several investigations have used interface tracking methods, such as the Volume Of Fluid (VOF) method (Khatir et al., 2017; Theobald et al., 2018; Theobald, 2020; Theobald et al., 2020). VOF is an established computational technique for modelling resolved interfaces, however, numerical diffusion of the interface may occur when the mesh resolution is insufficient to capture droplet interfaces, artificially suppressing dispersed phase holdup. Therefore, simulations are computationally expensive and time-consuming and, at present, a full column simulation is not feasible.

The Generalised Multifluid Modelling Approach (GEMMA) is a hybrid methodology which can dynamically switch between interface averaging and interface tracking and therefore

model both the dispersed phase in the inter-plate region and coalesced droplets in the near-plate region. It has been coupled with a droplet population balance model and used to simulate a PSEC, however, the results are not validated against experimental data (Theobald, 2020). As the model is based on a conventional Euler-Euler formulation, there are opportunities to further develop this using previous work based on conventional Euler-Euler formulations.

#### 2.6.1.3. Turbulence

Most investigations into PSEC hydrodynamics have used the URANS equations with turbulence predicted by the k-epsilon model. This has been compared with LES for single-phase systems (Khatir et al., 2016) and multiphase systems (Khatir et al., 2017; Theobald, 2020) and it has been found that the predicted turbulence is significantly different between the two. This has important implications for the accurate modelling of PSEC hydrodynamics, however, due to the difficulty in measuring flow fields in multiphase systems, no suitable experimental dataset exists which would enable the identification of the correct approach. As most PSEC CFD simulations are carried out in 2D, this precludes the use of LES, however, further investigations should aim to identify if more appropriate turbulence formulations exist.

#### 2.6.1.4. Interfacial momentum transfer

Interface averaging models are widely used in investigations of PSECs, which necessitates modelling the interfacial exchange of momentum. Generally, the consensus is that the main contribution to this is the drag force on dispersed droplets, with the effect of lift, virtual mass, and turbulent dispersion largely ignored. Most investigations use the Schiller-Naumann drag model (Yadav and Patwardhan, 2009; Din et al., 2010; Alzyod et al., 2017; Theobald, 2020; Yi et al., 2020; Tu et al., 2021), however, this does not consider the effect of other droplets and often leads to inaccurate prediction of dispersed phase holdup. Sen (2016; 2018) compared several drag models and identified that the Kumar and Hartland model can better predict holdup, however, its accuracy decreases when changing operating conditions. Several attempts have been made to improve it by the modification of model coefficients (Sen et al., 2018; Sen et al., 2019), and it can be concluded that in the absence of a drag model specifically formulated over a range of column geometries, operating conditions and fluidic systems,

system-specific tuning of the drag model is still necessary to accurately represent the hydrodynamics of a PSEC.

#### 2.6.1.5. Droplet size

Interfacial momentum transfer depends on droplet diameter as it is important to determine the drag coefficient and predict the available surface area for mass transfer. The most common method is via the specification of a constant droplet diameter throughout the computational domain based on either experimental observations (Sen et al., 2016; Yi et al., 2020; Tu et al., 2021) or empirical correlations (Yadav and Patwardhan, 2009; Sen et al., 2018; Theobald, 2020). This is the least computationally expensive approach, however, this method does not consider the effect of changing droplet diameter along the column height or the impact of droplet size distribution, resulting in an inaccurate representation of column hydrodynamics, most notably dispersed phase holdup and rise velocity. A more appropriate approach is the calculation of droplet size distribution, which can be done using a droplet PBM

The One Primary One Secondary Particle Model (OPOSPM) is an implementation of the general Section Quadrature Method of Moments (SQMOM) that has been implemented in several investigations (Alzyod et al., 2017; Alzyod et al., 2018; Theobald, 2020). It is a relatively simple and efficient approach where the population balance is calculated using a single transport equation for the droplet number density, which is a function of the modelled droplet breakage and coalescence.

Alternatively, the method of classes has been implemented in several investigations (Sen et al., 2019; Sen et al., 2021). This approach represents the DSD using bins over the range of droplet diameters, which requires the solution of a transport equation for each class. Sen (2019) found that increasing the number of bins caused the calculated droplet diameter to change, however, this resulted in a significant increase in calculation time, and 10 bins were chosen as a balance between solution accuracy and simulation time.

Both approaches are dependent on the modelling of droplet breakage, which has been done with models of Gourdon (1994), Coualoglou and Tavlarides (1977) and Martinez-Bazan (1999) and coalescence using models of Delichatsios and Probstein (1976), Coualoglou and Tavlarides (1977) and Prince and Blanch (1990). These correlations are empirical, and the model coefficients must be fitted to data from batch experiments to achieve representative

droplet diameters. Typically this is performed using batch data generated as a function of fluid properties and turbulence kinetic energy dissipation

In summary, the calculation of droplet size is an important parameter affecting column hydrodynamics and should use one of the presented population balance models. Currently, there is no consensus on the selection of appropriate breakage and coalescence models, which require the fitting of model coefficients before use in CFD simulations.

#### 2.6.1.6. Axial dispersion

Axial dispersion is an important phenomenon that impacts the degree of back mixing in a PSEC, negatively affecting mass transfer performance. It is often investigated by performing residence time distribution or step change experiments and is quantified using the axial dispersion coefficient which is used in axial dispersion models for predicting mass transfer.

The most physically representative and commonly used approach is via the advection of a passive scalar which is achieved by the solution of an additional transport equation. This has been used to characterise the continuous phase using single-phase (Kolhe et al., 2011; Sen et al., 2015) and multi-phase simulations (Din et al., 2010; Yi et al., 2020; Sen et al., 2021) with reasonable accuracy for predicted RTD curves and calculated axial dispersion coefficients. However, in all investigations, these results consider the entire column and do not fully utilise the fidelity provided by CFD. Therefore, there is potential to perform a more detailed analysis to understand tracer evolution within column stages. Additionally, there has been no CFD investigation into dispersed phase axial dispersion.

Unfortunately, performing RTD experiments is time-consuming due to the many time steps required to complete an experiment. However, several investigations have been into alternative techniques that could generate the equivalent information in a much shorter time frame.

Sen (2015) investigated the "snapshot" method, where the continuous phase velocity fields at each quarter of the pulse cycle are ensemble averaged and used to advect a passive scalar throughout the domain. This resulted in a significant speedup, and the results were compared to experimental and CFD-predicted data, which showed excellent agreement. However, the investigation was performed using only the continuous phase and Sen (2021) chose not to use

this technique in a more recent study into axial dispersion in PSECs, suggesting that this technique is unsuitable for multifluid formulations.

Tu (2021) investigated the use of mean age theory, which is often used to assess air quality and is analogous to the time taken for fluid to travel from the inlet to a point in space. It is a development of the advection of a passive scalar, however, the equations can be solved alongside the simulation, and it does not require long simulation times to purge the scalar from the system. The investigation identified that a 3D axisymmetric representation of the domain is more accurate than 2D, however, the results were only compared to theoretical values and have not been experimentally validated. This approach has only been tested using the continuous phase, however it is a promising development that significantly reduces the time associated with characterising axial dispersion and merits further investigation.

In summary, quantifying axial dispersion and residence time in PSECs through the advection of a passive scalar is a well-established technique and offers scope for further investigation of column hydrodynamics. Although the mean age approach could provide considerable time savings, it is not an established technique but is worth further development and validation.

#### **2.6.1.7. Mass transfer**

The overall goal of modelling and simulating PSECs is to predict their mass transfer performance, however, this requires large meshes and long simulation times to achieve steady state. As a result, it is not currently computationally feasible to perform mass transfer simulations without relying on simplifying assumptions to enable simulation in a timely manner. Despite the numerous investigations into the use of CFD in PSECs, only a single study into CFD-predicted mass transfer is presented in the literature. Alzyod (2018) used a 2D axisymmetric mesh, the Euler-Euler method with URANS and the k-epsilon turbulence model, the OPOSPM droplet PBM, the Kumar and Hartland drag model and two-film theory for mass transfer. The CFD predicted results for droplet diameter and dispersed phase axial solute concentration agreed with experimental observations, but the paper is brief and does not present results for dispersed phase holdup or continuous phase axial solute concentration. This indicates that these values were not reasonably predicted and therefore it can be concluded that the approach requires further development.

### **3. THE DESIGN AND COMMISSIONING OF A PULSED SIEVE-PLATE EXTRACTION COLUMN**

This chapter provides a comprehensive overview of the design and commissioning of a Pulsed Sieve-plate Extraction Column suitable for performing hydrodynamic and mass transfer experiments at the University of Leeds.

#### **3.1. Introduction**

PSECs are an important unit operation for liquid-liquid extraction. Despite decades of continuous development, limited satisfactory design correlations are available, and design is typically dependent on costly and time-consuming pilot plant operations (Treybal, 1980). Traditional empirical approaches to correlating column performance are limited in their range of applicability, and therefore, more advanced modelling approaches such as CFD and CM could be used, however, this requires experimental data, which can be used for model validation. Therefore, an experimental apparatus was designed, commissioned and further developed to provide the data needed to model and simulate PSECs. The apparatus can be operated over various PSEC operating configurations and plate designs, providing insight into the effects of the different operational and design parameters on extraction performance. In addition, the apparatus can also provide data on mass transfer and other parameters necessary for accurate modelling and simulation of PSECs. The apparatus is a valuable tool for developing design correlations and simulation models for PSECs, reducing the need for costly and time-consuming pilot plant operations.

#### **3.2. Design**

The first part of the engineering design process was the development of a functional specification. To do this, the available literature was reviewed to gain an understanding of the process and the geometric parameters of a PSEC. Additionally, a walk down of an existing PSEC pilot plant at Idaho National Laboratory was attended, allowing discussions with people who had previously designed such systems (Mann, 2009). This enabled a more comprehensive understanding of the system and made it possible to identify potential areas of improvement. A summary of typical PSEC geometric parameters presented in the literature is shown in Table 1 (Yadav and Patwardhan, 2008).



**Figure 15:** Pulsed Sieve-plate Extraction Column pilot plant.

The next stage of the design process was producing a Process and Instrumentation Diagram (P&ID), mechanical design drawings and a bill of materials. These documents provided an overview of the construction process, detailing each component, function, and installation requirements. These documents were reviewed and upon acceptance, procurement and construction began.

The PSEC pilot plant, shown in Figure 15, consists of a glass column with a 65 mm internal diameter (ID) composed of 5 sections of 97 mm height. Due to the low ceiling, the column height was limited, resulting in a shorter column compared to others and despite the decrease in mass transfer performance, this was deemed acceptable. Plate spacing was based on the requirement to effectively capture droplet hydrodynamics using cameras. Between each section is a stainless-steel sieve plate with a thickness of 3 mm, hole diameters of 1, 2 or 4 mm and a free area of 23 %. An image of the plates is shown in Figure 16.



**Figure 16:** 3 mm thick Sieve-plates with a constant fractional free area of 0.23 and hole diameters of 1, 2 and 4 mm.

For the hydrodynamic characterisation experiments performed in chapter 4, the top and bottom column sections consist of an inlet port with a 23 mm ID. The upper port is connected to the heavy feed, and the lower port is connected to the pulse leg and the solvent feed, which is fed via a 1/8<sup>th</sup> pipe-in-pipe. This report will refer to this configuration of the PSEC pilot plant as “PSEC configuration A”. For mass transfer experiments discussed in chapter 7, the solvent feed and pulse leg ports were separated and an alternative configuration consisting of two opposing ports with an ID of 23 mm, offset 90° from the upper inlet was used. In addition, the new lower column section is supported by a stainless-steel plate with a vertical height of 135 mm. This report will refer to this configuration as “PSEC configuration B”.

For “PSEC configuration A”, glass column separators with an ID and height of 190 mm and vertical 23 mm ID outlets were connected to the support plate and the upper column inlet port, giving an approximate column volume of 12.4 L. A schematic representation showing dimensions is presented in Figure 17. For “PSEC configuration B”, the lower separator was replaced with a smaller alternative with a 65 mm ID, a height of 110 mm, domed ends and a horizontal 23 mm ID outlet port to give an approximate column volume of 14.8 L. A schematic representation showing dimensions is presented in Figure 18. A summary of the column parameters is shown in Table 4.

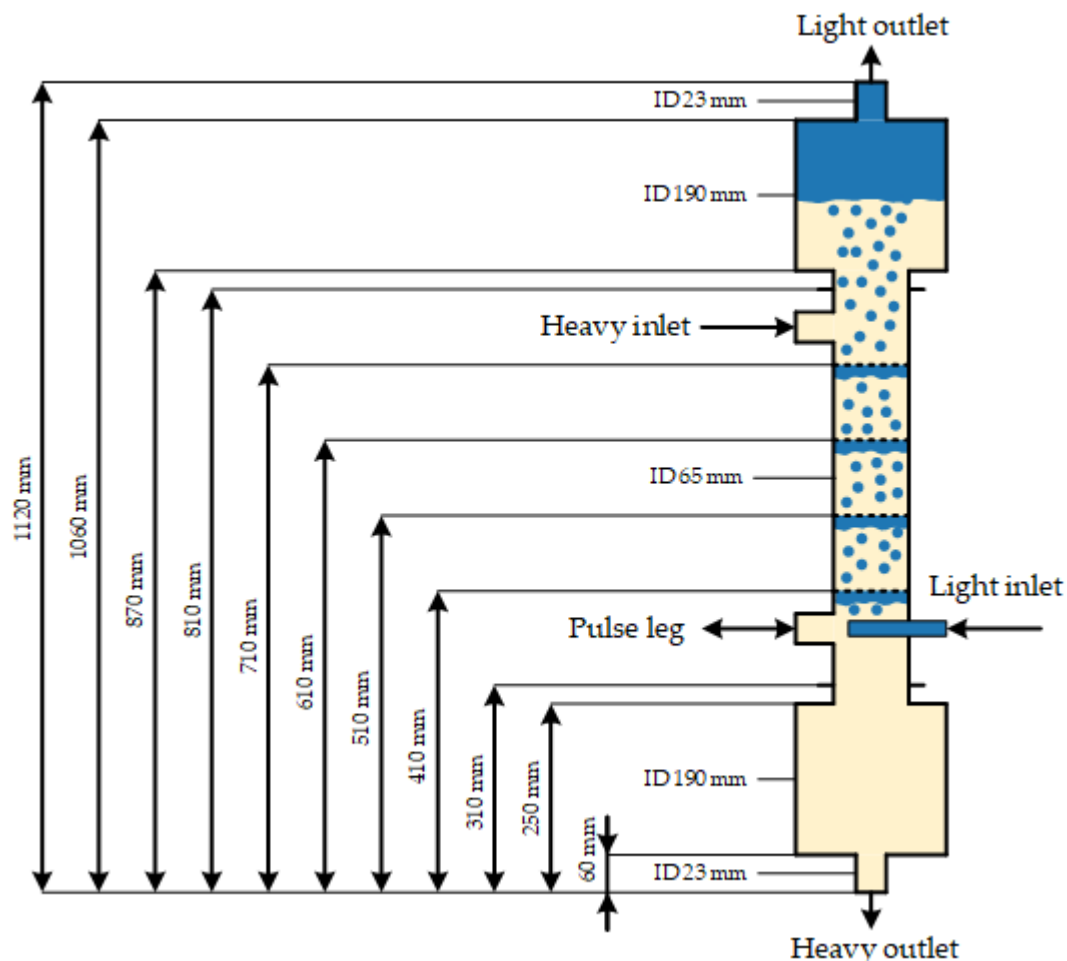


**Figure 17:** Dimensions of “PSEC configuration A”.

Glass sections are connected using clamps with a thin layer of hydrocarbon grease applied to flange faces with polytetrafluoroethylene (PTFE) gaskets sandwiched between them. Column sections feature one flat flange and one flange with a groove to install a Fluorinated Ethylene Propylene (FEP) O-ring. Both flange faces are greased, and a 3 mm stainless steel plate and PTFE gasket are placed between them. Column ports are connected to 3/8<sup>th</sup> Swagelok tubing via QVF compression fittings.

The column contents is pneumatically agitated via a pulse leg, which consists of a 1.60 m tall glass column with an ID of 23 mm connected via one of the lower outlet ports. Compressed air is fed to a 3-way actuated solenoid controlled by a timer that provides and vents air into the pulse leg, as shown in Figure 19. To prevent the release of any aerosols generated during pulsing, the air is vented to a breakpot. The pulse amplitude is controlled by needle valves on

the air feed and vent lines, and the duty cycle and frequency of the solenoid actuation are controlled via a control cabinet shown in Figure 20.

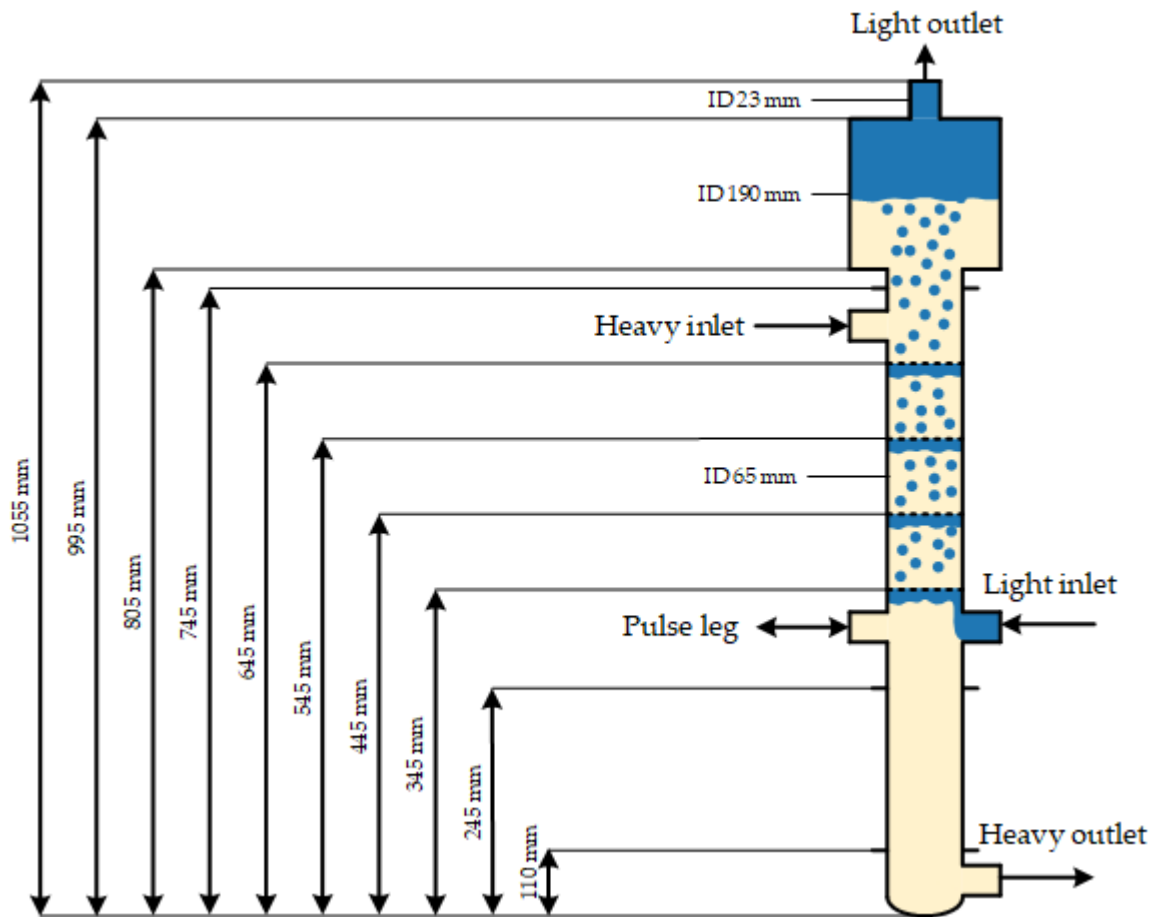


**Figure 18:** Dimensions of "PSEC configuration B".

4 x 60 L high-density polypropylene tanks feed and receive materials from the extraction column. The plant pipework can be configured so that feed materials come from either the feed or the receipt tanks, allowing the column to be operated in a batch or continuous mode, depending on whether mass transfer or hydrodynamic testing is taking place. The aqueous feed vessel is fitted with a stainless-steel impellor to ensure that the contents are homogeneous before column operation.

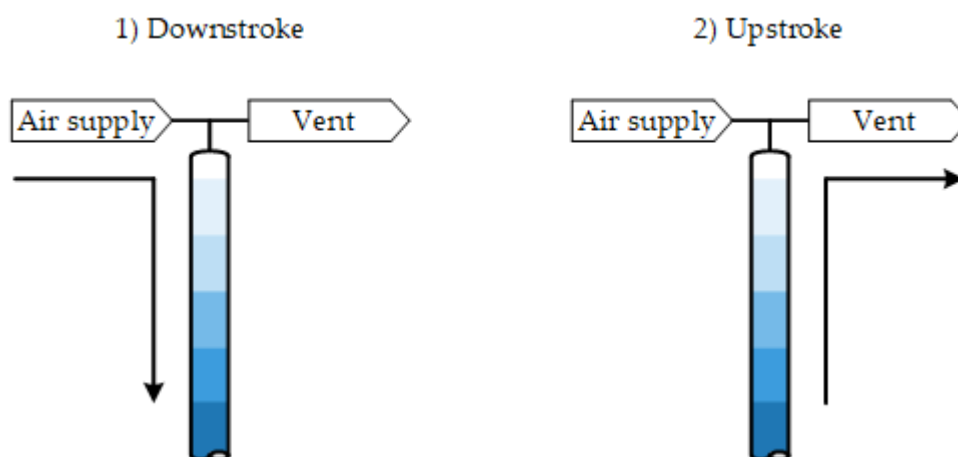


**Figure 19:** Pneumatic pulsation via the pulse leg.

The heavy feeds and outlets are transported to the column via peristaltic pumps fitted with Tygon tubing. The heavy feed is fed to the column via the upper column inlet, and the heavy product exits via the port on the lower separator. The solvent feed is pumped using a diaphragm pump. Hydrodynamic testing was performed using a pipe-in-pipe configuration via the pulse leg connection to feed to solvent; however, due to the small diameter, this was changed so that it was provided via a second port opposite the pulse leg connection. A detailed P&ID of “PSEC configuration B” is shown in Figure 21 and equipment, instrument and valve lists are given in appendices 1, 2 and 3.

**Table 4:** Summary of column geometry and operating parameters

| Parameter  | Value            |
|--|------------------|
| Column diameter (mm)                             | 65               |
| Column height (mm)                               | 303              |
| Plate hole diameter (mm)                         | 1, 2, 3, 4 and 5 |
| Plate spacing (mm)                               | 97               |
| Plate free area (%)                              | 23               |
| Material of construction                         | Stainless-steel  |
| Heavy phase flow rate (L.hr <sup>-1</sup> )      | 90               |
| Light volumetric flow rate (L.hr <sup>-1</sup> ) | 50               |
| Pulse frequency (s <sup>-1</sup> )               | 0 to 10          |
| Pulse amplitude (mm)                             | 0 to 4.5         |

Pressure relief valves are installed on the pulsed leg air feed line and the light phase feed so that excess fluid is released safely to the bund in case of blockage and overpressure. Flow rates are monitored using Pelton wheel flow meters fitted on the inlets and outlets. The differential

pressure over the column is monitored using pressure transducers connected to the column outlets. Samples of the heavy and light phase outlets can be taken using three-way valves on the column outlets.

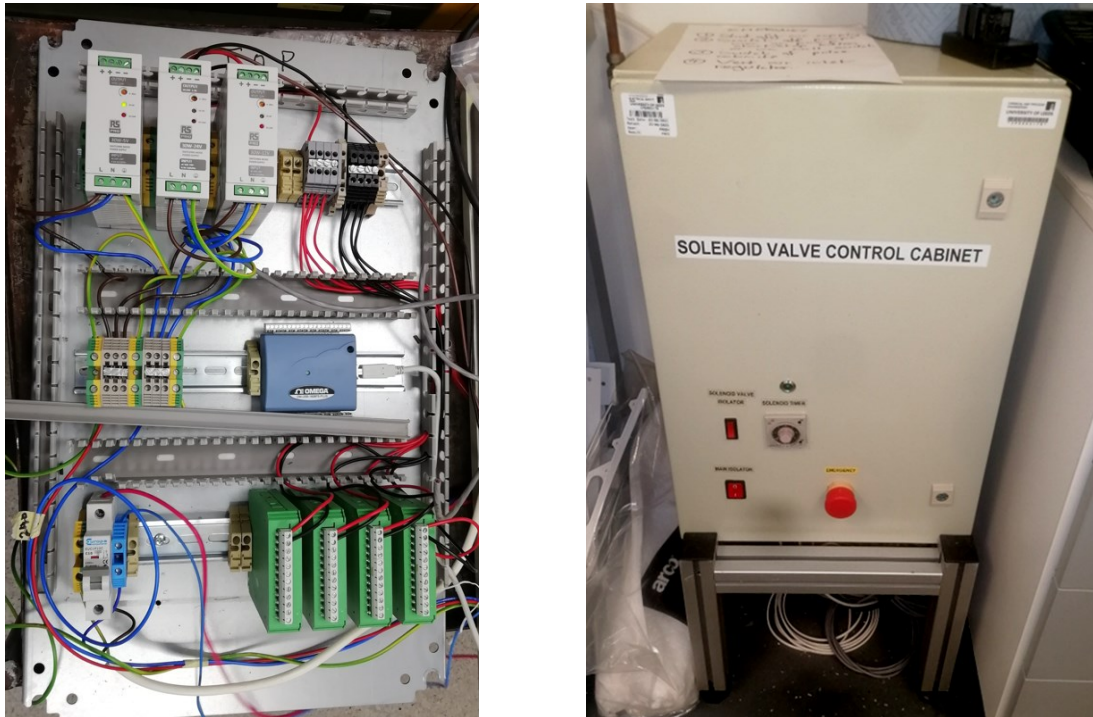


**Figure 20:** Pulsation control and instrumentation cabinet.

The column is supported using metal framing constructed from Unistrut and associated fittings. The frame is situated within a 250 L stainless steel bund with Plexiglass shutters installed so that all fluids are contained in the event of column breakage.

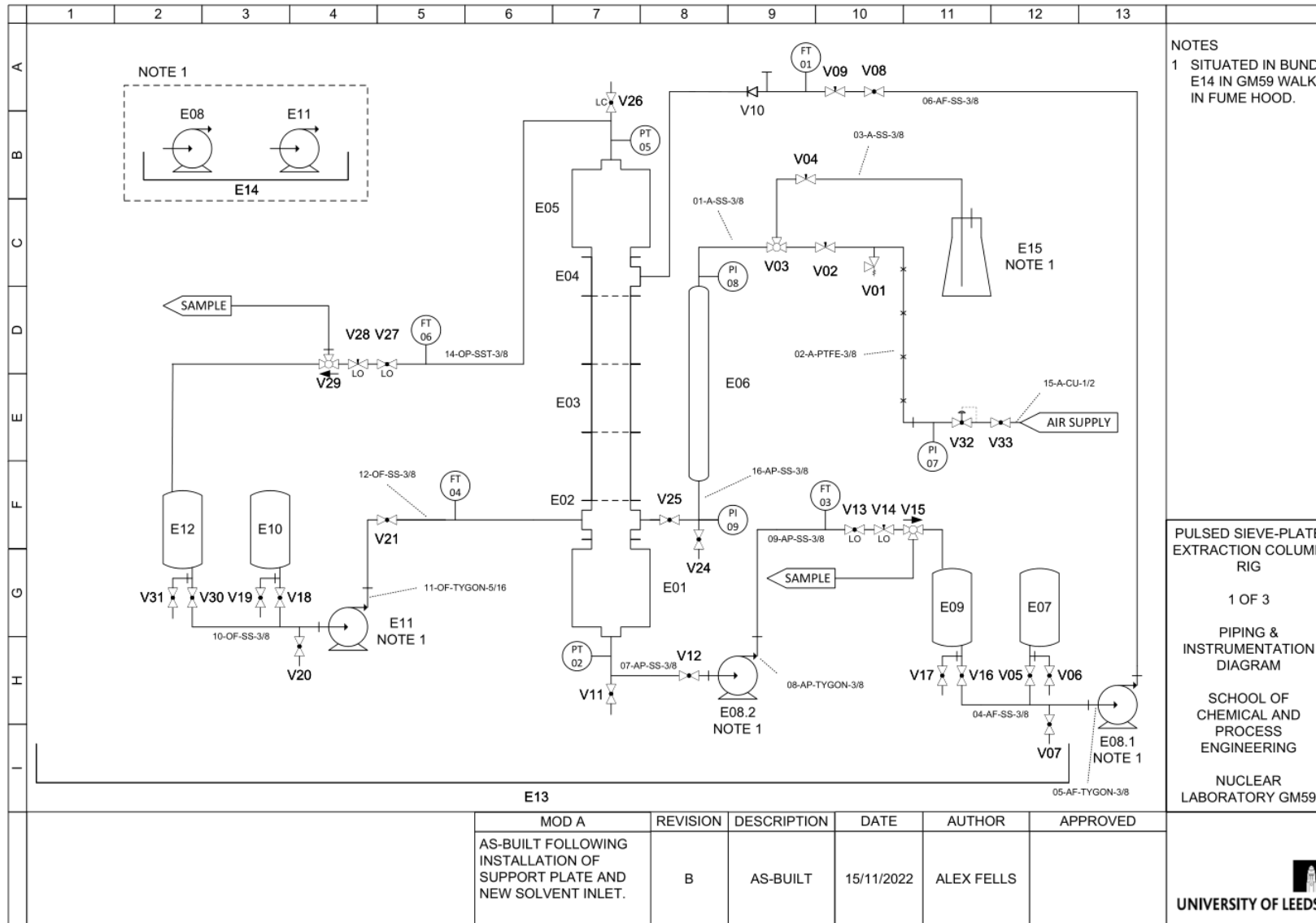


Figure 21: Process and Instrumentation Diagram (P&ID) of the Pulsed Sieve-plate Extraction Colum Pilot Plant

### **3.3. Commissioning**

Initial column commissioning consisted of assembling the PSEC per the P&ID, followed by a single-phase operation with water to identify any leaks that were subsequently repaired. Two-phase column commissioning using water and Exxsol D80 identified any additional leaks.

Initial column operations, outlined in chapter 4, consisted of extensive experimentation using water and Exxsol D80 and a risk assessment and standard operating procedure were prepared in advance. The operational experience gained was used to inform updated documentation for mass transfer operations using nitric acid and TBP, outlined in chapter 7. These documents were further modified to account for the operation of the column with radioactive materials. The final documentation covered the following procedures: pre-operation checks, additional checks when working with radioactive material, charging tanks, pre-experimentation configuration, PSEC operation, post-operation clean out, sampling, emergency shut down and operator decontamination procedure.

## 4. THE DISPERSED PHASE HYDRODYNAMICS OF A PULSED SIEVE-PLATE EXTRACTION COLUMN

This chapter presents the results of an experimental investigation into characterising the operational envelope and dispersed phase hydrodynamics of a PSEC. Operating conditions and plate designs were varied to explore the operational envelope and droplets mean size, distribution and rise velocities were measured. The relationship between the maximum column throughput and pulse amplitude and plate hole diameter was characterised and droplet mean size, distribution and rise velocities were measured and found to be highly dependent on plate hole size. Furthermore, a consistent relationship was observed between the Sauter and volume-weighted mean droplet diameters. This data provides valuable data to inform future investigations into PSECs.

### 4.1. Introduction

As discussed previously, numerous experimental investigations have been carried out to characterise the hydrodynamics of PSECs. Generally, these experiments have been concerned with generating experimental data which is used to empirically correlate the performance of the PSEC. However, previous investigations have identified that these correlations are limited in their application (Yadav and Patwardhan, 2008). An alternative approach to modelling the hydrodynamics of the PSEC is to use CFD which would facilitate insight into the system that is not possible by conventional experimental techniques. Previous investigations have been concerned with verifying and validating various modelling methods, such as the representation of the geometry and mesh, multiphase formulations, turbulence modelling, interphase momentum transfer, calculation of droplet size, axial dispersion and mass transfer, however, there is still considerable uncertainty with regards to the validation of models for interfacial momentum transfer, droplet breakage and coalescence.

Validation of these models requires the generation of suitable experimental data, which has not been presented in the scientific literature to date. Generally previous investigations have been concerned with measuring averaged quantities such as the Sauter Mean Droplet diameter,  $d_{3,2}$ , which is of interest for its use in modelling mass transfer but does not capture the full droplet size distribution and offers limited opportunity for validating the coalescence

and breakage models. While holdup is often used to identify an appropriate drag model, it is better to use droplet rise velocity, which is dependent on the dispersed phase interfacial momentum transfer, as it is more likely to provide better approximations of the inter-plate holdup.

This chapter will outline the results of investigations into the operational envelope, droplet size distribution, Sauter and volume-weighted mean droplet diameters and rise velocity as a function of column throughput, pulse amplitude and plate designs. Experimental observations have been carried out in the absence of mass transfer using water and Exxsol D80, a PSEC pilot plant, high-speed video and image analysis. Through this combination of techniques, it is possible to collect sufficient data to accurately validate the models used to simulate the hydrodynamics of the PSEC in chapter 4.

## **4.2. Methodology**

The experimental apparatus consists of a glass column with an ID of 65 mm and an active height of 303 mm. The column contains  $4 \times 3$  mm thick stainless steel plates, each with a 23% free area and a plate hole diameter of 1, 2 or 4 mm. For a more detailed explanation of the column design please refer to “PSEC Configuration A” in chapter 2.

### **4.2.1. Droplet size distribution**

Droplet footage was recorded using three GoPro Hero 4 cameras located 10 cm from each column stage, with footage recorded at 1080p resolution, 30 fps, an ISO of 1200, and a shutter speed of 240 Hz. Droplets were illuminated with white LED lighting, and a diffuser was used to ensure even illumination. Using a 5 mm checkerboard and ball bearings of 1 to 10 mm diameter, the perspective distortion in the near, mid and far fields caused by the curvature of the glass and the difference in the refractive index of water and air were quantified to be -4.3 % in the x-axis and -17.2 % in the y-axis. For each experiment, 3 minutes of footage was collected, totalling 5400 frames.

Individual frames were segmented using Ilastik, an image analysis tool that uses labelled data and machine learning algorithms to segment images (Berg et al., 2019). For each dataset, 100 frames were allocated as training data, and 30 frames were labelled as either droplets, borders or backgrounds. Pixel classification using the “Simple segmentation” workflow was used, and

additional labels were added until the results were deemed satisfactory. The full dataset was then segmented using the trained classifier by running Ilastik in headless mode on a HPC.

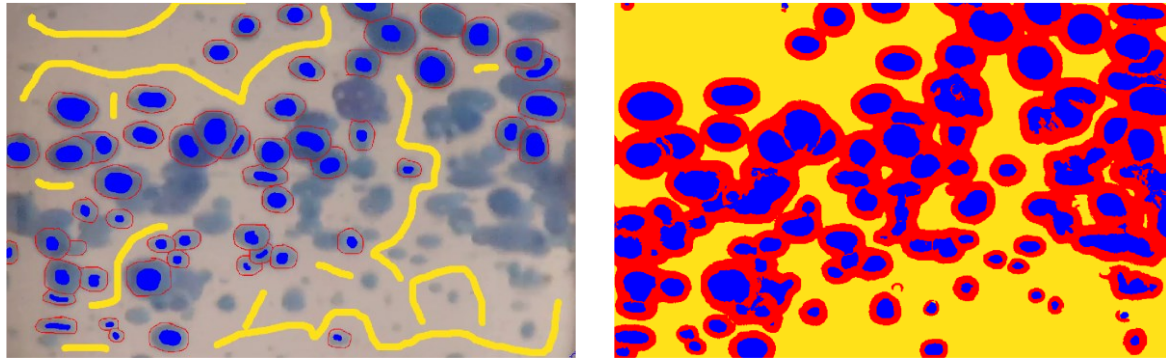


**Figure 22:** Segmentation workflow using Ilastik with labelled data (left) and segmented image (right). Droplets are blue, edges are red and background is yellow.

Post-processing of segmented images was performed using OpenCV, a library of tools for computer vision and image analysis (Bradski and Kaehler, 2000). First, frames are rotated to ensure the vertical orientation of the column, cropped so that only the column internals are included and then resized to correct for perspective distortion. Next, an image mask is produced using pixels labelled as droplets and the droplet's position, width, height and area are calculated. The code loops through each droplet and keeps those located in the mid 50% of the image, with a diameter greater than 0.25 mm and an aspect ratio within  $\pm 25\%$ . A distance transform calculates the minimum distance to the background for each remaining drop and writes the maximum value for each droplet to a file. A step-by-step representation of this is presented in Figure 23.

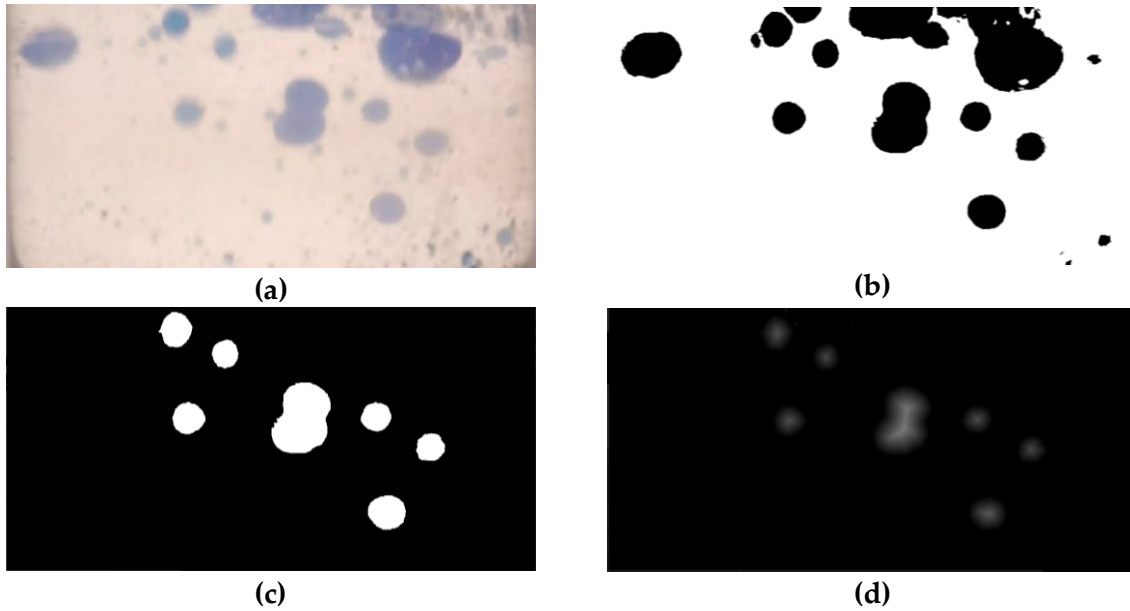


**Figure 23:** Droplet measurement workflow using OpenCV with: **(a)** the original image; **(b)** the masked image; **(c)** the down selected drops; and **(d)** the distance transform.

The Sauter mean diameter is calculated using:

$$d_{3,2} = \frac{\sum d^3}{\sum d^2} \quad (4.1)$$

The volume-weighted mean is calculated using:

$$d_{3,0} = \sqrt[3]{\frac{\sum d^3}{\sum d^0}} = \frac{\sum d^3}{n} \quad (4.2)$$

#### 4.2.2. Droplet swarm rise velocity

Droplet swarm rise velocities were determined manually by recording the number of frames taken for a single drop to travel a known distance. The diameter of a pixel in mm is measured based on the number of pixels between the column walls, and then two horizontal lines are overlaid. The droplets rise velocity is calculated using the number of frames taken for droplets to travel from the lower to the upper line and the time taken based on the camera's frame rate.

#### 4.2.3. Fluid System

Experiments with water and Exxsol D80 dyed using Sudan Blue II were conducted to characterise the PSEC operational envelope, droplet diameters and swarm rise velocities. The

density of Exxsol D80 was measured gravimetrically using a calibrated mass balance and air displacement pipette. For the dynamic viscosity and interfacial tension, values for dodecane were used. Fluid properties are presented in Table 5.

**Table 5:** Physical properties of water and Exxsol D80 at 20 °C (Zeppieri et al., 2001; Caudwell et al., 2004; Bajoria et al., 2013).

| Parameter                                | Heavy                   | Light                   |
|--|-------------------------|-------------------------|
| Density (kg.m <sup>-3</sup> )            | 996                     | 802                     |
| Dynamic viscosity (N.s.m <sup>-2</sup> ) | 1.00 × 10 <sup>-3</sup> | 1.34 × 10 <sup>-3</sup> |
| Interfacial tension (N.m <sup>-1</sup> ) | 52.9 × 10 <sup>-3</sup> |                         |

#### 4.2.4. Experimental conditions

Identification of the operating regime is as per the definitions in chapter 2. A full factorial experimental design was prepared, consisting of 228 experimental conditions. Experiments blocked by plate hole diameter and column throughput and the order of pulse amplitude randomised. Throughput is defined as the sum of the volumetric flow rates of both phases, with all experiments being performed with a S:A of 2:1. The investigated experimental parameters are outlined in Table 6.

**Table 6:** Investigated experimental conditions.

| Parameter                              | Values                            |
|--|-----------------------------------|
| Total throughput (L.hr <sup>-1</sup> ) | 15*, 30, 45, 60, 75, 90, 105, 120 |
| Pulse amplitude (mm)                   | 1.48, 2.22, 2.96, 3.70            |
| Plate hole diameter (mm)               | 1, 2, 4                           |

\* value only used for  $d_p = 1$  mm experiments.

### 4.3. Results and discussion

#### 4.3.1. Operational envelope

The operational envelope for PSEC operation was characterised for all three plate designs at the 76 operational conditions. The results of the experiments showed which conditions were designated as either operational or flooding. To illustrate the results, a graphical representation was created for each of the three plate designs and is presented in Figure 24. Due to limitations inherent in the design of the experimental apparatus, it was not possible to investigate the effect of higher pulse amplitudes on column operation.

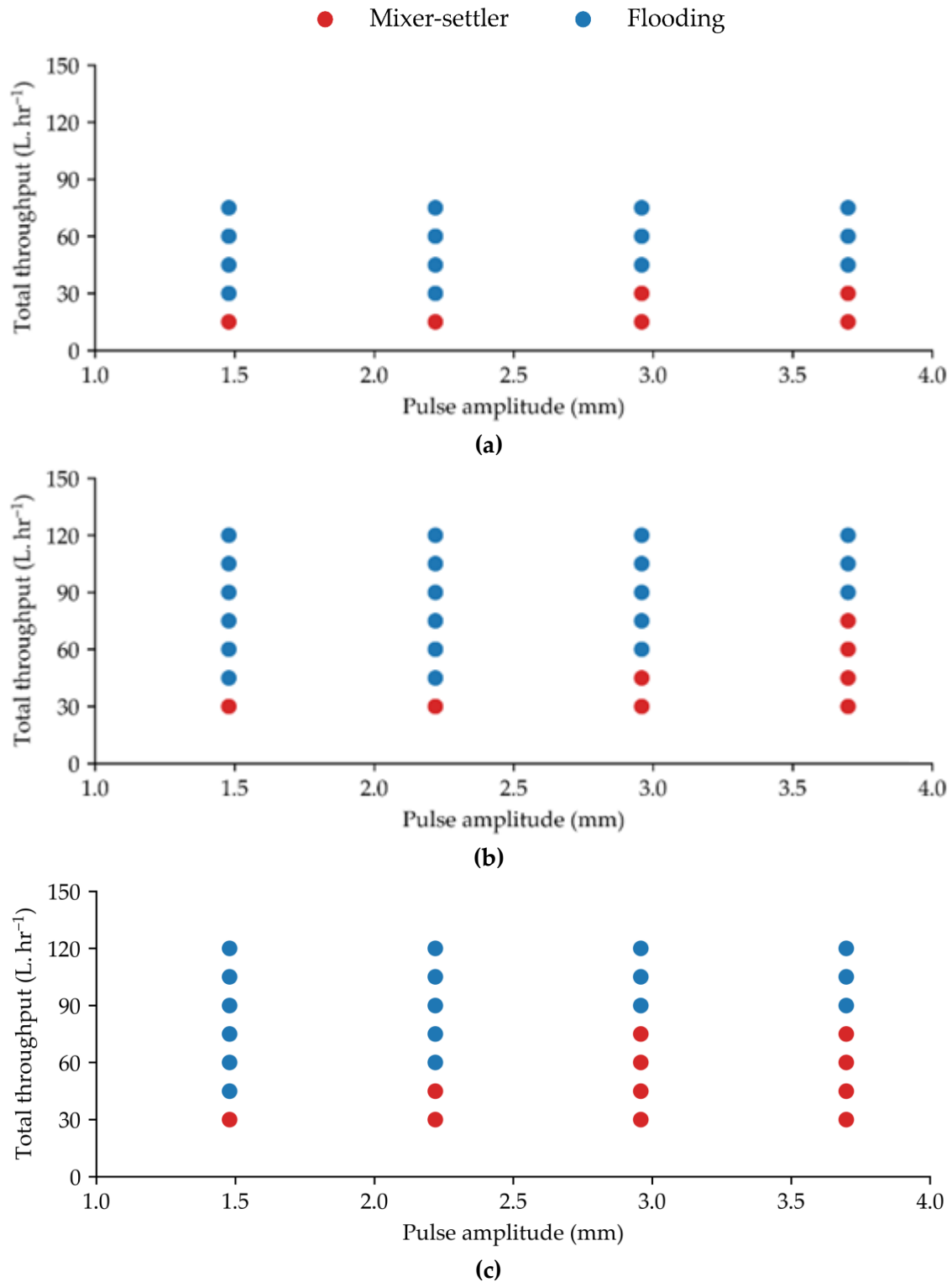


**Figure 24:** PSEC operational envelope for: (a)  $d_p = 1$  mm; (b)  $d_p = 2$  mm; (c)  $d_p = 4$  mm.

The data from these experiments was presented in 3D to visually represent the effects and is shown in Figure 25. Linear regression was used to further analyse the data to gain insight into the relationship between the parameters which are consistent with those presented in the

literature. The results of this regression can be used to better understand the relationship between pulse amplitude and plate hole diameter and their impact on maximum throughput, specifically that they both exhibit a positive correlation with the maximum throughput.

$$Q_{tot,max} = 16.9A + 10.4d_p - 26.9 \quad (4.3)$$

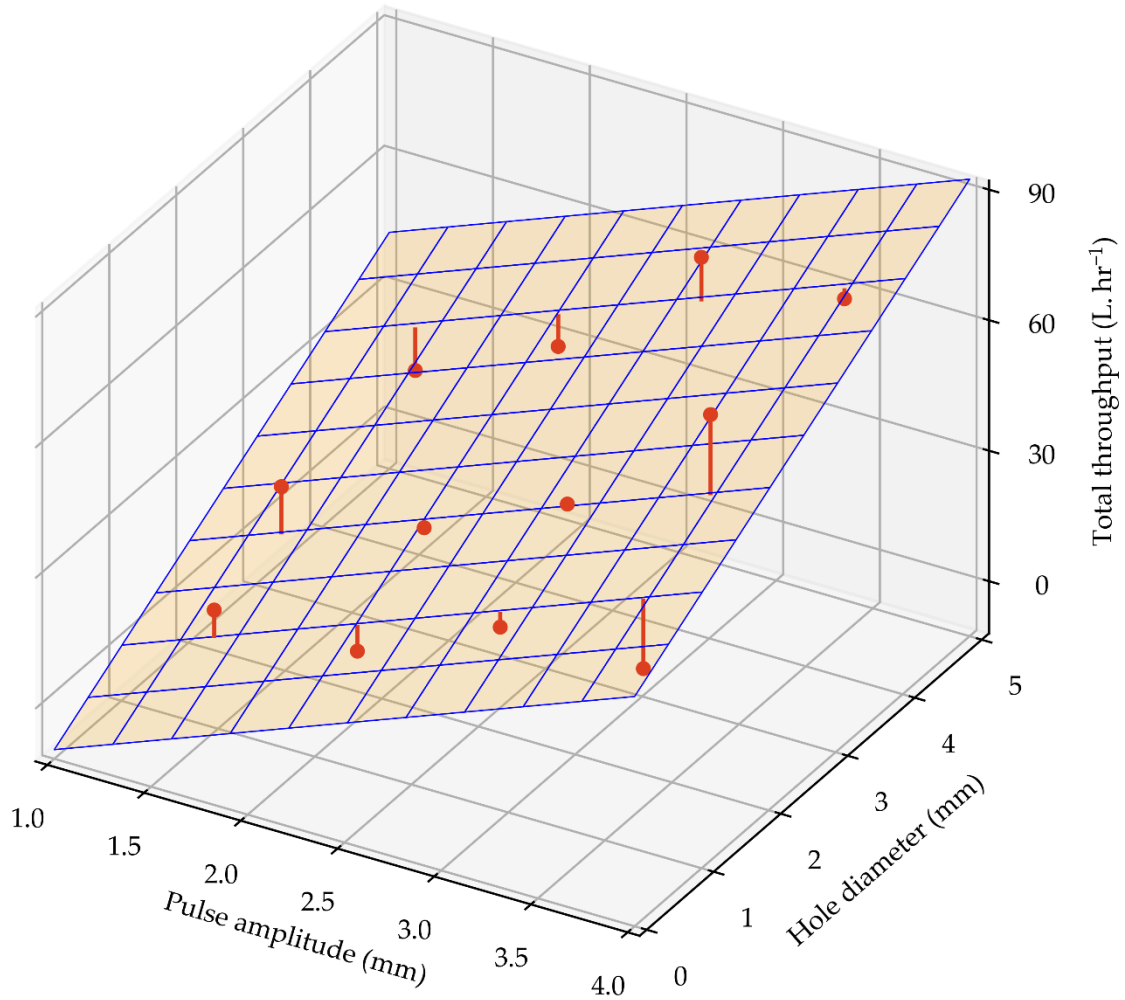


**Figure 25:** Linear regression and experimental data showing maximum column throughput as a function of pulse amplitude and plate hole diameter.

The column typically operated in the mixer settler regime, with the droplets experiencing minimal recirculation and rising upwards to the next plate. However, upon the approach to the maximum throughput of the column, the dispersed phase holdup appeared to significantly increase, although as this was not measured experimentally, this is not quantified, see Figure 26. It was observed that small droplets were observed to recirculate

within the column, while larger droplets had sufficient buoyancy force to continue upwards to the next plate.

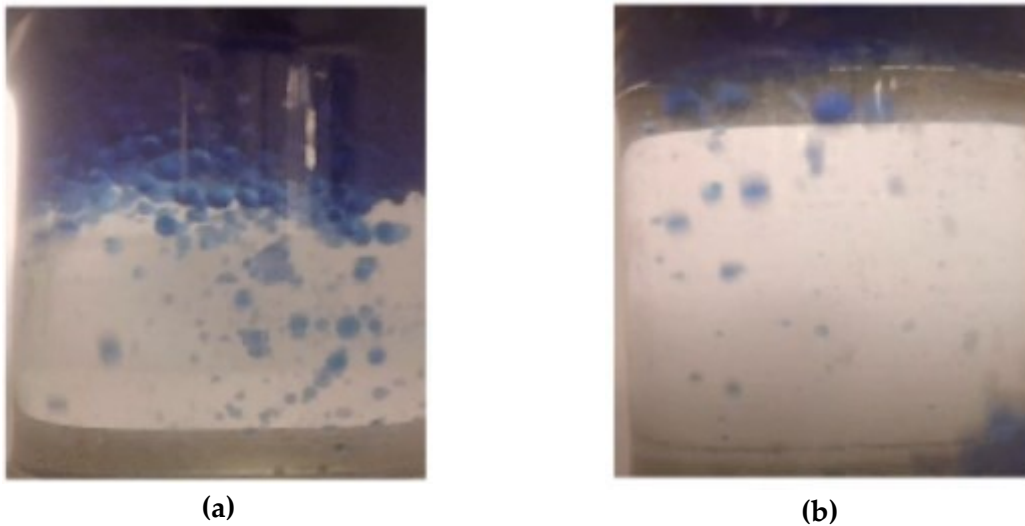


**Figure 26:** Comparing the recirculation and accumulation of droplets in a PSEC that is: **(a)** flooding ( $d_p = 2$  mm,  $Q_{tot} = 60$  L.hr<sup>-1</sup>,  $A = 2.96$  mm) and; **(b)** operating ( $d_p = 2$  mm,  $Q_{tot} = 60$  L.hr<sup>-1</sup>,  $A = 3.70$  mm).

The ratio of the buoyancy and drag forces acting upon the droplets determines the hydrodynamic performance of the column. As mentioned in chapter 2, the buoyancy force is proportional to the cube of the droplet's diameter and the drag force is a function of both the square of the fluid velocity and droplet diameter. Thus, when column throughput is low, the buoyancy force dominates, allowing the droplets to ascend freely to the next plate and the column operates in the mixer-settler regime.

As column throughput increases, approaching the operational limit of the column, the dispersed phase holdup begins to significantly increase. This is due to the drag force, which increases with the square of velocity, overcoming the buoyancy force acting on the droplets. Initially, this causes small droplets to recirculate and the dispersed phase holdup to increase. Further increasing the throughput results in the recirculation of larger droplets, increasing holdup and eventually flooding the column.

During column operation, it was observed that droplets were formed uniformly across the plate surface which is consistent with the theory that energy input is evenly distributed over the column's cross-sectional area. However, all droplets in the inter-plate region of the column stage tended to rise on one side. Additionally, small recirculating droplets travelled down the

opposite side of the column, which became more pronounced as the column throughput and the number of recirculating droplets increased. This indicates that the aqueous phase is continuously recirculating, which is consistent with hydrodynamic observations by Theobald (2020) and is caused by the momentum transfer from the dispersed droplets.

The establishment of circulating regions within the stages implies that the continuous phase is well mixed and therefore aqueous fluid entering the column rapidly distributes itself throughout the stage. This has implications for axial dispersion throughout the column, as it means that as fluid enters a stage, some will bypass and enter the next stage with a residence time significantly lower than its space-time. Meanwhile, some fluid will recirculate within the stage for a period much larger than the space-time of the stage. As previously discussed, several investigations have been concerned with axial dispersion in LLEC, which is known to significantly impact mass transfer performance. It is recommended that the continuous phase flow fields in PSECs be characterised; however, this is difficult. Only two investigations using Particle Image Velocimetry (PIV) in Pulsed Donut-disk Columns (PDDCs) have been conducted, both for a single aqueous phase, and thus the effect of the dispersed phase on the hydrodynamics has not been examined (Bujalski et al., 2006; Amokrane et al., 2014).

#### **4.3.2. Mean droplet diameters**

A total of 1.8 million droplets were measured and used to calculate the mean diameter for each operating condition. Figure 27 displays the  $d_{3,2}$  as a function of total throughput for each plate hole size. The plot shows that  $d_{3,2}$  increases with increasing plate hole diameter, however, this increase does not appear linear. The droplet size increases more between 1 and 2 mm than between 2 and 4 mm. The plot also shows a slight inverse relationship between throughput and droplet size, likely due to increased turbulence resulting in the production of smaller droplets.

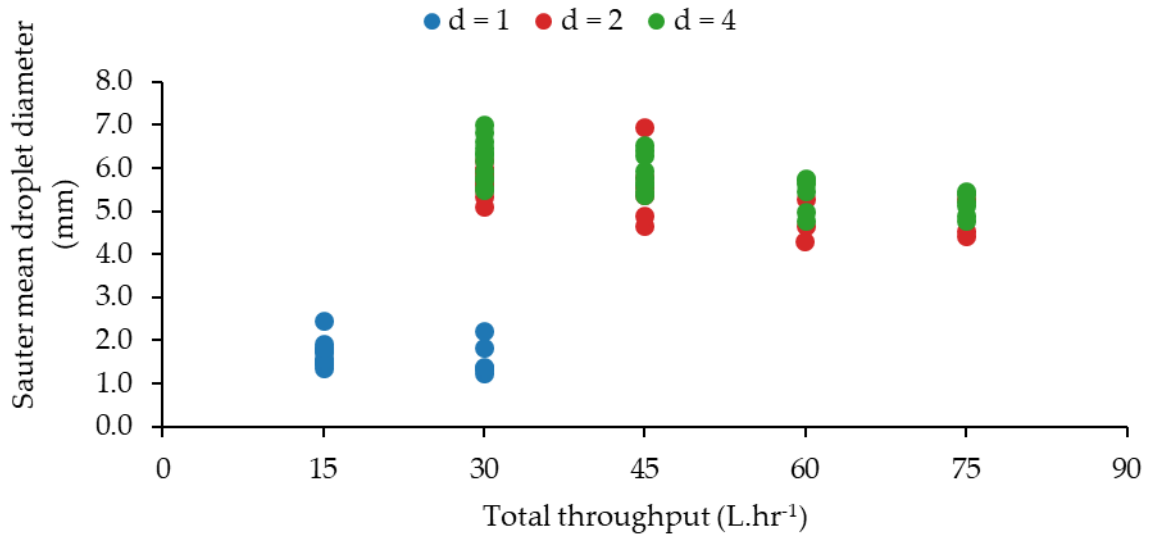


**Figure 27:** Sauter mean diameter as a function of total throughput ( $Q_{tot}$ ), grouped by hole diameter.

Two mean droplet diameters were measured across all three hole diameters for a total throughput of 30 L.hr<sup>-1</sup> and pulse amplitudes of 2.96 and 3.70 mm. This result, shown in Figure 28, confirms the nonlinear relationship between hole diameter and mean droplet diameter.

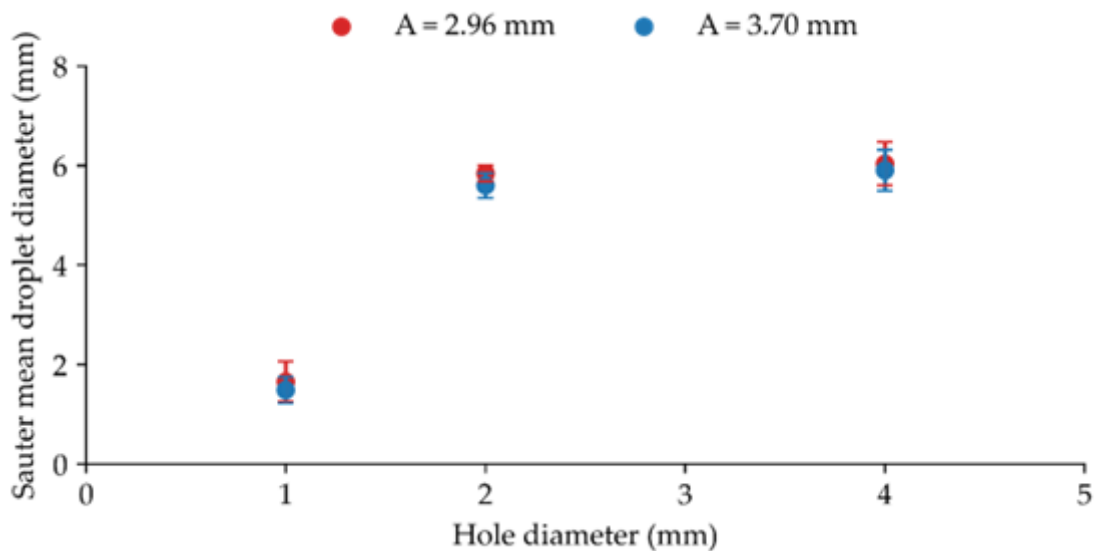


**Figure 28:** Sauter mean droplet diameter for a total throughput ( $Q_{tot}$ ) of 30 L.hr<sup>-1</sup> for pulse amplitudes (A) of 2.96 mm and 3.70 mm.

### 4.3.3. Ratio of $d_{3,0}$ to $d_{3,2}$

It is common to use the volume-weighted mean diameter,  $d_{3,0}$ , when modelling droplet population balances using CFD (Wardle, 2013; Theobald, 2020; De Santis, Hanson, et al., 2021; Fells et al., 2022). However, it is better to use the surface area-weighted mean,  $d_{3,2}$ , for modelling mass transfer. Therefore, it is necessary to be able to convert between the two. For liquid-liquid dispersions in Annular Centrifugal Contactors (ACCs), the ratio of  $d_{3,0}$  and  $d_{3,2}$  is typically 0.75-0.80 (Wardle, 2013). In Figure 29, the values for the experimentally measured  $d_{3,2}$  and  $d_{3,0}$  are plotted and correlated with the ratio calculated as 0.83, which is not significantly different from the values observed in ACCs.

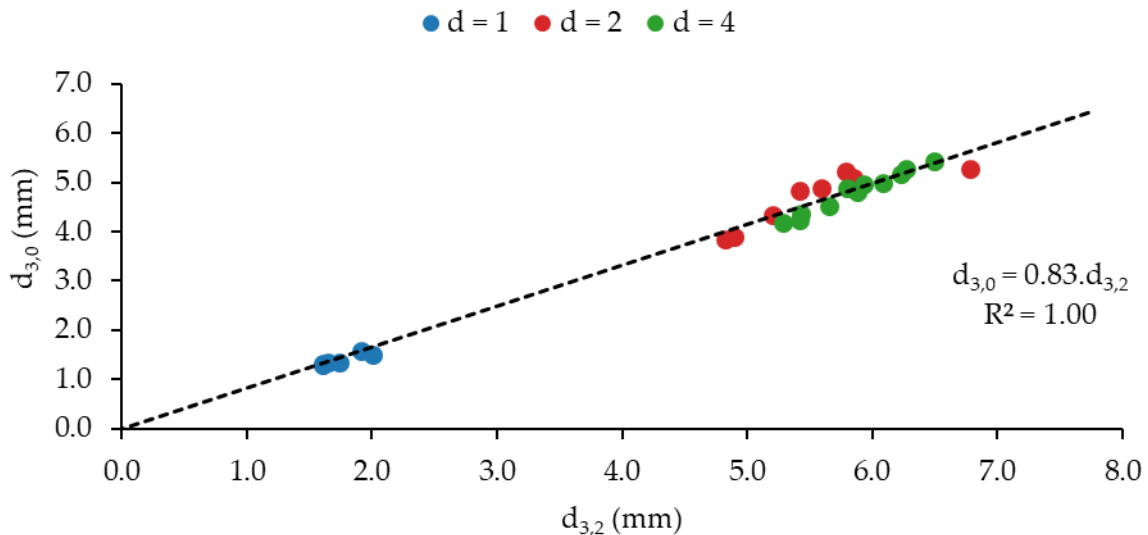
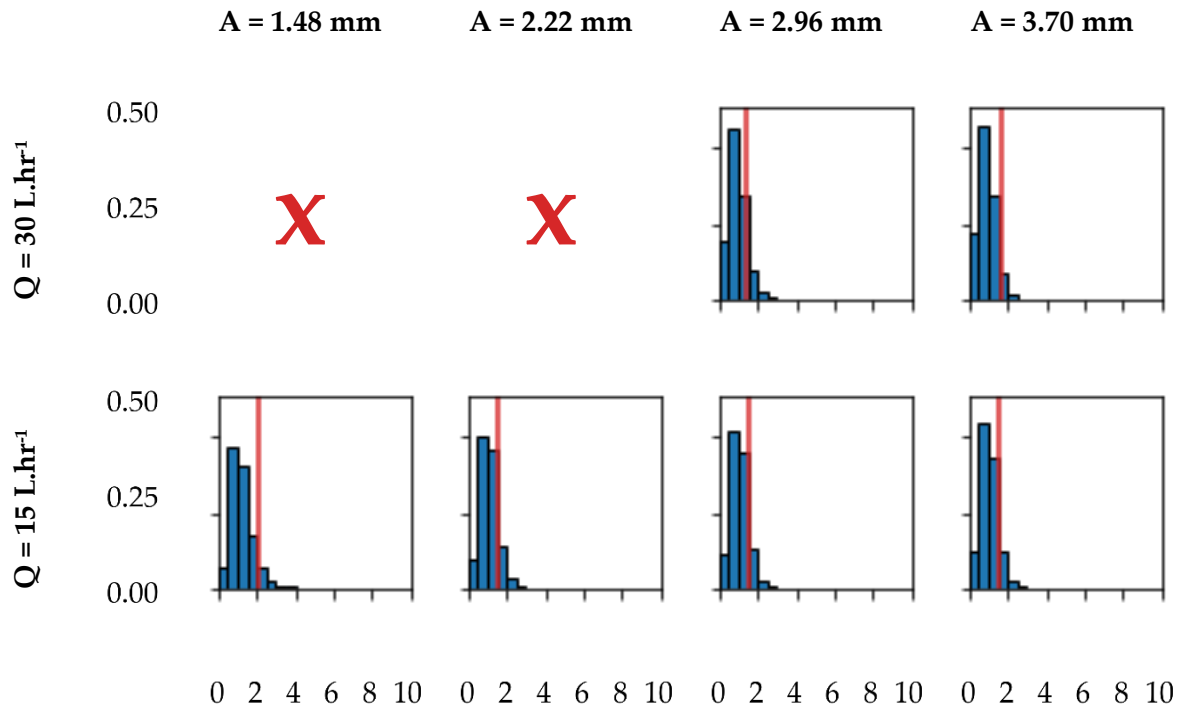


**Figure 29:** Parity plot showing the relationship between  $d_{3,0}$  and  $d_{3,2}$ .

### 4.3.4. Droplet size distribution

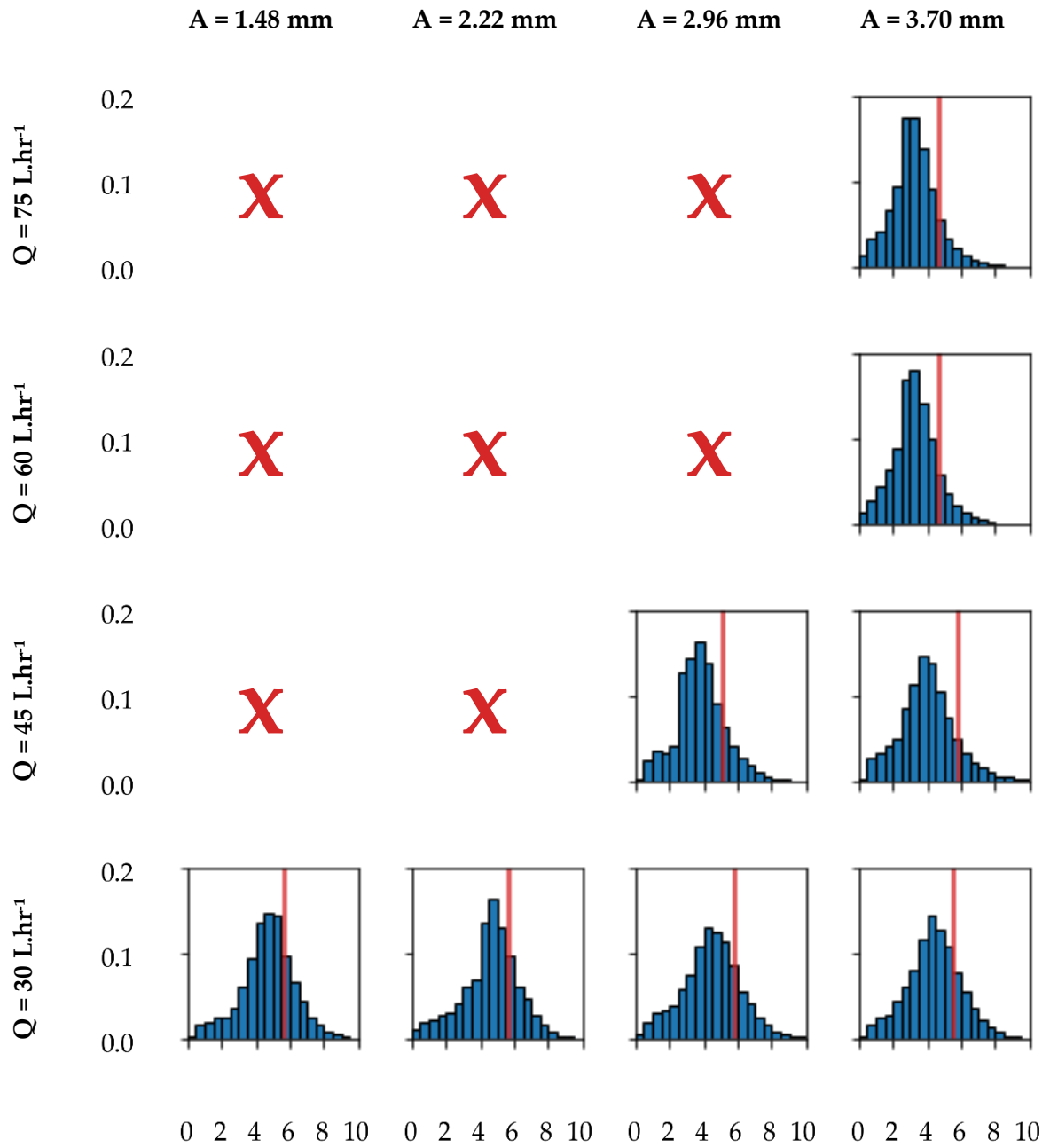
Previously, it was discussed that simply determining the mean droplet size is not enough to accurately assess column performance due to the impact of small droplets on the operating regime, axial dispersion, and flooding. Therefore, the entire droplet size distribution must be modelled, which requires experimental observations for model validation.

Figures 30, 31 and 32 show the droplet size distributions for each experimental condition in blue and the calculated  $d_{3,2}$  in red. When comparing the experiments, it is evident that the droplet diameters are much more tightly distributed for the 1 mm plate hole diameters than for the 2 mm and 4 mm plate hole diameters.

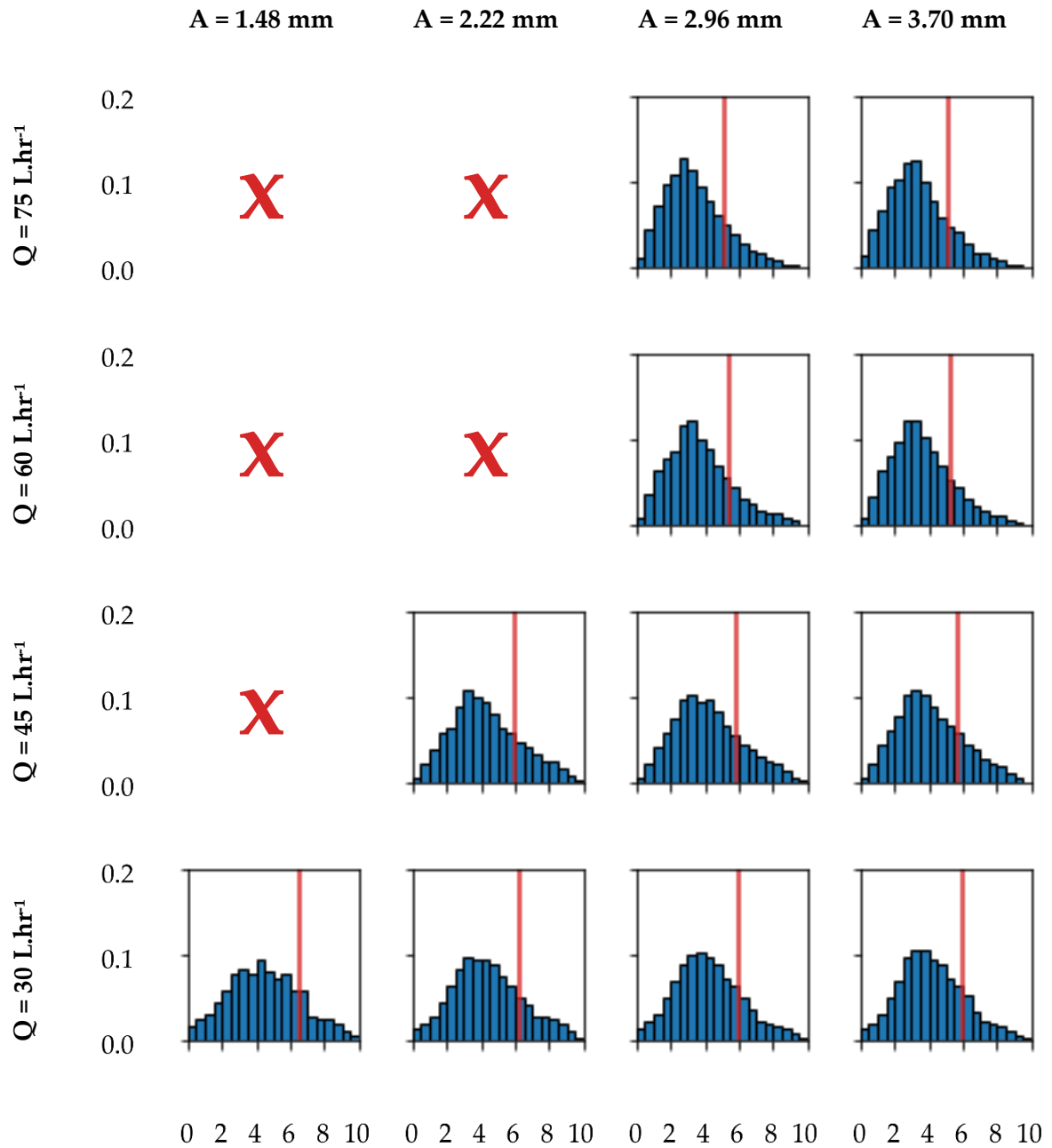


**Figure 30:** Droplet size distribution as a function of total throughput ( $Q_{tot}$ ) and pulse amplitude ( $A$ ) for a hole diameter ( $d_p$ ) of 1 mm.  $d_{3,2}$  values are denoted in red.

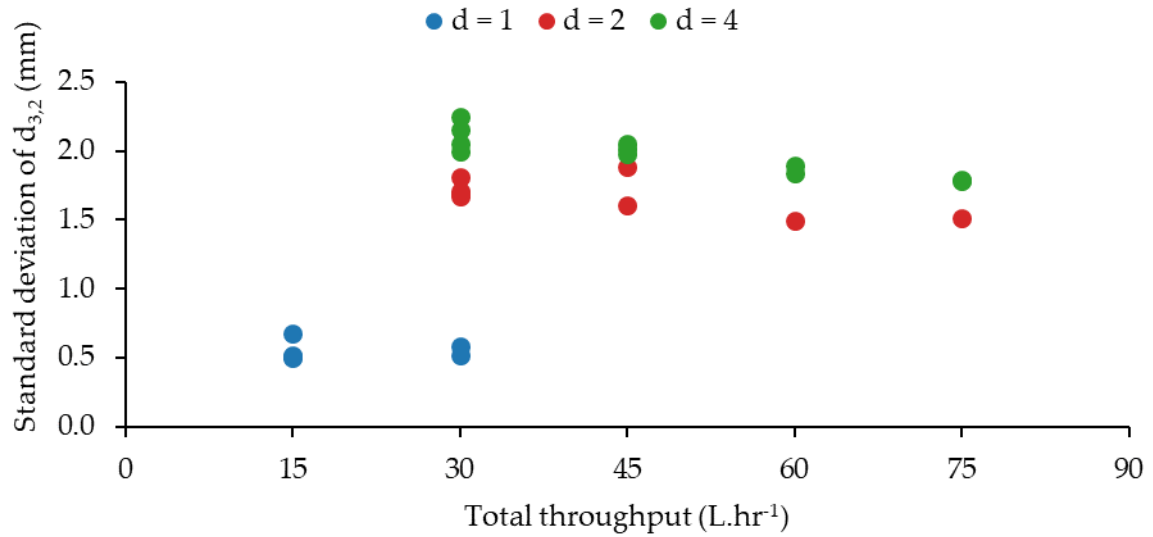
Figure 33 presents the standard deviation of droplet diameters as a function of total throughput for each plate design. It appears that the standard deviation of the DSD for a given hole size is either independent or weakly inversely proportional to the column throughput, however, this effect appears small and may be attributed to experimental error. As there are only a limited number of data points, it is recommended that this be investigated over a broader range of column throughputs to better understand the relationship between droplet diameter and column throughput.



**Figure 31:** Droplet size distribution as a function of total throughput ( $Q_{tot}$ ) and pulse amplitude ( $A$ ) for a hole diameter ( $d_p$ ) of 2 mm.  $d_{3,2}$  values are denoted in red.

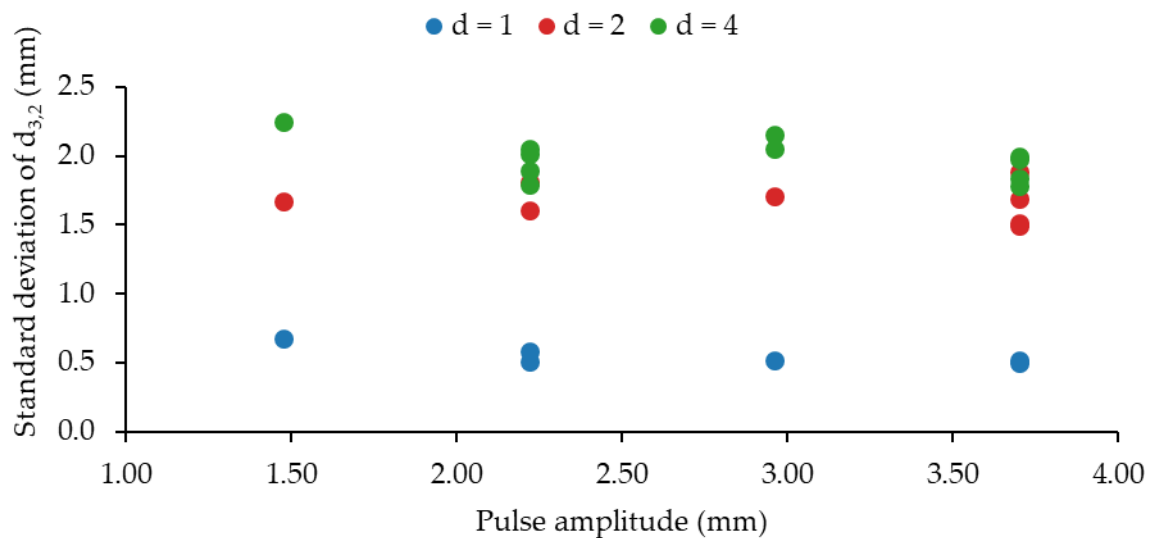


**Figure 32:** Droplet size distribution as a function of total throughput ( $Q_{tot}$ ) and pulse amplitude ( $A$ ) for a hole diameter ( $d_p$ ) of 4 mm.  $d_{3,2}$  values are denoted in red.



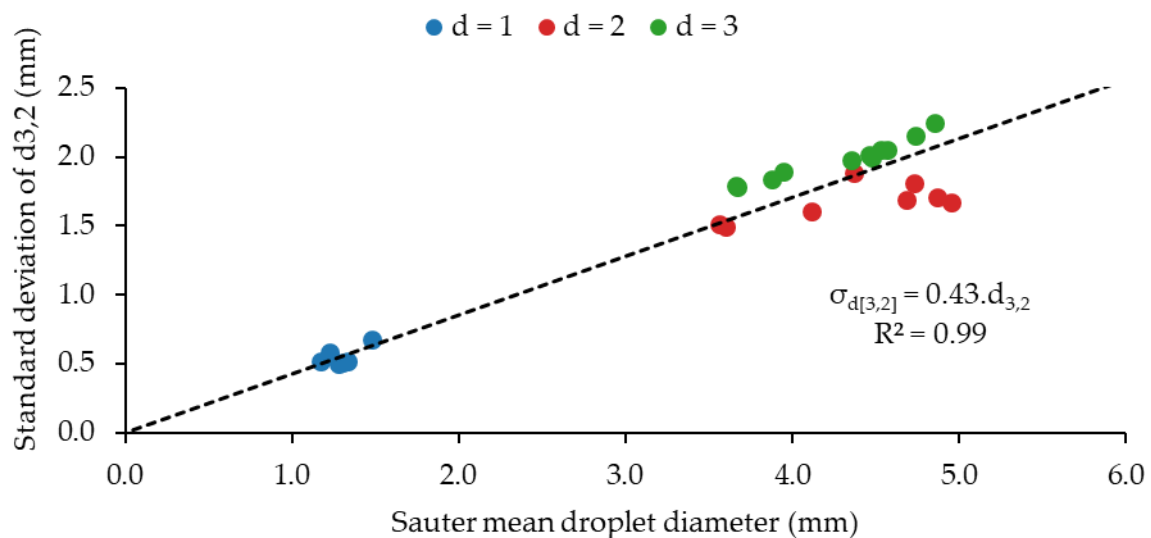
**Figure 33:** Standard deviation of the droplet size distribution grouped by hole diameter vs total throughput.

Figure 34 presents the standard deviation as a function of pulse amplitude. The results show that standard deviation appears independent of pulse amplitude, however, the maximum values for pulse amplitude used in this study are relatively low in terms of what is possible in a PSEC. Therefore, further work is recommended to investigate greater degrees of pulsation to see if the standard deviation remains independent of pulse amplitude.



**Figure 34:** Standard deviation of the droplet size distribution grouped by hole diameter vs pulse amplitude.

Figures 30, 31 and 32 demonstrate that droplet size distribution increases with hole diameter, but the relationship is nonlinear, as seen in figures 27 and 28. A highly correlated relationship is observed by plotting the experimentally measured mean droplet size against its standard deviation in Figure 35. The plot exhibits two clusters, one for the 1 mm diameter holes and one for the 2 and 4 mm holes. The increase in standard deviation with droplet diameter is as a result of the relatively low pulse amplitudes used in the investigation and is consistent with operation in the mixer-settler regime. Similarly, the increase in standard deviation with plate hole diameter is caused by the highly correlated relationship between plate hole diameter and droplet size and demonstrated in Figure 28. To better understand the phenomenon, future work should investigate this relationship over a broader range of droplet sizes.

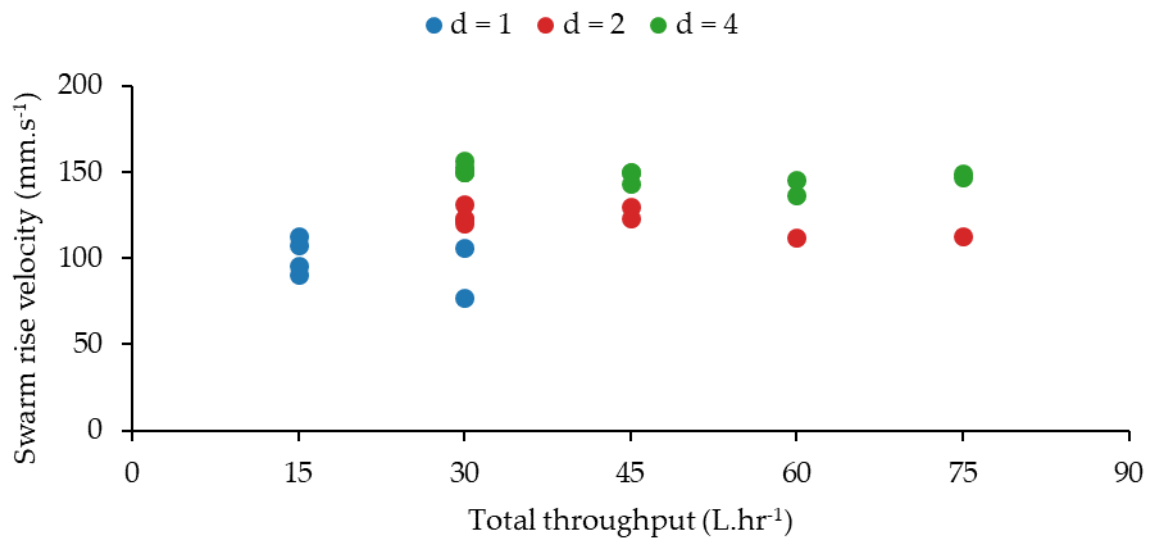


**Figure 35:** Standard deviation of the droplet size distribution grouped by hole diameter vs mean droplet size.

#### 4.3.5. Rise velocity

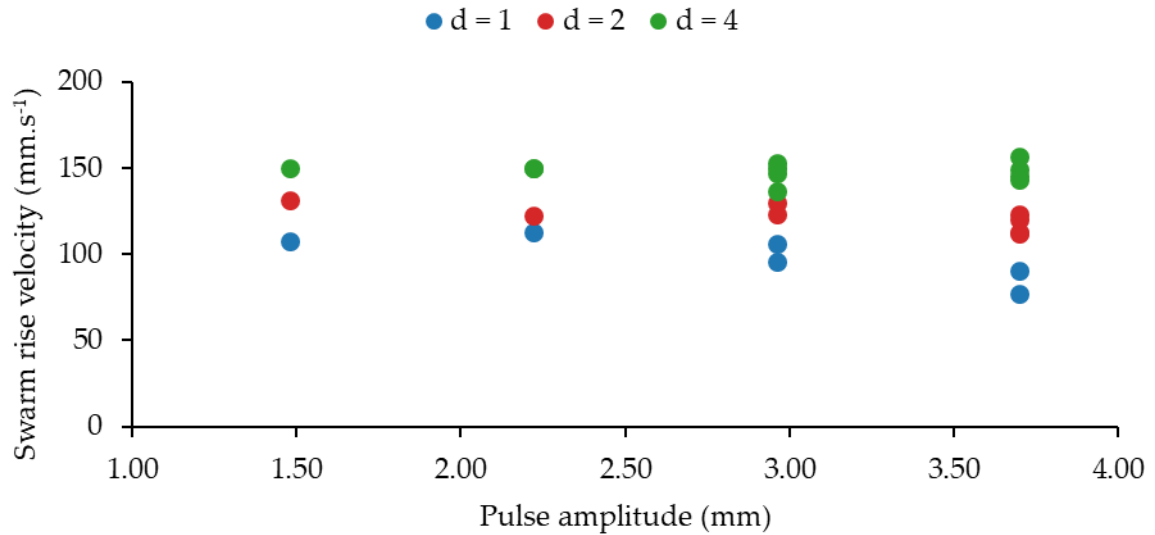
Knowledge of droplet rise velocities is important due to its role in modelling dispersed phase holdup, operating regime and mass transfer. This is because droplet rise velocity is highly dependent on interfacial momentum transfer and can be used to validate drag models used in CFD. Therefore, 20 rise velocity measurements were taken for each experimental condition, totalling 1520.

Figure 36 shows the averaged swarm rise velocity for each experiment plotted against column throughput. Comparing between experiments, swarm rise velocity increases with plate hole diameter, which is attributed to larger mean droplet size and buoyancy force. Swarm rise velocity appears to be largely independent of column throughput, however it would be expected to have a small effect due to an increase in the drag force and reduce the rise velocity. A possible explanation is that all experiments were conducted at a constant S:A ratio, meaning that increasing the continuous phase flow rate also increases the dispersed phase flow rate. As the mean droplet size is largely independent of throughput, there will be a greater number of droplets. There may be a slip-streaming effect, where droplets are shielded from the drag by other droplets, much like cyclists that conserve energy by cycling in a peloton. This would reduce the drag force experienced on individual droplets and increase the swarm's rise velocity. Therefore, future work should to investigate the effect of changing the continuous phase flow rate whilst the dispersed phase flow rate remains constant.



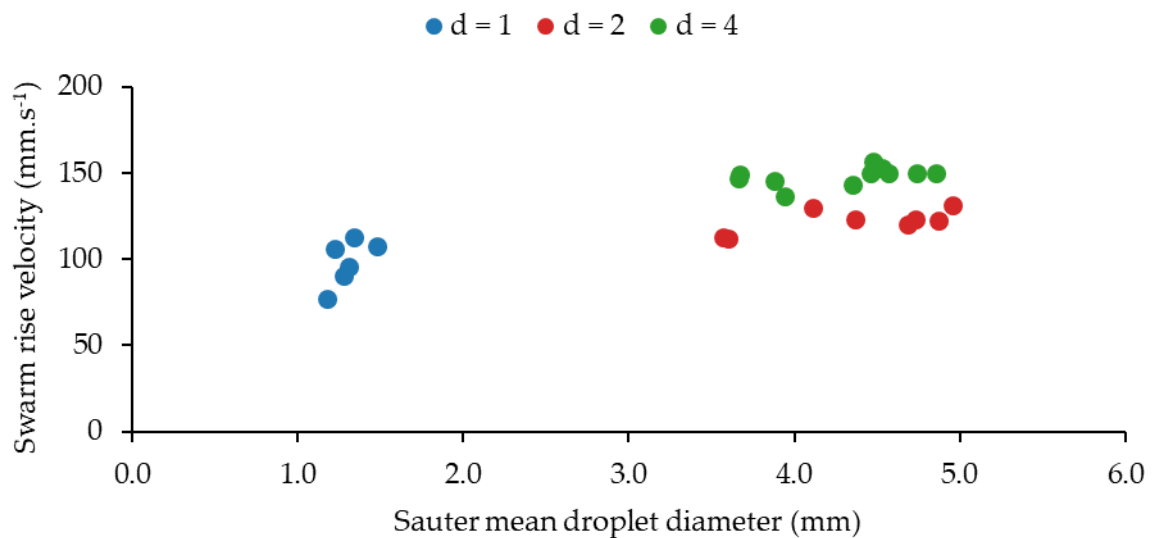
**Figure 36:** Droplet swarm rise velocity grouped by hole diameter vs total throughput.

Figure 37 shows the relationship between swarm rise velocity and pulse amplitude. Generally, the two appear to be either independent or have a weak inverse relationship, which is consistent with literature which found that droplet size and rise velocity are generally unaffected by column throughput. To further investigate this phenomenon, a significant number of additional experiments would need to be conducted over a wider range of column throughputs, pulse amplitudes, and hole diameters.



**Figure 37:** Droplet swarm rise velocity grouped by hole diameter vs pulse amplitude.

Plotting rise velocity against mean droplet diameter reveals a nonlinear correlation between the two variables, with swarm rise velocity increasing with mean droplet diameter. As with Figure 35, the plot exhibits two distinct clusters, one for the 1 mm diameter holes and one for the 2 and 4 mm diameter holes.



**Figure 38:** Droplet swarm rise velocity grouped by hole diameter vs pulse amplitude.

Using equations 2.17, 5.7 and 5.8 and the measured values, it is possible to calculate the swarm rise velocity. The results, shown in Figure 39, show reasonable agreement with the experimental data, however there are notable differences between the accuracy of predicted

values for smaller and larger droplets which can largely be attributed to the choice of drag model which is not formulated to account for the complex hydrodynamics observed in PSECs. To better understand the phenomenon, future work should investigate this relationship over a broader range of droplet sizes.

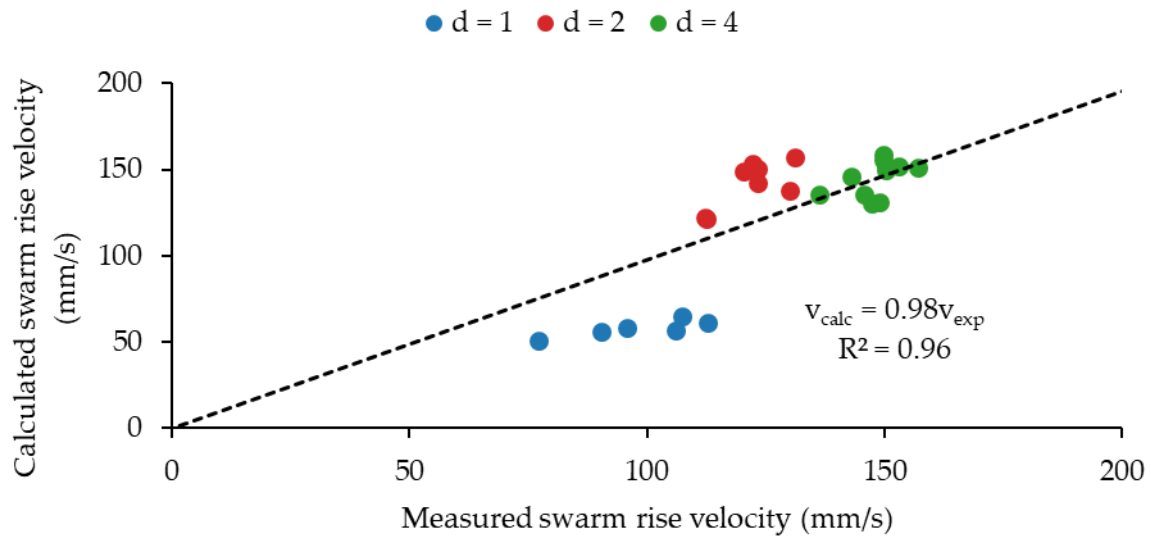


**Figure 39:** Calculated and measured droplet swarm rise velocities grouped by hole diameter vs pulse amplitude.

The results of the experiment, shown in Figure 38, confirm the nonlinear relationship between hole diameter and mean droplet diameter, indicating the 1 mm holes induces jetting and subsequent breakage of droplets while for the 2 and 4 mm holes, droplet size is dependent on the fluid properties and column hydrodynamics. Two swarm rise velocities were measured across all three plate hole diameters for a total throughput of 30 L.hr<sup>-1</sup> and pulse amplitudes of 2.96 and 3.70 mm and are shown in Figure 40. This experiment demonstrates that as hole diameter increases, the swarm rise velocity increases, caused by the increase in mean droplet diameter and buoyancy force as shown in Figure 28.

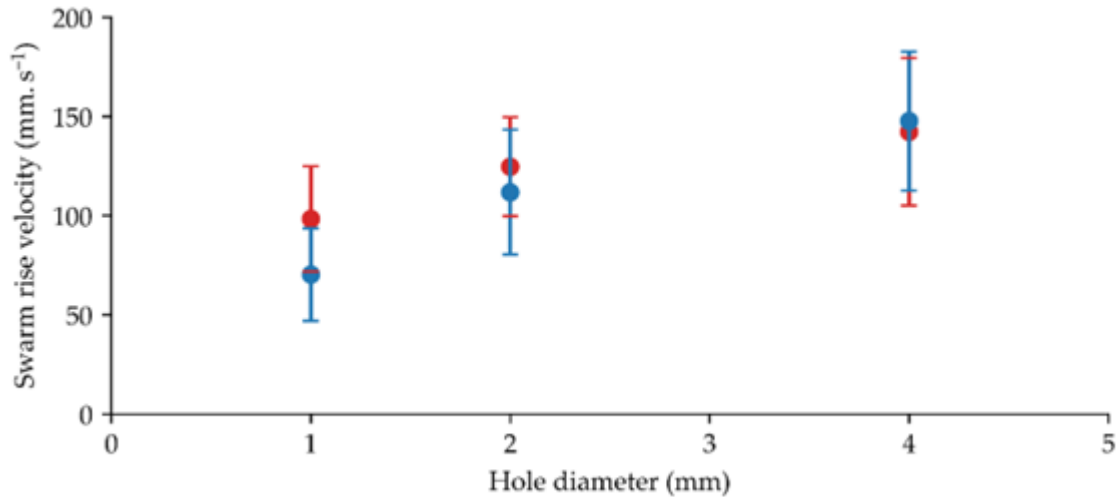


**Figure 40:** Droplet swarm averaged rise velocities for a total throughput ( $Q_{tot}$ ) of 30 L.hr<sup>-1</sup> for pulse amplitudes ( $A$ ) of 2.96 mm and 3.70 mm.

#### 4.4. Summary

The maximum PSEC throughput was found to positively correlate with the hole diameter and pulse amplitude, consistent with previous investigations' results. Additionally, it was identified that when the column is close to its maximum throughput before flooding, recirculating regions are formed within the column stage, causing the accumulation of smaller droplets and eventually leading to flooding.

The mean droplet diameters were measured and found to be nonlinearly correlated with hole diameter. There was a distinct difference in size between the 1 and 2 mm diameter holes, while similar droplets were produced for the 2 and 4 mm holes. The ratio of  $d_{3,0}$  to  $d_{3,2}$  was also measured and found consistent with values used in previous investigations.

The droplet size distribution measurements across the range of throughputs, pulse amplitudes and hole diameters showed that the size distribution of the droplets was highly dependent on their mean diameter. In contrast, size distribution is either weakly proportional or invariant with throughput and pulse amplitude.

The experiments identified that while the rise velocity of individual droplets is highly variable, the rise velocity of a swarm is strongly correlated to the mean droplet diameter since it influences the buoyancy force. On the other hand, the column throughput and pulse amplitude had a negligible effect on the swarm rise velocity.

Due to limitations with the experimental apparatus, it is impossible to fully explore the operational envelope, as the maximum pulse amplitude is limited. This has prevented a complete characterisation of the dispersed phase hydrodynamics up to the flooding point caused by excessive pulsation. As the investigation has only been carried out with a single chemical system, it is not possible to investigate the impact of fluid properties on column operability and hydrodynamics and it is recommended that future studies include additional fluids to study these effects.

The current method for optical characterisation of the dispersed phase presents opportunities for improvement. Several sources of geometric distortion are caused by the existing imaging and experimental setup. Geometric distortion caused by magnification can be reduced by implementing a bi-telecentric lens, facilitating more accurate measurement of droplet diameters across the depth of field (Hu et al., 2022). Refraction due to the curvature of glass column walls can be overcome by situating the column in a square box filled with a fluid with the same refractive index as the glass (Rida et al., 2019). The methods for measuring droplet diameters and rise velocities outlined in this report are time-consuming and not technically accessible to those unfamiliar with python, OpenCV and Linux. It is therefore recommended that recent developments in the use of Convolutional Neural Networks (CNN) for the segmentation of droplets are implemented, as they offer significantly faster processing (Schmitt et al., 2021).

There are a variety of advanced optical techniques that can be used to further investigate column hydrodynamics. Using iso-refractive fluids for the continuous and dispersed phase will make it possible to measure local holdup by adding a phase-specific dye, colour intensity, and the Beer-Lambert law (Leleu and Pfennig, 2022). In addition, instantaneous droplet velocities can be measured using either Digital In-line Holography (DIH) or Particle Tracking Velocimetry (PTV) (Lamadie and Bruel, 2013; Dabiri and Pecora, 2020). Finally, the continuous phase velocity field can be measured using PTV or PIV (Raffel et al., 1998). Using a combination of these techniques, it could be possible to generate sufficient data to perform droplet-specific force balance, enabling the identification of an appropriate model for interfacial momentum transfer.

## 5. COMPUTATIONAL FLUID DYNAMICS SIMULATION OF PULSED SIEVE-PLATE EXTRACTION COLUMNS

This chapter presents the application of the Generalised Multifluid Modelling Approach to the simulation of PSECs. A 3D LES and 2D URANS model were developed and compared to experimental data. Results show that 3D LES reasonably agrees with experimental data for stagewise droplet size distribution, mean diameters, and rise velocities, while 2D URANS slightly under-predicted droplet diameters and rise velocities. Furthermore, a local approach to modelling mass transfer directly within GEMMA was developed and successfully predicted the dispersed-phase holdup, mean droplet diameter, and axial solute concentrations. This modelling method provides an accurate predictive tool for PSECs, thus offering an alternative approach to column design rather than traditional empirical correlations or pilot-plant studies.

### 5.1. Introduction

Computational fluid dynamics is a useful tool which can be used to improve the predictive capability of multiphase flows, however, this is hindered by the complexity of flows that are of interest to industrial applications. A PSEC includes a broad range of interfacial scales, ranging from small droplets to large segregated free-surface interfaces observed in the near plate region. Off-the-shelf multiphase flow numerical models generally assume either small or large interfacial scales, resulting in the so-called interface-averaging and interface-resolving approaches (Prosperetti and Tryggvason, 2009; Marschall, 2011).

Interface averaging methods are mainly used for dispersed flows where the interfacial scales are smaller than the size of the numerical grid, where scale separation is assumed, and the governing equations are conditionally averaged, resulting in the so-called multifluid formulation. Due to the averaging operation, suitable closures are needed to account for the interfacial transfer of momentum, heat and mass.

Interface-resolving approaches require a mesh size that is small enough to allow for an adequate interface resolution and are generally applied to large segregated interfaces. This approach leads to interface-tracking and interface-capturing models. In the former, the interface position is tracked in a Lagrangian fashion, whilst in the latter, it is reconstructed

from a known indicator function. The VOF approach (Hirt and Nichols, 1981) is an example of an interface-capturing model.

In the case of PSECs, the multiphase flows of practical interest exhibit a marked multiscale behaviour necessitating a generalised multiphase modelling approach capable of handling the broad range of interfacial scales in the same computational domain. Several of these approaches have been proposed, mainly following the idea of embedding some form of large interface resolution within a standard multifluid framework (Štrubelj and Tiselj, 2011). However, most of these approaches either rely on a priori regime maps based on the local volume fraction (Štrubelj and Tiselj, 2011; Hänsch et al., 2012; Mathur et al., 2019) or lack the capability of adapting to the local flow regime altogether (Marschall and Hinrichsen, 2013).

The GEMMA method for simulating multiscale multiphase flows has been recently developed (De Santis, Colombo, et al., 2021). The approach adapts its formulation to the local resolution of the interfacial scales. The GEMMA approach reduces to a standard multifluid formulation suitable for small/dispersed interfaces in the numerical cells where the interfacial scales are small compared to the mesh size. In the cells where the mesh size is fine enough to guarantee an acceptable resolution of the interfacial morphology, a novel multifluid formulation suitable for the simulation of large/segregated interfaces is introduced. The latter formulation aims at mimicking the behaviour of an interface-resolving approach such as VOF within the multifluid framework. However, given that the model is based on a multifluid description, dedicated closures for interfacial momentum transfer and surface tension remain necessary to describe the underlying physics of interfacial momentum exchange in large interface regions.

The model has been assessed against different fundamental test cases (De Santis, Colombo, et al., 2021), where it has been shown that it is as accurate as the VOF approach for cases characterised by large/segregated interfaces, whilst a standard multifluid behaviour is recovered in dispersed flows. In the same work, the authors demonstrated the capability of the approach to adapt its formulation locally in a prototypical multiscale flow, i.e., a water jet plunging in a quiescent pool.

Furthermore, it has been demonstrated that the GEMMA approach can accurately represent the complex multiphase hydrodynamics encountered in liquid–liquid extraction devices (Theobald, 2020; De Santis, Hanson, et al., 2021; Fells et al., 2022). This section builds on

previous findings and presents two investigations. The first, a detailed assessment of the hydrodynamics, comparing the use of LES to model the column in three-dimensional form and the URANS equations to model the column in two-dimensional form. Furthermore, the second investigation demonstrated the implementation of local mass transfer modelling capabilities directly within GEMMA.

## 5.2. Methodology

### 5.2.1. Hydrodynamics

The GEMMA method has been implemented in the open-source CFD code OpenFOAM v7.0 (Weller et al., 1998; Greenshields, 2019). GEMMA is built on top of the standard multifluid modelling framework suitable for small/dispersed interfaces given by the OpenFOAM native reactingMultiPhaseEulerFoam solver. GEMMA introduces two different formulations within the multifluid framework; in each cell of the computational domain, which is selected based on the numerical grid's local capability to resolve the interface's morphology. The two formulations are:

1. A standard multifluid formulation suitable for small/dispersed interfacial scales: this approach is used in the cells where the local mesh size is larger than the local interfacial scales, and, therefore, it is not possible to directly resolve the morphology of the interface.
2. An ad-hoc multifluid formulation suitable for large/segregated interfacial scales: this approach is used in the cells where the local mesh size is smaller than the local interfacial scales and the mesh resolution is fine enough to guarantee an adequate resolution of the interface. This formulation aims to provide interface resolution, similar to interface-resolving approaches, in the context of the multifluid framework.

A large interface identifier,  $C_\alpha$ , is introduced to identify which formulation is used in each cell.  $C_\alpha$  is equal to zero in the cells where the dispersed formulation is employed and is equal to one in the cells where the large interface formulation is used. A flow diagram describing the switching logic is shown in Figure 41. A detailed description of the logic controlling the local  $C_\alpha$  value and of the multifluid formulation for large/segregated interfaces is provided in (De Santis, Colombo, et al., 2021).

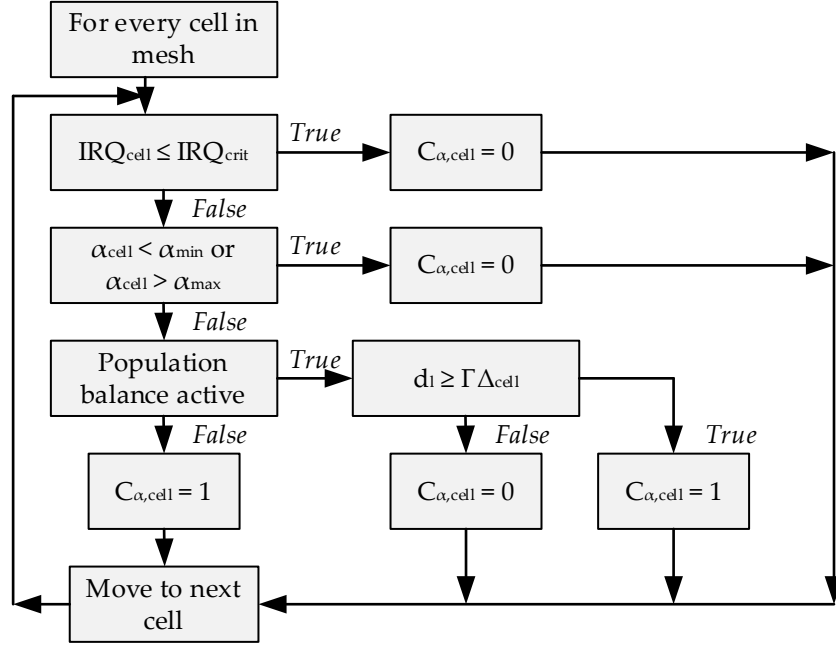


**Figure 41:** Flow chart showing logic for the switching of the large interface identifier  $C_\alpha$ .

The Interface Resolution Quality (IRQ) index is a numerical indication of interface resolution and is a function of the local mesh size and the local interface curvature,  $\kappa$ . A user-specified IRQ value is used to determine whether there is sufficient interface resolution for  $C_\alpha$  to be activated. A value of 16 was used in these simulations. IRQ and local interface curvature are defined as:

$$IRQ = \frac{2}{\sqrt[3]{V_{cell}}\kappa} \quad (5.1)$$

$$\kappa = -\nabla \cdot \left( \frac{\nabla \alpha}{|\nabla \alpha|} \right) \quad (5.2)$$

To ensure  $C_\alpha$  is only enabled in cells where an interface exists, and minimum and maximum values for the dispersed phase volume fraction are specified. These simulations used a dispersed phase volume fraction of 0.01 to 0.99. Finally,  $C_\alpha$  is enabled if the calculated diameter of the dispersed phase is larger than the current cell size multiplied by a user-defined value,  $\Gamma$ , which was set to 4.

In the case of adiabatic flows without mass transfer, the volume-averaged continuity equation for phase  $x$  is:

$$\frac{\delta\alpha_x}{dt} + \nabla \cdot (\alpha U_x) + \nabla \cdot (U_c \alpha_x (1 - \alpha_x)) = 0 \quad (5.3)$$

where the  $\alpha_x(1 - \alpha_x)$  term ensures the included compressive velocity term is only active in the presence of a large interface to maintain sharpness by preventing diffusion. The compressive velocity term,  $U_c$ , is:

$$U_c = C_\alpha |U_c| \frac{\nabla \alpha}{|\nabla \alpha|} \quad (5.4)$$

The corresponding momentum conservation equation is:

$$\frac{\delta\alpha_x U_x}{\delta t} + \nabla \cdot (\alpha_x U_x U_x) = -\frac{\alpha_x \nabla p}{\rho_x} + \nabla \cdot (v_x \alpha_x \nabla U_x) + \alpha_x g + \frac{(F_x + F_{st,x})}{\rho_x} \quad (5.5)$$

where the interfacial exchange is described via the momentum exchange force,  $F_x$ , and the surface tension force,  $F_{st,x}$ . The underpinning phenomena for these are different depending on if the fluid is dispersed or segregated, and these are formulated accordingly. The formulation for a generic force is as follows:

$$F = (1 - (1 - C_\alpha)f_x - (1 - C_\alpha)f_z)F_{LI} + (1 - C_\alpha)f_x F_{xy} + (1 - C_\alpha)f_z F_{zx} \quad (5.6)$$

Interphase momentum transfer of dispersion is modelled with the drag model of Schiller and Naumann (Yilmaz and Gundogdu, 2009). For both the 3D and 2D simulations, the magnitude of drag was scaled by 1.5 to fit the number weighted droplet rise velocity, while for the mass transfer case, this was scaled by 2.3 to match the dispersed phase holdup.

$$\text{For } Re \leq 1000 \quad C_D = \frac{24(1 + 0.15Re^{0.687})}{Re} \quad (5.7)$$

$$\text{For } Re > 1000 \quad C_D = 0.44 \quad (5.8)$$

The surface tension force,  $F_{st,x}$ , is formulated as:

$$F_{st,k} = \alpha_x \sum_{i=1}^{n_k} \left( C_{\alpha_{k,i}} \sigma_{k,i} \alpha_{smooth} \nabla \alpha \frac{2\rho}{\nabla \rho_{k,i}} \right) \quad (5.9)$$

## 5.2.2. Turbulence

### 5.2.2.1. Large Eddy Simulation

For the 3D case, the LES approach is used to model both phases. This technique separates the flow into two turbulence scales where large scales are resolved and small scales are modelled.

This is achieved using a filtering operation  $G$  (Germano et al., 1991). The filtered fields, denoted by  $\overline{(\ )}$ , are expressed as:

$$\overline{f}(x) = \int f(x') \overline{G}(x, x') \delta x' \quad (5.10)$$

Filtering the incompressible continuity and momentum conservation equations gives:

$$\frac{\delta \overline{U}_i}{\delta x_i} = 0 \quad (5.11)$$

$$\frac{\delta \overline{U}_i}{\delta t} + \frac{\delta \overline{U}_i \overline{U}_j}{\delta x_j} = -\frac{1}{\rho} \frac{\delta \overline{P}}{\delta x_i} + \nu \frac{\delta}{\delta x_j} \left( \frac{\delta \overline{U}_i}{\delta x_j} + \frac{\delta \overline{U}_j}{\delta x_i} \right) = -\frac{1}{\rho} \frac{\delta \overline{P}}{\delta x_i} + 2\nu \frac{\delta^2}{\delta x_j \delta x_j} \overline{S}_{ij} \quad (5.12)$$

Where  $\overline{S}_{ij}$  is the resolved rate-of-strain tensor, given by:

$$\overline{S}_{ij} = \frac{1}{2} \left( \frac{\delta \overline{U}_i}{\delta x_j} + \frac{\delta \overline{U}_j}{\delta x_i} \right) \quad (5.13)$$

Decomposition of velocity into the resolved and Sub-Grid Scale (SGS) components (Leonard, 1975) gives:

$$\overline{U_i U_j} = \tau_{ij} + \overline{U}_i \overline{U}_j$$

This enables reformulation of the NS equations to eliminate the filtered advection term and group unclosed terms into the SGS stress tensor,  $\tau_{ij}$ .

$$\frac{\delta \overline{U}_i}{\delta t} + \frac{\delta \overline{U}_i \overline{U}_j}{\delta x_j} = -\frac{1}{\rho} \frac{\delta \overline{P}}{\delta x_i} + 2\nu \frac{\delta^2}{\delta x_j \delta x_j} \overline{S}_{ij} - \frac{\delta \tau_{ij}}{\delta x_j} \quad (5.14)$$

The SGS stress tensor is split into its isotropic and deviatoric parts, with the first bracket denoting the deviatoric component and the second bracket representing the isotropic component:

$$\tau_{ij} = \left( \tau_{ij} - \frac{1}{3} \tau_{kk} \delta_{ij} \right) + \left( \frac{1}{3} \tau_{kk} \delta_{ij} \right) \quad (5.15)$$

Using the Boussinesq hypothesis, the deviatoric part of the SGS stress tensor is modelled.

$$\tau_{ij} - \frac{1}{3} \tau_{kk} \delta_{ij} = -2\nu_t \overline{S}_{ij} \quad (5.16)$$

Eddy viscosity is modelled using the Smagorinsky model (1963), where  $c_k$  is 0.094.

$$\nu_t = c_k \Delta \sqrt{k} \quad (5.17)$$

The turbulent kinetic energy,  $k$ , is solved using the following quadratic equation, where  $c_e$  is 1.048.

$$\left(\frac{c_e}{\Delta}\right)k^2 + \left(\frac{2}{3}tr(\overline{S_{ij}})\right) + \left(2c_k\Delta(dev(\overline{S_{ij}}):\overline{S_{ij}})\right) = 0 \quad (5.18)$$

The length scale is calculated by taking the cubed root of the cell volume.

$$\Delta = V_c^{\frac{1}{3}} \quad (5.19)$$

### 5.2.2.2. Unsteady Reynolds-averaged Navier-Stokes

As turbulence is a three-dimensional phenomenon, simulating a two-dimensional case using LES would not be realistic as it would not be able to resolve large eddies, therefore, both phases are modelled using the URANS approach where turbulence is not resolved and is instead modelled (Greenshields, Christopher and Weller, 2022). URANS is based on Reynolds decomposition, which splits the instantaneous value into its time-averaged component, denoted by  $\overline{(\ )}$ , and time-varying component denoted by  $(\ )'$ .

$$U(x, t) = \overline{U(x, t)} + U'(x, t) \quad (5.20)$$

The URANS equations for incompressible flows are:

$$\frac{\delta \overline{U_i}}{\delta x_i} = 0; \quad (5.21)$$

$$\rho \frac{\delta \overline{U_i}}{\delta t} + \frac{\delta}{\delta x_j} (\rho \overline{U_i U_j}) = \rho \overline{f_i} + \frac{\delta}{\delta x_j} \left( -\overline{P} \delta_{ij} + 2\nu \overline{S_{ij}} - \rho \overline{U_i' U_j'} \right) \quad (5.22)$$

Where the Reynolds stress tensor is defined as:

$$\tau'_{ij} = \rho \overline{U_i' U_j'} \quad (5.23)$$

The  $k$ - $\epsilon$  model is a commonly used two-equation model for achieving closure of the URANS equations. It models the Reynolds stresses by describing turbulence using transport equations for turbulent kinetic energy,  $k$ , and turbulent dissipation rate,  $\epsilon$ . Model constants have been determined by data fitting to a wide range of turbulent flows (Versteeg and Malalasekera, 2007). The values are  $C_\mu = 0.09$ ,  $\sigma_k = 1.00$ ,  $\sigma_\epsilon = 1.30$ ,  $C_{1\epsilon} = 1.44$  and  $C_{2\epsilon} = 1.92$ .

$$\frac{\delta(\rho k)}{\delta t} + \frac{\delta(\rho k U_i)}{\delta x_i} = \frac{\delta}{\delta x_j} \left( \frac{\mu_t}{\sigma_k} \frac{\delta k}{\delta x_j} \right) + \mu_t E_{ij} E_{ij} - \rho \epsilon \quad (5.24)$$

$$\frac{\delta(\rho\epsilon)}{\delta t} + \frac{\delta(\rho\epsilon U_i)}{\delta x_i} = \frac{\delta}{\delta x_j} \left( \frac{\mu_t}{\sigma_\epsilon} \frac{\delta\epsilon}{\delta x_j} \right) + C_{1\epsilon} \frac{\epsilon}{k} 2\mu_t E_{ij} E_{ij} - C_{2\epsilon} \rho \frac{\epsilon^2}{2} \quad (5.25)$$

$$\mu_t = \rho C_\mu \frac{k^2}{\epsilon} \quad (5.26)$$

### 5.2.3. Reduced population balance

A population balance approach can be used within GEMMA to evaluate the DSD when working in dispersed-interface mode; this feature is particularly important in cases involving mass transfer since the interfacial area available for the interfacial exchanges is directly related to the Sauter mean diameter of the dispersed phase in the regions of small/dispersed interfaces.

The One Primary One Secondary Particle Method (OPOSPM) (Drumm et al., 2010) is a reduced population balance approach to model droplet size. OPOSPM allows for the conservation of two low-order moments, and the selection of these moments is arbitrary; however, the total number and volume concentrations are the most commonly employed moments to guarantee the conservation of the total number and mass of the DPEs. Since the total number and volume concentration are conserved, the population density is represented by a single particle (assumed to have a spherical shape) whose size is characterised by the diameter:

$$d_{3,0} = \frac{\sqrt[3]{\sum d^3}}{\sqrt{\sum d^0}} = \sqrt[3]{\frac{6\alpha_d}{\pi N_d}} \quad (5.27)$$

where  $\alpha_d$  and  $N_d$  are the volume fraction and the particle number density of the dispersed phase, which are related to the zeroth and third moment of the distribution  $d^0$  and  $d^3$ . Since the volume fraction is already known from the resolution of the standard multifluid governing equations, the OPOSPM formulation only requires the solution of one additional conservation equation for  $N_{droplet}$ , which is given by:

$$\frac{\partial(\rho_d N_d)}{\partial t} + \nabla \cdot (\rho_d U_d N_d) = \rho_d S \quad (5.28)$$

where the source term,  $S$ , is:

$$S = (n_{daughter} - 1)r_{breakage}N_d - \frac{1}{2}r_{coalescence}N_d^2 \quad (5.29)$$

Within the source term, droplet formation due to breakage is described as a function of the mean number of daughter droplets,  $n_{daughter}$ , which is assumed to be 2, and the breakage rate,  $r_{breakage}$ , given by the break-up model of Martinez-Bazan et al. (1999):

$$r_{breakage} = \frac{\sqrt{8.2(\epsilon d_{3,0})^{\frac{2}{3}} - \frac{12\sigma}{\rho_c d_{3,0}}}}{4d_{3,0}} \quad (5.30)$$

Finally, the droplet coalescence rate,  $r_{coalescence}$ , is modelled using the coalescence model of Prince and Blanch (1990), where the initial film thickness,  $h_0$ , and final film thickness,  $h_f$ , are assumed to be  $10^{-4}$  and  $10^{-8}$  m, respectively. For both the 3D simulation and 2D simulations, the coalescence rate was scaled by 20 to fit the Sauter mean droplet diameter, while for the mass transfer case the breakage rate was scaled by 100.

$$r_{coalescence} = 1.409\epsilon^{\frac{1}{3}} d_{3,0}^{\frac{1}{3}} \exp\left(-\left(\frac{d_{3,0}}{2}\right)^{\frac{5}{6}} \frac{\rho_c^{\frac{1}{2}} \epsilon^{\frac{1}{3}}}{4\sigma^{\frac{1}{2}}} \ln\left(\frac{h_0}{h_f}\right)\right) \quad (5.31)$$

The OPOSPM formulation described above allows for the evaluation of  $d_{3,0}$ ; however, knowledge of the Sauter mean diameter  $d_{3,2}$  also allows evaluation of the interfacial area density as:

$$a = \frac{6\alpha_d}{d_{3,2}} \quad (5.32)$$

In the context of LLE, Wardle (2013) followed the approach of estimating the ratio  $d_{3,0}/d_{3,2}$  from known DSDs and combined this with the  $d_{3,0}$  evaluated with the reduced population balance to infer the  $d_{3,2}$ . For liquid–liquid dispersions in ACCs, it has been observed that the  $d_{3,0}/d_{3,2}$  ratio is consistently in the range of 0.75–0.80. As the work in this section was performed before the experimentally determined value in chapter 4, a value of 0.76 is used throughout the simulations presented in this work.

#### 5.2.4. Mass transfer

Mass transfer requires the solution of transport equations which describes the species concentration, where  $M_i$ , denotes the mass concentration of species  $i$  in  $\text{kg}\cdot\text{m}^{-3}$ ,  $D$  denotes the diffusion coefficient of species  $i$  in phase  $x$  and  $S_{mass}$  denotes the mass transfer rate source term expressed in  $\text{kg}\cdot\text{m}^{-3}\cdot\text{s}^{-1}$ .

$$\frac{\delta \alpha_x M_i}{\delta t} + \nabla \cdot (\alpha U_x M_i) - \nabla \alpha_x D_{i,x} \nabla (M_i) = S_{mass} \quad (5.33)$$

The approach relies on the two-film theory (Levenspiel, 1999) discussed in chapter 2, where  $k_c$  and  $k_d$  are the mass transfer coefficients expressed in  $\text{m.s}^{-1}$  of the continuous and dispersed phases. The correlation of Treybal (1980) is used for  $k_c$ , the correlation of Laddha and Degaleesan (1978) has been used for  $k_d$  and equation 2.21 expressed on a mass basis is used for  $S_{mass}$ .

### 5.2.5. Computational domain and geometry

The dimensions presented in Table 4 were used to produce a 3D geometry. The hex-dominant mesher snappyHexMesh was chosen to generate an unstructured three-dimension mesh with 1.26 M nodes with a typical edge length of 2.18 mm with refinement towards the plates and column walls, see Figure 42. The mesh in the near-plate region is resolved to capture droplet formation and fluid transfer across the plate, while the mesh in the inter-plate region is coarse to reduce computational requirement. The typical cell edge length chosen was in line with those identified for mesh independence by Sen (2015) and Tu (2021). It is important to note that in hybrid methodologies, successive mesh refinement leads to improved interface resolution at the expense of increased simulation times due to higher computational requirement. Regardless, the mesh is resolved to a sufficient level to capture at least 80% of the turbulence energy spectrum using LES and implicitly track the dispersed phase fluid motion.

Additionally a simplified 2D geometry was made. Due to the difficulty in translating a 3D geometry to 2D, all diameters for the column sections were kept the same. The hole diameters were kept the same, but the number of holes was changed to maintain the same fractional free area (23 %). Again, the hex-dominant mesher snappyHexMesh was chosen to produce an unstructured 2-dimension mesh with 34061 nodes with a typical edge length of 1.83 mm with refinement towards the plates and column walls, see Figure 43.

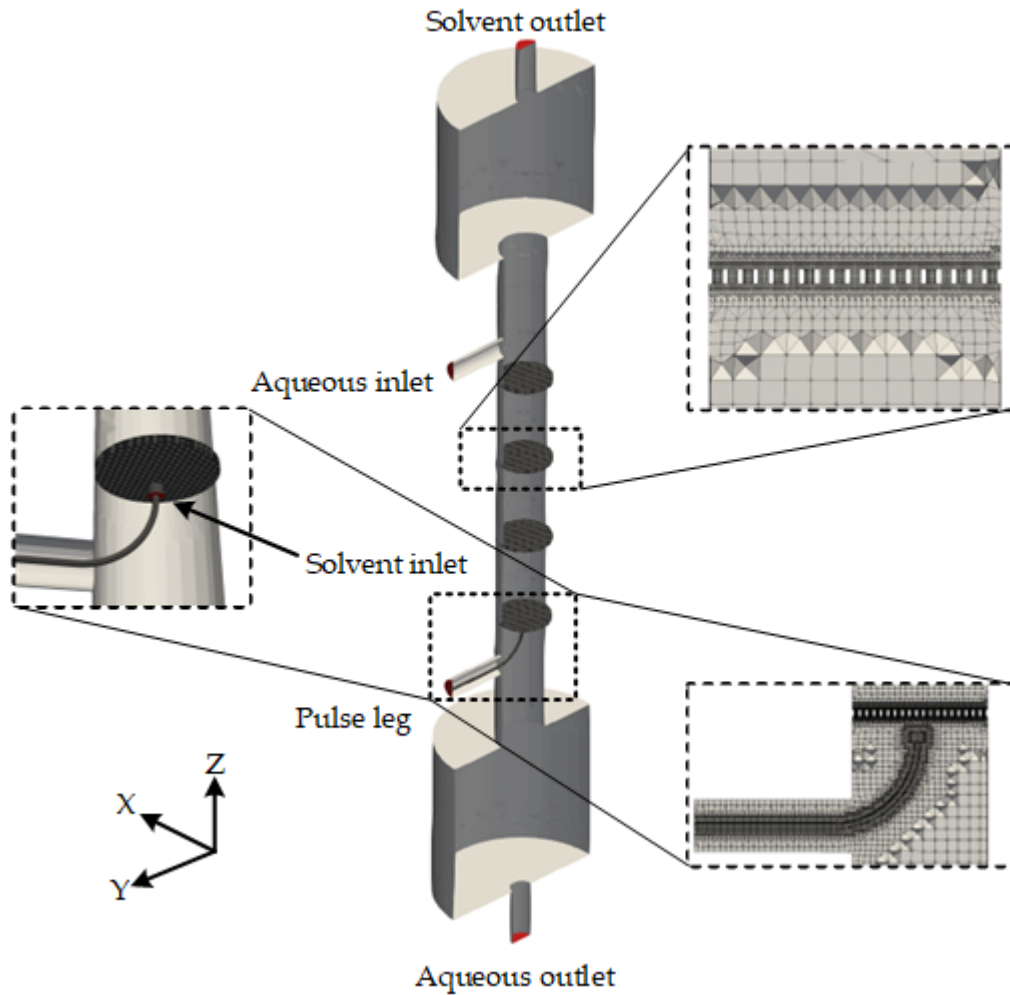


**Figure 42:** Geometry and mesh used in 3D CFD simulations. Boundary patches are highlighted in red.

To assess the local implementation of mass transfer within GEMMA, the same approach for the above 2D case was used to prepare a 2D geometry representing a PSEC operated by Garthe (2006), with dimensions outlined in Table 4. The hex-dominant mesher snappyHexMesh was chosen to produce an unstructured 2-dimension mesh with 176809 nodes with a typical edge length of 1.77 mm with refinement towards the plates and column walls.

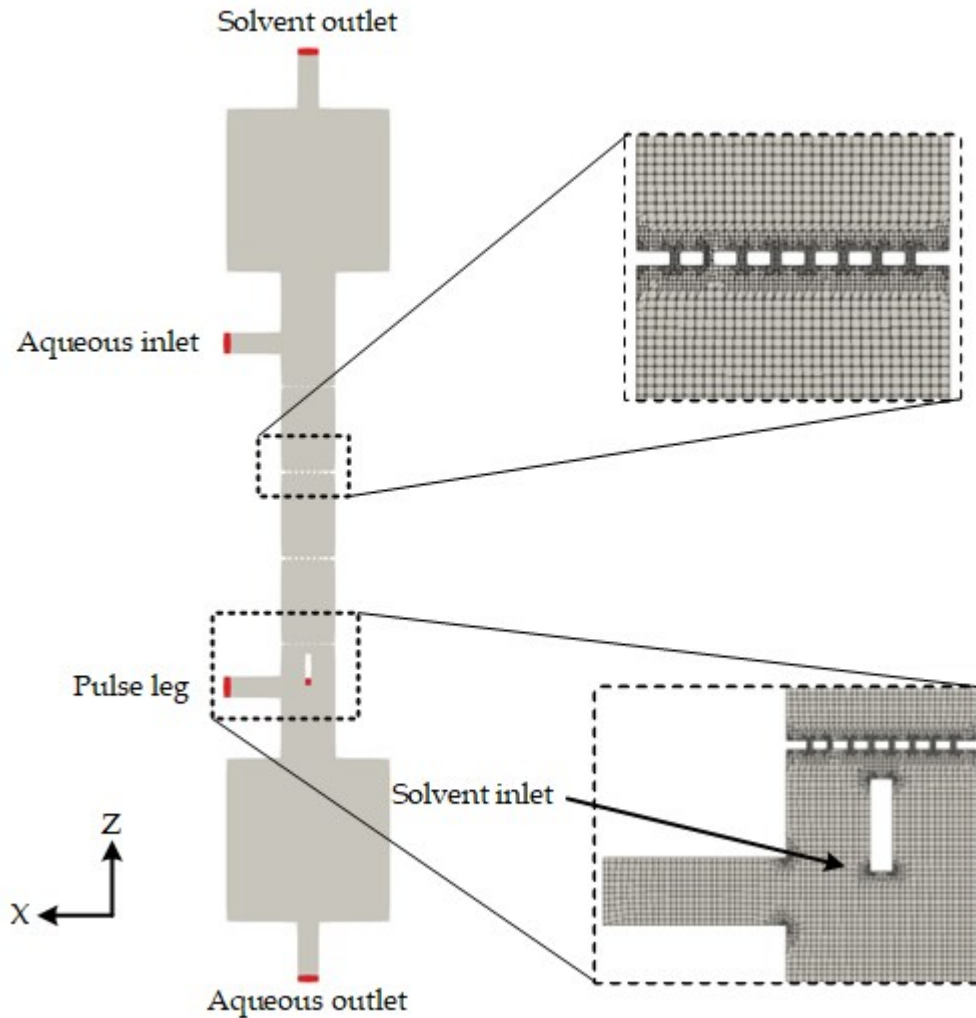


**Figure 43:** Geometry and mesh used in 2D CFD simulations. Boundary patches are highlighted in red.

**Table 7:** Summary of column geometry and operating parameters (Garthe, 2006)

| Parameter                | Value |
|--------------------------|-------|
| Column diameter (mm)     | 80    |
| Column height (mm)       | 4400  |
| Plate hole diameter (mm) | 2     |
| Plate spacing (mm)       | 99    |
| Plate free area (%)      | 23    |

All meshes were assessed using the OpenFOAM checkMesh tool, which determines the suitability of a mesh against several parameters, including the cell aspect ratio (the ratio between the longest and shortest edge length), cell volumes, mesh non-orthogonality (the

angle between the line connecting two cell centres and the normal of their common face) and skewness (the distance between the intersection of the line connecting two cell centres with their common face and the centre of that face). A summary of the output is shown in Table 8.

**Table 8:** Reported mesh quality using checkMesh utility.

|                           | LES                    | URANS                  | Garthe                 |
|---------------------------|------------------------|------------------------|------------------------|
| Dimensions                | 3D                     | 2D                     | 2D                     |
| Max cell openness         | $3.28 \times 10^{-16}$ | $3.22 \times 10^{-16}$ | $3.16 \times 10^{-16}$ |
| Max aspect ratio          | 9.55                   | 3.07                   | 3.54                   |
| Minimum face area         | $2.81 \times 10^{-9}$  | $1.12 \times 10^{-7}$  | $6.19 \times 10^{-8}$  |
| Maximum face area         | $1.56 \times 10^{-4}$  | $4.77 \times 10^{-6}$  | $4.81 \times 10^{-6}$  |
| Min volume                | $1.92 \times 10^{-12}$ | $1.12 \times 10^{-10}$ | $6.19 \times 10^{-11}$ |
| Max volume                | $1.30 \times 10^{-6}$  | $4.77 \times 10^{-9}$  | $4.81 \times 10^{-9}$  |
| Max non-orthogonality     | 60.1                   | 41.6                   | 40.2                   |
| Average non-orthogonality | 9.69                   | 4.39                   | 4.67                   |
| Max skewness              | 3.66                   | 1.95                   | 2.64                   |

### 5.2.6. Solution methodology

A summary of boundary conditions used for the 3D case is presented in Table 9. Conditions for volume fraction, phase velocities, pressure, turbulent viscosity, droplet number density and  $C_\alpha$  were specified at all column inlets and outlets, the pulse leg, walls and the initialised internal field. Fluid properties are those outlined in Table 5.

The volume fraction of inlets is assigned a fixed value corresponding to the relevant phase, while outlet values are assigned to a mixed condition, where a zero gradient condition applies during outflow and a value corresponding to the appropriate phase applies during inflow. Walls are given a zero gradient condition and the internal field is set, corresponding to the column filled with the heavy phase and a light phase layer occupying the upper separator's top half.



For the light phase velocity, a fixed volumetric flux of 20 L.hr<sup>-1</sup> is assigned to the light phase inlet and outlet and both the heavy phase inlet and outlet are assigned a mixed condition where during outflow a zero gradient condition is applied and during inflow the velocity is calculated from the patch-face normal component of the internal-cell value. For the heavy phase velocity field, a fixed volumetric flux of 10 L.hr<sup>-1</sup> is assigned to the heavy phase inlet and outlets and the light phase inlets and outlets are assigned the mixed condition. For both phases, walls are assigned a no-slip condition and the internal field is assigned as a zero vector. Pulse leg velocity is calculated using a time-varying sinusoidal boundary condition where the velocity is calculated for a pulse amplitude of 30 mm and a pulse frequency of 1 Hz.

$$U = Af \sin(2\pi ft) \quad (5.34)$$

Pressure at the heavy inlet, heavy outlet, pulse leg and walls are calculated from the boundary flux as specified by the velocity. The light outlet is assigned a static atmospheric pressure and the internal field is initialised with uniform atmospheric pressure.

The turbulent viscosity at the inlets and pulse leg is assigned a zero gradient condition and is calculated at the outlets. The internal field is set to 0 to initialise the solution and walls are modelled using a wall function to relax mesh requirements (Launder and Spalding, 1983).

An initial estimate for droplet number density is provided for the internal field based on a droplet diameter of 2 mm and a dispersed phase holdup of 10%. A zero gradient condition is applied at all boundaries.

For the 2D case, the boundary conditions for volume fraction, pressure, turbulent viscosity, droplet number density and  $C_\alpha$  are the same as the 3D case presented in Table 9. A summary of the boundary conditions for velocity, turbulent kinetic energy and turbulent dissipation rate are presented in Table 10.

Table 10: Boundary conditions used for 2D URANS case

|                    | Internal field                          | Heavy inlet   | Heavy outlet  | Light inlet   | Light outlet  | Pulse leg   | Wall             |
|--------------------|---|---|---|---|---|---|------------------|
| $U_{heavy}$        | Uniform value<br>(0, 0, 0)              | Fixed value<br>( $2.37 \times 10^{-3}$ , 0, 0)                  | Fixed value<br>(0, 0, $-2.37 \times 10^{-3}$ )                      | Outflow:<br>Fixed normal<br>gradient 0<br>Inflow:<br>Calculated | Outflow:<br>Fixed normal gradient<br>0<br>Inflow: Calculated        | Time-varying<br>sinusoidal<br>$A = 30 \text{ mm}$<br>$f = 1$            | No slip          |
| $U_{light}$        | Uniform value<br>(0, 0, 0)              | Outflow:<br>Fixed normal<br>gradient 0<br>Inflow:<br>Calculated | Outflow:<br>Fixed normal gradient<br>0<br>Inflow: Calculated        | Fixed value<br>(0, 0, $-1.45 \times 10^{-2}$ )                  | Outflow:<br>Fixed normal gradient<br>0<br>Inflow: Calculated        | Time-varying<br>sinusoidal<br>$A = 30 \text{ mm}$<br>$f = 1 \text{ Hz}$ | No slip          |
| $\epsilon_{heavy}$ | Uniform value<br>$8.54 \times 10^{-14}$ | Fixed value<br>$2.30 \times 10^{-9}$                            | Outflow: Fixed value<br>$2.30 \times 10^{-9}$<br>Inflow: Calculated | Fixed value<br>$2.03 \times 10^{-7}$                            | Outflow: Fixed value<br>$2.30 \times 10^{-9}$<br>Inflow: Calculated | Fixed value<br>$2.30 \times 10^{-9}$                                    | Wall<br>function |
| $\epsilon_{light}$ | Uniform value<br>$1.91 \times 10^{-10}$ | Fixed value<br>$1.22 \times 10^{-8}$                            | Outflow: Fixed value<br>$1.22 \times 10^{-8}$<br>Inflow: Calculated | Fixed value<br>$1.08 \times 10^{-6}$                            | Outflow: Fixed value<br>$1.22 \times 10^{-8}$<br>Inflow: Calculated | Fixed value<br>$1.22 \times 10^{-8}$                                    | Wall<br>function |
| $k_{heavy}$        | Uniform value<br>$1.78 \times 10^{-10}$ | Fixed value<br>$7.97 \times 10^{-8}$                            | Outflow: Fixed value<br>$7.97 \times 10^{-8}$<br>Inflow: Calculated | Fixed value<br>$7.50 \times 10^{-7}$                            | Outflow: Fixed value<br>$7.97 \times 10^{-8}$<br>Inflow: Calculated | Fixed value<br>$7.97 \times 10^{-8}$                                    | Wall<br>function |
| $k_{light}$        | Uniform value<br>$3.03 \times 10^{-8}$  | Fixed value<br>$2.42 \times 10^{-7}$                            | Outflow: Fixed value<br>$2.42 \times 10^{-7}$<br>Inflow: Calculated | Fixed value<br>$2.28 \times 10^{-6}$                            | Outflow: Fixed value<br>$2.42 \times 10^{-7}$<br>Inflow: Calculated | Fixed value<br>$2.42 \times 10^{-7}$                                    | Wall<br>function |

For velocity fields, the boundary conditions for all patches are the same as with the 3D case except for the fixed volumetric flux conditions which are replaced with fixed velocities. Flow rates are scaled based on the ratio of column cross-sectional area to ensure fluid velocities remain comparable between the two cases. Turbulent kinetic energy,  $k$ , and turbulence dissipation rate,  $\epsilon$ , at the boundary patches for all inlets, walls and internal fields for both phases are calculated using the following equations (ANSYS, 2009):

$$I = 0.16Re^{-\frac{1}{8}} \quad (5.35)$$

$$k = \frac{3}{2}(UI)^2 \quad (5.36)$$

$$L = 0.07d \quad (5.37)$$

$$\epsilon = 0.09^{\frac{3}{4}} \frac{k^{\frac{3}{2}}}{L} \quad (5.38)$$

For the mass transfer case, the boundary conditions were configured using the same method as the above 2D case, corresponding to a heavy phase flow rate of 40 L.hr<sup>-1</sup> with a solute concentration of 0.922 mol.L<sup>-1</sup>, a light phase flow rate of 48 L.hr<sup>-1</sup> with a solute concentration of 0.131 mol.L<sup>-1</sup>, a pulse amplitude of 8 mm and a pulse frequency of 1.25 Hz. The column was operated using a heavy phase consisting of water, a light phase of toluene and acetone as the solute. Fluid properties are outlined in Table 11. The solution of mass transfer required the specification of additional fields for weight fraction of solute in both phase, the heavy phase in the light phase and the light phase in heavy which are presented in Table 12.

**Table 11:** Fluid properties for mass transfer investigation (Garthe, 2006)

| Parameter  | Heavy                   | Light                    |
|--|-------------------------|--------------------------|
| Density (kg.m <sup>3</sup> )                     | 998                     | 868                      |
| Dynamic viscosity (N.s.m <sup>-2</sup> )         | 1.03 × 10 <sup>-3</sup> | 0.596 × 10 <sup>-3</sup> |
| Interfacial tension (N.m <sup>-1</sup> )         | 34.3 × 10 <sup>-3</sup> |                          |
| Solute diffusion coefficient (m <sup>2</sup> .s) | 1.15 × 10 <sup>-9</sup> | 2.79 × 10 <sup>-9</sup>  |
| Distribution coefficient (dim)                   | 1.186                   |                          |

Table 12: Boundary conditions used for mass transfer case

|                     | Internal field          | Heavy inlet           | Heavy outlet   | Light inlet           | Light outlet   | Pulse leg           | Wall                |
|---------------------|-------------------------|-----------------------|--|-----------------------|--|---------------------|---------------------|
| <i>solute.heavy</i> | Uniform value<br>0.0544 | Fixed value<br>0.0544 | Outflow:<br>Fixed normal gradient<br>0<br>Inflow: 0.0544 | Fixed gradient 0      | Fixed gradient 0   | Fixed gradient<br>0 | Fixed gradient<br>0 |
| <i>solute.light</i> | Uniform value<br>0.0076 | Fixed gradient<br>0   | Fixed gradient 0   | Fixed value<br>0.0076 | Outflow:<br>Fixed normal gradient<br>0<br>Inflow: 0.0076 | Fixed gradient<br>0 | No slip             |
| <i>heavy.light</i>  | Uniform value<br>0.9456 | Fixed value<br>0.9456 | Outflow:<br>Fixed normal gradient<br>0<br>Inflow: 0.9456 | Fixed gradient 0      | Fixed gradient 0   | Fixed gradient<br>0 | Fixed gradient<br>0 |
| <i>light.heavy</i>  | Uniform value<br>0.9924 | Fixed gradient<br>0   | Fixed gradient 0   | Fixed value<br>0.9924 | Outflow:<br>Fixed normal gradient<br>0<br>Inflow: 0.9924 | Fixed gradient<br>0 | No slip             |

### 5.2.7. Numerical schemes

First-order Eulerian scheme was used to discretise the temporal derivative terms and second-order unbounded schemes were used for spatial discretisation of the convective terms. The simulation was performed using the transient pressure-velocity coupling algorithm PIMPLE, which is a combination of the Pressure Implicit with Splitting of Operators (PISO) and Semi-Implicit Method for Pressure Linked Equations (SIMPLE) algorithms (Greenshields, Christopher and Weller, 2022). The semi-implicit Multidimensional Universal Limiter for Explicit Solution (MULES) was used with an adjustable time step to ensure a maximum Courant number of 1.

### 5.3. Results and discussion

Figure 44 presents the velocity field magnitude for both 2D and 3D cases. To enable comparison, the 3D case is illustrated as a 2D slice along the column's central axis, however, it is important to note that this does not capture the hydrodynamics of the entire column and therefore this is not a like-for-like comparison. The plots showcase instantaneous values at four points during the pulse cycle, alongside the ensemble average.

The 2D case clearly shows the presence of distinct circulating regions between the plates, which are characterised by a range of velocity magnitudes. While these features are represented in the 3D case, the range of velocity magnitudes is much smaller and is due to the representation of a 3D domain via a 2D slice, however these features are clearly shown by the mean flow field.

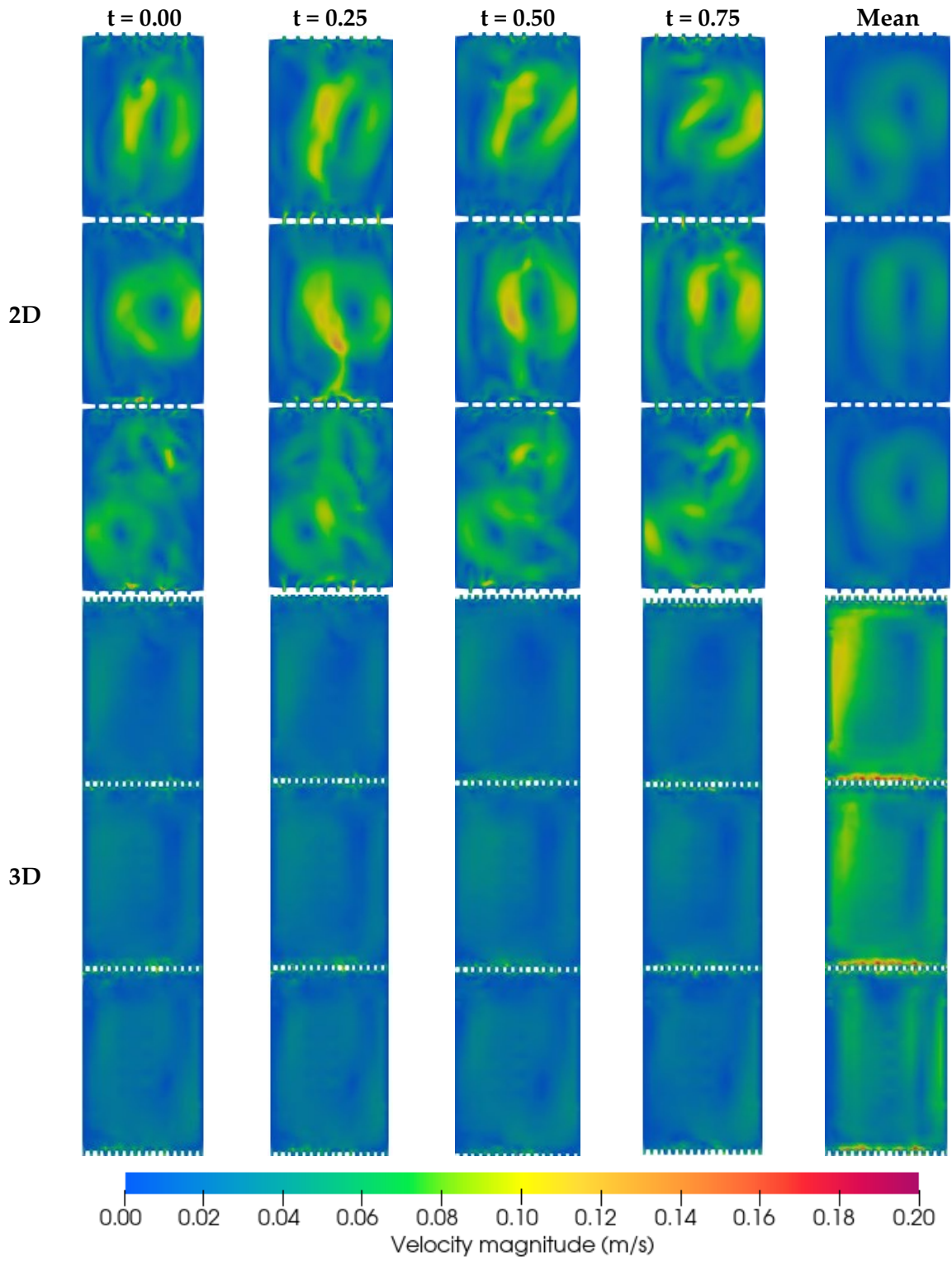


**Figure 44:** Instantaneous and mean velocity magnitude plots for the 2D and 3D cases.

### 5.3.1. Droplet size

The 3D and 2D cases were operated for 100 seconds to allow the column to achieve pseudo-steady-state operation and run for an additional 100 seconds to generate ensemble-averaged results. The time-averaged droplet size distributions and mean values (denoted in red) for each stage, both from LES and URANS simulations, have been measured and are presented in Figure 45. The values for the time-averaged mean and standard deviations, grouped by stage for experimental, LES and URANS, are presented in Table 13, with values for standard deviation enclosed in brackets. The RMSE for LES and URANS for the  $d_{3,2}$  and standard deviation are also provided.

**Table 13:**  $d_{3,2}$  and standard deviation, enclosed in brackets, for experimental, LES and URANS.

|         | Experimental (mm) | LES (mm)    | URANS (mm)  |
|---------|-------------------|-------------|-------------|
| Stage 3 | 4.53 (1.66)       | 5.61 (1.20) | 4.25 (2.11) |
| Stage 2 | 5.07 (1.72)       | 5.14 (1.20) | 3.63 (1.76) |
| Stage 1 | 4.44 (1.61)       | 4.24 (1.45) | 3.05 (1.60) |
| Column  | 4.68 (1.66)       | 4.99 (1.28) | 3.64 (1.82) |
| RMSE    | n/a               | 0.63 (0.41) | 1.17 (0.26) |

The RMSE for the LES predicted mean droplet size and standard deviation was calculated to be 0.63 mm and 0.41 mm, while the URANS predicted mean droplet size and standard deviation were calculated to be 1.17 mm and 0.26 mm. Figure 46 highlights that while the mean droplet size and DSD are reasonably approximated using LES, these values are under predicted using URANS. It is important to note that while the CFD-predicted droplet diameter in all areas of the column stage are considered when calculating the droplet size and distribution, experimentally measured droplets are more likely to be in the near field as those in the far field are more likely to be obscured. Due to the inherently chaotic movement of droplets, a large number of measurements were taken over an extended time frame to minimise this effect and ensure that a more representative sample of droplets were measured.

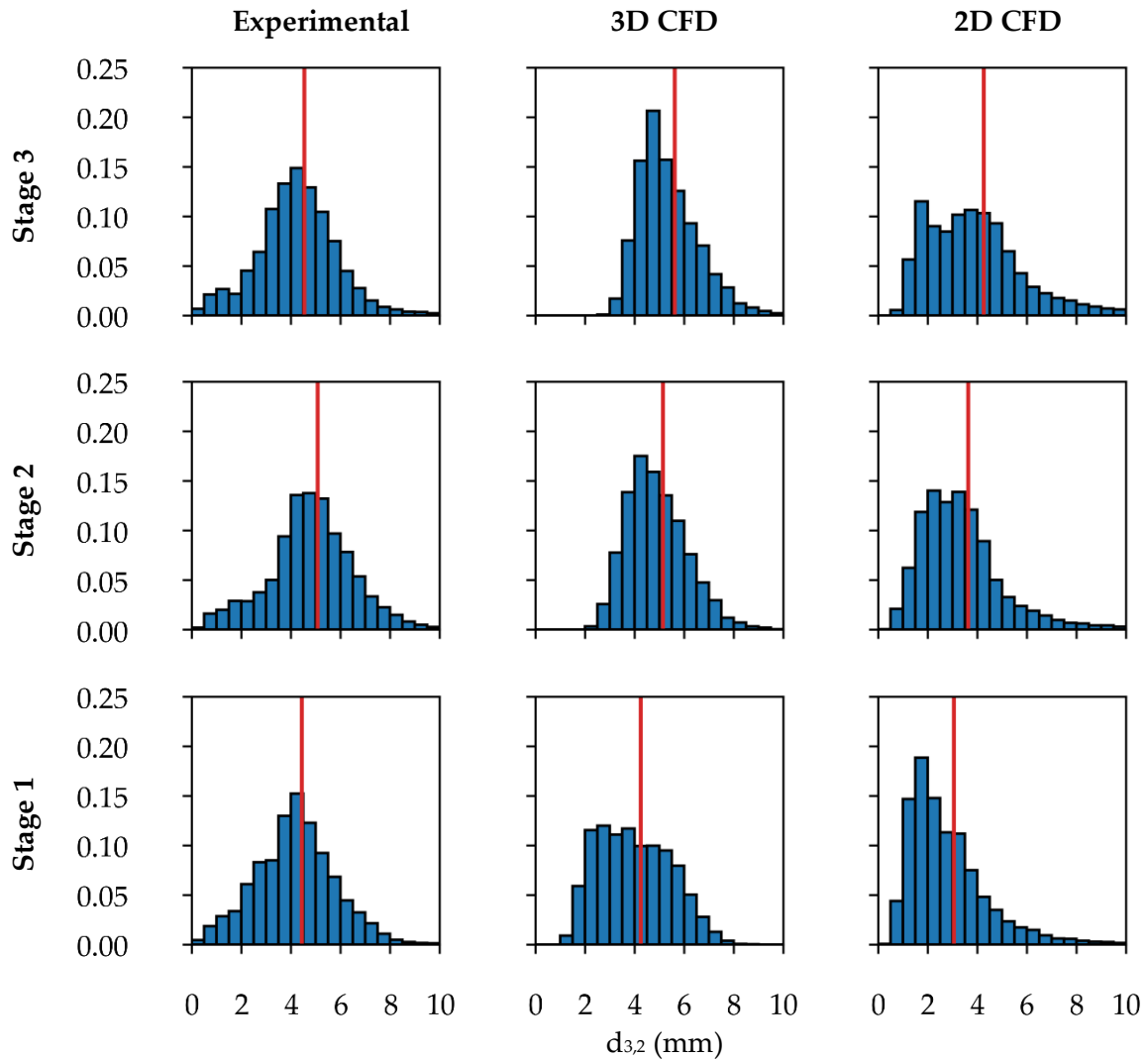


**Figure 45:** Time-averaged DSD for experimental (left), LES (middle) and URANS (right). Mean values are denoted in red.

Modelling droplet diameter is complicated due to the highly non-linear underpinning equations. Equation 5.27 is a function of dispersed phase holdup and droplet number density. In the case of dispersed phase holdup, this is calculated using equation 5.6, a function of the drag coefficient, which is dependent on the droplet diameter. Similarly, droplet number density is a function of the source term  $S$ , which is determined by modelling breakage and coalescence via equations 5.30 and 5.31, which also depend on the calculated droplet diameter.

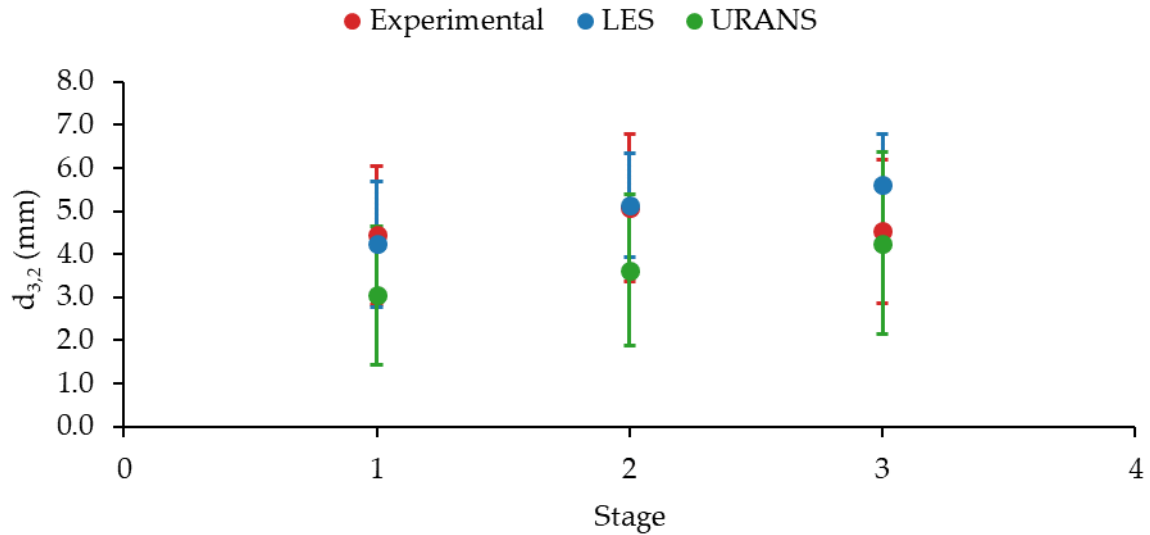


**Figure 46:**  $d_{3,2}$  plotted for stage number with error bars corresponding to the standard deviation.

Droplet breakage and coalescence are modelled using empirical correlations developed by Martinez-Bazan (1999) and Prince and Blanch (1990) which are both a function of the fluid properties, turbulence kinetic energy dissipation rate,  $\epsilon$ , and several constants which are fitted to experimental data. These have been previously used in other LLE applications (Wardle, 2013; Theobald, 2020; De Santis, Hanson, et al., 2021; Fells et al., 2022), however there are many other alternatives available which have been implemented in conventional interface averaging CFD simulations of PSECs and may be more suitable (Alzyod et al., 2017; Alzyod et al., 2018; Sen et al., 2019; Sen et al., 2021). Since there was a lack of experimental data, a simplified approach was used to approximate the mean droplet diameter where the magnitude of breakage and coalescence was scaled. As a result, it is not expected that these correlations be applicable over a wider range of PSEC operating conditions, but it is expected that for these conditions, the hydrodynamics are reasonably approximated allowing further investigation.

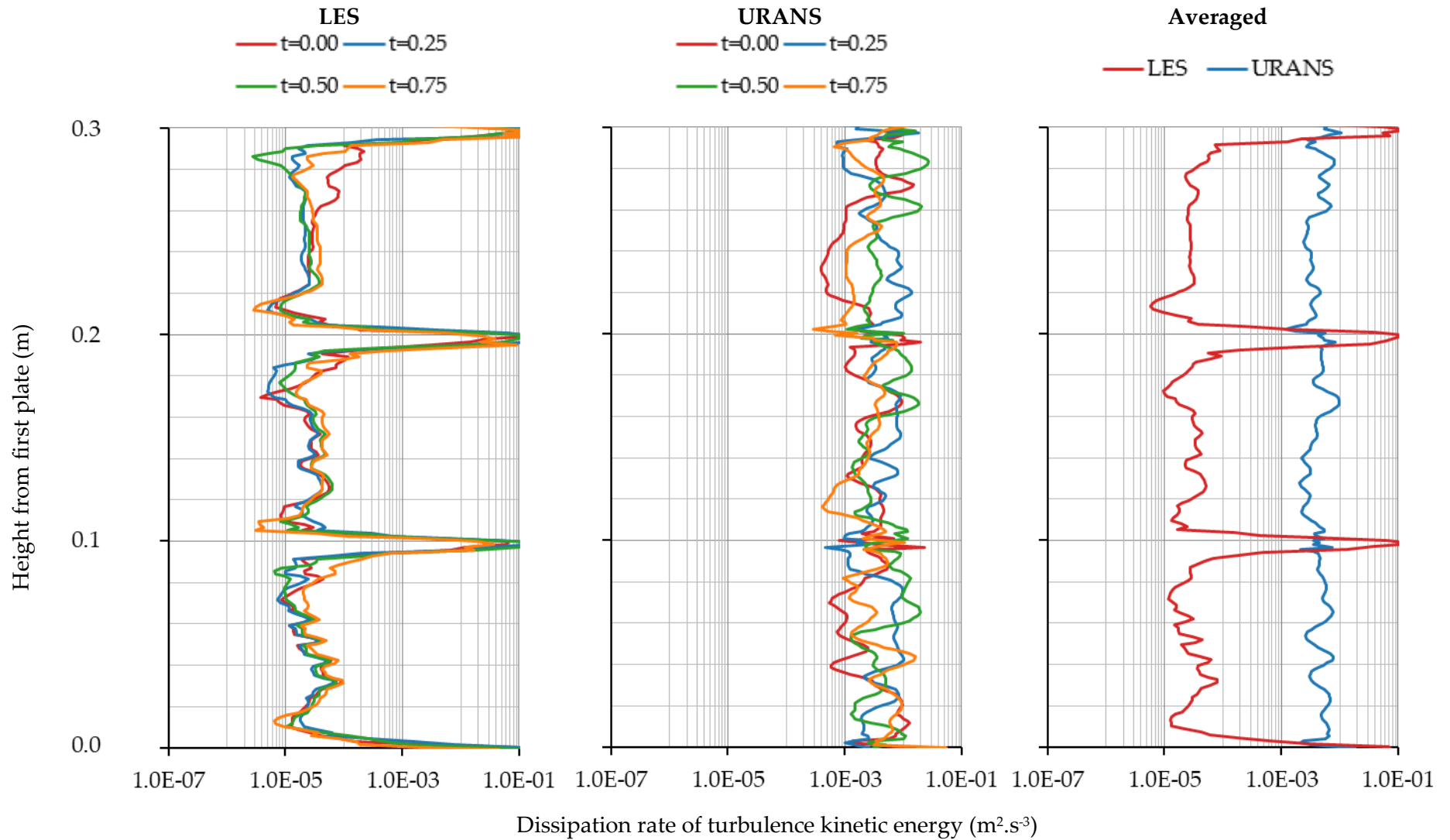


**Figure 47:** LES (left), URANS (middle) and averaged values (right) for turbulent kinetic energy dissipation rate.

The turbulent kinetic energy along the centre line of the PSEC for both URANS and LES simulations is presented in Figure 47. The results show that, while the values for each of the four points during the pulse are similar for both cases, the averaged value of the turbulence kinetic energy dissipation rate is around two orders of magnitude smaller when modelled using URANS as opposed to LES. This agrees with previous investigations performed using the same turbulence models in a 3D case, which found the value similarly under-predicted (Theobald, 2020).

Analysis of  $\epsilon$  in the breakage and coalescence models, equations 5.30 and 5.31, for a given droplet diameter identifies that breakage is proportional to the cubed root of  $\epsilon$ , while coalescence is proportional to the cubed root of  $\epsilon$  multiplied by the exponent of the negative cubed root of epsilon. For larger epsilon values, similar to those modelled using URANS, the value of the second term decreases, resulting in an increase in the breakage relative to the coalescence rate, producing smaller droplets.

As the experimental values for turbulence kinetic energy dissipation rate in the system are unknown, future investigations should aim to determine the rate of breakage and coalescence of the chemical systems studied at known levels of turbulent kinetic energy dissipation rates. This could be done with a stirred cell and the results used to identify appropriate values for the coefficients in the breakage and coalescence models which can then be used with CFD to predict PSEC performance over other operating conditions. Without reliable experimental data for turbulence kinetic energy dissipation, future investigations are limited to scaling the magnitude of breakage and coalescence to achieve a representative droplet size distribution regardless of the method used. However, by using an experimentally fitted droplet model, it can also be possible to perform a top-down investigation to identify which turbulence modelling approach is more appropriate for applications such as in PSECs or other LLE systems.

Both modelling approaches presented in this report have their drawbacks; the k-epsilon model is unable to accurately handle rotational, impinging and buoyancy-driven flows, which are critical components of PSEC hydrodynamics (Theobald, 2020), while SGS turbulence modelling in LES is linked to the selection of an appropriate value for the Smagorinsky coefficient, although this could be improved using more dynamic (Germano et al., 1991) or

Lagrangian approaches (Meneveau et al., 1996), at the expense of increased complexity of the model.

### 5.3.2. Droplet rise velocity

The values for the time-averaged droplet rise velocity, grouped by stage for experimental, LES and URANS, along with calculated RMSE are presented in Table 14.

**Table 14:** Droplet rise velocity for experimental, LES and URANS.

|         | Experimental (mm.s <sup>-1</sup> ) | LES (mm.s <sup>-1</sup> ) | URANS (mm.s <sup>-1</sup> ) |
|---------|------------------------------------|---------------------------|-----------------------------|
| Stage 3 | 100                                | 103                       | 112                         |
| Stage 2 | 106                                | 114                       | 97.8                        |
| Stage 1 | 128                                | 121                       | 91.1                        |
| Column  | 111                                | 113                       | 100                         |
| RMSE    | n/a                                | 6.70                      | 23.0                        |

A graphical representation of the rise velocity is presented in Figure 48. The results show a general agreement between the experimental and LES values for the rise velocity. However, the URANS values were under predicted. This can be attributed to underestimating the droplet size, which reduces the buoyancy force, further highlighting the importance of accurately modelling droplet size.

Aside from droplet diameter, the parameters affecting droplet rise velocity are the interphase momentum transfer modelling and the continuous phase velocity. The Schiller-Naumann drag model was used due to its use in previous investigations (Yadav and Patwardhan, 2009; Din et al., 2010; Alzyod et al., 2017; Theobald, 2020; Yi et al., 2020; Tu et al., 2021; De Santis, Hanson, et al., 2021; Fells et al., 2022), however initial studies found that droplet rise velocity was significantly over predicted. There are many different available drag models presented in the literature, most notably the Kumar and Hartland model (Sen et al., 2018; Sen et al., 2019), however no generalisable model exists and it is customary for model parameters to be adjusted to better fit experimental results. Therefore in this investigation, it was decided that the magnitude of the Schiller-Naumann calculated drag would instead be scaled by 1.5 to achieve results which can be said to be considered representative. One notable limitation of the chosen model is that it does not account for the effect of droplet swarms via the dispersed phase holdup, resulting in a slipstreaming effect reducing the drag experienced on a droplet.

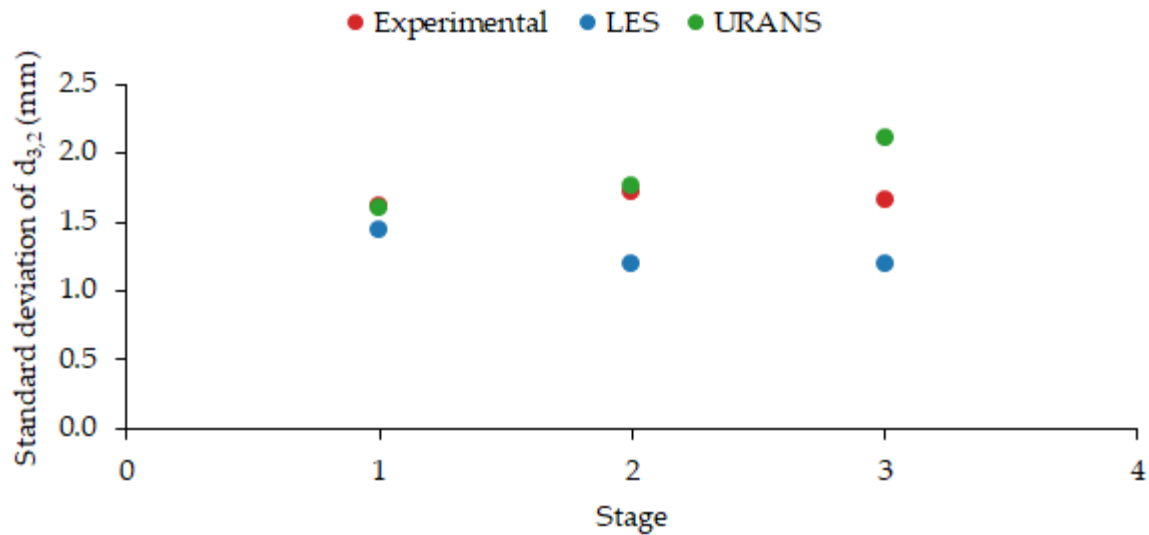


**Figure 48:** Stage and time-averaged droplet rise velocity.

It is recommended that future investigations aim to generate an experimental data set comprising the measurement of droplet size, rise velocity and dispersed phase holdup which can be used to identify a more suitable model.

### 5.3.3. Mass transfer

A simplified case using the above URANS approach has been prepared to demonstrate the local implementation of mass transfer within GEMMA, representing a large pulsed column and industrially relevant operational parameters (Garthe, 2006). The stage-averaged dispersed phase holdup and Sauter mean diameter along the column are compared with the experimental measurements in Figure 49 and Figure 50. A RMSE of error of 1.13 % for the dispersed phase holdup and 0.68 mm for the Sauter mean diameter was calculated.

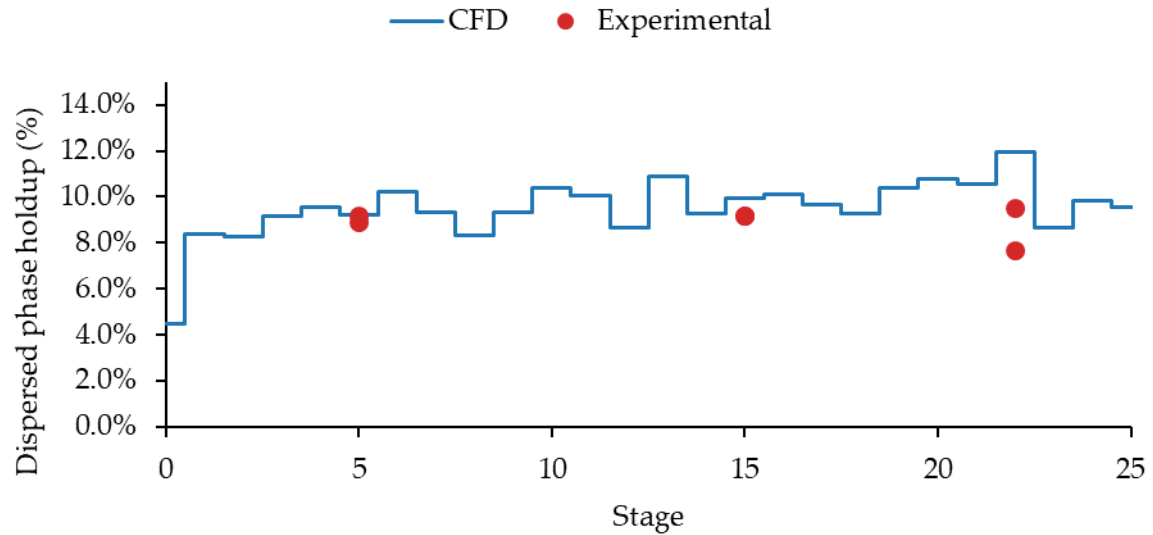


**Figure 49:** Axial dispersed phase holdup.

A degree of variability is observed in both the experimental and modelled results which is expected due to the dynamic flow conditions observed in a PSEC, with each pulse consisting of an initial jetting phase with droplet breakage followed by coalescence at the next plate. The CFD-predicted values reasonably agree with the experimental observations and, therefore, can be considered a good representation of the system's hydrodynamics. It is important to note that a different value has been used to scale the magnitude of drag than the previous experiments, emphasising the need for further investigation into the suitability of the models used. It is anticipated that simulating the entire column in 3D with an LES approach would help give a more accurate hydrodynamic field; however, this is not considered computationally feasible. Nevertheless, good agreement with available data was obtained using the URANS approach adopted.

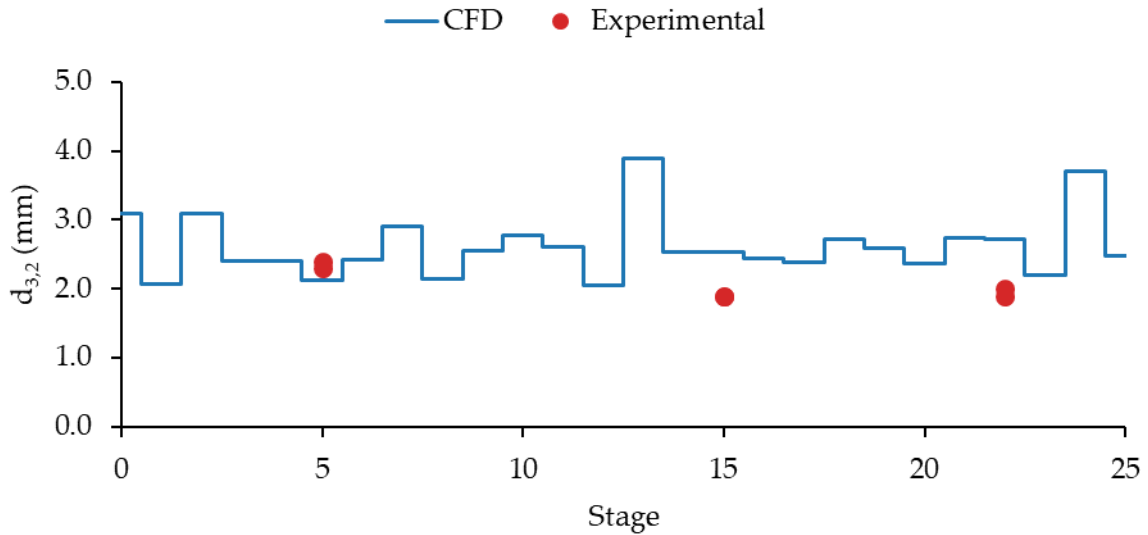


**Figure 50:** Axial Sauter mean droplet diameter.

The axial concentration of the aqueous and solvent phases in the column section was modelled with good results obtained over the entire column length. The RMSE for the aqueous and solvent phases were calculated to be 0.0863 and 0.0352 mol.L<sup>-1</sup>, giving an overall error of 0.0659 mol.L<sup>-1</sup>. The model accurately predicts the dispersed phase solute concentration along the length of the column, however, the aqueous phase solute concentration is less representative with an under prediction of mass transfer in the upper section and a slight over prediction in the region of the aqueous phase outlet.

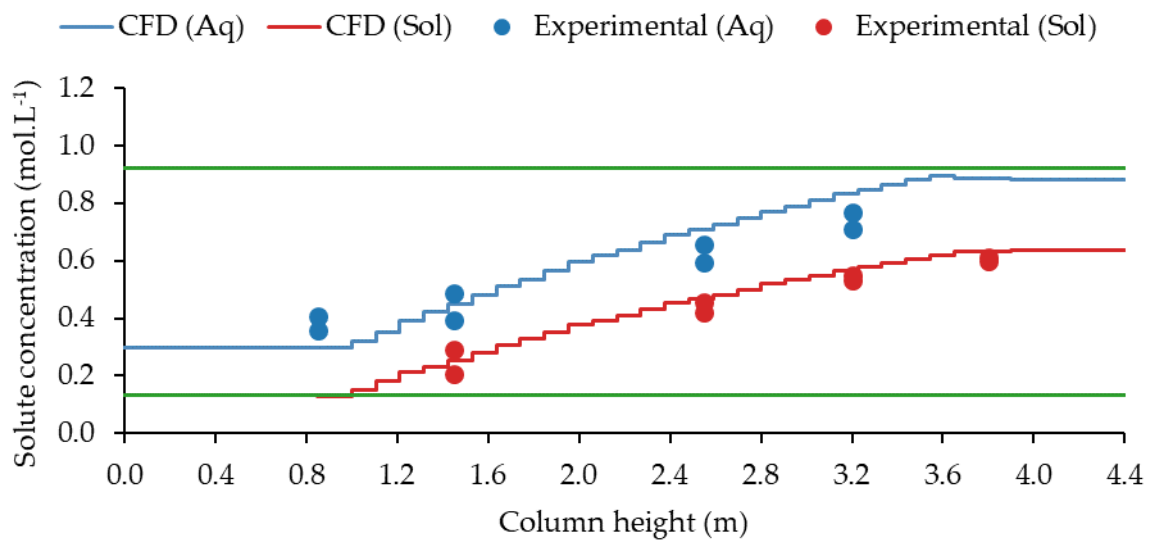


**Figure 51:** Axial solute concentration.

Although the model indicates good predictive capability when using CFD to model mass transfer, this simulation was exceptionally computationally expensive and required 3 months to complete when running on 80 cores, totalling to 20 core years. This is due to the short time steps required to describe column hydrodynamics and the long time scales associated with mass transfer, making it not currently practical to perform CFD mass transfer investigations in large-scale columns. The simulation was performed using a relatively small computational domain and URANS for turbulence modelling, and at present, it is not currently computationally feasible to perform 3D CFD simulations to model mass transfer behaviour.

#### **5.4. Summary**

CFD simulations of a PSEC have been carried out using the GEMMA approach and compared to experimental data. Results showed that 3D LES reasonably agreed with experimental results for stagewise droplet size distribution, mean diameters and rise velocities, while a 2D URANS approach slightly under-predicted droplet diameters and rise velocity. This difference can be attributed to the predicted turbulence kinetic energy dissipation and the under-prediction in droplet diameter resulting in a lower buoyancy force acting on the droplets. However, reasonable agreement with experimental values can be achieved for the underpinning models for droplet breakage, coalescence and drag with the inclusion of an appropriate scaling factor, although further modification is needed for their general application to PSECs.

A local mass transfer formulation was implemented within GEMMA and a 2D URANS case, which reasonably approximated mean droplet size, dispersed phase holdup and axial solute concentrations. However, this approach was very computationally expensive and without increased availability of computational resources, it is not feasible to utilise in a 3D LES case. Nevertheless, it is a useful predictive tool that can provide detailed information that is not accessible through experiments or other modelling approaches.

Due to uncertainty in the underpinning models for droplet breakage, coalescence and drag, current formulations are limited in their applicability to other operational conditions. Therefore, it is recommended that experimental investigations be done to identify an

appropriate formulation from the published literature or develop new correlations. For droplet breakage and coalescence, droplet size is recommended to be characterised as a function of turbulence kinetic energy dissipation and this data used to fit the coefficients in the breakage and coalescence models. For droplet drag, droplet rise velocity is recommended to be characterised as a function of droplet size and dispersed phase holdup.

Due to the difficulty of measuring turbulence experimentally and the large computational overhead associated with Direct Numerical Simulation (DNS), validating turbulence models via a bottom-up approach has proven to be difficult and no such investigations have been published to date. Similarly, attempting a top-down approach to validation is also difficult, given the complex and interrelated equations for breakage, coalescence, interphase momentum transfer and turbulence, which must be validated first. Therefore, due to current limitations in experimental fluid dynamics, it is recommended that future investigations focus on a top-down approach to the validation.

Despite its limitations, CFD is still highly useful in modelling PSECs. Due to the large time scales required to model mass transfer, it is recommended that CFD be used to perform hydrodynamic assessments of PSEC performance, such as identification of the operational envelope or design optimisation. Using a LES approach, it would be possible to perform a CFD-based design optimisation, where parameters such as the surface area to volume ratio are used as an alternative to mass transfer, allowing for the assessment of new column internals which is not currently achievable with existing empirical correlations. Alternatively, a reduced order 2D approach could be used to identify the column operational envelope, perform sensitivity analysis of operational parameters or inform the development of reduced order models for mass transfer modelling.

## 6. COMPARTMENT MODELLING OF PULSED SIEVE-PLATE EXTRACTION COLUMNS

This chapter presents a novel approach to predict the performance of PSECs by using Compartment Models. CFD simulations were used to predict dispersed phase holdup and  $d_{3,2}$  and using a simplified steady-state model the axial solute concentrations were predicted for the absorption of acetone from water by toluene with good agreement with experimental results, however this model is limited in its application due to the manual fitting of the backflow ratio. CFD was used to predict the aqueous and organic phase RTD which were used to inform the creation of the CM with good agreement between the two simulations. The absorption of acetone from water to toluene was implemented within the CM, which was validated against 17 experiments, with good agreement with the experimental values. This proposed modelling method provides an accurate predictive tool for PSECs, providing an alternative to traditional empirical correlations or pilot-plant studies.

### 6.1. Introduction

Although CFD is useful for predicting the hydrodynamic and mass transfer performance of PSECs, its application is best suited for hydrodynamic assessment since high-fidelity simulations require large, highly resolved geometries and long simulation times. Reduced order approaches such as Compartment Modelling, can be used to model mass transfer processes. This novel approach which has not been applied to PSECs, involves creating a network of connected sub-volumes that are assumed to be phenomenologically similar and well mixed. This makes it possible to represent a PSEC using several hundred compartments as opposed to several hundred thousand cells required for CFD. This significantly reduces the number of calculations required to complete a single iteration, which makes it possible to include longer term time-varying phenomena such as mass transfer despite simulations taking significantly less time to run.

In this chapter, CFD will be used to perform a hydrodynamic simulation of a PSEC to predict axial droplet diameter and dispersed phase holdup. This information will then be used in a simplified steady-state compartment model to estimate axial solute concentrations for the absorption of acetone from water by toluene. The same CFD model will then be used to

conduct a RTD study to evaluate the transient evolution of a tracer throughout the aqueous and organic phases. This information will be used to inform the development of a CM to ensure that the hydrodynamics are reasonably approximated. Finally, mass transfer will be incorporated into the CM, and the model-predicted axial solute concentrations will be validated over various operating conditions.

## 6.2. Methodology

### 6.2.1. Experimental

This investigation used experimental data presented by Garthe (2006). The experimental dataset consists of 17 experiments with an overview of the range of operational conditions and performance parameters given in Table 15. Details of the column geometry are presented in Table 4, and fluid properties are shown in Table 11.

**Table 15:** Overview of operational and performance parameters (Garthe, 2006)

| Parameter  | Value       |
|--|-------------|
| Aqueous flow rate (L.hr <sup>-1</sup> )                  | 40-93       |
| Solvent flow rate (L.hr <sup>-1</sup> )                  | 48-112      |
| Total flow rate (L.hr <sup>-1</sup> )                    | 88-205      |
| Pulse velocity (cm.s <sup>-1</sup> )                     | 1-2         |
| Dispersed phase holdup (%)                               | 7.2-36      |
| Sauter mean droplet diameter (mm)                        | 1.8-2.6     |
| Aqueous feed solute concentration (mol.L <sup>-1</sup> ) | 0.885-1.02  |
| Solvent feed solute concentration (mol.L <sup>-1</sup> ) | 0.505-0.716 |

### 6.2.2. Steady-state compartment model

A simplified steady-state model of the PSEC was prepared, which assumes each stage is approximated as a single CSTR, with the heavy and light phases operated in counter-current flow (Garthe, 2006; Attarakih et al., 2012). Pulsation of the heavy phase was accounted for via a backflow ratio representing the degree of recirculation between adjacent compartments. This allows the development of a system of one-dimensional differential equations which can

characterise the axial solute concentration of both phases. The model requires the molar flow rates and solute concentration for both phases at the inlet as input parameters.

Figure 52 presents a block flow diagram showing the schematic representation of the compartments and the continuous and dispersed phase flows within the PSEC.  $Q$  represents volumetric flowrate in  $\text{mol}\cdot\text{s}^{-1}$ ,  $C$  represents solute concentration,  $n$  represents the stage number,  $N$  represents the upper stage and subscripts  $c$  and  $d$  denote the phase. As above, axial solute concentrations for the aqueous and organic phases were calculated based on the assumption that each stage of the PSEC is equivalent to a CSTR. Pulsation of the continuous phase was accounted for via the backflow ratio  $\beta$ .

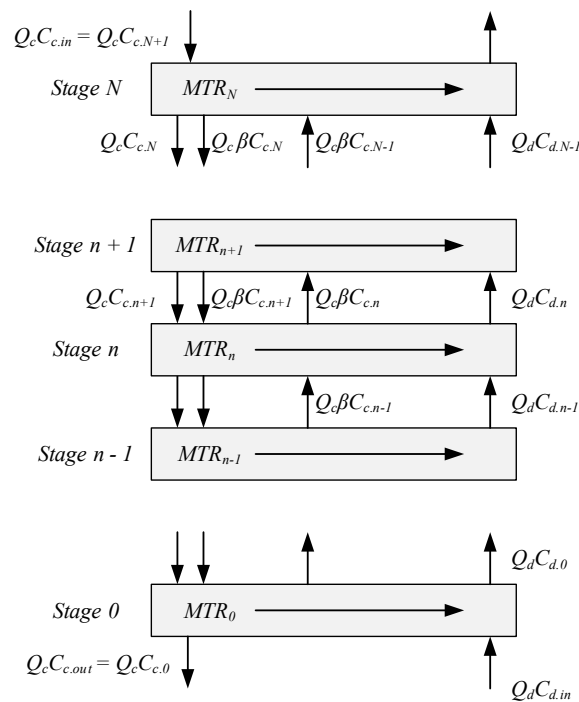


**Figure 52:** Counter-current extraction model block flow diagram.

Three equations were used to give the continuous phase mass balance. For the aqueous phase inlet, where  $n = N$ , equation 6.1 was used. For all stages between the aqueous phase inlet and the organic phase inlet, where  $0 < n < N$ , equation 6.2 was used. For the organic phase inlet, equation 6.3 was used:

$$Q_c C_{c,in} + Q_c \beta C_{c,N-1} = Q_c C_{c,N} + Q_c \beta C_{c,N} + V_N MTR_N \quad (6.1)$$

$$Q_c C_{c,n+1} + Q_c \beta C_{c,n+1} + Q_c \beta C_{c,n-1} = Q_c C_{c,n} + Q_c \beta C_{c,n} + Q_c \beta C_{c,n} + V_n MTR_n \quad (6.2)$$

$$Q_c C_{c,1} + Q_c \beta C_{c,1} = Q_c C_{c,0} + Q_c \beta C_{c,0} + V_n MTR_0 \quad (6.3)$$

The following equations, 6.4 6.5 and 6.6 then give the dispersed phase mass balance for the organic phase inlet, stages  $0 < n < N$  and the aqueous phase inlet:

$$Q_d C_{d,n} = Q_d C_{d,in} + V_n MTR_n \quad (6.4)$$

$$Q_d C_{d,n} = Q_d C_{d,n-1} + V_n MTR_n \quad (6.5)$$

$$Q_d C_{d,out} = Q_d C_{d,n-1} + V_n MTR_n \quad (6.6)$$

The mass transfer rate is calculated using equations 2.21, 2.23 and 2.27. Equations 6.1 to 6.6 were solved iteratively until the axial solute concentrations were invariant with subsequent iterations.

### 6.2.3. Residence time distribution

A CFD simulation was performed using the geometry and boundary conditions detailed in chapter 5, with the solution of the mass transfer equations disabled so that only the column hydrodynamics were modelled. To investigate the residence time distribution, first, the simulation was run for 100 seconds to achieve pseudo-steady-state operation and then run for an additional 100 seconds to collect time-averaged statistics for the dispersed phase holdup and  $d_{3,2}$ .

A residence time distribution experiment was performed, where for 1 ms, a passive scalar was injected into both the heavy and light phase inlets. Transport of the scalar throughout the domain was solved using the following transport equation:

$$\frac{\delta(\alpha_x S_x)}{\delta t} + \nabla \cdot (\alpha_x U_x S_x) - \nabla^2 (\alpha_x D_x S_x) = 0 \quad (6.7)$$

### 6.2.4. Transient compartment modelling

A transient model of the PSEC was developed using a compartment modelling approach using CompArt (Jervis, 2022). Spatial zones within the PSEC are designated as compartments with a defined volume, a single phase and a species composition assumed to be homogeneous.

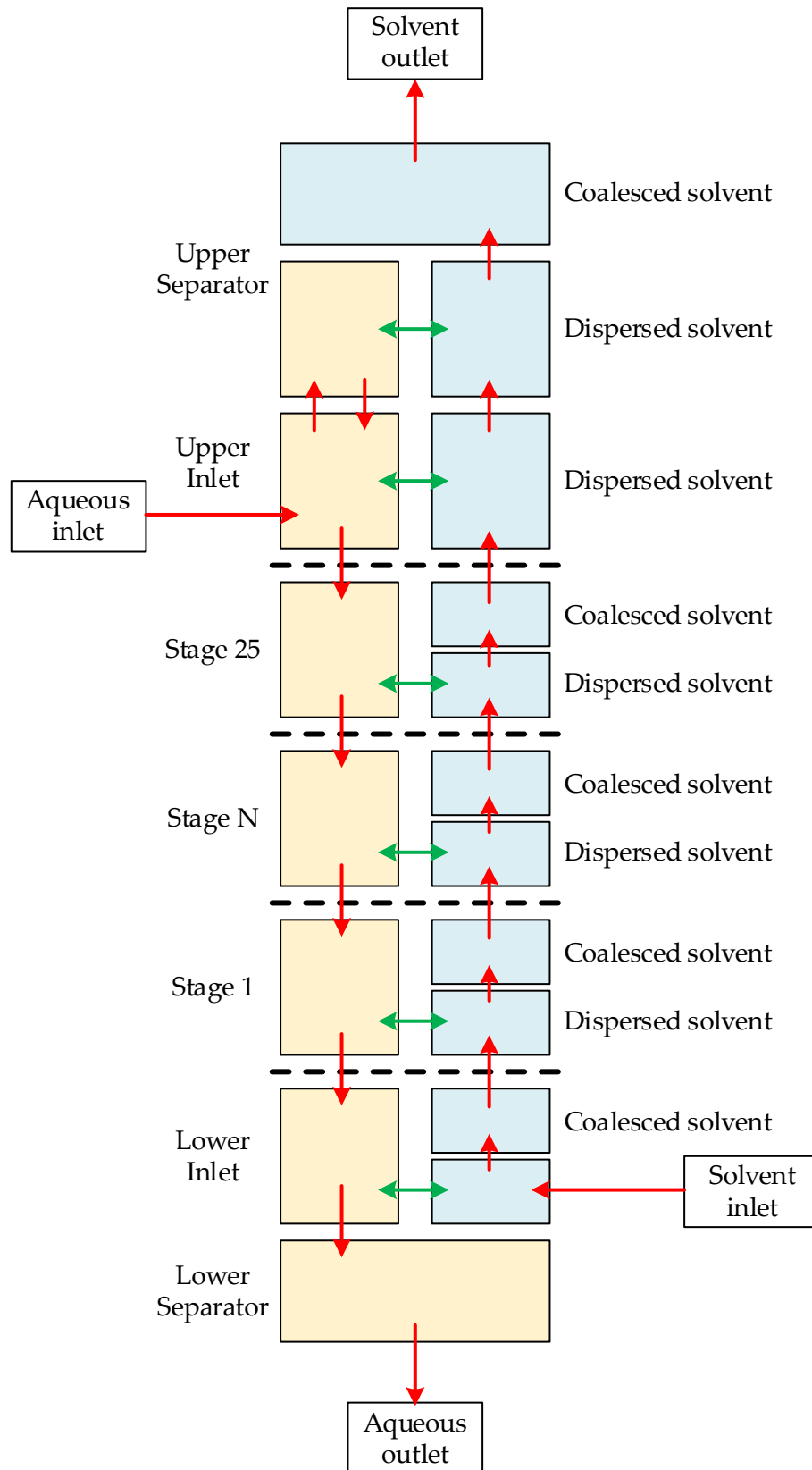


**Figure 53:** Compartmentalisation strategy for a PSEC. Yellow boxes represent the aqueous phase, blue boxes represent solvent phase. Red arrows represent fluid transport and green arrows represent mass transfer.

Due to the long timeframes required to evaluate a transient simulation, the pulsation was not accounted for in the model. For a given time step, the volume is calculated using the following equation, where  $j$  denotes the phase and the  $k$  denotes the compartment:

$$V_{j,k} = \frac{M_{j,k}}{\rho_{j,k}} \quad (6.8)$$

And the total mass of a phase is calculated using the following equation, where  $i$  denotes the species:

$$M_{j,k} = \sum_i n_{i,j,k} M w_i \quad (6.9)$$

Intercompartment flows are specified by specifying the source and termination compartments and the volumetric flow rates, with the composition calculated from the species concentrations within the source compartment. Mass transfer between compartments is defined by specifying the source and termination compartments and the flux is calculated using two-film theory using equations 2.21, 2.23 and 2.27. A representation of the model is presented in Figure 53. For a detailed overview of the software, see Jervis (2022).

## 6.3. Results and discussion

### 6.3.1. Steady-state model

A steady state simulation was prepared for a heavy phase flow rate of 40 L.hr<sup>-1</sup> with a solute concentration of 0.922 mol.L<sup>-1</sup>, a light phase flow rate of 48 L.hr<sup>-1</sup> with a solute concentration of 0.131 mol.L<sup>-1</sup>, a pulse amplitude of 8 mm and a pulse frequency of 1.25 Hz. To account for pulsation, a backflow ratio of 12 was used. The stage-averaged dispersed phase holdup and Sauter mean diameter along the column are compared with the experimental measurements in Figure 54 and Figure 55. A RMSE of error of 1.26 % for the dispersed phase holdup and 0.57 mm for the Sauter mean diameter was calculated, indicating a reasonable approximation of the column hydrodynamics.

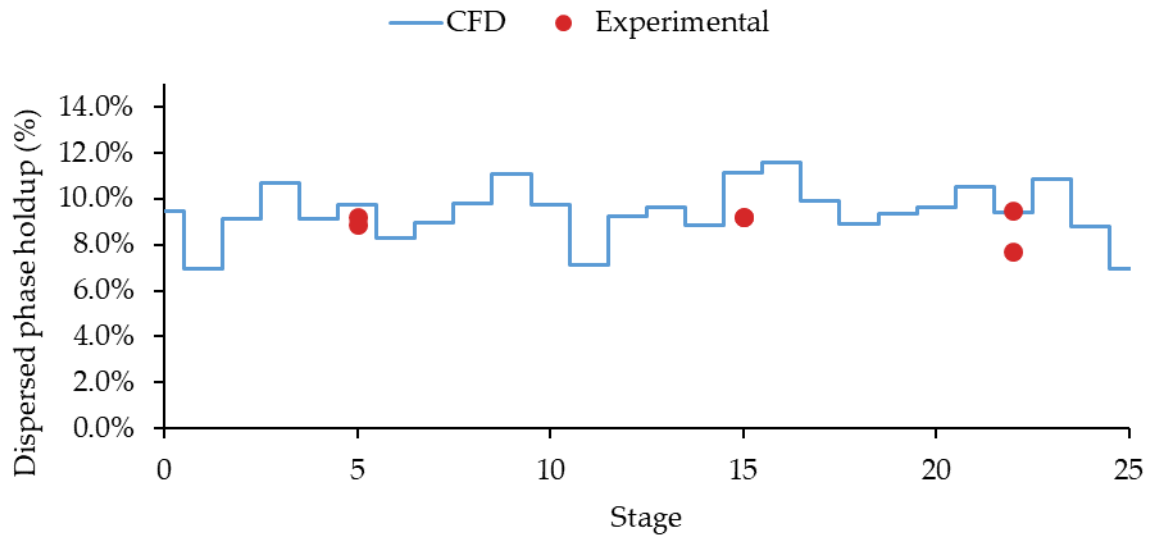


**Figure 54:** Experimental and modelled axial dispersed phase holdup.

The axial concentration of the both phases in the column section was modelled and is shown in Figure 56. The overall RMSE of  $0.0710 \text{ mol.L}^{-1}$  indicates good agreement with results obtained over the entire column length. A good fit is observed with the aqueous phase solute concentration with a RMSE of  $0.0485 \text{ mol.L}^{-1}$ . A slight over prediction of dispersed phase solute concentration is observed, most notably in the lower section of the column, while the general trend in the upper section is consistent with the experimental results. Despite this, the RMSE is calculated to be  $0.0879 \text{ mol.L}^{-1}$ , generally indicating good agreement.

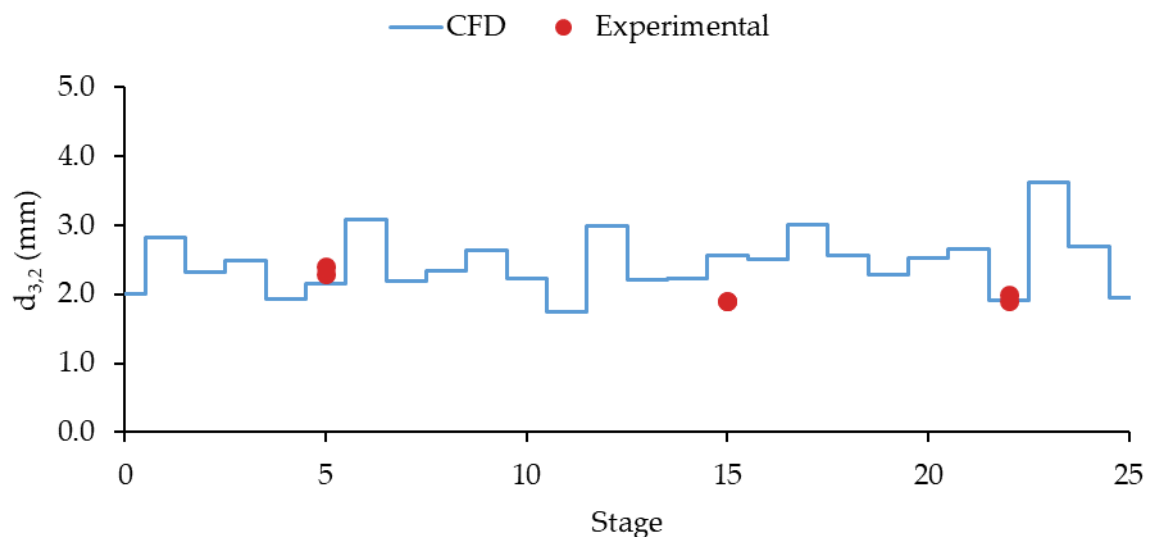


**Figure 55:** Experimental and modelled Sauter mean droplet diameter.

Although there is generally good agreement between the predicted axial solute concentrations, it is important to note that this is primarily due to fitting the backflow ratio, which reduces the concentration gradient and, thus, the mass transfer rate. Consequently, this method is limited in its application and cannot be used to model other columns without further parameterisation using an extensive dataset. Therefore, a modelling approach is recommended to be adopted that considers mass transfer in the upper separator and further compartmentalisation of the PSEC stage, with the near-plates and inter-plate regions modelled separately and the volumes associated with each accounted for. This would allow for a more realistic representation of the column's hydrodynamics.

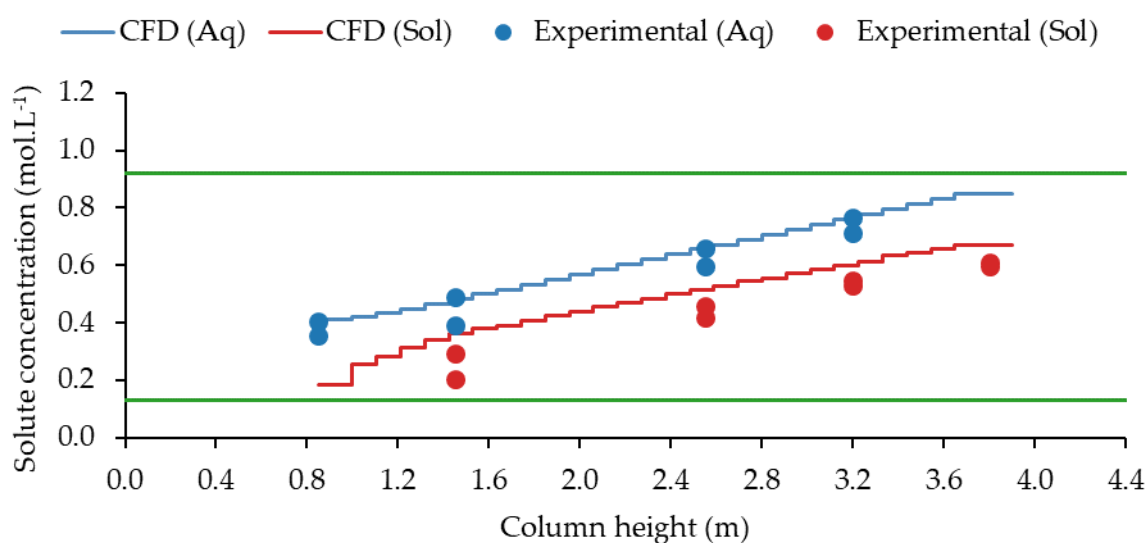


**Figure 56:** Experimental and modelled profiles of PSEC solute concentration in the organic and aqueous phase.

### 6.3.2. Transient hydrodynamic model

To better understand PSEC hydrodynamics, a residence time distribution experiment was conducted using the CFD simulation from the previous section. The experiment involved injecting a tracer into the heavy and light phase inlets over 1 ms and running it for 4000 seconds. Due to the large number of iterations required, the simulation took approximately 3 months to complete running on 80 cores, totalling around 20 core-years of simulation time.

The results of the CFD predicted number of moles of tracer in the aqueous phase in the separators, inlets and column stages are presented in Figure 57 and Figure 58.

Figure 57 shows the initial transient associated with the tracer injection into the upper inlet, characterized by an initial peak followed by a rapid decrease. After this, the number of moles of tracer in the adjacent upper separator and column section rises. The rate of increase in these sections is similar, indicating that the flow rates from the source compartment are similar. The presence of the long tail in the upper inlet can be attributed to the transport of the tracer from the upper separator, as indicated by the long tail in both compartments. The slow decrease in the tracer in the upper separator is due to the compartment being relatively large and well-mixed due to the upcoming droplets, reducing the tracer concentration. As a result, a long tail is observed in all downstream compartments. The large tracer residence time in the upper separator indicates that, providing sufficient time for droplet disengagement, the upper separator is oversized, resulting in the column being slow to respond to operational changes and taking longer to achieve pseudo-steady-state operation than necessary.

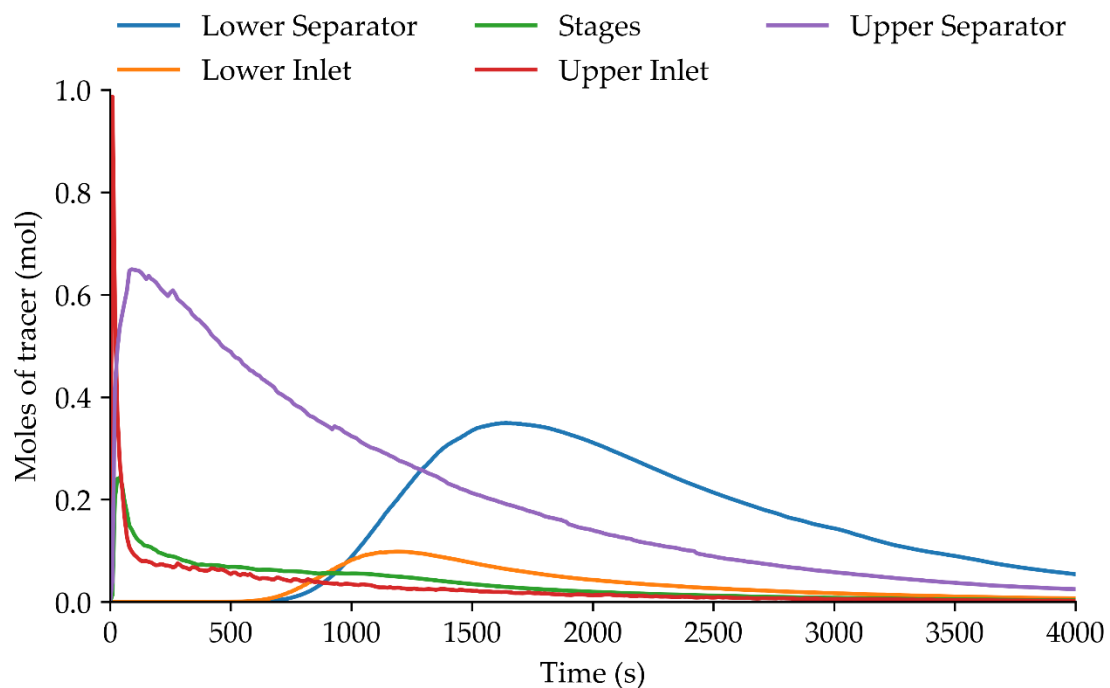


**Figure 57:** CFD predicted aqueous phase RTD curve for lower separator, lower inlet, all stages grouped, upper inlet and upper separator.

Figure 58 shows the evolution of the tracer along the length of the column, with curves becoming flatter and wider corresponding to increased axial dispersion. After exiting the column section, the tracer amount increases in the lower inlet, followed by a larger increase in the lower separator. All of these sections display large tails due to the recirculation of the tracer in the upper separator.

The results of the solvent phase CFD-predicted number of moles of tracer in the solvent for all sections of the column is shown in Figure 59. The initial transient associated with the tracer is shown along with the gradual progression along the column length with increasing axial dispersion.

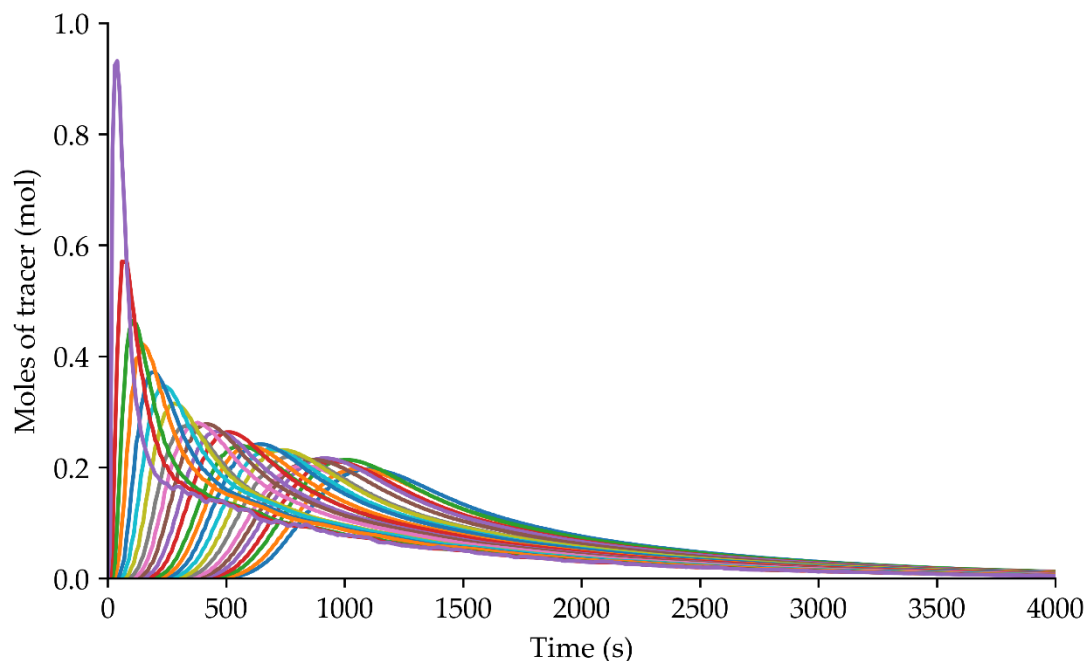
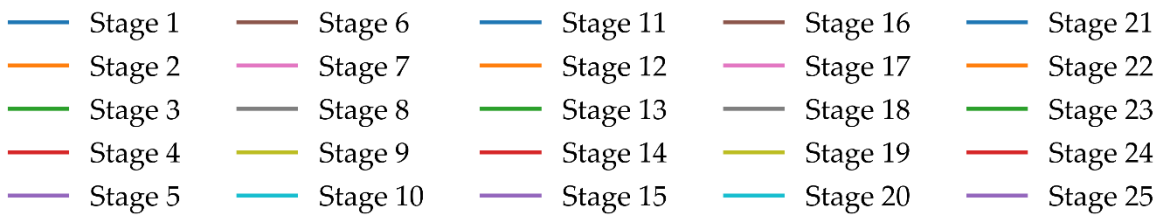


**Figure 58:** CFD predicted aqueous phase RTD curve for column stages.

Based on the results from above, a preliminary structure for a compartment model was developed, shown in Figure 53. The aqueous phase will consist of separate compartments for

the upper inlet, upper separator, all column sections, lower inlet and lower separators. The aqueous feed will enter the upper inlet, which will be connected to the upper separator via exchange flows of equal magnitude to the column throughput and the upper column section. The feed will flow through all column stages before entering the lower inlet and the lower separator. For both inlets and all stages, the compartment volumes will be based on the volume of the compartment minus the volume associated with the dispersed phase holdup. Due to their large sizes, some recirculating or stagnant regions are anticipated to exist in both separators and will be reduced accordingly.

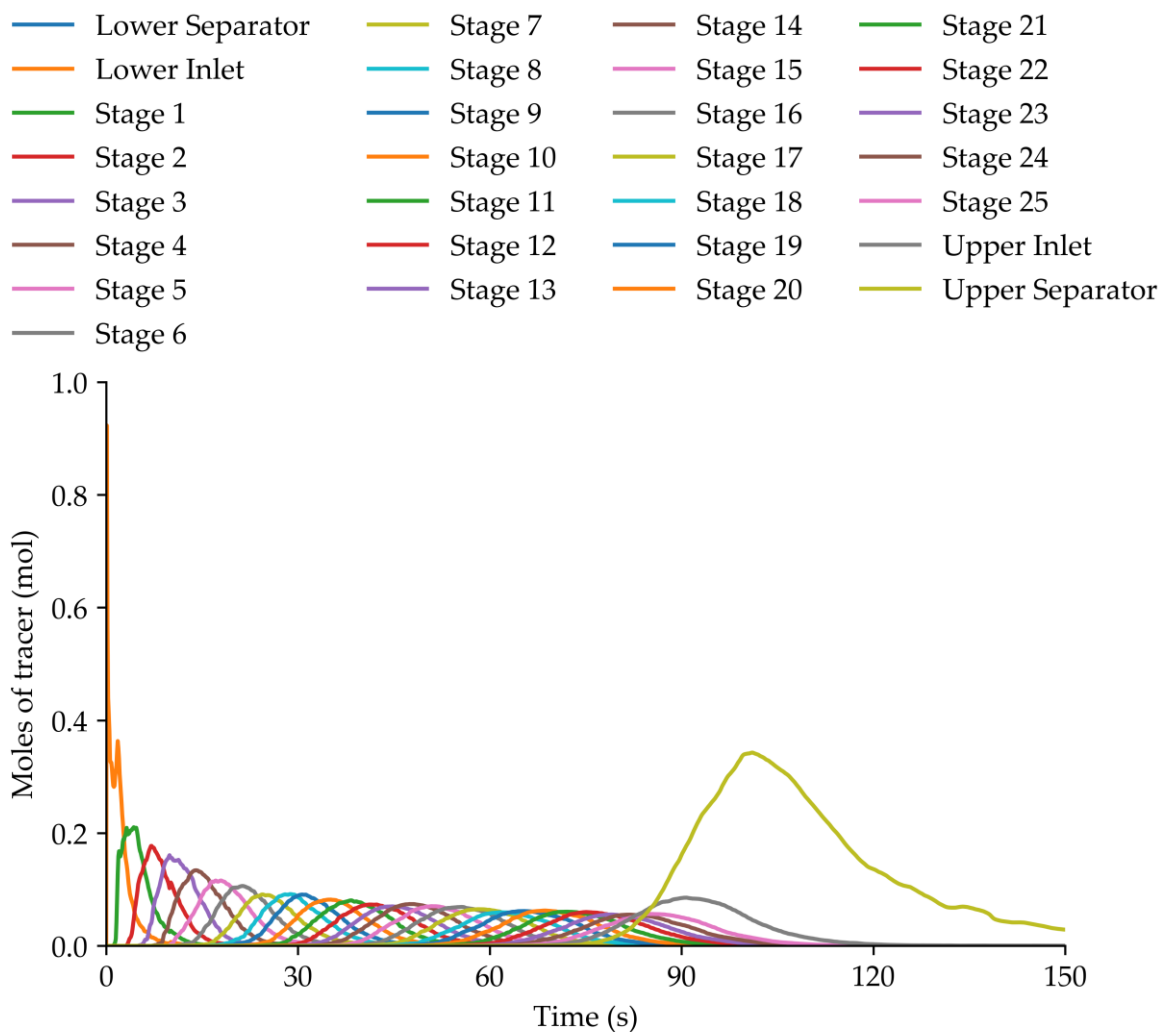


**Figure 59:** CFD predicted dispersed phase RTD curve for lower separator, lower inlet, all stages, upper inlet and upper separator.

For the solvent phase, the lower inlet and all column stages will be separated into two compartments, the first corresponding to the droplet dispersion and the second corresponding to the coalesced solvent below the plate. The upper inlet, dispersed solvent in the upper separator and coalesced solvent in the upper separator will also be designated into their own compartments. Inter-compartment flows will be based on the solvent feed flow rate, and the compartments will be connected linearly along the height of the column with no recirculation between them. The compartment volumes will be calculated from the volume of dispersed phase holdup in their respective zones, and due to its large size, it is anticipated that stagnant regions exist within the upper separator, so its volume will be reduced accordingly. Figure 53 shows a graphical representation of the Compartment Model structure.

The intercompartment mass transfer will be specified for all zones containing an aqueous continuum and dispersed solvent, specifically inlets, all column stages, and the upper separator's bottom half. Mass transfer between the aqueous continuum and the coalesced solvent below the plate is not considered due to the low surface area-to-volume ratio.

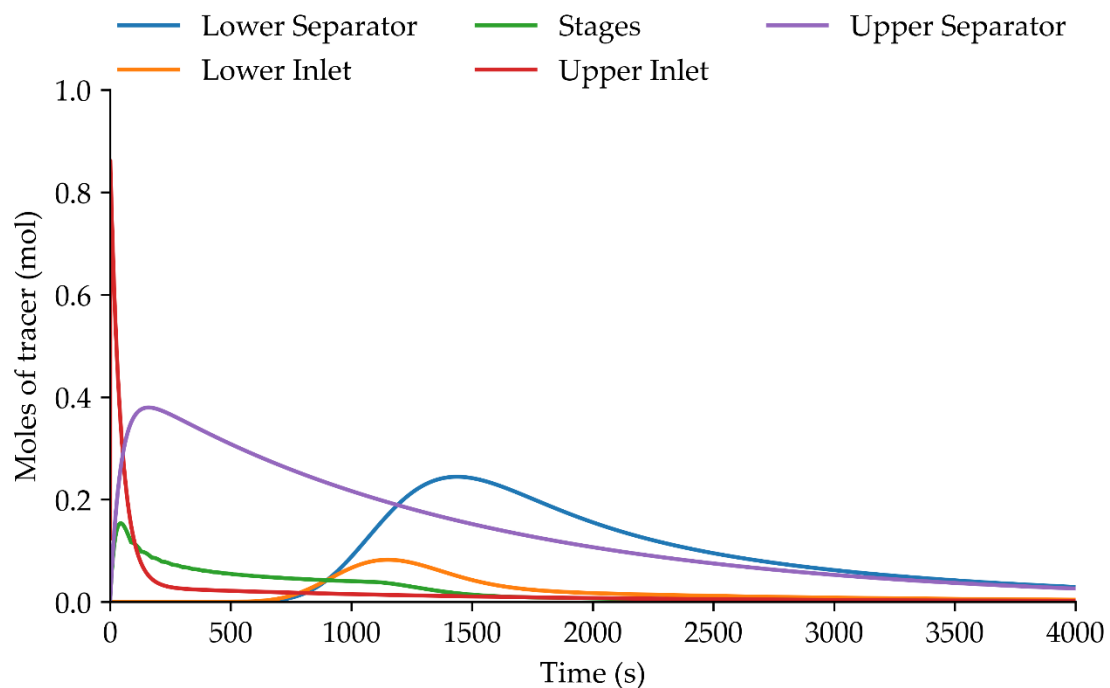


**Figure 60:** CM predicted aqueous phase RTD curve for lower separator, lower inlet, all stages grouped, upper inlet and upper separator.

A residence time distribution experiment was performed using the compartment model in both the aqueous and solvent phases. Due to the reduced complexity of the model compared to the CFD simulation, the simulation was completed in approximately 10 minutes running on a single core, indicating a speedup of roughly  $10^6$ .

The results of the aqueous phase RTD are presented in Figure 60 and Figure 61. Visual comparison with Figure 57 and Figure 58 shows that all the significant characteristics are represented, however, there are slight differences in the predicted curves.

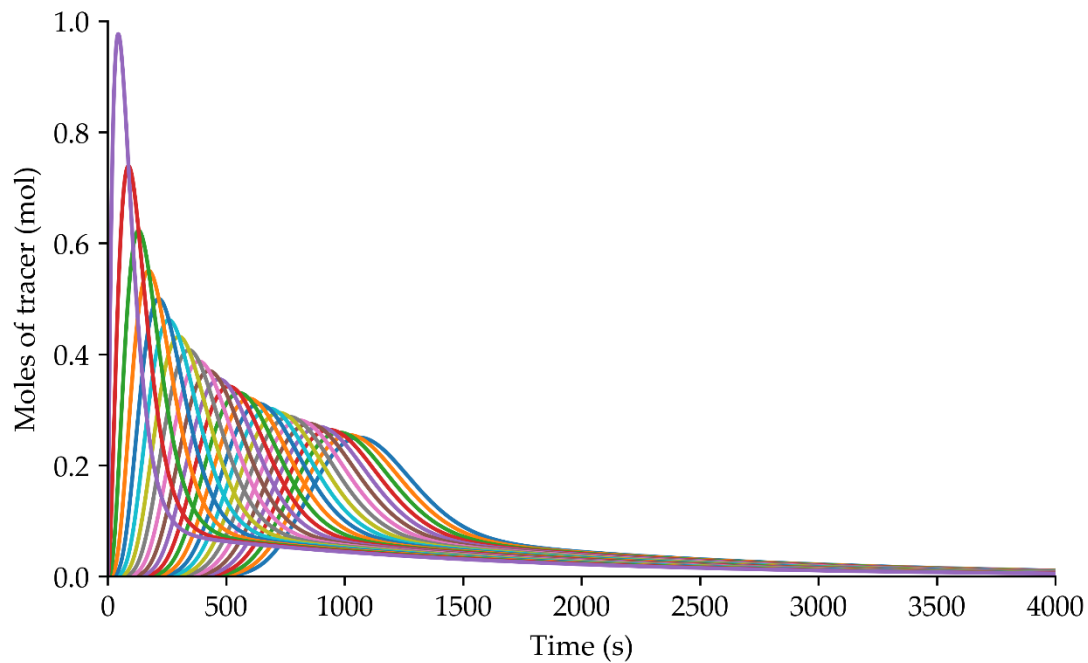
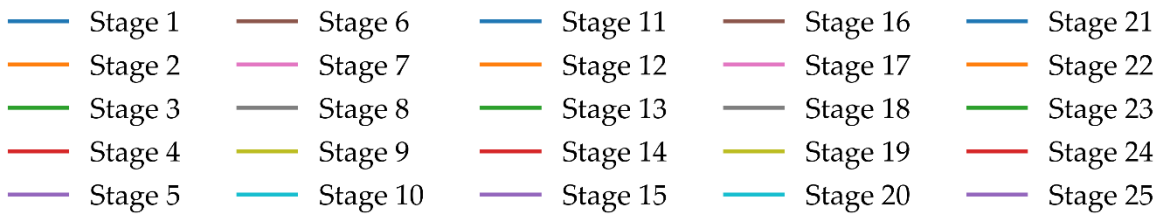


**Figure 61:** CM predicted aqueous phase RTD curve for column stages.

To compare the two aqueous phase RTD experiments, a box and whisker diagram is presented in Figure 62, with the CFD simulation denoted in blue and the CM simulation marked in red. The whiskers represent the 10th and 90th percentiles, the box shows the 25th and 75th percentiles, and the yellow line shows the 50th percentile of the distributions.

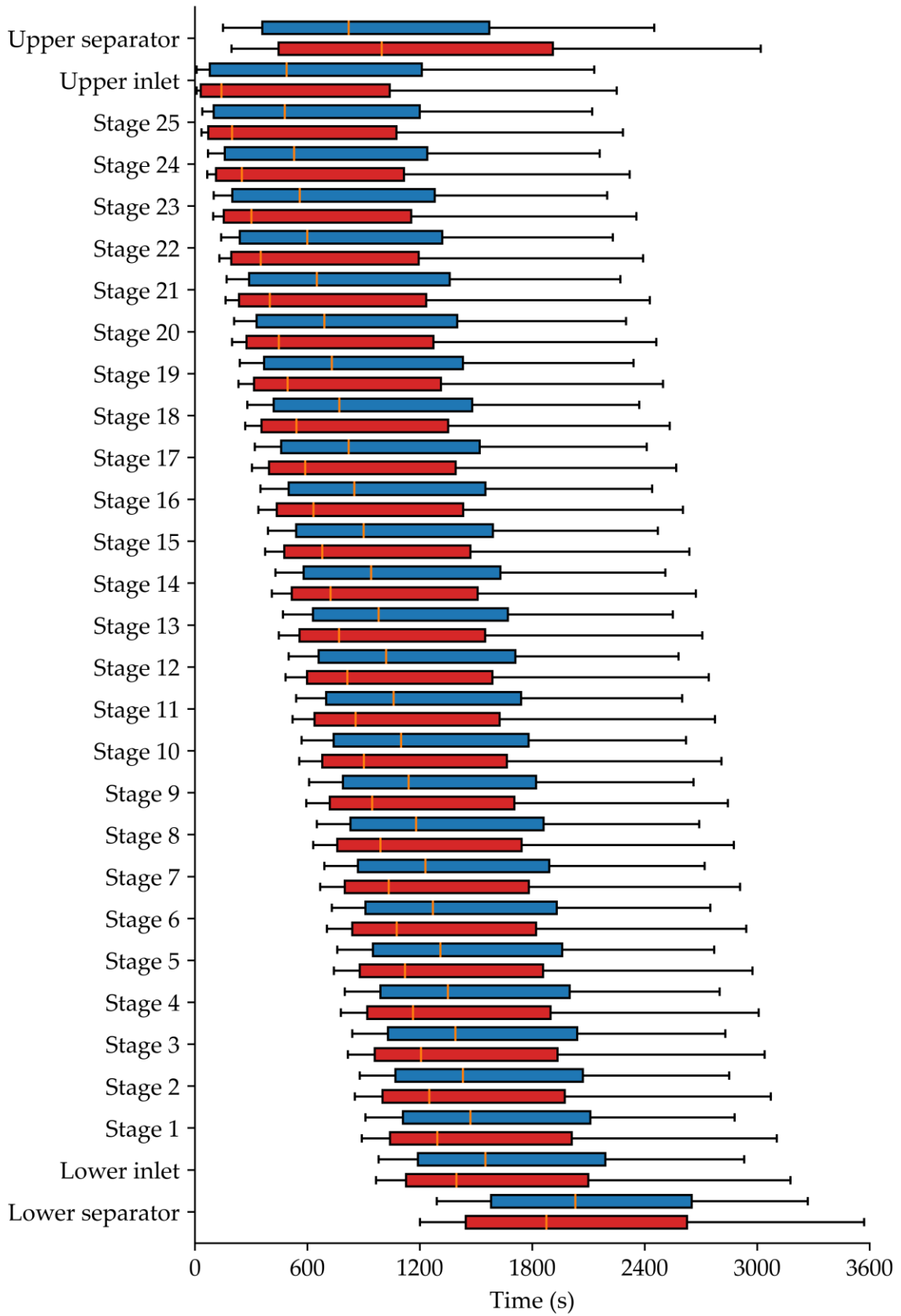


**Figure 62:** Box and whisker plots showing the aqueous phase RTD curves for CFD in blue and the CM in red.

The plots show a general agreement with the distribution for all compartments, although the CM RTD is slightly early. This is likely caused by the inlet pipe to the column which was not modelled. Regardless, the propagation of the tracer down the column is well approximated. There is a slight difference in the distribution of the upper separators and this fit could be improved by adjusting the size of the upper separator to account for the presence of stagnant and recirculating regions and the magnitude of the exchange flows with the upper inlet.

The results of the solvent phase RTD are presented in Figure 63. Visual comparison with Figure 59 shows that all the significant characteristics are represented, however, there are slight differences in the predicted curves. To compare the two solvent phase RTD experiments, a box and whisker diagram is presented in Figure 64.

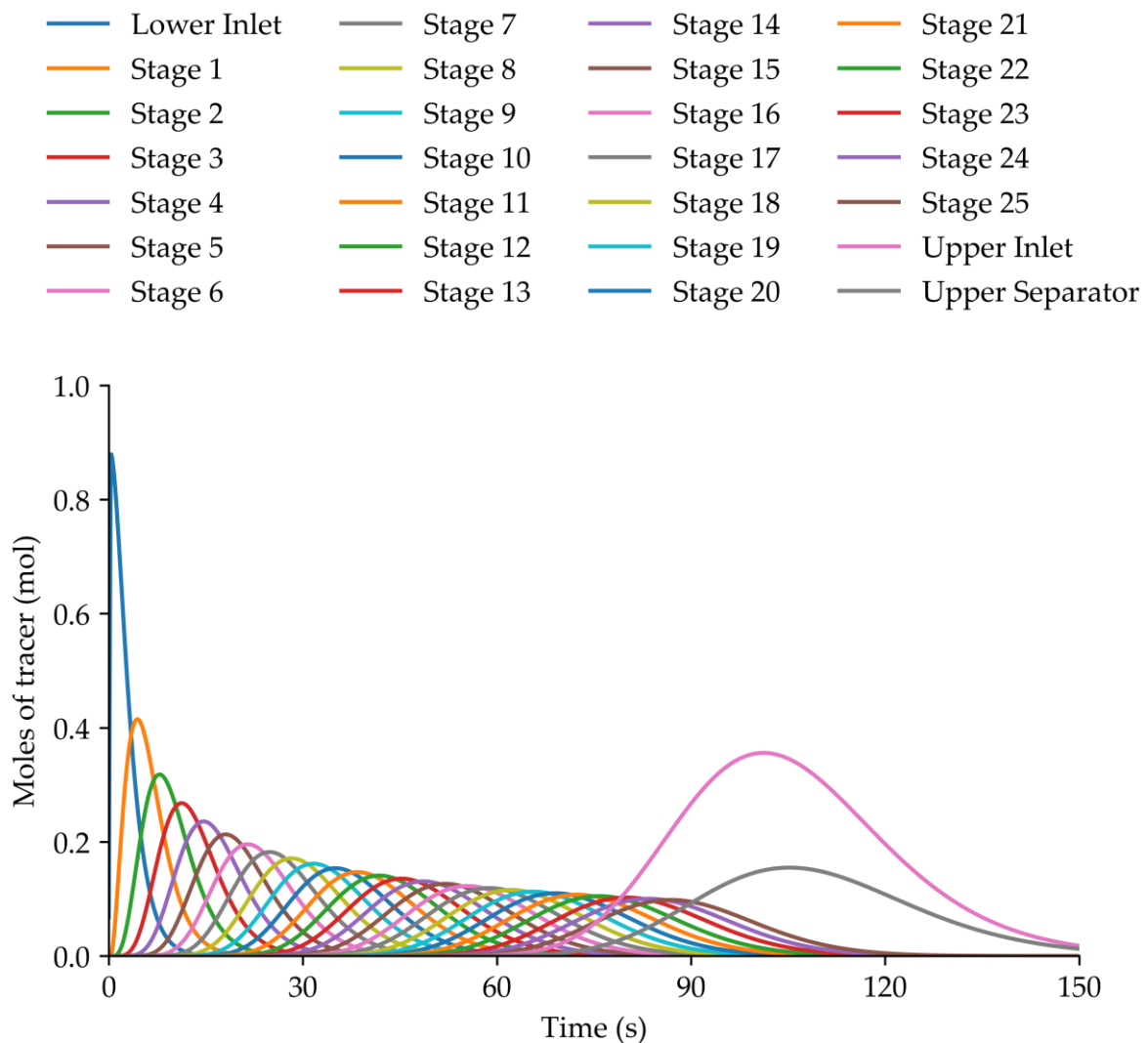


**Figure 63:** CM predicted dispersed phase RTD curve for lower separator, lower inlet, all stages, upper inlet and upper separator.

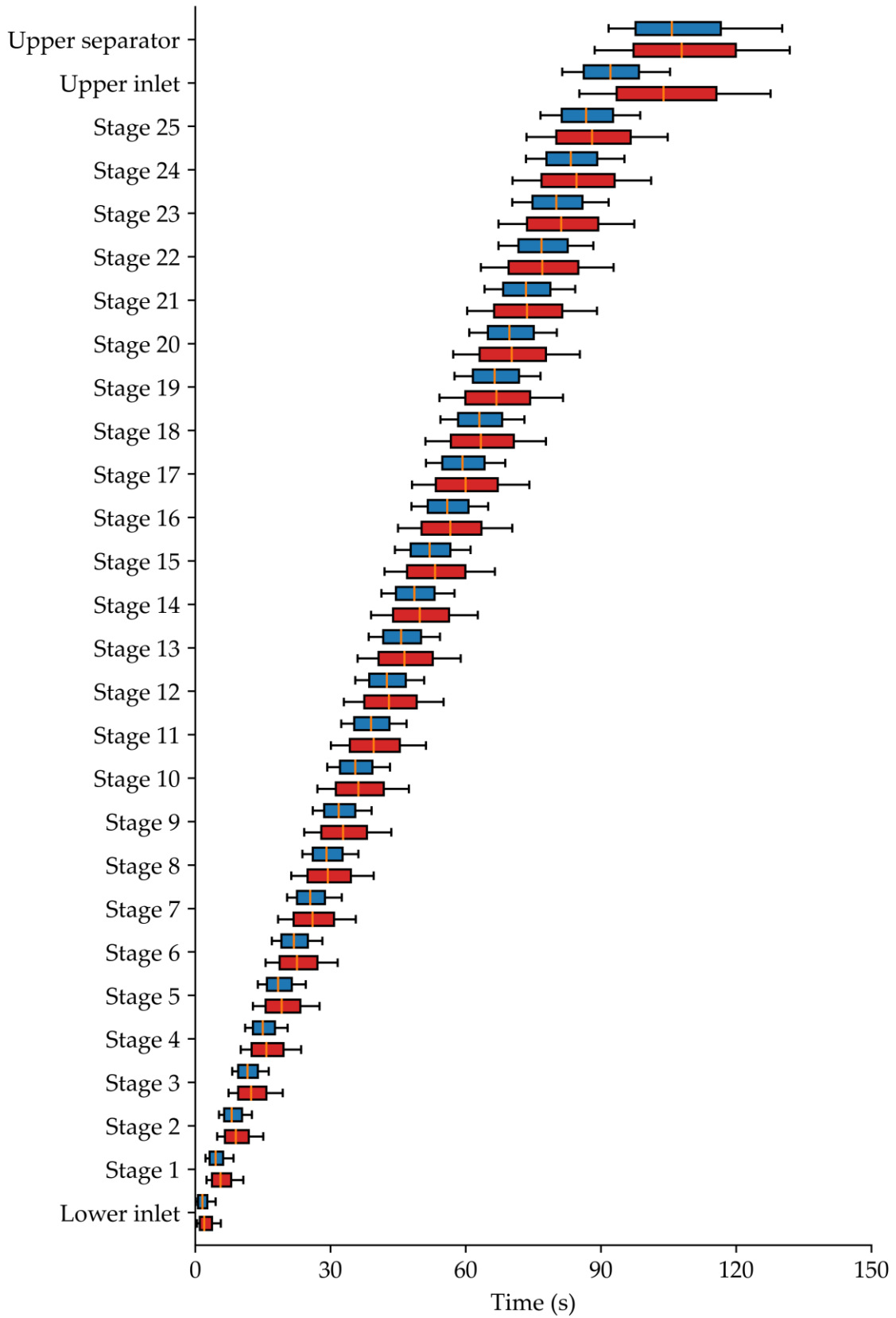


**Figure 64:** Box and whisker plots showing the solvent phase RTD curves for CFD in blue and the CM in red.

The plots show that all the general characteristics of the solvent side RTD are represented however, axial dispersion is overpredicted in all compartments. This implies that the residence time in each stage is over-estimated. A sensitivity analysis of the relative allocation of volume between dispersion and the coalesced solvent was performed however, this did not have a significant impact. Instead, this could be attributed towards solvent wetted to the plates, which could be accounted for by reducing the solvent volume. Additionally, the modelling of solvent within the upper inlet is poorly represented, likely caused by a combination of the accumulated excess dispersion from the column stages and some bypassing of the solvent, possibly caused by recirculation of the aqueous in the region of the inlet.

### 6.3.3. Transient mass transfer model

Before the implementation of mass transfer within the PSEC model, initial verification tests were conducted to investigate the equilibrium values of acetone distributed between two 50 mL volumes of water and toluene, corresponding to an S:A ratio of 1:1. These tests considered an initial aqueous phase acetone concentration of 0 to 1.91 mol.L<sup>-1</sup>, covering the range of concentrations reported by Garthe (2006). A schematic representation of the verification tests is shown in Figure 65.

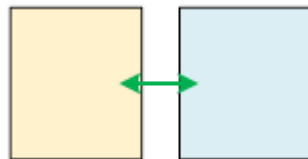


**Figure 65:** Compartment diagram showing implementation of batch mass transfer using two compartments.

The calculated equilibrium solute concentrations are presented in Figure 66. The gradient of the curve is used to determine the equilibrium distribution, and it matches the expected value of 0.843, indicating that the mass transfer is implemented correctly.

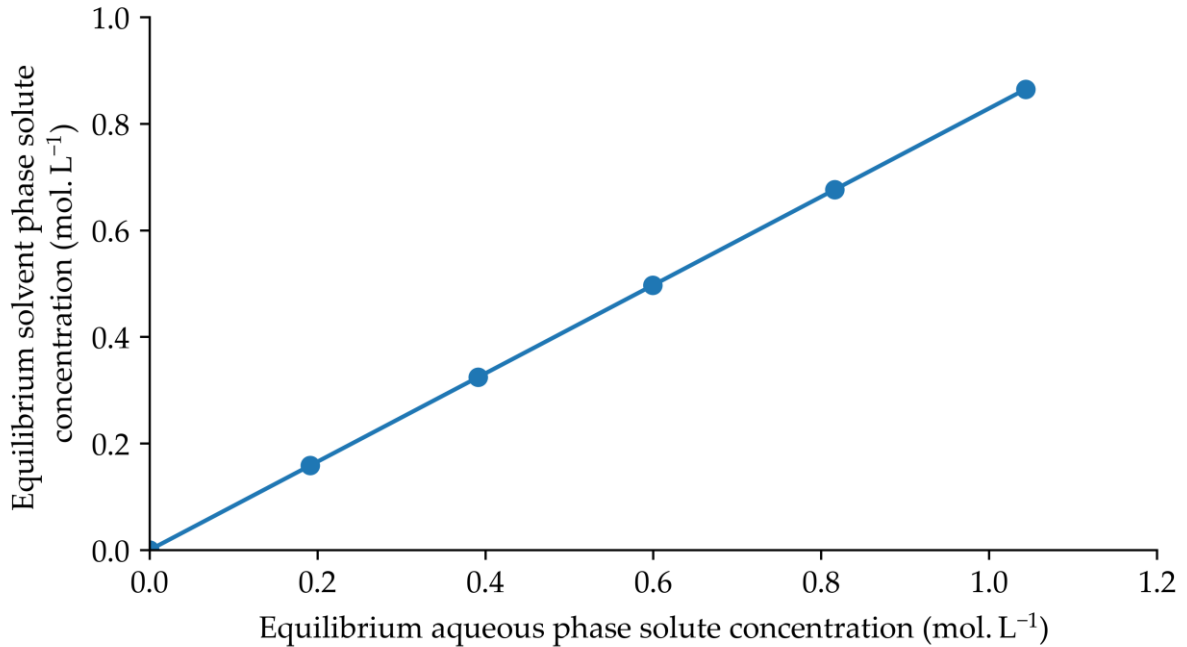


**Figure 66:** Isotherm showing equilibrium concentrations for acetone between the aqueous and solvent phases with distribution ratio given by the gradient.

Mass transfer was implemented in the case by calculating the mass transfer coefficients using equations 2.23 and 2.27 and the specific surface area using the experimentally measured (Garthe, 2006) dispersed phase holdup and mean droplet diameter. The column operated at a heavy phase flow rate of 40 L.hr<sup>-1</sup> with a solute concentration of 0.922 mol.L<sup>-1</sup>, a light phase flow rate of 48 L.hr<sup>-1</sup> with a solute concentration of 0.131 mol.L<sup>-1</sup>, a pulse amplitude of 8 mm and a pulse frequency of 1.25 Hz. The simulation was run for 5 hours, taking around 10 minutes to complete using a single core.

The steady-state axial solute concentrations are presented in Figure 67 and show relatively good agreement with experimental observations. The total, aqueous phase and solvent phase RMSE are 0.0528, 0.0650 and 0.0369 mol.L<sup>-1</sup>, respectively.

Figure 68, left, shows the transient evolution of aqueous phase solute concentration within stages 22, 15 and 5 and the column outlet compared to the measured equilibrium values. An initial delay before the increase in solute concentration can be observed, caused by the column being initialised without solute and corresponding to the solute transport down the column, shown by the increasing delay in lower column sections.

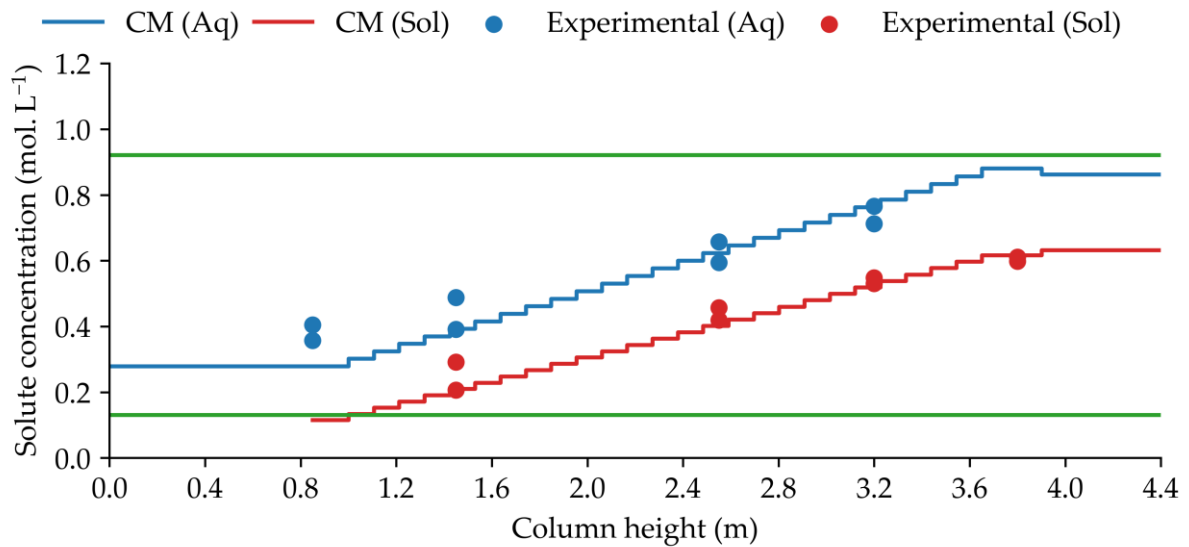


**Figure 67:** Axial solute concentration for  $Q_{tot} = 88 \text{ L.hr}^{-1}$ ,  $Af = 1 \text{ cm.s}^{-1}$ .

The predicted equilibrium values show that solute concentration is under predicted in the lower column, indicating that mass transfer is over predicted. Numerous reasons could cause this, one of which is the mass transfer rate which is dependent on the mass transfer coefficients and surface area to volume ratio of the system.

The mass transfer rate is a function of the empirical correlations of 5.34 and 5.35, which may overestimate its value. Therefore, to assess the accuracy of these correlations, future work should be conducted to investigate the suitability of these correlations using benchtop experiments, for example, single drop experiments.

The available surface area ratio may be overestimated due to an overestimation of compartment volumes, which can be linked to the increased residence times of the compartment model when compared to the CFD model in Figure 64. Although it is possible that the allocation of relative volumes of the dispersion and coalesced regions can have an effect, a sensitivity analysis found that setting these values at a ratio of 1:2, 1:1 and 2:1 did not change the mass transfer performance significantly. Therefore, it is recommended that future work should consider the allocation of stagnant regions within the dispersed phase compartment structure.

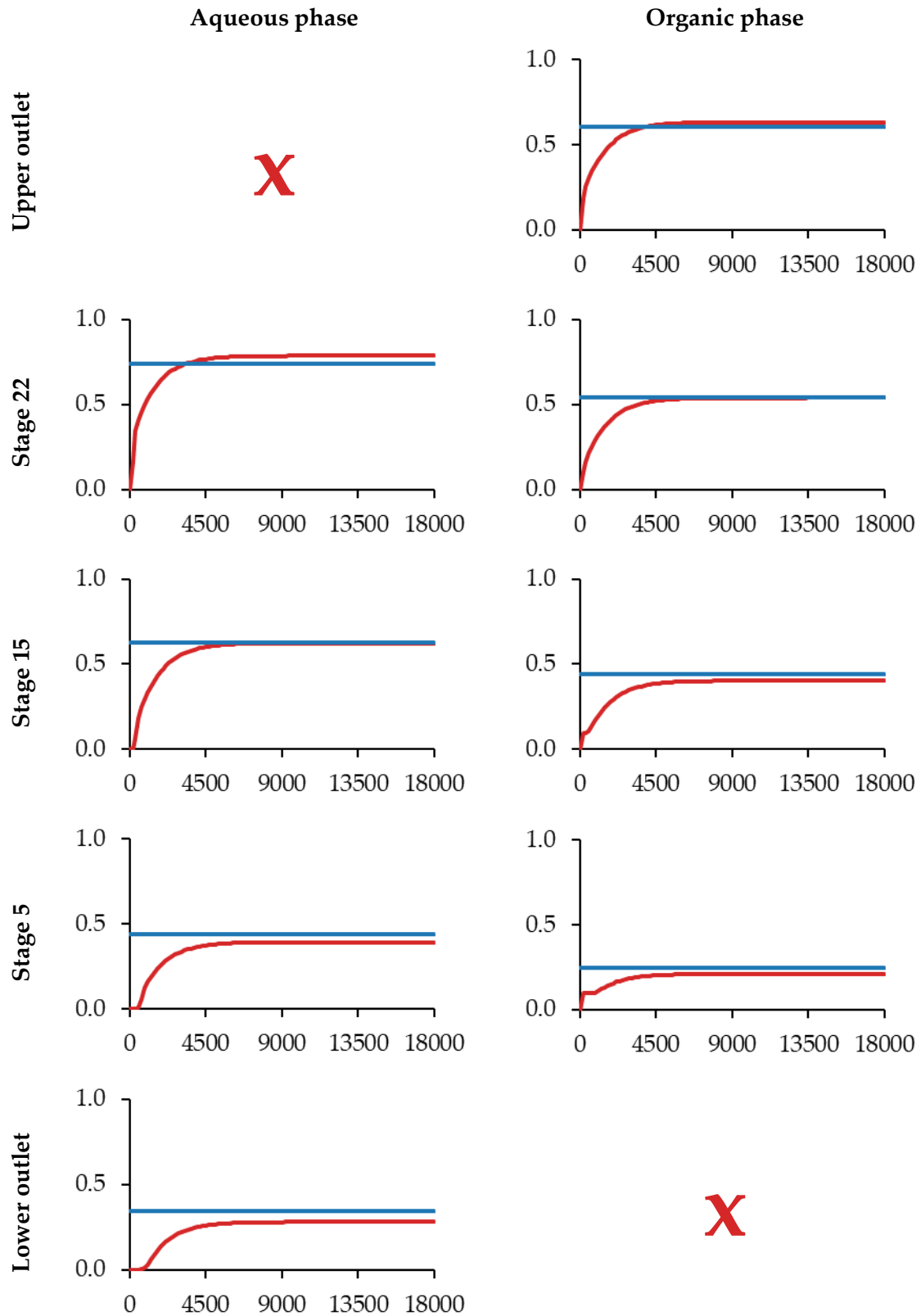


**Figure 68:** Transient solute concentration for aqueous (left) and organic (right) phase for lower outlet, stage 5, stage 15, stage 22 and upper outlet. Y axis denotes solute concentration (mol.L<sup>-1</sup>) and X axis denotes time (s).

Figure 68, right, shows the transient evolution of organic phase solute concentration within the light phase outlet and stages 22, 15 and 5 compared to the measured equilibrium values. Initially, there was an increase in concentration in stages 5 and 15 due to the column being initialised without solute and the subsequent feeding in of solute contained in the organic feed. After this, the solute concentration increased until an equilibrium value was achieved. These values generally agree with the values reported by Garthe, (2006) however, the values in stages 5 and 15 are slightly lower.

Simulations of 17 experiments conducted by Garthe (2006) covering a range of 10 different operating conditions were performed to assess the validity of the modal, representing the conditions usually seen in most columns. Throughputs ranged up to  $205 \text{ L.hr}^{-1}$  and a dispersed phase holdup of 36 %, indicating the column was operating well within the dispersion regime. The results, illustrated in Table 16, presented calculated RMSEs of 0.0547, 0.0643 and  $0.0419 \text{ mol.L}^{-1}$  for the total, aqueous phase and solvent phase, respectively. The maximum overall RMSE was calculated to be  $0.0684 \text{ mol.L}^{-1}$  for a column throughput of  $182 \text{ L.hr}^{-1}$  and a pulse amplitude of  $2 \text{ cm.s}^{-1}$ , which shows the modal can accurately predict mass transfer over the full range of experimental conditions. To avoid repetition due to the large number of similar steady-state axial solute concentration plots generated, these are presented in Appendix 4.

Using the compartment model, it is possible to calculate values useful for designing PSECs, specifically the HTU, the NTU and the PSEC stage efficiency. These results are presented in Table 17 and are generally invariant with column operation, with the average values being calculated as 1.60, 1.75 m and 25 %. This indicates that these parameters are not primarily dependent on the throughput or pulsation of a fluidic system, and instead, these are primarily concerned with ensuring the column operates without flooding. Therefore, for a given fluidic system, the maximum throughput for a PSEC is predominantly dependent on the column geometry, specifically the diameter and column internals.

**Table 16:** Simulated experimental conditions and aqueous, solvent and total errors.

| $Q_{tot}$ (L.hr <sup>-1</sup> ) | $Af$ (cm.s <sup>-1</sup> ) | RMSE <sub>aq</sub> (mol.L <sup>-1</sup> ) | RMSE <sub>sol</sub> (mol.L <sup>-1</sup> ) | RMSE <sub>tot</sub> (mol.L <sup>-1</sup> ) |
|---------------------------------|----------------------------|---|--|--|
| 88                              | 1                          | 0.0650                                    | 0.0369                                     | 0.0528                                     |
| 88                              | 2                          | 0.0577                                    | 0.0566                                     | 0.0571                                     |
| 135                             | 1                          | 0.0679                                    | 0.0325                                     | 0.0532                                     |
| 135                             | 2                          | 0.0456                                    | 0.0426                                     | 0.0441                                     |
| 159                             | 1                          | 0.0544                                    | 0.0336                                     | 0.0452                                     |
| 159                             | 2                          | 0.0482                                    | 0.0483                                     | 0.0482                                     |
| 182                             | 1                          | 0.0746                                    | 0.0404                                     | 0.0600                                     |
| 182                             | 2                          | 0.0880                                    | 0.0401                                     | 0.0684                                     |
| 205                             | 1                          | 0.0766                                    | 0.0511                                     | 0.0651                                     |
| 205                             | 2                          | 0.0650                                    | 0.0369                                     | 0.0528                                     |

**Table 17:** Calculated NTU and HTU.

| $Q_{tot}$ (L.hr <sup>-1</sup> ) | $Af$ (cm.s <sup>-1</sup> ) | NTU <sub>aq</sub> | HTU <sub>aq</sub> (m) | SE <sub>av</sub> (%) |
|---------------------------------|----------------------------|-------------------|-----------------------|----------------------|
| 88                              | 1                          | 1.58              | 1.77                  | 24.0                 |
| 88                              | 2                          | 1.61              | 1.74                  | 25.7                 |
| 135                             | 1                          | 1.58              | 1.77                  | 23.4                 |
| 135                             | 2                          | 1.62              | 1.73                  | 25.7                 |
| 159                             | 1                          | 1.57              | 1.78                  | 22.9                 |
| 159                             | 2                          | 1.60              | 1.75                  | 24.9                 |
| 182                             | 1                          | 1.61              | 1.75                  | 25.8                 |
| 182                             | 2                          | 1.62              | 1.73                  | 26.1                 |
| 205                             | 1                          | 1.56              | 1.80                  | 22.6                 |
| 205                             | 2                          | 1.65              | 1.69                  | 29.3                 |

The calculated stage efficiency of the column was found to be relatively low, with the column operating far away from an efficiency of 100 %, thus providing an opportunity for process intensification. Mass transfer on a stage primarily depends on contact time, mass transfer rates

and specific surface area; however, the design of PSECs is usually driven by the fluidic system, leaving only surface area to volume ratio and residence time able to be optimised. By operating the column with smaller droplets, both these can be increased, however, the likelihood of flooding increases as the operating point approaches the flooding limit. Therefore, the optimum mass transfer should be achieved by operating the column as close to the flooding limit as possible. To further optimise column operation, efforts should focus on reducing the likelihood of flooding, which can be done by developing new plate designs or using alternative column internals such as disk and doughnuts.

#### **6.4. Summary**

A 2D URANS CFD simulation without mass transfer was used to predict the stagewise dispersed phase holdup and  $d_{3,2}$  with reasonable accuracy. This was then used in a simplified steady-state model to predict axial solute concentrations with good agreement with experimental results. However, this method relies on manual adjustment of the backflow ratio and cannot be applied to other systems without further parameterisation.

A 2D URANS CFD simulation was employed to examine the RTD of the aqueous and organic phases and the findings of this study informed the creation of a CM. The CM's predicted RTD curves were comparable to the CFD simulation results. However, the organic phase RTD curves were slightly more axially dispersed, and future investigations could benefit from additional compartmentalisation to account for this discrepancy.

The CM was used to study the absorption of acetone from water into toluene. Good agreement with experimental results was obtained when the steady-state axial solute concentrations were validated against 17 experiments for 10 different operating conditions. This model can also calculate the stage efficiency, NTU, HTU, and the transient evolution of solute within the column. Further research should focus on validating the transient solute concentrations and incorporating more complex chemistry into the model.

## 7. URANIUM EXTRACTION IN A PULSED SIEVE-PLATE EXTRACTION COLUMN

This work presents the results of an experimental investigation and the validation of a compartment modelling approach for extracting and stripping uranium and nitric acid using TBP in Pulsed Sieve-plate Extraction Columns. A total of 8 experiments were performed to measure the transient changes in nitric acid and uranium concentrations, and the results were found to have an average mass balance of 2.2 % and 8.7 %, respectively. A compartment modelling approach was validated with RMSEs of 0.0724 mol.L<sup>-1</sup> and 0.00584 g.L<sup>-1</sup> for nitric acid and uranium. This proposed modelling methodology is accurate and can provide useful design information not typically available.

### 7.1. Introduction

PUREX is a hydrometallurgical solvent extraction process that separates uranium and plutonium from aqueous nitric acid with an organic phase composed of TBP and an inert diluent. This process is the primary technique for reprocessing SNF on an industrial scale and in the latest generation of reprocessing plants, pulsed columns are employed to carry out this separation. Due to its widespread implementation, several methods for modelling this process have been developed including the SEPHIS, SOLVEX, AMUSE and PAREX codes, however due to commercial confidentiality, these are not made readily available (Tranter and Haefner, 2008; Law et al., 2011; Sorel et al., 2011).

An overview of the chemistry of the PUREX process is presented in section 2.1.1, however, mechanistically representing this on a thermodynamic basis is complicated. Instead the chemistry is typically represented by modelling the solute distribution ratio, presented in equation 2.1, as a function of the aqueous phase nitric acid concentration.

In this chapter, we expand the capabilities of the CM developed in chapter 6 to include the chemistry of uranium and nitric acid extraction using TBP, the main components of the PUREX process. Using experimental data generated using the PSEC pilot plant designed in chapter 3, the model predicted transient evolution of solute concentrations at the outlet is validated.

## 7.2. Methodology

### 7.2.1. Experimental apparatus

The experimental apparatus consisted of a glass column with an ID of 65 mm and an active height of 303 mm. The column contained  $4 \times 3$  mm thick stainless steel plates, each with a 23 % free area and a plate hole diameter of 2 mm. A graphic representation of the column is presented in Figure 18. For a detailed explanation of the column design, see chapter 3.

Before column operation, feed materials were prepared and loaded into their respective feed tanks and the column was charged with aqueous to the midpoint of the upper separator. The aqueous feed and receipt pumps were then set to their respective flow rates, and the solvent was introduced into the column at a reduced flow rate until the upper separator was filled. During column operation, the location of the interface was maintained by varying the aqueous receipt flow rate, while aqueous and solvent outlet concentrations were sampled at 5-minute intervals.

The column was operated until the solvent feed tank was depleted. As the column was being used with radioactive material, additional checks and Personal Protective Equipment (PPE) were required to ensure that the working area and operators were monitored for radiation and contamination.

### 7.2.2. Fluid properties

Experiments with nitric acid and 30 v% TBP in Exxsol D80 were performed to characterise the mass transfer of uranyl nitrate. The uranium mass concentrations used in this investigation are not anticipated to be over  $5 \text{ g.L}^{-1}$ , corresponding to less than 1 wt%, and the fluid physical properties were considered independent of uranium concentration. For the dynamic viscosity and interfacial tension of the solvent phase, literature values for a 30 v% TBP in dodecane solution were used. The mutually saturated fluid properties for extraction experiments with a  $3 \text{ mol.L}^{-1}$  nitric acid solution are outlined in Table 18.

**Table 18:** Physical properties of 3 mol.L<sup>-1</sup> nitric acid and 30 v% TBP in dodecane at 20 °C in the absence of uranium (Tian and Liu, 2007; Bajoria et al., 2013).

| Property                                 | Heavy                   | Light                   |
|--|-------------------------|-------------------------|
| Density (kg.m <sup>-3</sup> )            | 1145                    | 820                     |
| Dynamic viscosity (N.s.m <sup>-2</sup> ) | 1.19 × 10 <sup>-3</sup> | 1.65 × 10 <sup>-3</sup> |
| Interfacial tension (N.m <sup>-1</sup> ) | 47.3 × 10 <sup>-3</sup> |                         |

The mutually saturated fluid properties for stripping experiments with a 0.001 mol.L<sup>-1</sup> nitric acid solution, approximated by water, are outlined in Table 19.

**Table 19:** Physical properties of 0.001 mol.L<sup>-1</sup> nitric acid and 30 v% TBP in dodecane at 20 °C in the absence of uranium (Tian and Liu, 2007; Bajoria et al., 2013).

| Property                                 | Heavy                   | Light                   |
|--|-------------------------|-------------------------|
| Density (kg.m <sup>-3</sup> )            | 1020                    | 820                     |
| Dynamic viscosity (N.s.m <sup>-2</sup> ) | 1.02 × 10 <sup>-3</sup> | 1.65 × 10 <sup>-3</sup> |
| Interfacial tension (N.m <sup>-1</sup> ) | 44.1 × 10 <sup>-3</sup> |                         |

### 7.2.3. Distribution ratio

The distribution ratio,  $K_d$ , of nitric acid between the aqueous and organic phases varies with nitric acid concentration and is shown in Figure 69.

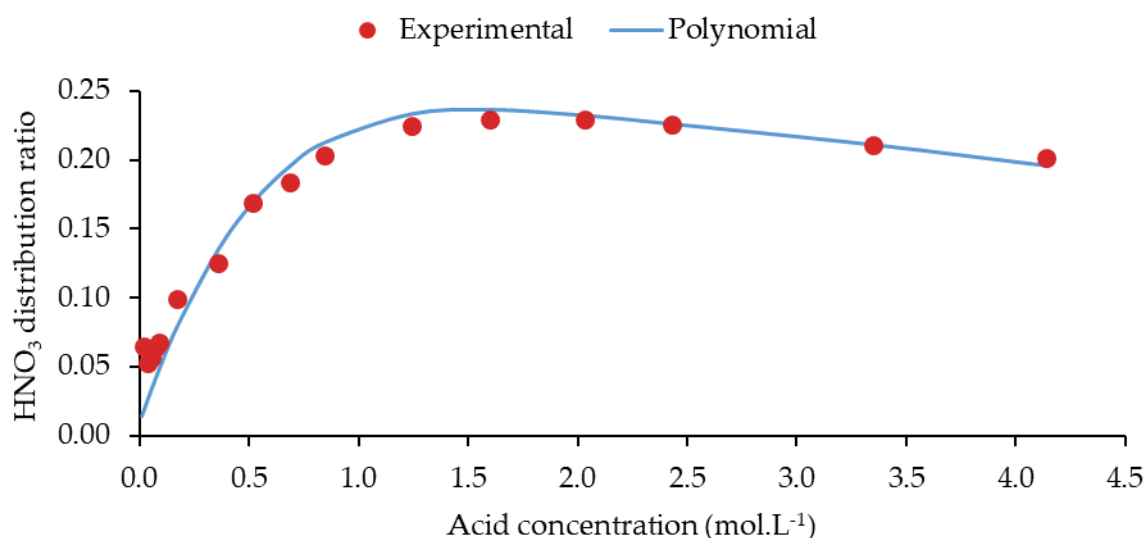


**Figure 69:** Distribution ratio of nitric acid between aqueous and solvent phases as a function of aqueous phase acid concentration (Davis Jr, 1962).

The distribution ratio,  $K_d$ , of uranium between the aqueous and organic phases is shown in Figure 70.

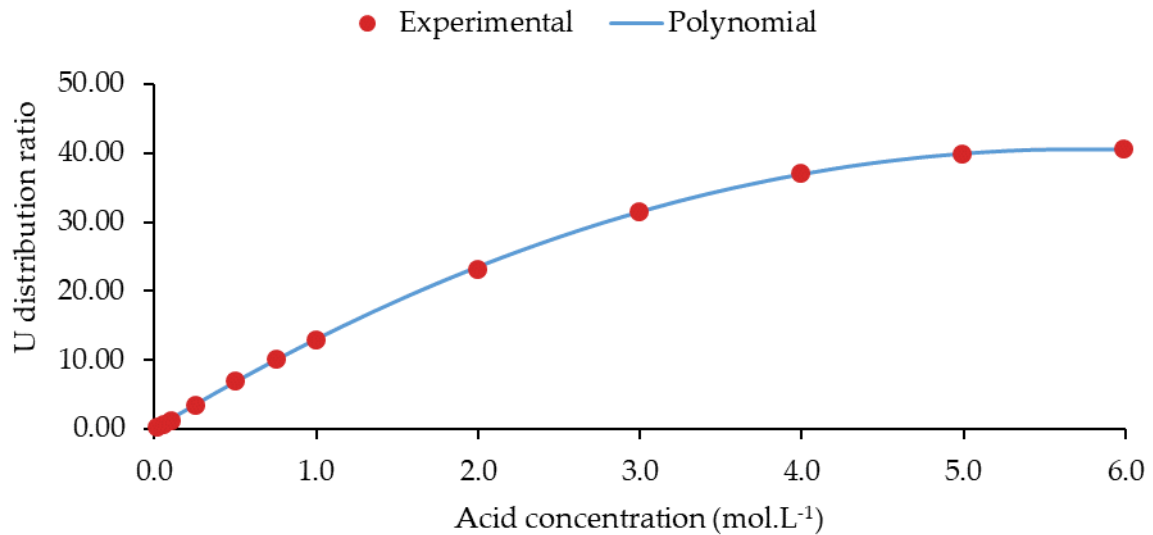


**Figure 70:** Distribution ratio of uranium between aqueous and solvent phases as a function of aqueous phase acid concentration (Apelblat and Faraggi, 1966).

#### 7.2.4. Acid concentration

The nitric acid concentration was determined for both aqueous and organic samples. Using a calibrated air displacement pipette, a volume of analyte was transferred to a beaker which was diluted with deionised water and a small amount of phenolphthalein indicator was added. Using a burette filled with a standard sodium hydroxide solution, the titrant was added to the solution until the indicator changed colour, representing the endpoint of the titration. The concentration of nitric acid in the analyte is calculated as follows:

$$C_{analyte} = \frac{C_{titrant}V_{titrant}}{V_{analyte}} \quad (7.1)$$

Determination of nitric acid concentration in the presence of uranium was performed using the method for acid concentration in the absence of uranium; however, before the addition of titrant, an excess solution of 1 mol.L<sup>-1</sup> potassium fluoride was added to the sample. The potassium fluoride complexes with the uranium ion to prevent hydrolysis, allowing the accurate determination of free acidity within the analyte (Suh et al., 1999).

### 7.2.5. Uranium concentration

The mass concentration of uranium is determined using an Ocean Optics Flame UV-Visible spectrometer, a light source, and a thermoregulator to prevent spectrometer peak intensity variations due to changing temperature. The Beer-Lambert law, expressed on a mass basis, relates the dimensionless absorbance ( $A$ ) to the mass attenuation coefficient ( $i$ ) in  $\text{m}^2.\text{kg}^{-1}$ , the path length ( $l$ ) in m and the species mass concentration ( $M$ ) in  $\text{kg}.\text{m}^{-3}$  and is expressed as follows:

$$A = i.l.M \quad (7.2)$$

Uranium mass concentration is calculated using a glass cuvette and 5 averaged absorbance measurements taken over 45 ms. Previous investigations have calibrated the difference in peak intensity at 415 nm and 550 nm against uranium mass concentration (Hanson et al., 2021). For aqueous solutions, the mass attenuation coefficient is  $0.3423 \text{ m}^2.\text{kg}^{-1}$ , and for solvent solutions, it is  $0.0414 \text{ m}^2.\text{kg}^{-1}$ .

### 7.2.6. Compartment modelling

Using the methodology outlined in chapter 6, a compartment model representing the experimental apparatus was prepared. A graphical representation of the compartment structure is shown in Figure 71, showing the 18 compartments, consisting of 7 aqueous and 11 solvent compartments. The aqueous phase was compartmentalised into the upper separator, upper inlet, stages 1 to 3, lower inlet and lower separator. The solvent phase was compartmentalised into the lower inlet, stages 1 to 3, upper inlet and the upper separator. For the lower inlet and stages 1 to 3, these compartments were further subdivided in a 1:1 ratio to represent the dispersion and coalesced solvent. Compartment volumes are calculated based on their geometry minus the dispersed phase holdup calculated using equation 2.18.

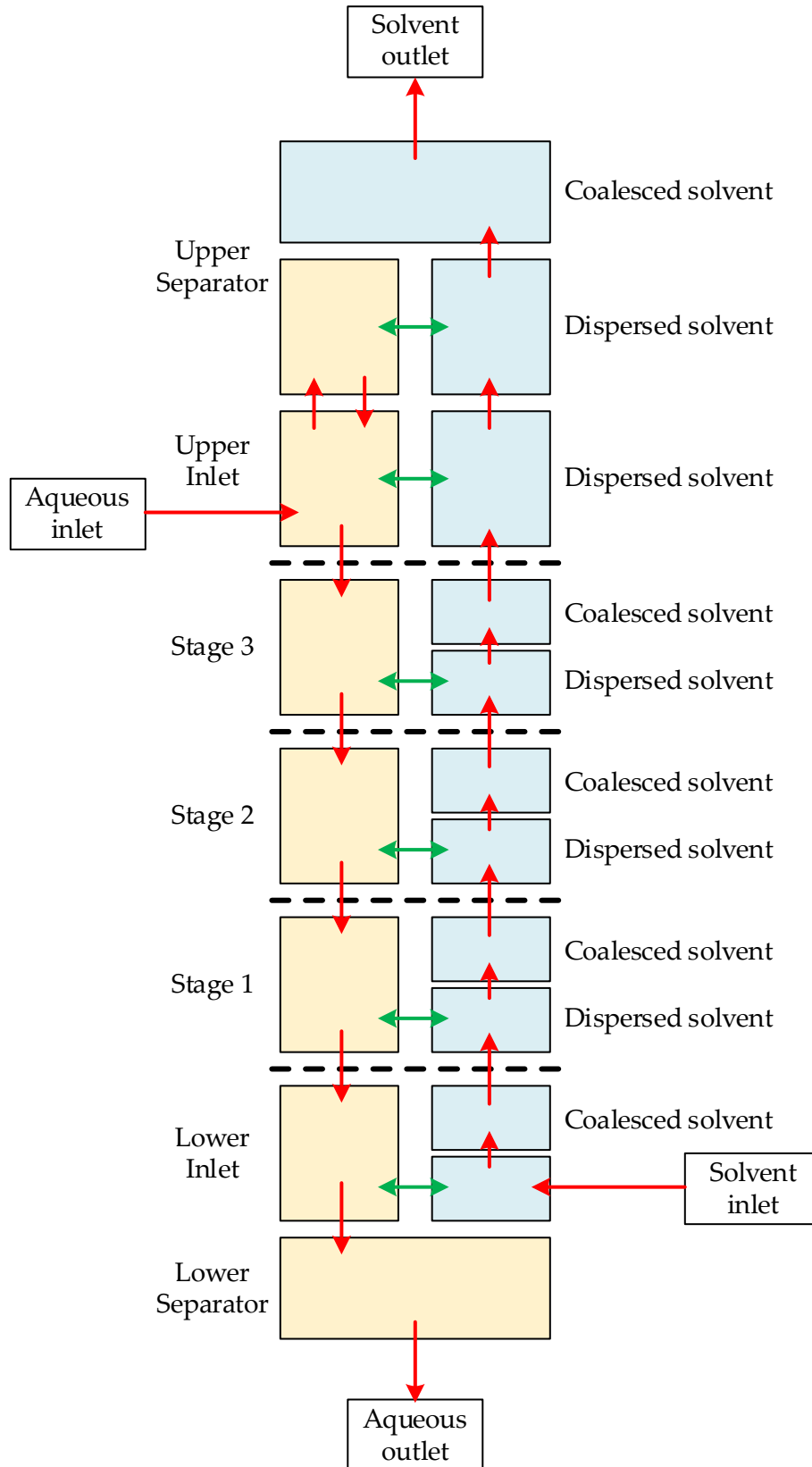


**Figure 71:** Compartment model structure for PSEC. Yellow boxes represent the aqueous phase, blue boxes represent solvent phase. Red arrows represent fluid transport and green arrows represent mass transfer.

The composition of all compartments is derived from the feed material, except for the coalesced regions of the upper separator, which was determined based on the first solvent outlet sample obtained from the experimental data. The intercompartment flow rates in red in Figure 55 are based on the specified inlet flow rates for each phase.

As shown in green in Figure 55, intercompartment mass transfer is specified between all compartments with an aqueous continuum and a droplet dispersion. The mass transfer rate is calculated using two film theory, which is explained in chapter 2. The distribution ratio for nitric acid and U are calculated dynamically based on the aqueous phase acid concentration. This is done using polynomials fitted to published data which is presented in Figure 69 and Figure 70. The surface area is calculated using the dispersed phase holdup and droplet diameter, calculated using equation 2.11.

Due to uncertainty and a lack of reliable data, previous investigations have specified mass transfer coefficients (Chen et al., 2016), however, to ensure this work is consistent with the work in chapter 6, the aqueous and dispersed phase mass transfer coefficients are calculated using equations 2.23 and 2.27 which are scaled by 5 and 0.1 to account for the different kinetics of nitric acid and uranium.

## **7.3. Results and discussion**

### **7.3.1. Experimental**

A total of 8 experiments were conducted for column total throughputs of 40, 50 and 60 L.hr<sup>-1</sup> with a constant S:A ratio, plate hole diameter and pulse amplitude. Each experiment used fresh aqueous feed, while the solvent product of each experiment was retained and used in the following experiment. The aqueous phase of the extraction experiments consisted of approximately 3 mol.L<sup>-1</sup> nitric acid and 3 g.L<sup>-1</sup> of uranium when used. Stripping experiments used a solution of roughly 0.05 mol.L<sup>-1</sup> nitric acid. The first two runs were carried out with nitric acid only, and the subsequent 6 runs included uranium. The generated aqueous and solvent raffinates were consolidated for retreatment and disposal. A summary of the experimental conditions and results is presented in Table 20.

**Table 20:** Experimental conditions and steady-state results.

| Experiment                              | 1       | 2     | 3       | 4     | 5       | 6     | 7       | 8     |
|---|---------|-------|---------|-------|---------|-------|---------|-------|
| $Q_{tot}$ (L.hr <sup>-1</sup> )         | 60      | 60    | 60      | 60    | 50      | 50    | 40      | 40    |
| S:A ratio                               | 2:1     | 2:1   | 2:1     | 2:1   | 2:1     | 2:1   | 2:1     | 2:1   |
| Type                                    | Extract | Strip | Extract | Strip | Extract | Strip | Extract | Strip |
| $C_{HNO_3, aq}$ (mol.L <sup>-1</sup> )  | 2.88    | 0.05  | 3.15    | 0.04  | 3.34    | 0.51  | 3.08    | 0.1   |
| $C_{HNO_3, sol}$ (mol.L <sup>-1</sup> ) | 0.12    | 0.33  | 0.15    | 0.44  | 0.17    | 0.44  | 0.26    | 0.39  |
| $M_{U, aq}$ (g.L <sup>-1</sup> )        | n/a     | n/a   | 3.57    | 0.26  | 3.27    | 0.02  | 2.45    | 0     |
| $M_{U, sol}$ (g.L <sup>-1</sup> )       | n/a     | n/a   | 0.36    | 1.29  | 1.4     | 2.56  | 3.07    | 3.19  |
| $MB_{HNO_3}$ (%)                        | 2.5     | 1.5   | 1.4     | 1.5   | 0.9     | 3.7   | 3.3     | 2.9   |
| $MB_U$ (%)                              | n/a     | n/a   | 4.5     | 9.5   | 8.4     | 5.4   | 12.9    | 11.3  |
| $NTU_{HNO_3}$                           | 0.705   | 0.708 | 0.692   | 0.738 | 0.698   | 0.759 | 0.694   | 0.72  |
| $HTU_{HNO_3}$ (m)                       | 0.443   | 0.441 | 0.451   | 0.423 | 0.447   | 0.441 | 0.45    | 0.434 |
| $NTU_U$                                 | n/a     | n/a   | 0.628   | LOD   | 0.639   | LOD   | 0.617   | LOD   |
| $HTU_U$ (m)                             | n/a     | n/a   | 0.497   | LOD   | 0.488   | LOD   | 0.506   | LOD   |

The average steady-state mass balance for nitric acid and uranium was calculated to be 2.2 % and 8.7 % respectively, indicating excellent solute accountancy across both phases for all experiments. The values for uranium were less good compared to nitric acid, which can be attributed to the relatively low concentrations of uranium used in the investigation, and it is anticipated that if higher concentrations were used, this value would decrease.

The calculated NTU and HTU remained relatively constant across all operating conditions, which is consistent with the findings in chapter 6. For the extraction and stripping of nitric acid, the average values were 0.71 and 0.44 m. For uranium extraction, the average values were 0.63 and 0.50 m, however, it was not possible to calculate these values for stripping experiments as the outlet concentrations were below the limit of detection (LOD). It is noted that the NTU for nitric acid was larger than that of uranium due to the extraction rate being larger for nitric acid than for uranium.

Over several experiments, it was found that the quantity of uranium in the solvent increased, as less uranium was transferred when stripping compared to extraction. This can be attributed to the selection of the continuous phase, which was always the aqueous phase and the S:A ratio which was kept constant. To increase stripping, the solvent can be used as the continuous phase, resulting in a longer residence time and more mass transfer and a lower S:A ratio

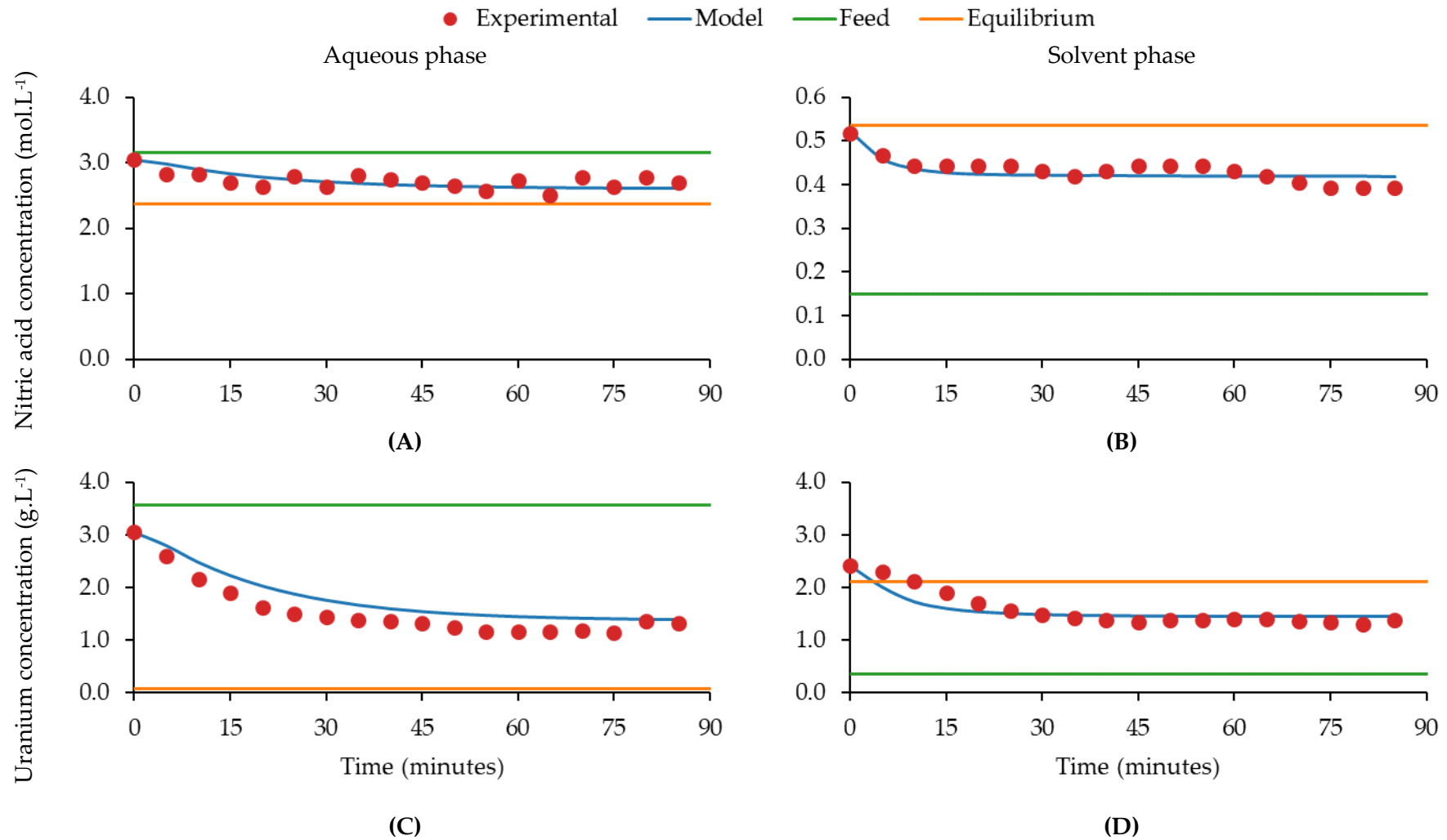
would result in the solvent being contacted with a greater quantity of the aqueous phase, leading to more solute being removed over a given column height.

### 7.3.2. Model validation

The experimental data was used to validate the compartment model. To avoid repetitive discussion, the results of uranium extraction experiment 3 will be discussed, with the results of the other experiments presented in appendix 5.

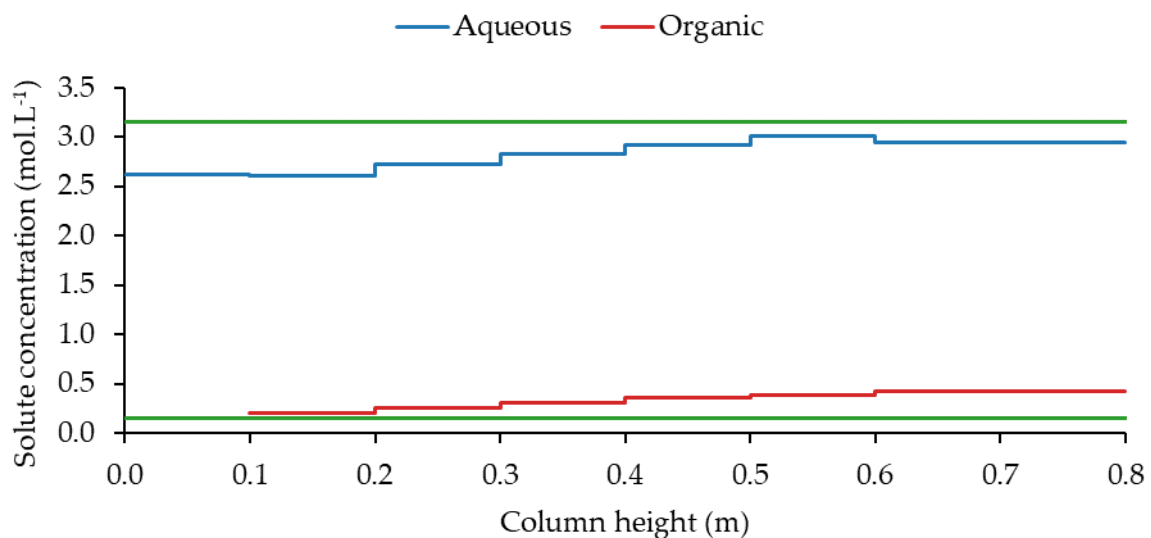
Figure 72 presents the simulated results for extraction experiment 3 compared to the transient experimental data. Plots A and B show the nitric acid aqueous and solvent product concentrations, and plots C and D show the analogous plots for the uranium aqueous and solvent product concentrations. The green and yellow lines represent the feed and equilibrium composition corresponding to 1 transfer unit. The calculated RMSE for nitric acid was  $0.073 \text{ mol.L}^{-1}$  and  $0.014 \text{ g.L}^{-1}$  uranium, and visual assessment of the modelled results show they agree with the experimental results, giving confidence that the system is reasonably approximated.

Figure 72 A and C show that the measured and predicted solute composition of the aqueous phase leaving the column is close to the feed at the start but gradually decreases as the column approaches equilibrium. This is due to the column being initially charged with an aqueous phase which has not had its solute removed, resulting in the initial solute concentration exiting the column being highest before decreasing, shown in Figure 72 B and C. As the solute composition in the aqueous phase reaches its steady state value, the mass transfer reduces, decreasing the solute concentration. As the transient behaviour of the column is accurately captured, this provides confidence in the models reliability.



**Figure 72:** Experiment 3 results and modelled solute concentrations for: (A) aqueous outlet nitric acid; (B) solvent outlet nitric acid; (C) aqueous outlet uranium; and (D) solvent outlet uranium.

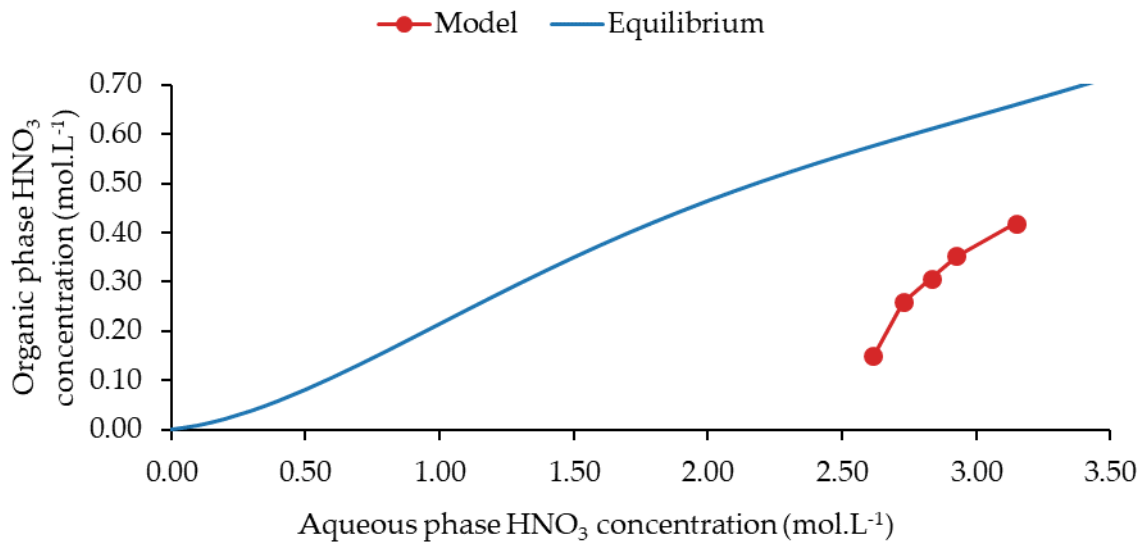
While the steady-state concentration values are reasonably approximated, Figure 72 C and D show that the modelled gradient of the uranium concentration change differs from the measured values. This may be caused by incorrect compartmentalisation of the domain or the chemical kinetics. If the solvent compartments are slightly larger, it could make the model take longer to change solute concentrations, but this would also be visible in the nitric acid outlet compositions, which it is not. Uranium extraction is dependent on the aqueous phase acid concentration via the modelled distribution ratio, however, the transient profile for nitric acid concentration is reasonably predicted, and therefore it is most likely that the issue is due to an under prediction in uranium mass transfer, which could be due to several factors such as the mass transfer rates or distribution which are approximated based of literature values for similar but different fluidic systems. As the model uses a simplified approximation of uranium kinetics, future work would benefit from more representative underpinning data on fluid properties such as density, viscosity, interfacial tension, diffusion coefficients, distribution and mass transfer coefficients.



**Figure 73:** Model predicted axial nitric acid concentration.

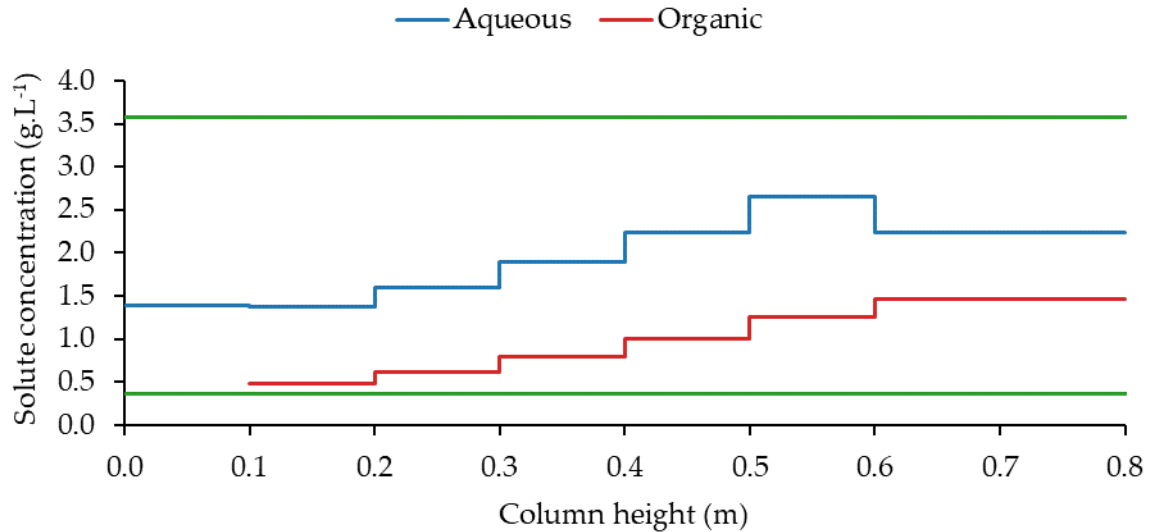
The model-predicted axial solute concentration plots are presented in Figure 73 and show the axial plot for nitric acid concentration in the column, which only varies slightly along the column length for both phases. We observe a decrease in the aqueous phase concentration

from around  $3.15 \text{ mol.L}^{-1}$  to  $2.62 \text{ mol.L}^{-1}$  and an increase in the solvent phase concentration from  $0.15 \text{ mol.L}^{-1}$  to  $0.42 \text{ mol.L}^{-1}$ . The small change in acid concentration is driven primarily by the low distribution ratio of acid between the organic and aqueous phases which, using Figure 69 and the range of acid concentrations observed in the column, is around 0.22. While the decrease in acid concentration is relatively small along the length of the column, for larger columns this decrease will be more pronounced and, although the distribution of nitric acid will remain relatively invariant, Figure 70 shows us that this will result in the equilibrium distribution of uranium being lower, reducing uranium extraction performance in the lower regions of the column.



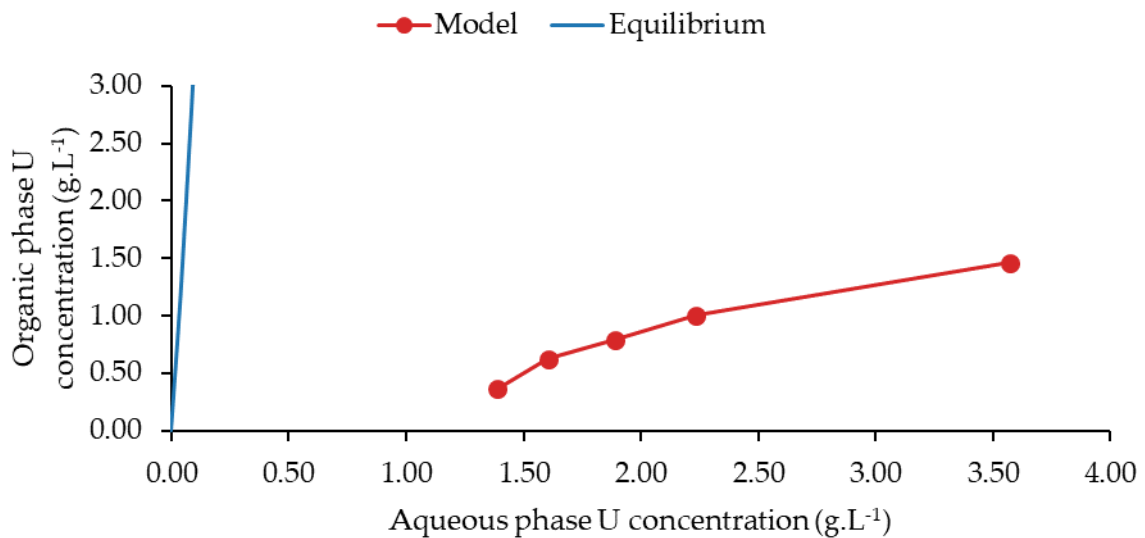
**Figure 74:** Modelled nitric acid operating and equilibrium lines.

Figure 74 shows the nitric acid operating line for the lower inlet, stages 1 to 3 and the upper inlet in red and the blue line denotes the equilibrium values. The distance from the operating line indicates the column efficiency, with a lower distance indicating a more efficient column. This information is helpful for design engineers, as it can be used to assess column performance relative to a proposed flowsheet and make necessary adjustments.



**Figure 75:** Model predicted axial uranium concentration.

Figure 75 displays the model-predicted axial solute concentrations for uranium in a column with the aqueous phase concentration decreasing from 3.57 g.L<sup>-1</sup> to 1.39 g.L<sup>-1</sup>, while the organic phase increases from 0.36 g.L<sup>-1</sup> to 1.46 g.L<sup>-1</sup>. The relative change in concentration is larger than that of nitric acid due to the greater distribution ratio of uranium compared to nitric acid, where Figure 70 shows the distribution ratio for uranium to be around 30, compared to 0.22 for nitric acid.



**Figure 76:** Modelled uranium operating and equilibrium lines.

Figure 76 illustrates the uranium operating line for both inlets and stages 1 to 3. Compared to the nitric acid operating line, the uranium line is much steeper due to the difference in distribution ratio. This means that despite the similar trend in the operating lines, the column is operating much further from equilibrium for uranium than nitric acid.

Further comparison of the model-predicted transient solute outlet compositions was performed. The overall calculated RMSE for nitric acid was  $0.0724 \text{ mol.L}^{-1}$  with a standard deviation of  $0.0189 \text{ mol.L}^{-1}$  and the RMSE for uranium was  $0.0169 \text{ g.L}^{-1}$  with a standard deviation of  $0.00584 \text{ g.L}^{-1}$ . This demonstrates that the model has good predictive capability and consistency and can be used to make accurate predictions. The calculated RMSE for both species in both phases for all experiments is presented in Table 21.

**Table 21:** Calculated RMSE from modelled experiments.

| Experiment                                      | 1     | 2     | 3     | 4     | 5     | 6     | 7     | 8     | Mean  |
|---|-------|-------|-------|-------|-------|-------|-------|-------|-------|
| RMSE <sub>HNO3.aq</sub> (mol.L <sup>-1</sup> )  | 0.087 | 0.077 | 0.102 | 0.072 | 0.135 | 0.086 | 0.014 | 0.061 | 0.079 |
| RMSE <sub>HNO3.sol</sub> (mol.L <sup>-1</sup> ) | 0.062 | 0.021 | 0.017 | 0.059 | 0.018 | 0.040 | 0.020 | 0.015 | 0.032 |
| RMSE <sub>HNO3.tot</sub> (mol.L <sup>-1</sup> ) | 0.076 | 0.056 | 0.073 | 0.066 | 0.096 | 0.067 | 0.100 | 0.045 | 0.072 |
| RMSE <sub>U.aq</sub> (g.L <sup>-1</sup> )       | n/a   | n/a   | 0.017 | 0.004 | 0.018 | 0.009 | 0.027 | 0.014 | 0.015 |
| RMSE <sub>U.sol</sub> (g.L <sup>-1</sup> )      | n/a   | n/a   | 0.010 | 0.015 | 0.012 | 0.013 | 0.026 | 0.028 | 0.017 |
| RMSE <sub>U.tot</sub> (g.L <sup>-1</sup> )      | n/a   | n/a   | 0.014 | 0.011 | 0.016 | 0.011 | 0.027 | 0.022 | 0.017 |

## 7.4. Summary

A total of 8 experiments were conducted to study the transient changes in nitric acid and uranium concentrations when extracted and stripped with the PUREX solvent TBP. The average nitric acid and uranium mass balances were 2.2 % and 8.7 % respectively, showing that the solutes were accurately tracked between the two phases.

The chemistry of the PUREX process was implemented within the CM and validated against the experimental results, resulting in a calculated RMSE for nitric acid and uranium at the column outlets of  $0.0724 \text{ mol.L}^{-1}$  and  $0.00584 \text{ g.L}^{-1}$  respectively. This demonstrates that the proposed modelling methodology can accurately model the transient behaviour of PSEC operation and provide useful design information such as the axial solute concentrations and column operating lines .

To improve the quality of the underpinning data used, it is recommended that the values for density, viscosity, interfacial tension, and diffusion coefficients be experimentally determined. This is due to the lack of suitable data for the specific chemical system being studied and the need to use values for different but similar fluids instead.

The current implementation of mass transfer models the solute distribution as a function of acid concentration in the aqueous phase, however this approach neglects the saturation of the solvent and the impact of other species. This information is available for other chemical systems, and it is recommended that the distribution model be expanded to include this data to provide a more accurate representation of the process.

In addition to assuming equilibrium at the interface, the existing model also uses an empirical approach to adjust the magnitude of the species mass transfer coefficients to achieve representative results. Future research is recommended to expand on this to account for better representation of the underpinning mechanism of mass transfer.

Due to radiological limitations, the quantities of uranium used in this investigation are low and not representative of those used in industrial reprocessing facilities which are typically 300 gU/L and the process has not been tested with the presence of fission products or other actinides. However, implementing their chemistry using the methods discussed in this chapter is feasible. It is recommended that future investigations validate the presented modelling approach using data from industrially relevant PSECs such as those used in the UKs THORP facility.

In summary, the model accurately predicts the transient evolution of uranium and nitric acid in the aqueous and solvent phase outlets. Furthermore, it provides detailed information not usually accessible to design engineers, such as axial solute concentration and the column operating lines which can inform the design and operation of PSECs in the future.

## 8. CONCLUSIONS AND FUTURE WORK

### 8.1. Conclusions

This PhD thesis presents the development and implementation of a modelling and simulation framework for Pulsed Columns, which combines CFD and CM. The primary motivation is to reduce the requirement for repetitive and time-consuming scale-up of pilot plant facilities and enable more accurate prediction of column operation. This is achieved by using CFD to simulate the hydrodynamics of the column which can be used in conjunction with a CM to accurately simulate the column's mass transfer and transient behaviour.

Chapter 2 presented a literature review of the relevant theory underpinning PSEC operation and previous investigations and was used to inform the design and commissioning of a PSEC pilot plant in chapter 3. Appropriate modelling and simulation approaches were also discussed and identified for inclusion in the developed CFD and compartment models in chapters 5 and 6.

The detailed design and commissioning of the PSEC pilot plant was presented in chapter 3, suitable for performing hydrodynamic investigations in chapter 4 and mass transfer experiments in chapter 7.

In chapter 4, the operational envelope and droplet size distributions, mean values and rise velocities were characterised as a function of operating conditions and different hole diameters. The results revealed that:

- The maximum column throughput correlated positively with hole diameter and pulse amplitude.
- Flooding was induced by the presence of recirculating regions which causes the accumulation of smaller droplets within column stages.
- The mean droplet diameter was nonlinearly correlated with hole diameter and the ratio of  $d_{3,0}$  to  $d_{3,2}$  was measured to be 0.83.
- The droplet size distribution was characterised and found to be highly dependent on the mean diameter and weakly proportional or invariant with throughput and pulse amplitude.

- The swarm rise velocity was strongly correlated to the mean droplet diameter which is attributed to the relationship between droplet volume and buoyancy, while column throughput and pulse amplitude had a negligible effect on the swarm rise velocity.

These observations are consistent with anticipated PSEC performance, and the dataset, specifically formulated to identify appropriate models for droplet breakage, coalescence and drag, was used to validate CFD-predicted PSEC hydrodynamics in chapter 5.

In chapter 5, simulations of a PSEC were carried out using the GEMMA methodology and compared to experimental data. The 3D LES results agreed well with the experimental results for stagewise droplet size distribution and mean diameters with a calculated RMSE and standard deviation of 0.63 mm and 0.41 mm. However, the 2D URANS results slightly under predicted these values with a calculated RMSE and standard deviation of 1.17 mm and 0.26 mm, attributed to differences in the predicted turbulence kinetic energy dissipation. As a result, rise velocities were similarly affected due to the effect of droplet diameter and the RMSE were calculated to be 6.70 mm.s<sup>-1</sup> and 23.0 mm.s<sup>-1</sup>. Without more appropriate models, scaling factors can be included to ensure that the hydrodynamics are reasonably approximated. This demonstrates that both the 3D LES and 2D URANS approaches can be used to model PSEC hydrodynamics using the GEMMA methodology. Despite differences in the predicted levels of turbulence kinetic energy, providing appropriate formulations are used for breakage, coalescence and drag, a 2D URANS approach offers an opportunity for reduced simulation times while still retaining relevant hydrodynamic information. Additionally, a local mass transfer formulation was implemented within GEMMA which was modelled using a 2D URANS approach as this is not computationally feasible using a 3D LES. This was found to accurately approximate both hydrodynamics and mass transfer performance with calculated RMSE for the  $d_{3,2}$ , dispersed phase holdup and axial solute concentrations of 0.68 mm, 1.13 % and 0.0659 mol.L<sup>-1</sup> respectively. This demonstrates that CFD can provide spatially resolved information regarding mass transfer performance within PSECs which cannot be accessed using experimental or other reduced order modelling techniques.

In chapter 6, CFD was used to develop a novel CM for predicting mass transfer in PSECs. A 2D URANS simulation of the hydrodynamics in a PSEC was used to predict the stagewise dispersed phase holdup and  $d_{3,2}$  with a RMSE of 1.26 % and 0.57 mm which was then used in

a simplified steady-state model to predict axial solute concentrations with a RMSE of  $0.0710 \text{ mol.L}^{-1}$  indicating good agreement with experimental results. However, the method depends on manual adjustment of the backflow ratio and is limited in its applicability to other systems. A CFD-based RTD experiment was used to produce a CM that replicated the CFD simulation results. The model was then used to study the absorption of acetone from water into toluene and validated against 10 operating conditions. The CM displayed an overall RMSE of  $0.0547 \text{ mol.L}^{-1}$  indicating excellent predictive capability when compared against the steady-state axial solute concentrations. This confirms that despite a reduction in the spatial resolution of column hydrodynamics and mass transfer, Compartment Modelling is an accurate technique for predicting mass transfer performance in PSECs over a range of operating conditions with the benefit of significantly reduced simulation times when compared to CFD simulations.

In chapter 7, a series of experiments were conducted to study the transient changes in nitric acid and uranium concentrations when extracted and stripped with the PUREX solvent TBP. The chemistry of the PUREX process was implemented within the CM and validated against the transient profiles of nitric acid and uranium at the aqueous and organic outlets. The nitric acid and uranium calculated overall RMSE were  $0.073 \text{ mol.L}^{-1}$  and  $0.014 \text{ g.L}^{-1}$ , indicating excellent agreement between the modelled and experimental results. This model demonstrates the implementation of reactive extraction with the dynamic calculation of solute distribution ratios for multiple species, which can be further modified to account for more complicated chemistry. It is readily expandable to account for other species or hydrometallurgical extraction processes using experimental data presented in the literature, and can be used to simulate PSECs to inform design and development. The model provides detailed information not typically available to design engineers, such as axial solute concentrations, column operating lines, and transient performance, allowing flowsheet optimisation, safety analysis, and investigation of the impact of varying process conditions.

In conclusion, Compartment Modelling is a fast and accurate way of predicting the performance of PSECs which has been developed using a combination of experiments and simulations. The model is valid for absorption and chemically reactive extraction in multi-component systems and provides detailed information on the transient evolution of solute

concentrations and column operating lines. The GEMMA method accurately provides spatially resolved hydrodynamic and mass transfer data that is not accessible using conventional experimental and reduced-order modelling techniques and can use both a 3D LES and 2D URANS approach, depending on the desired level of spatial resolution. Despite several simplifying assumptions, the 2D URANS approach can accurately represent both hydrodynamic and mass transfer performance with the benefit of significantly reduced simulation times. The proposed CFD and Compartment Modelling framework enables a modelling and simulation approach to column design, reducing the requirement for costly and time-consuming pilot plant study and providing a strong foundation for further exploration of the hydrodynamics and mass transfer performance of PSECs.

## 8.2. Future work

Future investigations should focus on improving the data that supports the model, expanding on the limitations of the current approach and design optimisation of PSEC internals.

The physical properties of the fluids used in chapters 4 and 7 have been estimated by using similar yet different fluids. This could lead to discrepancies in parameters such as density, viscosity, interfacial tension, and diffusion coefficients, which could impact model outputs. For this reason, it is recommended that these values be experimentally determined.

The formulations for droplet breakage, coalescence and drag in chapter 5 are empirical, and it was necessary to scale their magnitude to obtain representative diameters and rise velocities. This limits their applicability to other operational conditions. To improve this, it is recommended to characterise droplet size as a function of turbulence kinetic energy dissipation and droplet rise velocity as a function of droplet size, dispersed phase holdup and rise velocity. This data can be used to assess the suitability of different correlations and to fit model coefficients for generalised results.

The calculated turbulence kinetic dissipation values vary greatly depending on the modelling approach used in Chapter 5. Even though this difference could be attributed to the 2D representation of the PSEC when modelled with URANS, prior 3D comparisons of the same turbulence models show similar differences (Theobald, 2020) and therefore, there is uncertainty about the appropriate turbulence model. However, validating turbulence models

is challenging because of the difficulty of measuring turbulence experimentally and the large computational overhead associated with DNS. Additionally, a top-down approach to validation is difficult due to the complex and interrelated equations for breakage, coalescence and interphase momentum transfer, which must be validated first. Therefore, due to current limitations in experimental fluid dynamics, it is recommended that future investigations focus on a top-down approach to validation.

In chapter 7, a simplified method of implementing mass transfer is used to model the distribution of solutes according to acid concentration in the aqueous phase. This approach, however, does not account for solvent saturation or the effects of other species, which are available in other chemical systems. To improve the model's accuracy, it is recommended that the mass transfer distribution be expanded to include this data. Additionally, an empirical approach is used to adjust the magnitude of the species mass transfer coefficients to produce representative results. Future research should focus on better understanding the mass transfer mechanism to improve the process's accuracy and representation.

Due to restrictions in the maximum pulse amplitude that can be applied to the column, the operational envelope and dispersed phase hydrodynamics were not fully studied in chapter 4. Additionally, this investigation was only done with one chemical system and the effect of different fluid properties, which are known to have a significant impact on column operability, could not be examined. Consequently, it is recommended that the experimental apparatus be improved to enable greater pulse amplitudes and that future experiments be conducted with fluids of various densities, viscosities, and interfacial tensions.

The method used for characterizing droplet diameters in chapter 4 has several sources of geometric distortion. A bi-telecentric lens can be used to reduce magnification-induced distortion, leading to better accuracy when measuring droplet diameters across the field of view (Hu et al., 2022). Refraction caused by the curvature of glass column walls can be countered by placing the column inside a box filled with a fluid with the same refractive index as the glass (Rida et al., 2019). The methods described in this report for measuring droplet diameters and rise velocities are time-consuming and require an understanding of python, OpenCV and Linux, making them not technically accessible. Therefore, it is recommended that recent developments in the use of Convolutional Neural Networks for droplet

segmentation which are becoming available are implemented as they provide much faster processing (Schmitt et al., 2021).

Advanced optical techniques can be employed to further investigate column hydrodynamics. Using iso-refractive fluids for the continuous and dispersed phase, local holdup can be measured based on the addition of a phase-specific dye, colour intensity and the Beer-Lambert law (Leleu and Pfennig, 2022). In addition, instantaneous droplet velocities can be measured through Digital In-line Holography or PTV (Lamadie and Bruel, 2013; Dabiri and Pecora, 2020). Finally, the continuous phase velocity field can be determined by utilizing PTV or PIV (Raffel et al., 1998). Using a combination of these techniques, it is conceivable to accumulate enough data to carry out a droplet-specific force balance, enabling the identification of an appropriate model for interfacial momentum transfer.

Due to radiological limitations, the quantities of uranium used in chapter 7 are low and not representative of those typically used in industrial reprocessing facilities which are typically 300 gU/L. Furthermore, the process has not been tested with fission products or other actinides. Regardless, the implementation of their chemistry using the methods discussed is feasible. Further investigations are recommended to validate the proposed modelling approach with data from industrially relevant PSECs, such as those used in the UK's THORP facility.

Despite its limitations, CFD is an effective way of modelling PSEC hydrodynamics. It is recommended that future work use CFD to carry out a hydrodynamic evaluation of PSECs, such as defining the operational range or improving the design. A LES approach would make conducting a CFD-based design optimisation feasible, where parameters like the surface area to volume ratio can replace mass transfer to evaluate novel column internals that cannot be currently analysed by existing empirical correlations.

## BIBLIOGRAPHY

Alzyod, S., Attarakih, M., Bart, H.-J.J., Hasseine, A. and Bart, H.-J.J. 2018. CFD modelling of pulsed sieve plate liquid extraction columns using OPOSPM as a reduced population balance model *In: Computer Aided Chemical Engineering*. Elsevier, pp.451–456.

Alzyod, S., Attarakih, M., Hasseine, A. and Bart, H.J. 2017. CFD modelling of pulsed sieve plate liquid extraction columns using OPOSPM as a reduced population balance model *In: Computer Aided Chemical Engineering*.

Amokrane, A., Charton, S., Lamadie, F., Paisant, J.F. and Puel, F. 2014. Single-phase flow in a pulsed column: Particle Image Velocimetry validation of a CFD based model. *Chemical Engineering Science*. **114**, pp.40–50.

ANSYS 2009. Fluent 12.0 user guide. *Fluent Inc*.

Apelblat, A. and Faraggi, M. 1966. Extraction in the system: Uranyl nitrate-nitric acid-tributyl phosphate-diluent. *Journal of Nuclear Energy. Parts A/B. Reactor Science and Technology*. **20**(1), pp.55–65.

Attarakih, M., Al-Zyod, S., Abu-Khader, M. and Bart, H.-J. 2012. PPBLAB: A new multivariate population balance environment for particulate system modelling and simulation. *Procedia Engineering*. **42**, pp.1445–1462.

Bajoria, S.L., Rathod, V.K., Pandey, N.K., Mudali, U.K. and Natarajan, R. 2013. Effect of tri-n-butyl phosphate on physical properties of dodecane–nitric acid system. *Journal of Radioanalytical and Nuclear Chemistry*. **295**(1), pp.271–276.

Baker, A., Fells, A., Carrott, M.J., Maher, C.J. and Hanson, B.C. 2022. Process intensification of element extraction using centrifugal contactors in the nuclear fuel cycle. *Chemical Society Reviews*.

Bart, H.-J., Jildeh, H. and Attarakih, M. 2020. Population balances for extraction column simulations—an overview. *Solvent Extraction and Ion Exchange*. **38**(1), pp.14–65.

Berg, S., Kutra, D., Kroeger, T., Straehle, C.N., Kausler, B.X., Haubold, C., Schiegg, M., Ales, J., Beier, T. and Rudy, M. 2019. Ilastik: interactive machine learning for (bio) image analysis. *Nature methods*. **16**(12), pp.1226–1232.

- Berger, R. and Walter, K. 1985. Flooding in pulsed sieve plate extractors. *Chemical Engineering Science*. **40**(12), pp.2175–2184.
- Bertelsen, E.R., Antonio, M.R., Jensen, M.P. and Shafer, J.C. 2022. Electrochemistry of PUREX: R is for reduction and ion transfer. *Solvent Extraction and Ion Exchange*. **40**(1–2), pp.64–85.
- Bisson, J., Dinh, B., Huron, P. and Huel, C. 2016. PAREX, a numerical code in the service of La Hague plant operations. *Procedia Chemistry*. **21**, pp.117–124.
- Boyadzhiev, L. and Spassov, M. 1982. On the size of drops in pulsed and vibrating plate extraction columns. *Chemical Engineering Science*. **37**(2), pp.337–340.
- Bradski, G. and Kaehler, A. 2000. OpenCV. *Dr. Dobb's journal of software tools*. **3**, p.120.
- Brockkötter, J., Cielanga, M., Weber, B. and Jupke, A. 2020. Prediction and Characterization of Flooding in Pulsed Sieve Plate Extraction Columns Using Data-Driven Models. *Industrial & Engineering Chemistry Research*. **59**(44), pp.19726–19735.
- Bujalski, J.M., Yang, W., Nikolov, J., Solnordal, C.B. and Schwarz, M.P. 2006. Measurement and CFD simulation of single-phase flow in solvent extraction pulsed column. *Chemical Engineering Science*. **61**(9), pp.2930–2938.
- Carrott, M.J., Cook, P.M.A., Fox, O.D., Maher, C.J. and Schroeder, S.L.M. 2012. ATALANTE 2012 International Conference on Nuclear Chemistry for Sustainable Fuel Cycles The chemistry of (U,Pu)O<sub>2</sub> dissolution in nitric acid. *Procedia Chemistry*. **7**, pp.92–97.
- Caudwell, D.R., Trusler, J.P.M., Vesovic, V. and Wakeham, W.A. 2004. The viscosity and density of n-dodecane and n-octadecane at pressures up to 200 MPa and temperatures up to 473 K. *International Journal of Thermophysics*. **25**(5), pp.1339–1352.
- Chen, H., Taylor, R., Jobson, M., Woodhead, D. and Masters, A. 2016. Development and validation of a flowsheet simulation model for neptunium extraction in an advanced PUREX process. *Solvent Extraction and Ion Exchange*. **34**(4), pp.297–321.
- Clift, R., Grace, J.R. and Weber, M.E. 2005. *Bubbles, drops, and particles*. Courier Corporation.
- Cooper, V.R. and Groot, C. 1950. *Design Considerations for a Pulse Column System*. Hanford Works, Richland, Wash.

Coulaloglou, C.A. and Tavlarides, L.L. 1977. Description of interaction processes in agitated liquid-liquid dispersions. *Chemical Engineering Science*. **32**(11), pp.1289–1297.

Dabiri, D. and Pecora, C. 2020. *Particle tracking velocimetry*. IOP Publishing Bristol.

Davey, H.G. (UKAEA) 1958. *Reminiscences of an Atom Pioneer*.

Davis Jr, W. 1962. Thermodynamics of Extraction of Nitric Acid by Tri-n-Butyl Phosphate–Hydrocarbon Diluent Solutions: I. Distribution Studies with TBP in Amsco 125-82 at Intermediate and Low Acidities. *Nuclear Science and Engineering*. **14**(2), pp.159–168.

Delichatsios, M.A. and Probstein, R.F. 1976. The effect of coalescence on the average drop size in liquid-liquid dispersions. *Industrial & Engineering Chemistry Fundamentals*. **15**(2), pp.134–138.

Dijck, W.J.D. 1935. Process and apparatus for intimately contacting fluids.

Din, G.U., Chughtai, I.R., Inayat, M.H., Khan, I.H. and Qazi, N.K. 2010. Modeling of a two-phase countercurrent pulsed sieve plate extraction column—a hybrid CFD and radiotracer RTD analysis approach. *Separation and Purification Technology*. **73**(2), pp.302–309.

Drumm, C., Attarakih, M., Hlawitschka, M.W. and Bart, H.-J. 2010. One-group reduced population balance model for CFD simulation of a pilot-plant extraction column. *Industrial & engineering chemistry research*. **49**(7), pp.3442–3451.

Fells, A., De Santis, A., Colombo, M., Theobald, D.W., Fairweather, M., Muller, F. and Hanson, B. 2022. Predicting Mass Transfer in Liquid–Liquid Extraction Columns. *Processes*. **10**(5), p.968.

Garthe, D. 2006. Fluid dynamics and mass transfer of single particles and swarms of particles in extraction columns.

Germano, M., Piomelli, U., Moin, P. and Cabot, W.H. 1991. A dynamic subgrid-scale eddy viscosity model. *Physics of Fluids A: Fluid Dynamics*. **3**(7), pp.1760–1765.

Glatz, D. and Cross, B. 2022. Understanding When and How to Apply Liquid-Liquid Extraction (LLE) to a Separation Problem. *Koch*.

Gourdon, C. 1994. Population balance based modelling of solvent extraction columns. *Liquid-liquid extraction equipment.*, pp.137–226.

Greenshields, Christopher and Weller, H. 2022. *Notes on Computational Fluid Dynamics: General Principles*. Reading, UK: CFD Direct Ltd.

Greenshields, C. 2019. *OpenFOAM v7 User Guide* [Online]. London, UK: The OpenFOAM Foundation. Available from: <https://doc.cfd.direct/openfoam/user-guide-v7>.

Handlos, A.E. and Baron, T. 1957. Mass and heat transfer from drops in liquid-liquid extraction. *AIChE Journal*. **3**(1), pp.127–136.

Hänsch, S., Lucas, D., Krepper, E. and Höhne, T. 2012. A multi-field two-fluid concept for transitions between different scales of interfacial structures. *International Journal of Multiphase Flow*. **47**, pp.171–182.

Hanson, B.C., Baker, A., Pepper, S., Domenech-Garcia, N. and De Santis, A. 2021. *AFCP Recycle – Final Report*. Leeds.

Heertjes, P.M., Holve, W.A. and Talsma, H. 1954. Mass transfer between isobutanol and water in a spray-column. *Chemical Engineering Science*. **3**(3), pp.122–142.

Herbst, R.S., Baron, P. and Nilsson, M. 2011. Standard and advanced separation: PUREX processes for nuclear fuel reprocessing *In: Advanced Separation Techniques for Nuclear Fuel Reprocessing and Radioactive Waste Treatment*.

Hirt, C.W. and Nichols, B.D. 1981. Volume of fluid (VOF) method for the dynamics of free boundaries. *Journal of computational physics*. **39**(1), pp.201–225.

Hu, Y., Liang, Z., Feng, S., Yin, W., Qian, J., Chen, Q. and Zuo, C. 2022. Calibration and rectification of bi-telecentric lenses in Scheimpflug condition. *Optics and Lasers in Engineering*. **149**, p.106793.

Jervis, K.P. 2022. A universal approach to phenomenological compartment models of unit operations.

Jourdan, N., Neveux, T., Potier, O., Kanniche, M., Wicks, J., Nopens, I., Rehman, U. and Le Moullec, Y. 2019. Compartmental Modelling in chemical engineering: A critical review. *Chemical Engineering Science*. **210**, p.115196.

- Khatir, Z., Hanson, B.C., Fairweather, M. and Heggs, P.J. 2017. CFD Analysis of Liquid-Liquid Extraction Pulsed Sieve-Plate Extraction Columns *In: Computer Aided Chemical Engineering*. Elsevier, pp.19–24.
- Khatir, Z., Hanson, B.C., Fairweather, M. and Heggs, P.J. 2016. High-fidelity CFD simulations of pulsed sieve-plate extraction columns *In: Proceedings of the 11th International ERTOFACS Symposium on Engineering Turbulence Modelling and Measurements (ETMM11)*. Leeds.
- Kolhe, N.S.S., Mirage, Y.H.H., Patwardhan, A.V. V., Rathod, V.K.K., Pandey, N.K.K., Mudali, U.K., Natarajan, R., Mudali, U.K., Kolhe, N.S.S., Pandey, N.K.K., Rathod, V.K.K. and Mirage, Y.H.H. 2011. CFD and experimental studies of single phase axial dispersion coefficient in pulsed sieve plate column. *Chemical Engineering Research and Design*. **89**(10), pp.1909–1918.
- Kronig, R. and Brink, J.C. 1951. On the theory of extraction from falling droplets. *Applied Scientific Research*. **2**, pp.142–154.
- Kumar, A., Hartland, S. %J C.E. and Intensification, P.P. 1988. Prediction of dispersed phase hold-up in pulsed perforated-plate extraction columns. *Chemical Engineering and Processing: Process Intensification*. **23**(1), pp.41–59.
- Laddha, G.S. and Degaleesan, and T E. 1978. *Transport phenomena in liquid extraction*. McGraw-Hill Companies.
- Lamadie, F. and Bruel, L. 2013. In-line digital holographic measurement for liquid-liquid flows *In: Fluids Engineering Division Summer Meeting*. American Society of Mechanical Engineers, V01CT24A001.
- Lanham, W.B. and Runion, T.C. 1949. *PUREX process for Plutonium and Uranium recovery* [Online]. Tennessee. [Accessed 11 June 2019]. Available from: <https://www.osti.gov/servlets/purl/4165457>.
- Lauder, B.E. and Spalding, D.B. 1983. The numerical computation of turbulent flows *In: Numerical prediction of flow, heat transfer, turbulence and combustion*. Elsevier, pp.96–116.
- Law, J., Rutledge, V., Pereira, C., Copple, J., Frey, K., Krebs, J., Maggos, L., Nichols, K., Wardle, K. and Sadasivan, P. 2011. *Requirements for a dynamic solvent extraction module to support*

*development of advanced technologies for the recycle of used nuclear fuel.* Idaho National Lab.(INL), Idaho Falls, ID (United States).

Leleu, D. and Pfennig, A. 2022. Drop-Based Settler-Design Tool Developed Based on Iso-Optical Systems. *Chemie Ingenieur Technik*. **94**(9), pp.1340–1341.

Leonard, A. 1975. Energy cascade in large-eddy simulations of turbulent fluid flows *In: Advances in geophysics*. Elsevier, pp.237–248.

Levenspiel, O. 1999. Chemical reaction engineering. *Industrial & engineering chemistry research*. **38**(11), pp.4140–4143.

Lo, T.C., Baird, M.H.I. and Hanson, C. 1983. *Handbook of solvent extraction*. Wiley New York etc.

Mann, N.R. 2009. *Installation of the Pulse-Plate Column Pilot Plant*. Idaho National Lab.(INL), Idaho Falls, ID (United States).

Marschall, H. 2011. Towards the numerical simulation of multi-scale two-phase flows.

Marschall, H. and Hinrichsen, O. 2013. Numerical simulation of multi-scale two-phase flows using a Hybrid Interface-Resolving Two-Fluid Model (HIRES-TFM). *Journal of chemical engineering of Japan*. **46**(8), pp.517–523.

MARTÍNEZ-BAZÁN, C., Montanes, J.L. and Lasheras, J.C. 1999. On the breakup of an air bubble injected into a fully developed turbulent flow. Part 1. Breakup frequency. *Journal of Fluid Mechanics*. **401**, pp.157–182.

Mathur, A., Dovizio, D., Frederix, E.M.A. and Komen, E.M.J. 2019. A Hybrid Dispersed-Large Interface Solver for multi-scale two-phase flow modelling. *Nuclear Engineering and Design*. **344**, pp.69–82.

Meneveau, C., Lund, T.S. and Cabot, W.H. 1996. A Lagrangian dynamic subgrid-scale model of turbulence. *Journal of fluid mechanics*. **319**, pp.353–385.

Mewes, D. and Pilhofer, T. 1979. Prediction of fluid-dynamic properties of unpulsed sieve-plate extraction columns. *Ger. Chem. Eng.(Engl. Transl.);(Germany, Federal Republic of)*. **2**(2).

- Miller, J., Hanson, B. and Muller, F. 2019. Modification of an Agitated Tube Reactor for use in the Reprocessing of Spent Nuclear Fuel *In: WM Symposia, Inc., PO Box 27646, 85285-7646 Tempe, AZ (United States).*
- Misek, T. 1985. Standard test systems for liquid extraction studies. *EFCE Publ. Ser.* **46**.
- Nash, K.L. and Nilsson, M. 2015. Introduction to the reprocessing and recycling of spent nuclear fuels *In: Reprocessing and Recycling of Spent Nuclear Fuel.*
- Naylor, A. and Larkin, M.J. 1971. Some experiences in the development, design and scale-up of solvent extraction processes for the recovery of irradiated nuclear fuels *In: Proceedings International Solvent Extraction Conference [Online]. Hague: International Solvent Extraction Conference, pp.1356–1372. Available from: <http://isec.23x.cz/ISEC/1971/>.*
- Parrington, C.E. 2018. Plate-type separator for improved separation of liquid-liquid dispersions.
- Paviet-Hartmann, P., Riddle, C., Campbell, K. and Mausolf, E. 2013. Overview of reductants utilized in nuclear fuel reprocessing/recycling *In: International Nuclear Fuel Cycle Conference, GLOBAL 2013: Nuclear Energy at a Crossroads [Online]., pp.79–86. [Accessed 22 July 2019]. Available from: <https://inldigitalibrary.inl.gov/sites/sti/sti/6037803.pdf>.*
- Phillips, C. 1992. Uranium-plutonium partitioning by pulsed column in the first cycle of the three cycle thermal oxide reprocessing plant *In: Waste management'92: working towards a cleaner environment: Waste processing, transportation, storage and disposal, technical programs and public education. Volumes 1 and 2, Technology and programs for radioactive waste management and environmental restor.*
- Poinssot, C., Boullis, B. and Bourg, S. 2015. Role of recycling in advanced nuclear fuel cycles *In: Reprocessing and Recycling of Spent Nuclear Fuel.*
- Poinssot, C., Bourg, S., Grandjean, S. and Boullis, B. 2016. The Sustainability, a Relevant Approach for Defining the Roadmap for Future Nuclear Fuel Cycles. *Procedia Chemistry.* **21**, pp.536–544.
- Prince, M.J. and Blanch, H.W. 1990. Bubble coalescence and break-up in air-sparged bubble columns. *AIChE journal.* **36**(10), pp.1485–1499.

- Prosperetti, A. and Tryggvason, G. 2009. *Computational methods for multiphase flow*. Cambridge university press.
- Raffel, M., Willert, C.E. and Kompenhans, J. 1998. *Particle image velocimetry: a practical guide*. Springer.
- Ranz, W.E. and Marshall, W.R. 1952. Evaporation from drops. *Chemical Engineering Progress*. **48**(3).
- Rhodes, M.J. 2008. *Introduction to particle technology*. John Wiley & Sons.
- Rida, Z., Cazin, S., Lamadie, F., Dherbécourt, D., Charton, S. and Climent, E. 2019. Experimental investigation of mixing efficiency in particle-laden Taylor–Couette flows. *Experiments in Fluids*. **60**(4), pp.1–13.
- Rodríguez-Llorente, D., Cañada-Barcala, A., Muñoz, C., Pascual-Muñoz, G., Navarro, P., Santiago, R., Águeda, V.I., Álvarez-Torrellas, S., García, J. and Larriba, M. 2020. Separation of phenols from aqueous streams using terpenoids and hydrophobic eutectic solvents. *Separation and Purification Technology*. **251**, p.117379.
- De Santis, A., Colombo, M., Hanson, B.C. and Fairweather, M. 2021. A generalized multiphase modelling approach for multiscale flows. *Journal of Computational Physics*. **436**, p.110321.
- De Santis, A., Hanson, B.C. and Fairweather, M. 2021. Hydrodynamics of Annular Centrifugal Contactors: A CFD analysis using a novel multiphase flow modelling approach. *Chemical Engineering Science*. **242**, p.116729.
- Schmitt, P., Sibirtsev, S., Hlawitschka, M.W., Styn, R., Jupke, A. and Bart, H. 2021. Droplet Size Distributions of Liquid-Liquid Dispersions in Centrifugal Pumps. *Chemie Ingenieur Technik*. **93**(1–2), pp.129–142.
- Sege, G. and Woodfield, F.W.J. 1954. Pulse column variables. Solvent extraction of uranyl nitrate with tributyl phosphate in a 3-in.-diam. pulse column. . **50**.
- Sen, N., Singh, K.K., Patwardhan, A.W., Mukhopadhyay, S. and Shenoy, K.T. 2019. CFD-PBM simulations of a pulsed sieve plate column. *Progress in Nuclear Energy*. **111**(November 2017), pp.125–137.

- Sen, N., Singh, K.K., Patwardhan, A.W., Mukhopadhyay, S. and Shenoy, K.T. 2016. CFD simulation of two-phase flow in pulsed sieve-plate column – Identification of a suitable drag model to predict dispersed phase hold up. *Separation Science and Technology (Philadelphia)*.
- Sen, N., Singh, K.K., Patwardhan, A.W., Mukhopadhyay, S. and Shenoy, K.T. 2015. CFD simulations of pulsed sieve plate column: axial dispersion in single-phase flow. *Separation Science and Technology*. **50**(16), pp.2485–2495.
- Sen, N., Singh, K.K., Patwardhan, A.W., Mukhopadhyay, S. and Shenoy, K.T. 2018. CFD simulations to predict dispersed phase holdup in a pulsed sieve plate column. *Separation Science and Technology (Philadelphia)*.
- Sen, N., Singh, K.K., Patwardhan, A.W. and Shenoy, K.T. 2021. Computational fluid dynamics modelling to predict axial dispersion in pulsatile liquid-liquid two-phase flow in pulsed sieve plate columns. *Solvent Extraction and Ion Exchange*. **39**(3), pp.328–352.
- Smagorinsky, J. 1963. General circulation experiments with the primitive equations: I. The basic experiment. *Monthly weather review*. **91**(3), pp.99–164.
- Sorel, C., Montuir, M., Balaguer, C., Baron, P., Dinh, B., Hérès, X., Pacary, V. and Roussel, H. 2011. The PAREX code: a powerful tool to model and simulate solvent extraction operations *In: ISEC 2011-the 19th International Solvent Extraction Conference*.
- Sreenivasulu, K., Venkatanarasaiah, D. and Varma, Y.B.G. 1997. Drop size distributions in liquid pulsed columns. *Bioprocess engineering*. **17**(3), pp.189–195.
- Štrubelj, L. and Tiselj, I. 2011. Two-fluid model with interface sharpening. *International journal for numerical methods in engineering*. **85**(5), pp.575–590.
- Taylor, R., Bodel, W., Stamford, L. and Butler, G. 2022. A Review of Environmental and Economic Implications of Closing the Nuclear Fuel Cycle—Part One: Wastes and Environmental Impacts. *Energies*. **15**(4), p.1433.
- Theobald, D.W. 2020. *Computational Engineering for Nuclear Solvent Extraction Equipment*. Leeds: University of Leeds.

Theobald, D.W., Hanson, B., Fairweather, M. and Heggs, P. 2018. Multiphase Large Eddy Simulation of a Pulsed Sieve-Plate Extraction Column *In: Waste Management Symposia*. Waste Management Symposia, pp.1–15.

Theobald, D.W., Hanson, B., Fairweather, M. and Heggs, P.J. 2020. Implications of hydrodynamics on the design of pulsed sieve-plate extraction columns: A one-fluid multiphase CFD model using the volume of fluid method. *Chemical Engineering Science*. **221**, p.115640.

Thompson, P.J., Sinclair, W., Mowat, D., White, S., Kerr, R., Chalmers, T. and Calder, S.M. 2002. *Radiation Protection During The Early Stages of Site Decommissioning At the UKAEA's Dounreay Site* [Online]. [Accessed 24 June 2019]. Available from: <http://www.ukaea.org.uk>.

Tranter, T.J. and Haefner, D.R. 2008. *Survey of Dynamic Simulation Programs for Nuclear Fuel Reprocessing*. Idaho National Lab.(INL), Idaho Falls, ID (United States).

Treybal, R.E. 1980. Mass transfer operations. *New York*. **466**.

Tribess, A. and Brunello, G. %J B.J. of C.E. 1998. Flooding in pulsed sieve plate extraction columns with mass transfer effects. . **15**(1).

Tu, Y., Chen, H., Sun, Y. and Yu, J. 2021. High-efficient CFD-based framework for the comprehensive hydrodynamic evaluation of pulsed extraction columns. *Chemical Engineering Science*. **236**, p.116540.

Venkatanarasaiah, D. and Varma, Y.B.G. 1998. Dispersed phase holdup and mass transfer in liquid pulsed column. *Bioprocess Engineering*. **18**(2), pp.119–126.

Versteeg, H.K. and Malalasekera, W. 2007. *An introduction to computational fluid dynamics: the finite volume method*. Pearson education.

Wang, H., Zhang, B., Li, X., Xiao, Y. and Yang, C. 2022. Modeling total drag force exerted on particles in dense swarm from experimental measurements using an inline image-based method. *Chemical Engineering Journal*. **431**, p.133485.

Wardle, K.E. 2013. Hybrid multiphase CFD simulation for liquid-liquid interfacial area prediction in annular centrifugal contactors. *Proceedings of the Global 2013.*, p.7650.

Weller, H.G., Tabor, G., Jasak, H. and Fureby, C. 1998. A tensorial approach to computational continuum mechanics using object-oriented techniques. *Computers in Physics*. **12**(6), pp.620–631.

Yadav, R.L. and Patwardhan, A.W. 2009. CFD modeling of sieve and pulsed-sieve plate extraction columns. *Chemical Engineering Research and Design*. **87**(1), pp.25–35.

Yadav, R.L. and Patwardhan, A.W. 2008. Design aspects of pulsed sieve plate columns. *Chemical Engineering Journal*. **138**(1), pp.389–415.

Yi, H., Smith, K.H., Fei, W. and Stevens, G.W. 2020. CFD Simulation of Two-Phase Flow in a Hybrid Pulsed Sieve-Plate Solvent Extraction Column: Prediction of Holdup and Axial-dispersion Coefficients. *Solvent Extraction and Ion Exchange*. **38**(1), pp.88–102.

Yilmaz, F. and Gundogdu, M.Y. 2009. Analysis of conventional drag and lift models for multiphase CFD modeling of blood flow. *Korea-Australia Rheology Journal*. **21**(3), pp.161–173.

Zeppieri, S., Rodríguez, J. and López de Ramos, A.L. 2001. Interfacial tension of alkane+ water systems. *Journal of Chemical & Engineering Data*. **46**(5), pp.1086–1088.

## APPENDIX 1 – P&ID EQUIPMENT LIST

**Table 22: PSEC pilot plant equipment list**

| <b>ID</b> | <b>Description</b> |
|-----------|--------------------|
| E01       | Lower separator    |
| E02       | Lower inlet        |
| E03       | Extraction column  |
| E04       | Upper inlet        |
| E05       | Upper separator    |
| E06       | Pulse leg          |
| E07       | Heavy feed tank    |
| E08.1     | Heavy feed pump    |
| E08.2     | Heavy product pump |
| E09       | Heavy product tank |
| E10       | Light feed tank    |
| E11       | Light feed pump    |
| E12       | Light product tank |
| E13       | Column bund        |
| E14       | Pump bund          |
| E15       | Break pot          |

**APPENDIX 2 – P&ID INSTRUMENT LIST****Table 23: PSEC pilot plant instrument list**

| <b>ID</b> | <b>Description</b>        |
|-----------|---------------------------|
| FT01      | Heavy feed flow           |
| PT02      | Heavy product pressure    |
| FT03      | Heavy product flow        |
| FT04      | Light feed flow           |
| PT05      | Light product pressure    |
| FT06      | Light product flow        |
| PI07      | Air inlet pressure        |
| PI08      | Pulse leg air pressure    |
| PI09      | Pulse leg liquid pressure |

## APPENDIX 3 – P&amp;ID VALVE LIST

Table 24: PSEC pilot plant valve list

| ID  | Description                            |
|-----|--|
| V01 | Pulse leg pressure relief              |
| V02 | Air inlet flow control                 |
| V03 | Solenoid control valve                 |
| V04 | Air outlet flow control                |
| V05 | Heavy feed tank feed                   |
| V06 | Heavy feed tank drain                  |
| V07 | Heavy feed low point drain             |
| V08 | Heavy feed isolation                   |
| V09 | Heavy feed control                     |
| V10 | Heavy feed non return                  |
| V11 | Heavy product low point drain          |
| V12 | Heavy product pump isolation           |
| V13 | Heavy product isolation (locked open)  |
| V14 | Heavy product control (locked open)    |
| V15 | Heavy product sample                   |
| V16 | Heavy product tank feed                |
| V17 | Heavy product tank drain               |
| V18 | Light feed tank feed                   |
| V19 | Light feed tank drain                  |
| V20 | Light feed low point drain             |
| V21 | Light feed isolation                   |
| V24 | Pule leg low point drain               |
| V25 | Pulse leg isolation                    |
| V26 | Column high point vent (locked closed) |
| V27 | Light product isolation (locked open)  |
| V28 | Light product control (locked open)    |
| V29 | Light product sample                   |
| V30 | Light product tank feed                |
| V31 | Light product tank drain               |
| V32 | Air pressure Regulator                 |
| V33 | Air isolation                          |

## APPENDIX 4 – AXIAL SOLUTE CONCENTRATIONS

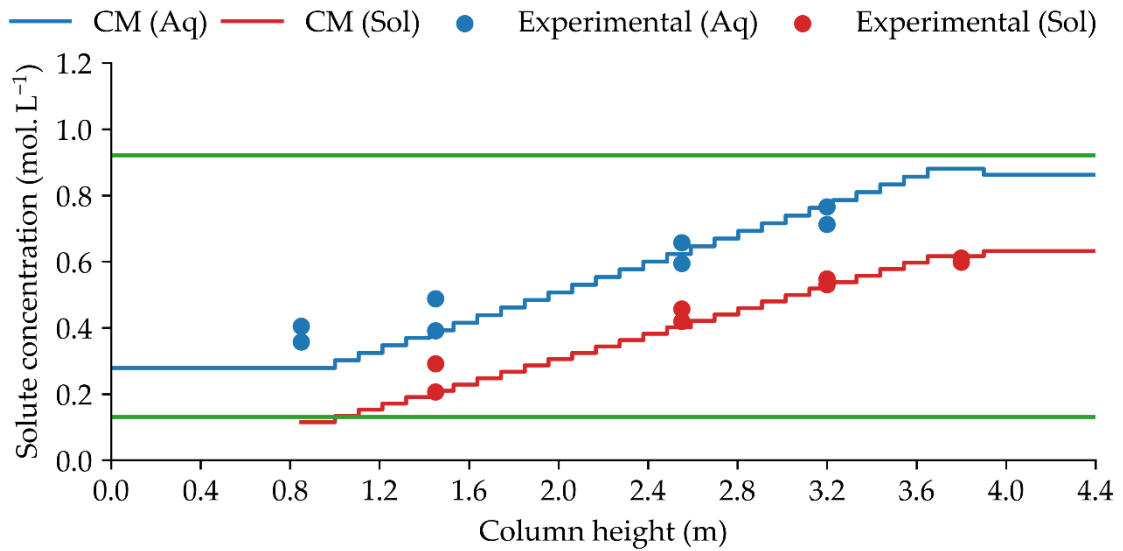


**Figure 77:** Axial solute concentrations for  $Q_{tot} = 88 \text{ L.hr}^{-1}$ ,  $A_f = 1 \text{ cm.s}^{-1}$ .

**Table 25:** Operating parameters and results associated with Figure 77.

|                                     |        |
|-------------------------------------|--------|
| $Q_{tot}$ (L.hr <sup>-1</sup> )     | 88     |
| S:A ratio                           | 1:1.2  |
| $A_f$ (cm.s <sup>-1</sup> )         | 1      |
| $C_{aq.in}$ (mol.L <sup>-1</sup> )  | 0.922  |
| $C_{sol.in}$ (mol.L <sup>-1</sup> ) | 0.131  |
| $NTU_{aq}$                          | 1.58   |
| $HTU_{aq}$ (m)                      | 1.77   |
| $SE_{av}$ (%)                       | 24.0   |
| $RMSE_{aq}$ (mol.L <sup>-1</sup> )  | 0.0650 |
| $RMSE_{sol}$ (mol.L <sup>-1</sup> ) | 0.0369 |
| $RMSE_{tot}$ (mol.L <sup>-1</sup> ) | 0.0528 |

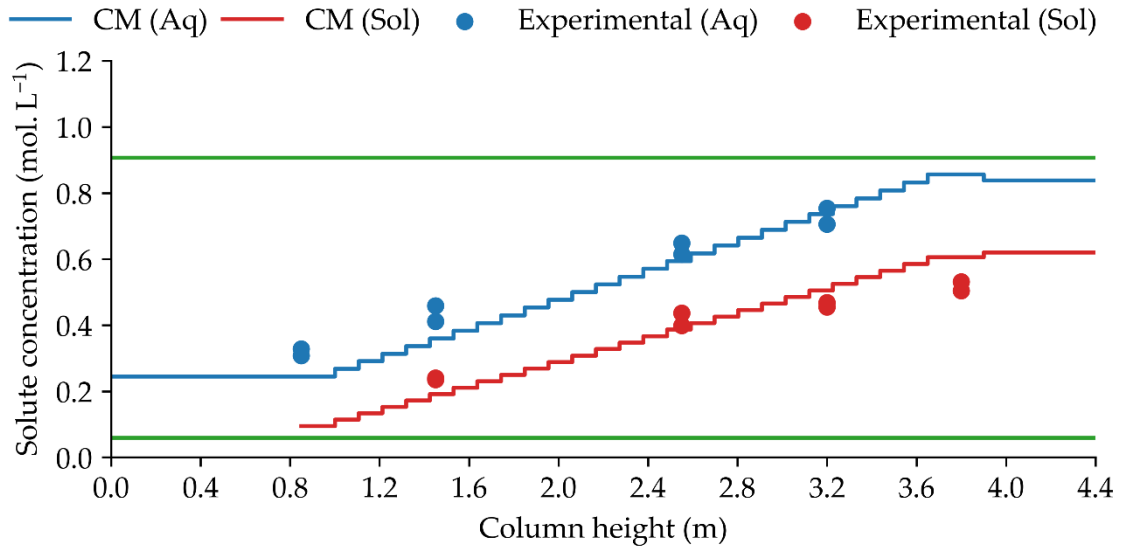


**Figure 78:** Axial solute concentrations for  $Q_{tot} = 88 \text{ L.hr}^{-1}$ ,  $A_f = 2 \text{ cm.s}^{-1}$ .

**Table 26:** Operating parameters and results associated with Figure 78.

|                                     |        |
|-------------------------------------|--------|
| $Q_{tot}$ (L.hr <sup>-1</sup> )     | 88     |
| S:A ratio                           | 1:1.2  |
| $A_f$ (cm.s <sup>-1</sup> )         | 2      |
| $C_{aq.in}$ (mol.L <sup>-1</sup> )  | 0.907  |
| $C_{sol.in}$ (mol.L <sup>-1</sup> ) | 0.060  |
| $NTU_{aq}$                          | 1.61   |
| $HTU_{aq}$ (m)                      | 1.74   |
| $SE_{av}$ (%)                       | 25.7   |
| $RMSE_{aq}$ (mol.L <sup>-1</sup> )  | 0.0577 |
| $RMSE_{sol}$ (mol.L <sup>-1</sup> ) | 0.0566 |
| $RMSE_{tot}$ (mol.L <sup>-1</sup> ) | 0.0571 |

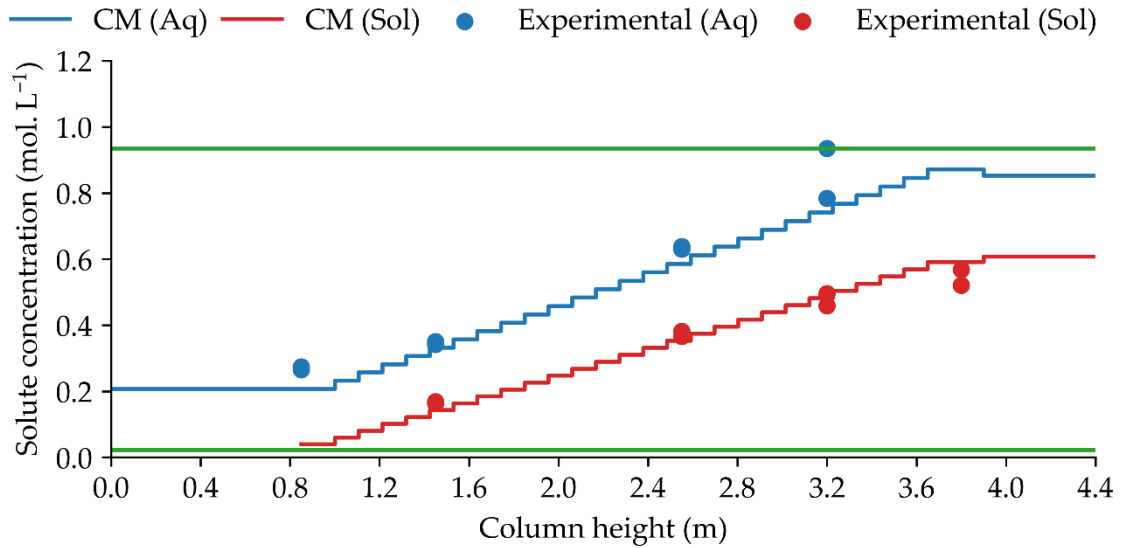


**Figure 79:** Axial solute concentrations for  $Q_{tot} = 135 \text{ L.hr}^{-1}$ ,  $A_f = 1 \text{ cm.s}^{-1}$ .

**Table 27:** Operating parameters and results associated with Figure 79.

|                                     |        |
|-------------------------------------|--------|
| $Q_{tot}$ (L.hr <sup>-1</sup> )     | 135    |
| S:A ratio                           | 1:1.2  |
| $A_f$ (cm.s <sup>-1</sup> )         | 1      |
| $C_{aq.in}$ (mol.L <sup>-1</sup> )  | 0.935  |
| $C_{sol.in}$ (mol.L <sup>-1</sup> ) | 0.022  |
| $NTU_{aq}$                          | 1.58   |
| $HTU_{aq}$ (m)                      | 1.77   |
| $SE_{av}$ (%)                       | 23.4   |
| $RMSE_{aq}$ (mol.L <sup>-1</sup> )  | 0.0679 |
| $RMSE_{sol}$ (mol.L <sup>-1</sup> ) | 0.0325 |
| $RMSE_{tot}$ (mol.L <sup>-1</sup> ) | 0.0532 |

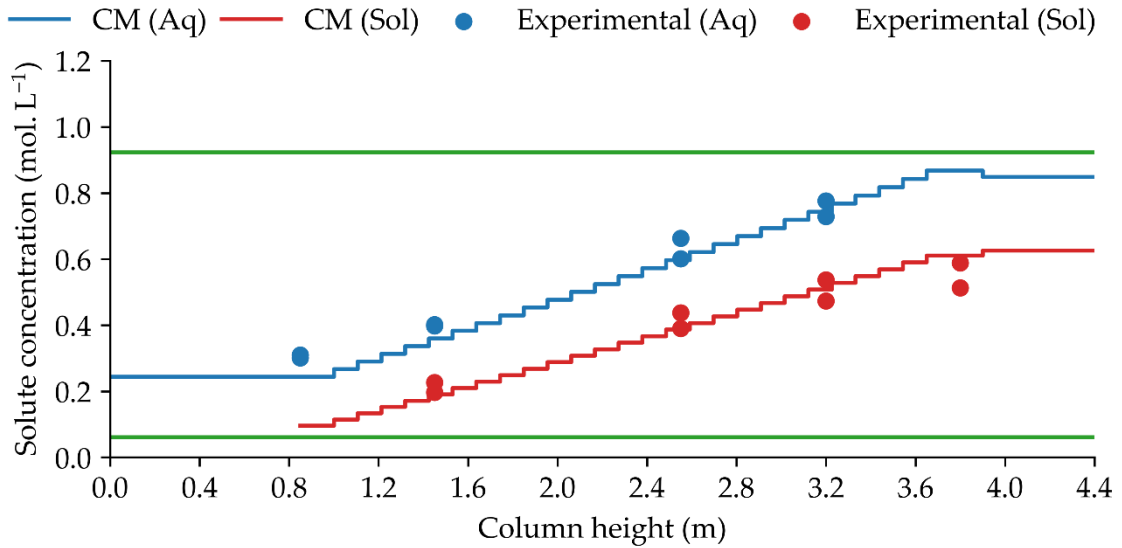


**Figure 80:** Axial solute concentrations for  $Q_{tot} = 135 \text{ L.hr}^{-1}$ ,  $A_f = 2 \text{ cm.s}^{-1}$ .

**Table 28:** Operating parameters and results associated with Figure 80.

|                                     |        |
|-------------------------------------|--------|
| $Q_{tot}$ (L.hr <sup>-1</sup> )     | 135    |
| S:A ratio                           | 1:1.2  |
| $A_f$ (cm.s <sup>-1</sup> )         | 2      |
| $C_{aq.in}$ (mol.L <sup>-1</sup> )  | 0.923  |
| $C_{sol.in}$ (mol.L <sup>-1</sup> ) | 0.061  |
| $NTU_{aq}$                          | 1.62   |
| $HTU_{aq}$ (m)                      | 1.73   |
| $SE_{av}$ (%)                       | 25.7   |
| $RMSE_{aq}$ (mol.L <sup>-1</sup> )  | 0.0456 |
| $RMSE_{sol}$ (mol.L <sup>-1</sup> ) | 0.0426 |
| $RMSE_{tot}$ (mol.L <sup>-1</sup> ) | 0.0441 |

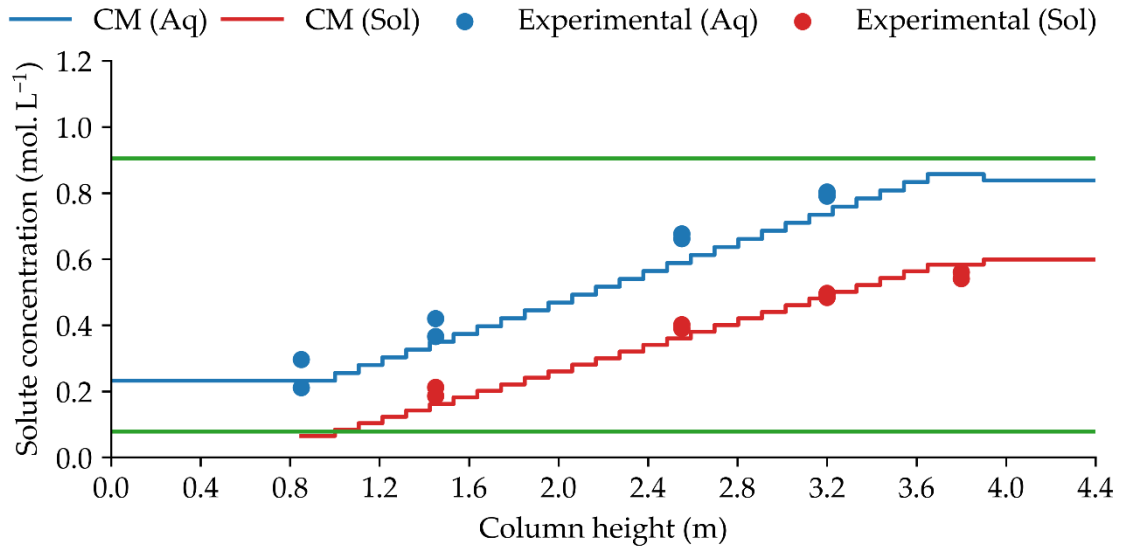


**Figure 81:** Axial solute concentrations for  $Q_{tot} = 159 \text{ L.hr}^{-1}$ ,  $Af = 1 \text{ cm.s}^{-1}$ .

**Table 29:** Operating parameters and results associated with Figure 81.

|                                     |        |
|-------------------------------------|--------|
| $Q_{tot}$ (L.hr <sup>-1</sup> )     | 159    |
| S:A ratio                           | 1:1.2  |
| $Af$ (cm.s <sup>-1</sup> )          | 1      |
| $C_{aq.in}$ (mol.L <sup>-1</sup> )  | 0.905  |
| $C_{sol.in}$ (mol.L <sup>-1</sup> ) | 0.079  |
| $NTU_{aq}$                          | 1.57   |
| $HTU_{aq}$ (m)                      | 1.78   |
| $SE_{av}$ (%)                       | 22.9   |
| $RMSE_{aq}$ (mol.L <sup>-1</sup> )  | 0.0544 |
| $RMSE_{sol}$ (mol.L <sup>-1</sup> ) | 0.0336 |
| $RMSE_{tot}$ (mol.L <sup>-1</sup> ) | 0.0452 |

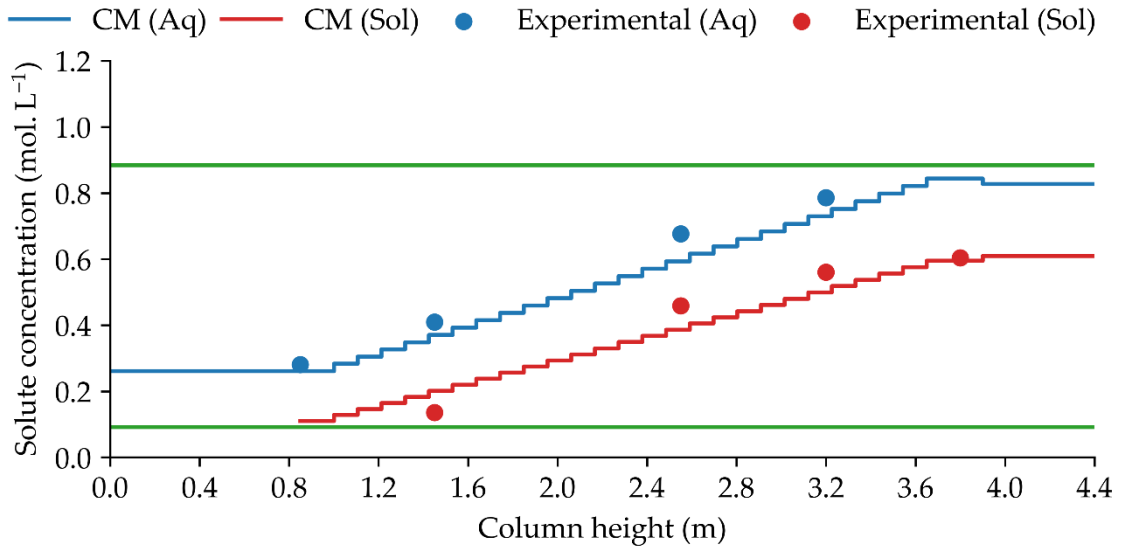


**Figure 82:** Axial solute concentrations for  $Q_{tot} = 159 \text{ L.hr}^{-1}$ ,  $Af = 2 \text{ cm.s}^{-1}$ .

**Table 30:** Operating parameters and results associated with Figure 82.

|                                     |        |
|-------------------------------------|--------|
| $Q_{tot}$ (L.hr <sup>-1</sup> )     | 159    |
| S:A ratio                           | 1:1.2  |
| $Af$ (cm.s <sup>-1</sup> )          | 2      |
| $C_{aq.in}$ (mol.L <sup>-1</sup> )  | 0.885  |
| $C_{sol.in}$ (mol.L <sup>-1</sup> ) | 0.093  |
| $NTU_{aq}$                          | 1.60   |
| $HTU_{aq}$ (m)                      | 1.75   |
| $SE_{av}$ (%)                       | 24.9   |
| $RMSE_{aq}$ (mol.L <sup>-1</sup> )  | 0.0482 |
| $RMSE_{sol}$ (mol.L <sup>-1</sup> ) | 0.0483 |
| $RMSE_{tot}$ (mol.L <sup>-1</sup> ) | 0.0482 |

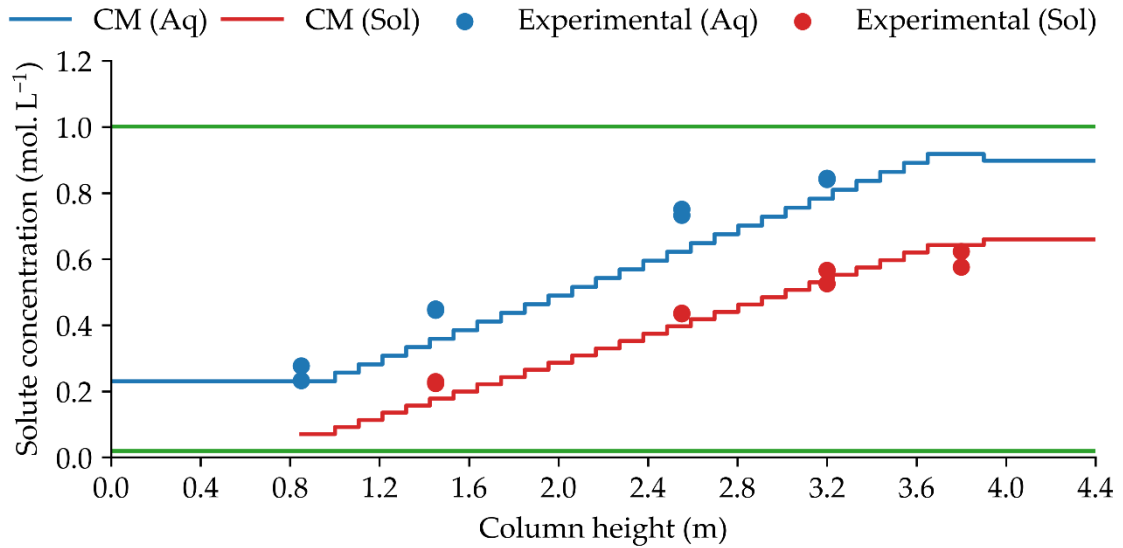


**Figure 83:** Axial solute concentrations for  $Q_{tot} = 182 \text{ L.hr}^{-1}$ ,  $A_f = 1 \text{ cm.s}^{-1}$ .

**Table 31:** Operating parameters and results associated with Figure 83.

|                                     |        |
|-------------------------------------|--------|
| $Q_{tot}$ (L.hr <sup>-1</sup> )     | 182    |
| S:A ratio                           | 1:1.2  |
| $A_f$ (cm.s <sup>-1</sup> )         | 1      |
| $C_{aq.in}$ (mol.L <sup>-1</sup> )  | 1.002  |
| $C_{sol.in}$ (mol.L <sup>-1</sup> ) | 0.019  |
| $NTU_{aq}$                          | 1.61   |
| $HTU_{aq}$ (m)                      | 1.75   |
| $SE_{av}$ (%)                       | 25.8   |
| $RMSE_{aq}$ (mol.L <sup>-1</sup> )  | 0.0746 |
| $RMSE_{sol}$ (mol.L <sup>-1</sup> ) | 0.0404 |
| $RMSE_{tot}$ (mol.L <sup>-1</sup> ) | 0.0600 |

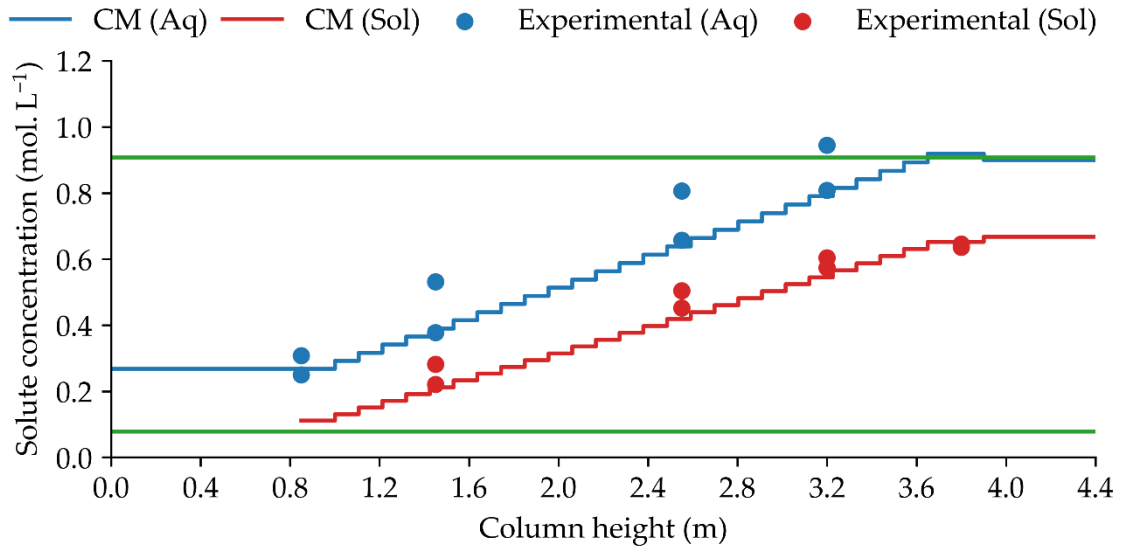


**Figure 84:** Axial solute concentrations for  $Q_{tot} = 182 \text{ L.hr}^{-1}$ ,  $Af = 2 \text{ cm.s}^{-1}$ .

**Table 32:** Operating parameters and results associated with Figure 84.

|                                     |        |
|-------------------------------------|--------|
| $Q_{tot}$ (L.hr <sup>-1</sup> )     | 182    |
| S:A ratio                           | 1:1.2  |
| $Af$ (cm.s <sup>-1</sup> )          | 2      |
| $C_{aq.in}$ (mol.L <sup>-1</sup> )  | 0.908  |
| $C_{sol.in}$ (mol.L <sup>-1</sup> ) | 0.079  |
| $NTU_{aq}$                          | 1.62   |
| $HTU_{aq}$ (m)                      | 1.73   |
| $SE_{av}$ (%)                       | 26.1   |
| $RMSE_{aq}$ (mol.L <sup>-1</sup> )  | 0.0880 |
| $RMSE_{sol}$ (mol.L <sup>-1</sup> ) | 0.0401 |
| $RMSE_{tot}$ (mol.L <sup>-1</sup> ) | 0.0684 |

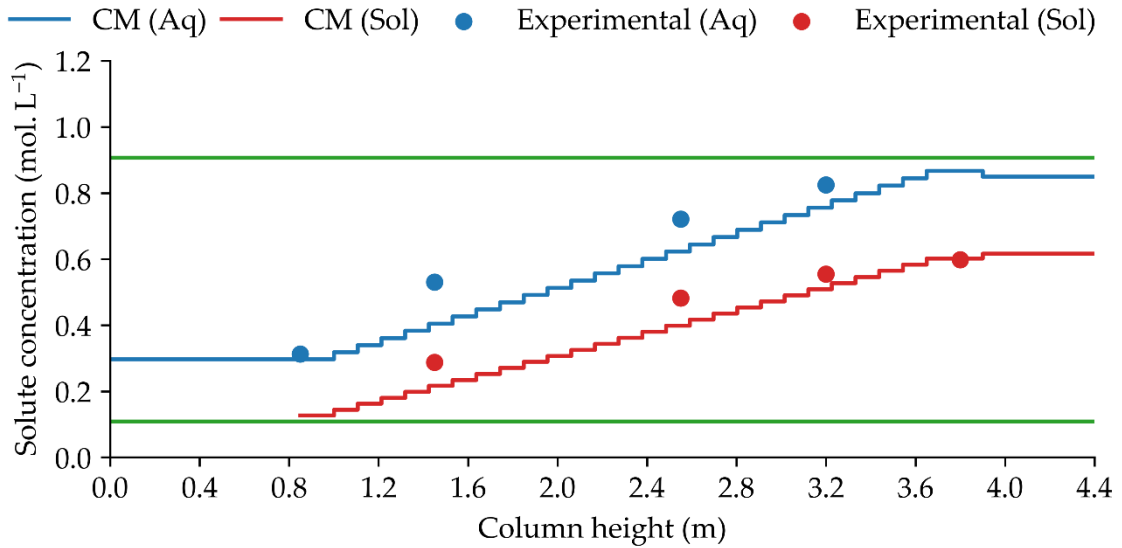


**Figure 85:** Axial solute concentrations for  $Q_{tot} = 205 \text{ L.hr}^{-1}$ ,  $A_f = 1 \text{ cm.s}^{-1}$ .

**Table 33:** Operating parameters and results associated with Figure 85.

|                                     |        |
|-------------------------------------|--------|
| $Q_{tot}$ (L.hr <sup>-1</sup> )     | 2015   |
| S:A ratio                           | 1:1.2  |
| $A_f$ (cm.s <sup>-1</sup> )         | 1      |
| $C_{aq.in}$ (mol.L <sup>-1</sup> )  | 0.907  |
| $C_{sol.in}$ (mol.L <sup>-1</sup> ) | 0.109  |
| $NTU_{aq}$                          | 1.56   |
| $HTU_{aq}$ (m)                      | 1.80   |
| $SE_{av}$ (%)                       | 22.6   |
| $RMSE_{aq}$ (mol.L <sup>-1</sup> )  | 0.0766 |
| $RMSE_{sol}$ (mol.L <sup>-1</sup> ) | 0.0511 |
| $RMSE_{tot}$ (mol.L <sup>-1</sup> ) | 0.0651 |

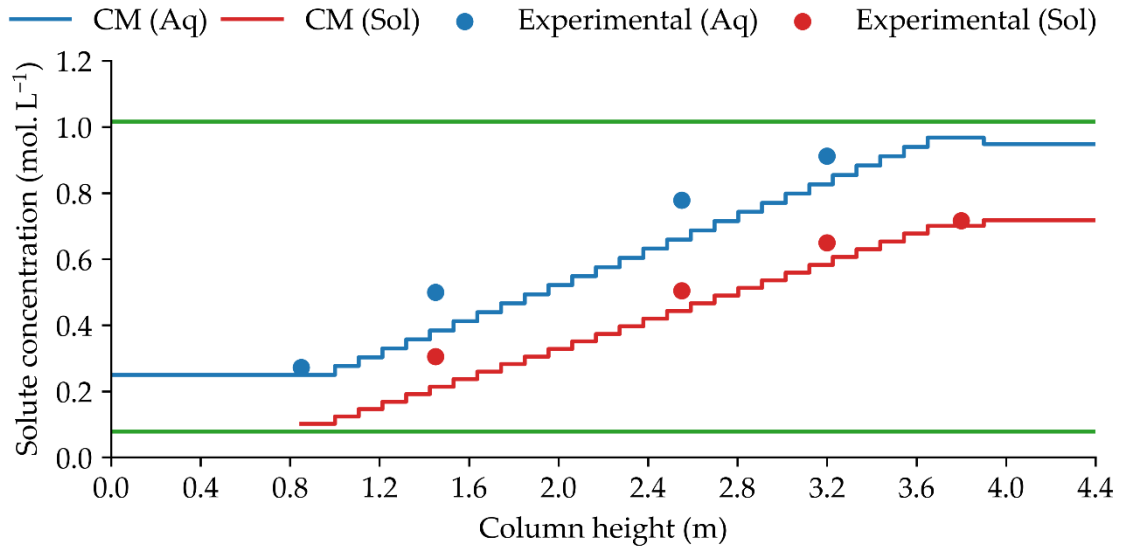


**Figure 86:** Axial solute concentrations for  $Q_{tot} = 205 \text{ L.hr}^{-1}$ ,  $Af = 2 \text{ cm.s}^{-1}$ .

**Table 34:** Operating parameters and results associated with Figure 86.

|                                     |        |
|-------------------------------------|--------|
| $Q_{tot}$ (L.hr <sup>-1</sup> )     | 205    |
| S:A ratio                           | 1:1.2  |
| $Af$ (cm.s <sup>-1</sup> )          | 2      |
| $C_{aq.in}$ (mol.L <sup>-1</sup> )  | 1.017  |
| $C_{sol.in}$ (mol.L <sup>-1</sup> ) | 0.079  |
| $NTU_{aq}$                          | 1.65   |
| $HTU_{aq}$ (m)                      | 1.69   |
| $SE_{av}$ (%)                       | 29.3   |
| $RMSE_{aq}$ (mol.L <sup>-1</sup> )  | 0.0650 |
| $RMSE_{sol}$ (mol.L <sup>-1</sup> ) | 0.0369 |
| $RMSE_{tot}$ (mol.L <sup>-1</sup> ) | 0.0528 |





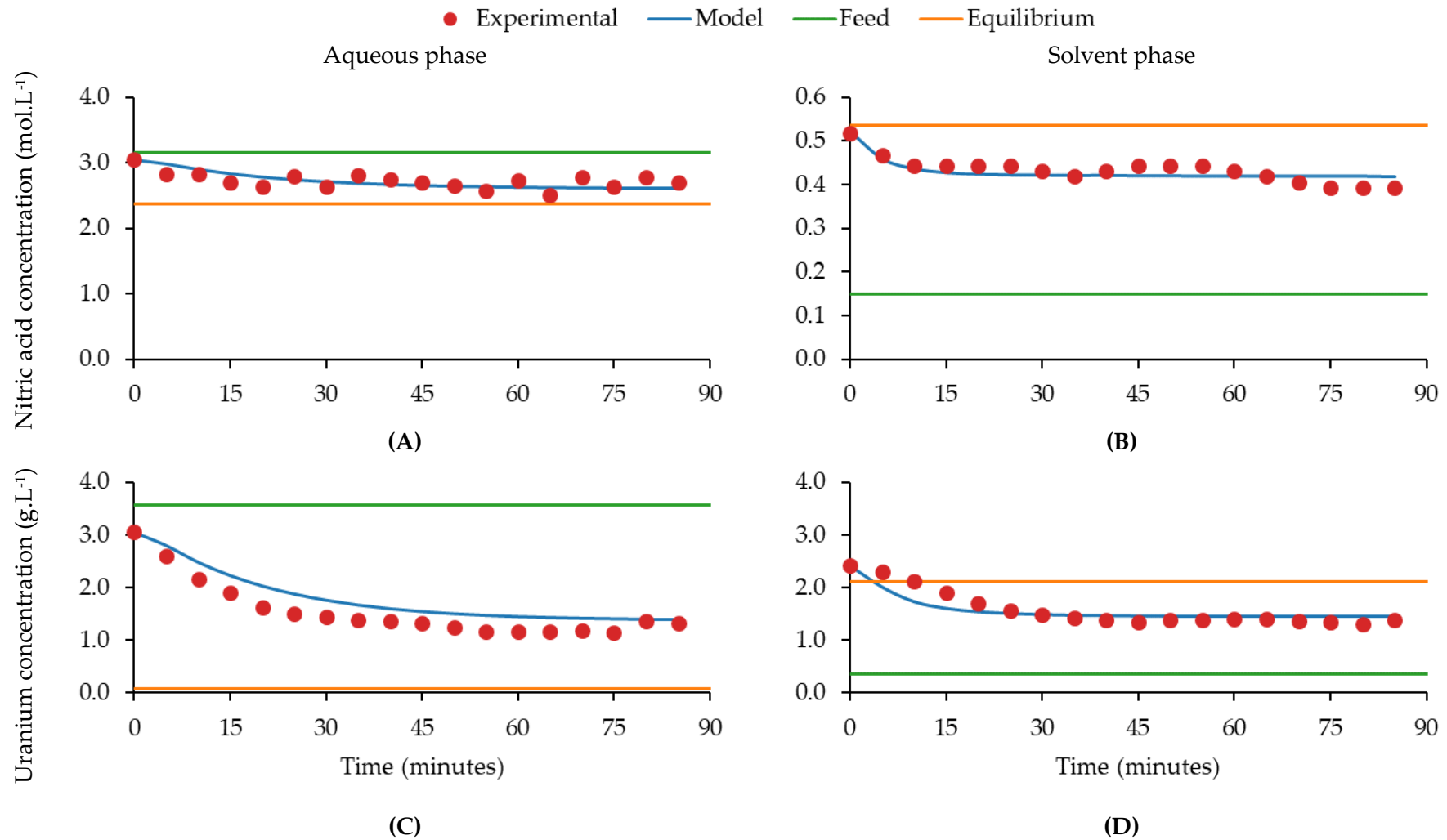


**Figure 89:** Experiment 3 results and modelled solute concentrations for: (A) aqueous outlet nitric acid; (B) solvent outlet nitric acid; (C) aqueous outlet uranium; and (D) solvent outlet uranium.

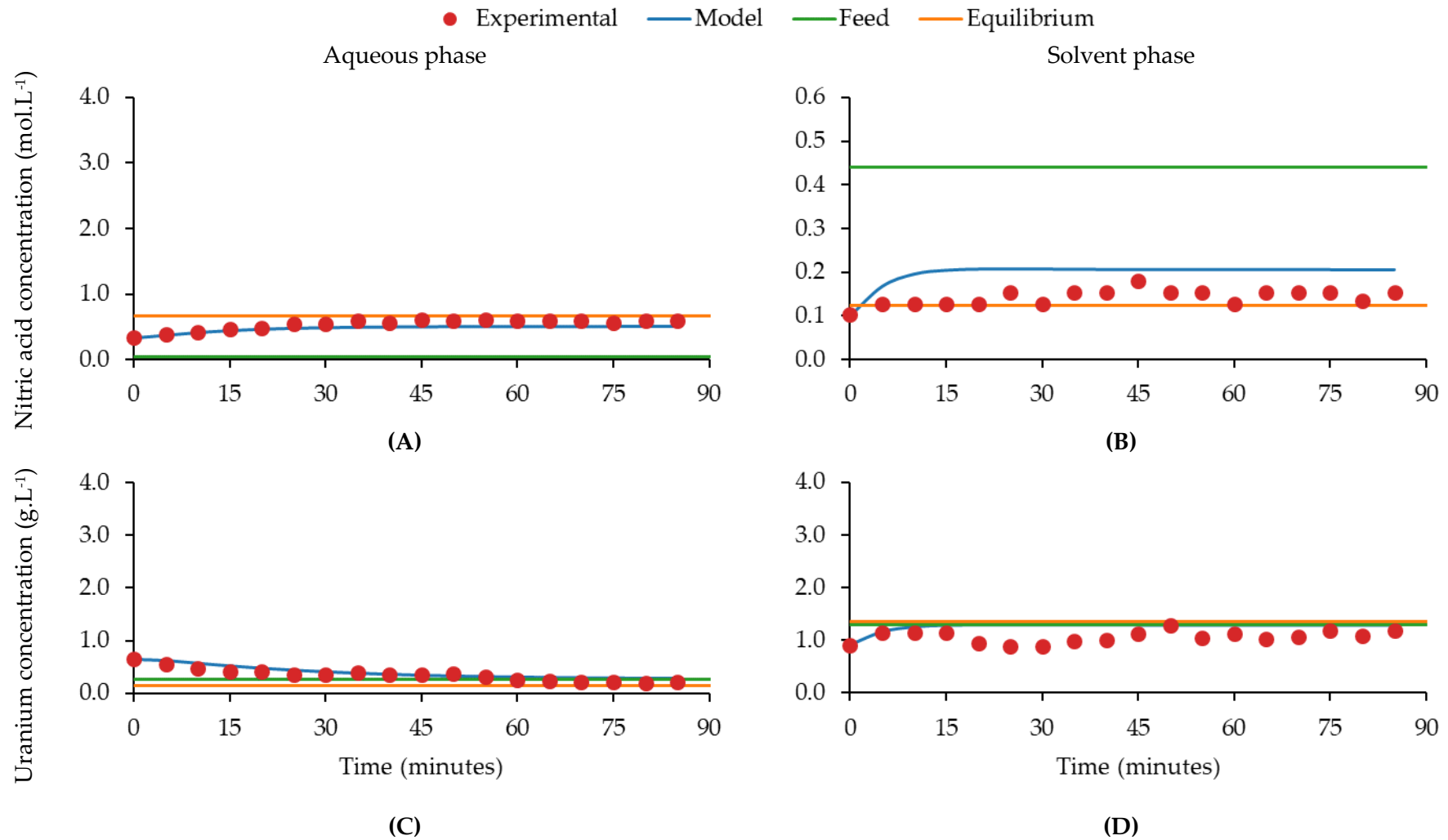


**Figure 90:** Experiment 4 results and modelled solute concentrations for: (A) aqueous outlet nitric acid; (B) solvent outlet nitric acid; (C) aqueous outlet uranium; and (D) solvent outlet uranium.

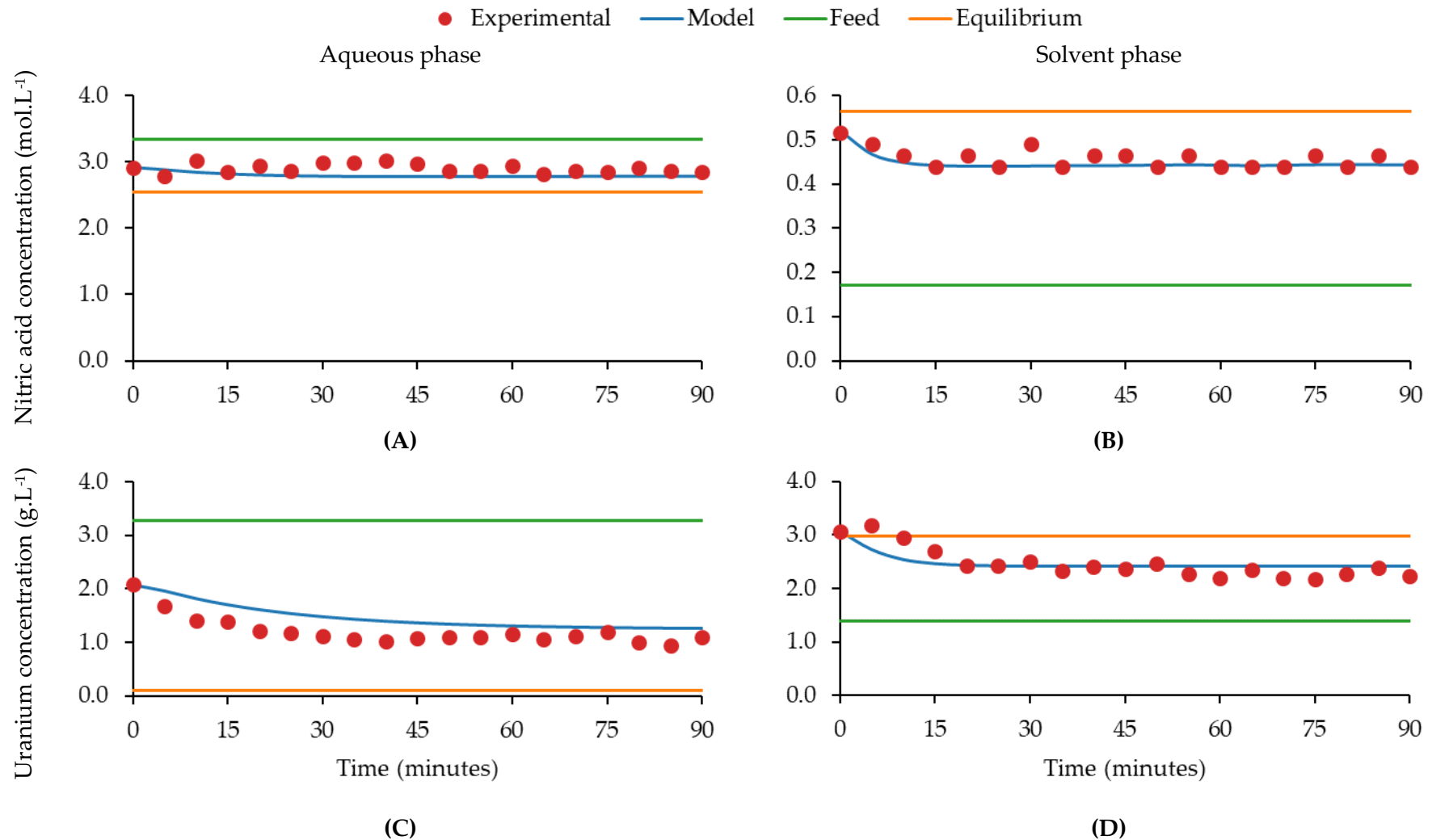


**Figure 91:** Experiment 5 results and modelled solute concentrations for: (A) aqueous outlet nitric acid; (B) solvent outlet nitric acid; (C) aqueous outlet uranium; and (D) solvent outlet uranium.

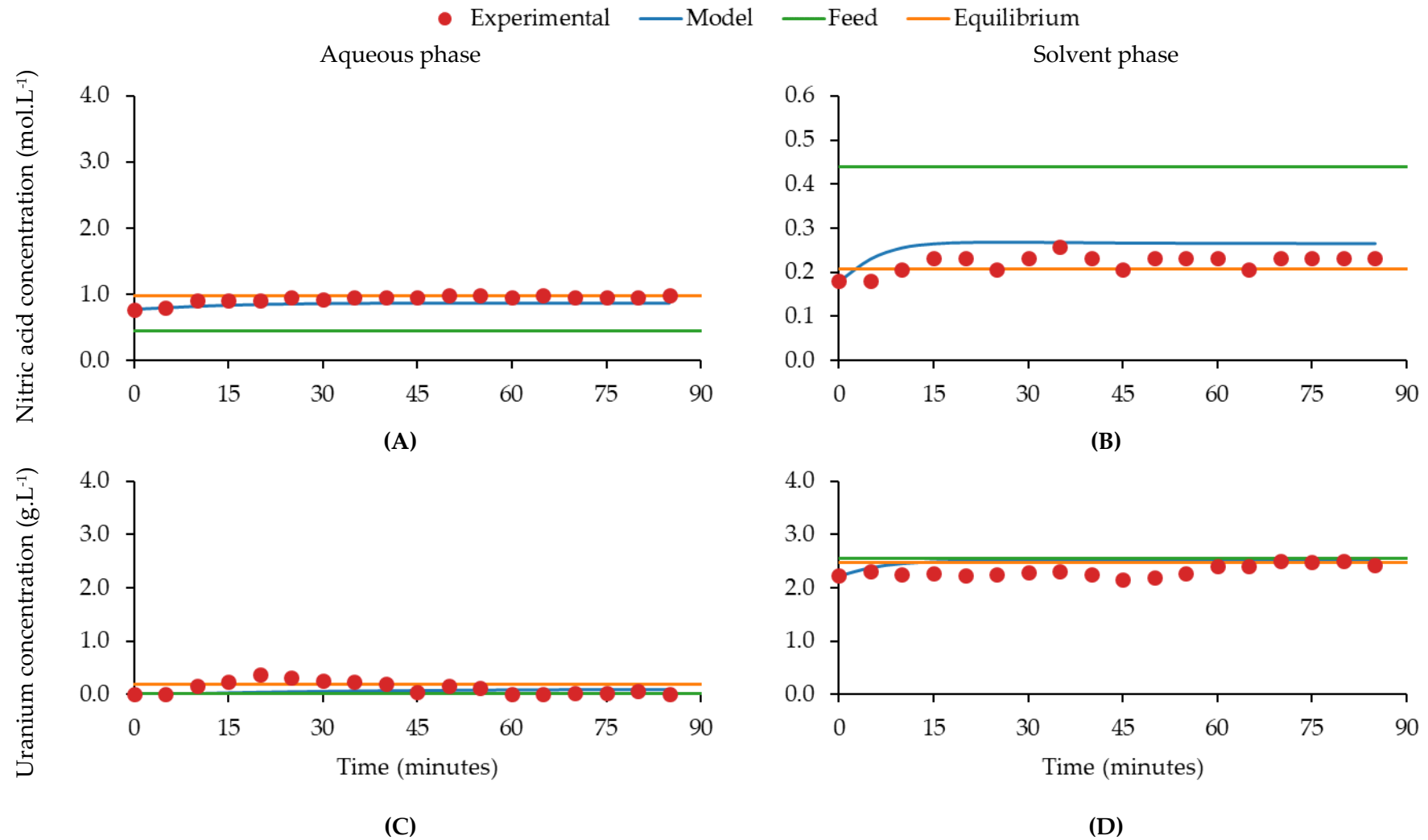


**Figure 92:** Experiment 6 results and modelled solute concentrations for: (A) aqueous outlet nitric acid; (B) solvent outlet nitric acid; (C) aqueous outlet uranium; and (D) solvent outlet uranium.

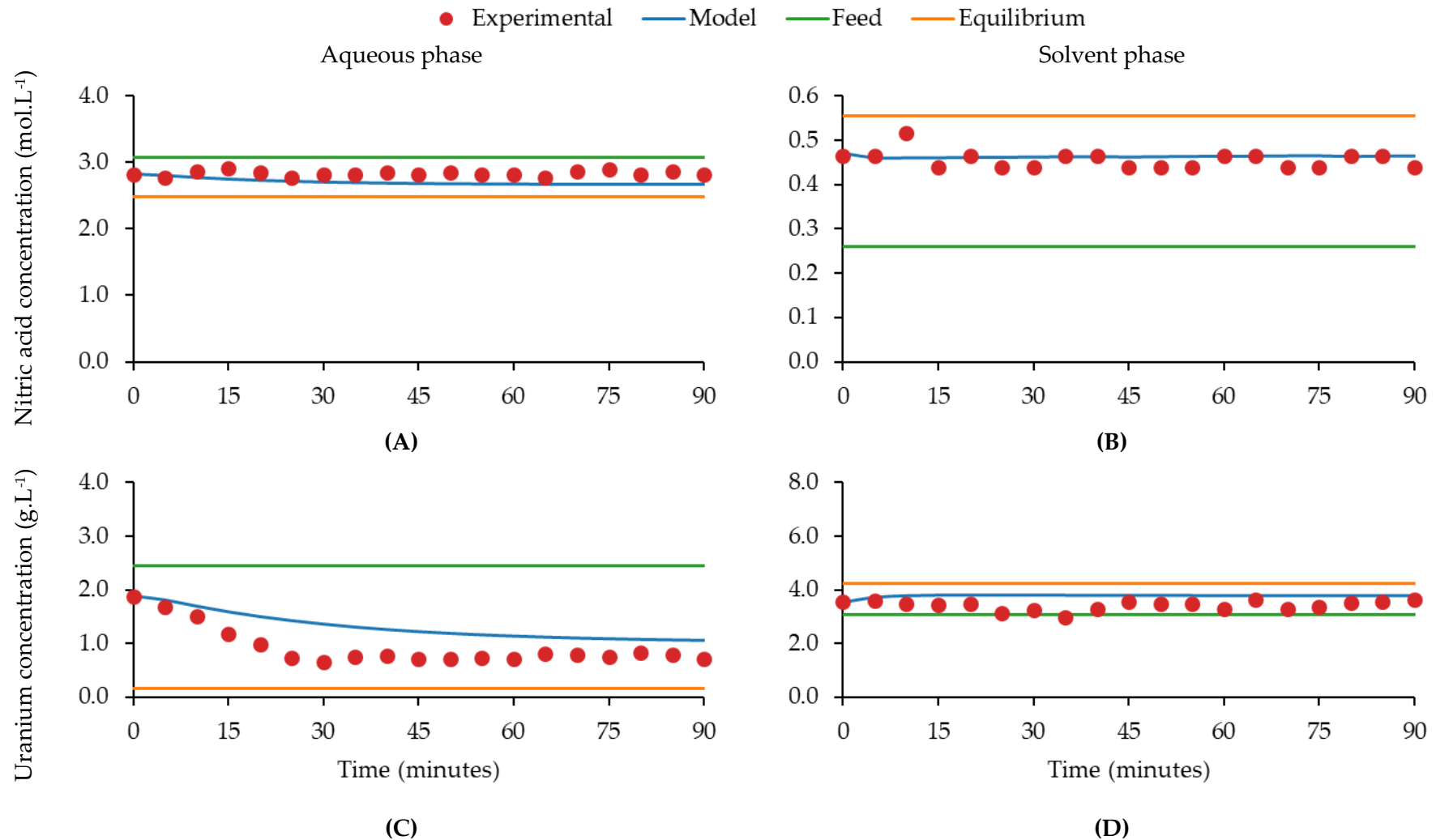


**Figure 93:** Experiment 7 results and modelled solute concentrations for: (A) aqueous outlet nitric acid; (B) solvent outlet nitric acid; (C) aqueous outlet uranium; and (D) solvent outlet uranium.

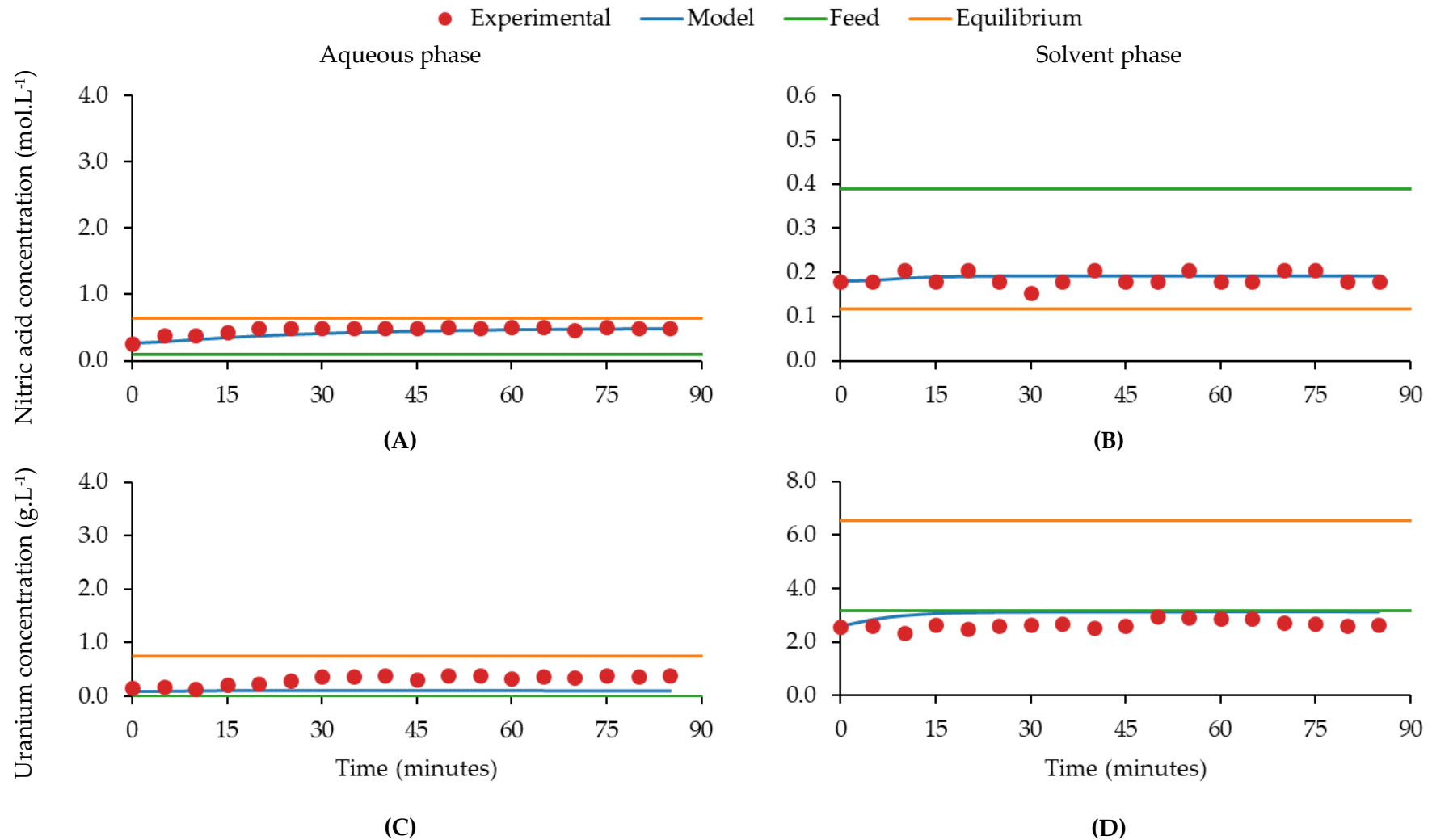


**Figure 94:** Experiment 8 results and modelled solute concentrations for: (A) aqueous outlet nitric acid; (B) solvent outlet nitric acid; (C) aqueous outlet uranium; and (D) solvent outlet uranium.